Inter-Period Correlations of Fourier Amplitude Spectra of Ground-Motions: Modeling, Calibration of Earthquake Simulations, and Significance in Seismic Risk

By

JEFFREY ROSS BAYLESS

DISSERTATION

Submitted in partial satisfaction of the requirements for the degree of

DOCTOR OF PHILOSOPHY

in

Civil & Environmental Engineering

in the

OFFICE OF GRADUATE STUDIES

of the

UNIVERSITY OF CALIFORNIA

DAVIS

Approved:

_____

Norman Abrahamson, Chair

_____

Sashi Kunnath

_____

Amit Kanvinde

Committee in Charge

2018

Jeffrey Ross Bayless
December 2018
Civil and Environmental Engineering

Inter-period correlations of Fourier amplitude spectra of ground-motions: modeling, calibration of earthquake simulations, and significance in seismic risk

Abstract

Physics-based earthquake simulations, which predict the ground-motions generated by scenario earthquakes, have the potential to be extremely useful in dynamic analyses of structures because they can be generated for scenarios not well represented in the empirical data set such as M8 earthquakes and for site/source-specific rupture geometries. But before simulations are accepted for engineering applications, they first need be validated against recorded data and empirical models. Recent efforts have made significant progress towards validation by considering the median predictions of simulations (e.g. Goulet et al., 2015), but further work is still required in order to validate other critical ground-motion properties. This dissertation develops the framework for validation of one important parameter: the inter-period correlation of epsilon (ϵ) of ground-motions. The purpose of this research is three-fold: (1) to illustrate that the inter-period correlation of ϵ (ρ_ϵ) is a critical feature of ground motions that influences variability of structural response and which should be considered as a validation parameter, (2) to develop an avenue for improving

the correlation in the simulations, and (3) to provide an example application which can help guide future calibrations.

To achieve these goals, an empirical ground-motion model (GMM) is developed for smoothed Fourier amplitude spectra (FAS), and the residuals from this model are used to develop a model for the ρ_ϵ of the FAS. The FAS is used because it is a more direct representation of the frequency content of the ground motions than response spectra and is better understood by seismologists. Using simple ground-motion simulations based on the point-source stochastic method, the importance of the ρ_ϵ of FAS in capturing the variability of structural response is demonstrated. Results show that without the adequate ρ_ϵ of FAS in the simulations, variability in the structural response may be under-estimated. This leads to structural fragilities which are too steep (under-estimated dispersion parameter β) and to non-conservative estimates of seismic risk.

To commence the validation process, ρ_ϵ of the smoothed FAS of several established ground-motion simulation methods are compared with the ρ_ϵ observed in data. None of the six finite-fault simulation methods tested adequately capture the ρ_ϵ over the entire frequency range evaluated, although several of the methods show promise, especially at low frequencies. The validation is performed for the FAS because this information provides the developers of the simulation methods better feedback in terms of how they can modify their methods that is not clear when using response spectra comparisons. Finally, the calibration of ρ_ϵ for one simulation method, EXSIM (Aktinson and Assatourians, 2014) is demonstrated and tested. Recommendations are provided for future ρ_ϵ calibration efforts.

Acknowledgements

Kanye West once said, “People never get the flowers while they can still smell them,” which I loosely interpret to mean: don’t hesitate to thank others when given the chance. This doctoral dissertation is an openly-accessible document, therefore it serves as a relatively rare opportunity to express my gratitude both publicly and in writing. To the many people who have made this achievement possible: I sincerely thank you.

First, I would like to acknowledge and thank my advisor, Professor Norm Abrahamson, for sharing his vision, for his guidance, and for his dedication not just to me, but to all of his students. Norm’s knowledge and influence in the engineering seismology field is well documented, and I consider it an honor to be one of his PhD students. Throughout my UC Davis experience, colleagues in professional practice frequently asked me how often I was in contact with Norm, knowing that he was extremely busy with other responsibilities, and invariably my answer was “all the time.” Professor Abrahamson’s long history of prioritizing his students, me among them, is something I will be forever grateful for. My favorite part of working with Norm has been experiencing his relentless focus on specialized engineering problems, no matter how far removed from the bigger picture they may seem at the time, which he (and others) tackle one by one as building blocks towards a larger goal.

I would also like to thank my dissertation committee members Professor Sashi Kunnath and Professor Amit Kanvinde. I am honored to have both as members of my committee. Additionally,

I would like to thank all of the CEE department staff and faculty for their hard work and for the superb educational environment they have created at UC Davis.

Financial support for this project, and my education, was provided by the Pacific Gas and Electric Company GeoSciences department.

My colleagues at AECOM have been truly supportive and are deserving of special recognition. I would like to thank my supervisor Dr. Paul Somerville, foremost for supporting my decision to pursue this degree, and also for his flexibility, patience, and leadership. Working with and for Paul has been delightful and fulfilling. I am also greatly appreciative of the other members of our engineering seismology group: Andreas Skarlatoudis, Hong Kie Thio, Wenwen Li, and Carla Willis. Particularly Andreas, who I would like to thank for his great friendship, and who has been a joy to work with and a tremendous partner in getting projects done. I would also like to thank many other colleagues and friends for their support and collaboration, in particular: Christine Goulet, Fabio Silva, Maha Kenawy, Ronnie Kamai, Rob Graves and Arben Pitarka. And to my closest friends; you know who you are.

Last but not least, I would like to thank my family. To my parents, Pam and Jim Bayless, who continue to inspire me with their love for others and for each other, and who have taught me by example how to be a good person. Thank you for everything. To my wife Dana, one day I hope to be able to express how lucky I am to share life with you, but today is not that day. Your innate kindness, patience, and tranquility are all so strong that they are infectious; you are a beautiful soul. Thank you. To my daughter Dylann and my son Devin, I love you both more than you know. This dissertation is dedicated to you.

Table of Contents

List of Figures

List of Tables

Chapter 1:

Introduction

Research Objectives

The seismological community has been developing methods to numerically simulate seismograms for engineering applications. To date, the amplitudes of numerical simulation have been used in engineering practice to constrain ground-motion models; however, the seismograms have not been adequately validated for other characteristics including the variability of the Fourier spectra. Without adequate validation, the time series from the numerical simulations are not ready for use in engineering applications.

This dissertation contributes to improving ground-motion simulations, precisely with respect to their inter-frequency correlation. The purpose of this research is three-fold: to illustrate that the inter-period correlation in ground-motion simulations is a critical feature which should be considered as a validation parameter, to develop an avenue for improving the correlation in the simulations, and to provide an example application which can help guide future calibrations.

This introduction chapter provides some background on the inter-frequency correlation of ground-motions, presents a literature review of the related topics, and closes with a description of the subsequent dissertation chapters.

Background and Motivation

To define the inter-frequency correlation, some background is first given on earthquake ground-motion models (GMMs, also called ground-motion prediction equations, GMPEs, or attenuation models). GMMs are used for estimating the level of ground shaking at a site, including the variability in that level, based on earthquake magnitude, source-to-site distance, local site

conditions, and other seismological parameters. Among other applications, GMMs are often used in probabilistic seismic hazard analyses (PSHA), including those performed to develop the U.S. Seismic Design Maps (ASCE, 2016). GMMs can be developed using recorded ground-motions, using numerical earthquake simulations, or a combination of both approaches.

Empirical GMM residuals are the difference, in logarithmic units, between the recorded ground shaking and the median ground shaking predicted by the GMM. These residuals are typically partitioned into between-event residuals (δB), and within-event residuals (δW), following the notation of Al Atik et al., (2010). For large numbers of recordings per earthquake, the between-event residual is approximately the average difference in logarithmic-space between the observed Intensity Measure (IM) from a specific earthquake and the IM predicted by the GMM. The within-event residual (δW) is the difference between the IM at a specific site for a given earthquake and the median IM predicted by the GMM plus δB. By accounting for repeatable site effects, δW can further be partitioned into a site-to-site residual ($\delta S2S$) and the single-station within-event residual (δWS) (e.g. Villani and Abrahamson, 2015).

The residual components δB, $\delta S2S$ and δWS are well-represented as zero-mean, independent, normally-distributed random variables with standard deviations τ, ϕ_{S2S}, and ϕ_{ss}, respectively (Al Atik et al., 2010). These GMM residual components are converted to epsilon (ϵ_B, ϵ_{S2S}, and ϵ_{WS}) by normalizing the residuals by their respective standard deviations. Because of the normalization, the random variables ϵ_B, ϵ_{S2S}, and ϵ_{WS} are represented by standard-normal distributions (mean=0, variance=1). If the total residual is used, then the resulting ϵ_{total} will, in general, not have zero mean due to the uneven sampling of recordings per earthquake in per site in the data set.

For a given recording, the values of ϵ at neighboring periods (T) are correlated. For example, if a ground motion is stronger than average at T=1.0 s, then it is likely to also be stronger than expected at nearby periods, e.g. T=0.8 s or T=1.2 s; however, for a widely-spaced period pair (e.g. T=10.0 s compared with T=1.0 s), the ϵ values will be weakly correlated. The inter-period correlation coefficient, ρ, quantifies the relationship of ϵ values between periods for a given recording. The correlation can also be described in terms of ground-motion frequency (f, where $f = 1/T$), and so the terms inter-period and inter-frequency are used interchangeably in this dissertation.

The correlation coefficient of two random variables is a measure of their linear dependence. In this case, ϵ calculated from a large set of ground motions at different frequencies (f) are random variates. The correlation coefficient between $\epsilon(f_1)$ and $\epsilon(f_2)$ can be estimated using a maximum likelihood estimator, the Pearson-product-moment correlation coefficient, ρ (Fisher, 1958). The correlation coefficient for a sample of ϵ at frequencies f_1 and f_2 is given by Equation 1-1,

$$\rho_{\epsilon(f_1),\epsilon(f_2)} = \frac{cov\big(\epsilon(f_1),\epsilon(f_2)\big)}{\sigma_{\epsilon(f_1)}\sigma_{\epsilon(f_2)}} = \frac{\sum_{i=1}^{n}\big(\epsilon_i(f_1) - \overline{\epsilon(f_1)}\big)\big(\epsilon_i(f_2) - \overline{\epsilon(f_2)}\big)}{\sqrt{\sum_{i=1}^{n}\big(\epsilon_i(f_1) - \overline{\epsilon(f_1)}\big)^2}\sqrt{\sum_{i=1}^{n}\big(\epsilon_i(f_2) - \overline{\epsilon(f_2)}\big)^2}} \quad (1-1)$$

where cov is the covariance, σ is the standard deviation, n is the total number of observations, i is the i^{th} observation of ϵ, and $\overline{\epsilon(f_1)}$ and $\overline{\epsilon(f_2)}$ are the sample means of ϵ at frequencies f_1 and f_2, respectively. The $\bar{\epsilon}$ will be equal to zero if the GMM is unbiased. The relation for $\rho_{\epsilon(f_1),\epsilon(f_2)}$ given in Equation 1-1 is reciprocal: the correlation coefficient between two given frequencies is the same regardless of which frequency is the conditioning frequency. To account for all three residual terms, the total correlation is calculated as shown in Equation 1-2,

$$\rho_{\epsilon,total}(f_1, f_2) =$$

$$\frac{\rho_B(f_1, f_2)\tau(f_1)\tau(f_2) + \rho_{S2S}(f_1, f_2)\phi_{S2S}(f_1)\phi_{S2S}(f_2) + \rho_{WS}(f_1, f_2)\phi_{ss}(f_1)\phi_{ss}(f_2)}{\sigma(f_1)\sigma(f_2)} \quad (1-2)$$

where $\rho_B(f_1, f_2)$ is the correlation of the normalized between-event residuals, $\rho_{S2S}(f_1, f_2)$ is the correlation of the normalized site-to-site residuals, and $\rho_{WS}(f_1, f_2)$ is the correlation of the normalized single-station within-event residuals.

Using a database of residuals, the calculation of $\rho_{\epsilon(f_1),\epsilon(f_2)}$ can be repeated for every frequency pair of interest. Figure 1-1 shows a graphical representation of this step at three example frequency pairs. The resulting correlation coefficients for each pair of frequencies can be saved as tables (e.g. Abrahamson et al., 2014; Al Atik, 2011; Akkar et al., 2014; Azarbakht et al., 2014; Jayaram et al., 2011), or can be empirically modeled. For modern GMMs, models of the correlation of ϵ are commonly created for PSA (e.g. Baker and Cornell, 2006; Baker and Bradley, 2017; Baker and Jayaram, 2008; Cimellaro 2013; Goda and Atkinson, 2009). Recently, correlation models for ϵ from Fourier amplitude spectra (FAS) have also been developed (e.g. Stafford, 2017; and Chapter 3 of this dissertation).

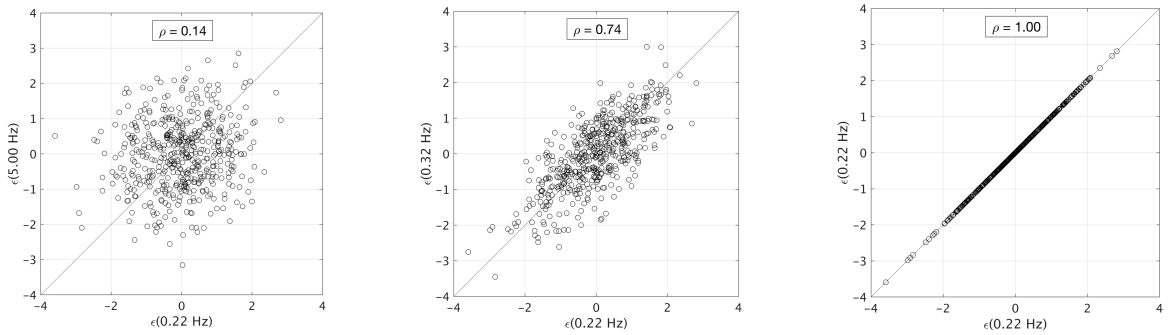

Figure 1-1. ϵ values at pairs of frequencies calculated from a database of ground motions, exhibiting the correlation dependent on frequency spacing. Left: f_1 = 0.2 Hz and f_2 = 5.0 Hz. Middle: f_1 = 0.2 Hz and f_2 = 0.3 Hz. Right: f_1 = 0.2 Hz and f_2 = 0.2 Hz

Physical Meaning and Relevance of ρ_ϵ

Because larger-than-average ground motions tend to be from local spectral peaks and lower-than-average ground motions tend to be from local spectral troughs, the parameter ϵ is an indicator of the peaks and troughs at a given frequency in a spectrum. And since ρ_ϵ is a measure of the linear dependence of ϵ between two frequencies, it follows that ρ_ϵ characterizes the relative width of these extrema. For example, very high ρ_ϵ (values close to one) over broad frequency pairs indicate wide peaks and troughs in the spectra; leading to smoother undulating spectra. Conversely, very low ρ_ϵ (values close to zero) between neighboring frequency pairs indicate very narrow peaks and troughs; leading to 'noisy' looking spectra.

The generic term 'spectra' can refer to either PSA or FAS. PSA spectra are the peak response from a single degree of freedom oscillator system. PSA spectra are influenced by a range of frequencies, and the breadth of that range is dependent on the oscillator period (discussed in Chapter 2) and on the damping. The FAS provides a more direct representation of the frequency content of the ground

motions, and because the Fourier transform is a linear operation, the FAS is a much more straightforward representation of the ground motion and is better understood by seismologists than PSA. This simpler behavior makes the FAS preferable over PSA for incorporating inter-period correlation into numerical methods for ground-motion simulations, and it is the primary IM adopted in this study.

Because ρ_ϵ is a measure of the width of spectral peaks, it has relevance in dynamic structural response. For linear response, a structure will be sensitive to the frequency content over a range of frequencies about the natural frequency of the structures. For the uncorrelated case, if the ϵ value at a given frequency is a high positive value (corresponding to a peak), the values of ϵ at the nearby frequencies will be randomly high or low, so the response of the structure will not be strongly affected by the ground motion at these neighboring frequencies; however, for the correlated case, the values of ϵ at the nearby frequencies will tend to also be positive values so the response of the structure will increase by a larger factor due to the increased response from the neighboring frequencies. During nonlinear seismic response, the effect of the correlation can be even greater than for linear response. For nonlinear response, structures can experience softening characterized by elongation of their natural vibration period (Lin et al., 2008; Bradford 2007). This occurs when damage to the structural elements leads to large strains which reduce the effective stiffness and increases effective damping. As a structure softens, its effective fundamental period increases, and the response will depend on if the structure is softening into a peak or a trough in the spectrum. For the correlated case, the chance of softening into a peak or a trough will depend on the breadth of a ground motion spectral peak or trough, thereby affecting the structural response. The aggregate

effect is the variability in structural response is higher for ground motions with realistic ρ_ϵ than for ground motions with unrealistically low ρ_ϵ; this point is demonstrated in Chapter 4.

Ground-Motion Simulations

Methods for simulating the ground motions generated by earthquakes have been developed and refined over the past several decades. "Physics-based" earthquake ground-motion simulations can be defined as the prediction of the ground-motion generated by earthquakes by means of numerical methods and models that explicitly incorporate the physics of the earthquake source and the resulting propagation of seismic waves (Taborda and Roten, 2014). Simulations methods described as "stochastic" rely less on solving the equation of motion and are calibrated empirically. "Hybrid" techniques employ some combination of the physics-based and stochastic-based approaches. These methods vary in technique and complexity, but most of them generate the same product; a simulated time series of ground motion at a select location on the earth surface. For more information, Burks (2014) provides an excellent review of existing simulation methods.

Engineering Utilization of Simulations

Simulations have the potential to be extremely useful in engineering applications, particularly when earthquake time series are required for input into dynamic structural analyses. There are limited numbers of ground-motion recordings for large magnitude earthquakes recorded at close distances, and simulations can fill this gap in the recorded databases. There are several potential applications of simulations of large magnitude, near source scenarios. First, for sites located near active major faults, simulations can provide scenario ground motions for deterministic design and

analyses. Similarly, simulations can be used to constrain the near-source magnitude scaling of ground-motion models (e.g. Chapter 2), which are in turn used in PSHA. Or, simulations can be used explicitly to perform PSHA, which has the potential to reduce uncertainties by capturing the complex physics that are ignored using traditional PSHA methods (e.g. CyberShake; Graves et al., 2011). Simulations also have application beyond just near-source, large magnitude scenarios. Because they provide the full time series of ground motion, the simulations can be used to analyze the dynamic response of geotechnical models and engineered structures. The source- and site-specific nature of simulations means the ground motions have the potential to contain rupture directivity pulses, static offset, and directionality.

Validation of Simulations

There is increasing recognition that simulations can be utilized as described above, but for the simulations to be accepted, they should be validated first. Validation means that the simulations should produce ground-motions consistent with observations (Burks, 2014). Validations can be broadly categorized as either comparisons with recorded data or with empirical models.

Several examples of validation exist in the literature. The earliest examples used qualitative measures for subjectively validating the methods, including comparisons of waveforms by the same researcher who developed the method and performed the simulation. More recent validations are performed by third parties and attempt to develop criteria for objectively assessing the simulations in a consistent manner. Examples of recent validations include Burks and Baker (2014), Goulet et al., (2015) and Luco et al., (2016).

Burks and Baker (2014) proposed a validation framework based off three main structural response proxies: the inter-period correlation of ϵ for response spectra, the ratio of maximum-to-median spectral acceleration across all horizontal orientations, and the ratio of inelastic-to-elastic displacement. The conclusions from Burks and Baker (2014) regarding the inter-period correlation of ϵ for response spectra are addressed in Chapter 4. In short, the simulation methods need calibration with respect to this parameter.

In the year 2013, the 'Broadband Platform Validation Exercise' was organized by the Southern California Earthquake Center (SCEC; Dreger et al., 2015 and Goulet et al., 2015). This exercise evaluated several simulation methods on the suitability of simulated PSA for use in engineering applications. This validation exercise focused on evaluating the median PSA for a gauntlet of subjective and objective validation criteria, using both recorded earthquakes and GMMs. The Dreger et al. (2015) validation exercise was an important first step towards a more complete validation of the simulation methods considered.

The SCEC Ground Motion Simulation Validation (GMSV) Technical Activity Group was planned in coordination with the Dreger et al., (2015) validation effort. As document in Luco et al., (2016), this group developed rating systems for collections of ground-motion parameters related to structural response. The inter-frequency correlation of ϵ was suggested for validation but was determined to be outside the scope of the project.

The aforementioned efforts are three examples of successful validation schemes, even though not all of the simulation methods were deemed acceptable for all metrics. For the simulations to continue on the path towards widespread approval, the methods must pass all previous validations,

and more validations for different properties are necessary. In addition to the Burks and Baker (2015), Goulet et al., (2015), and Luco et al., (2016) parameters, other ground-motion properties which need to be validated are listed below. Validations of the aleatory variability and the inter-frequency correlation of ϵ (FAS first, then PSA) should be the first priority after performing validations for the median response. This is because the appropriate ρ_ϵ is required for simulations to be used in seismic risk, as described in Chapter 4. The research described in this dissertation focuses on the inter-frequency correlation of ϵ, and beyond just validation, an avenue is developed for improving the correlation in the simulations. Validation of the remaining properties should be the topics of future research.

Additional ground-motion properties for validation

1. Median ground-motions
    a. PSA (5% damped). This is the Dreger et al., (2014) case, which did not address other features.
    b. FAS
    c. PSA and FAS, vertical component
2. Other FAS features
    a. Inter-frequency correlation of ϵ
    b. Aleatory variability
    c. Variability between horizontal components
3. Duration features
    a. Acceleration-based (high frequencies)
    b. Velocity-based (intermediate frequencies)
4. Damping scale factors
    a. Scale factors from 2% to 30% damping (high damping for base isolation)
5. Peak velocity scaling
    a. Ratio of peak ground velocity to PSA at T=1 sec
    b. Separation of within-basin and outside basin sites
6. V/H ratio for FAS
    a. Check for the linear site response range

Literature Review

Fourier amplitude spectra GMMs

GMMs for Fourier amplitude spectra are less common than their response spectrum counterparts. Douglas (2018) summarized all GMMs published worldwide between 1964 and early 2018 and found only 16 empirical models for the prediction of Fourier amplitude spectra out of 1,243 total models. From the past five years, only four FAS models are identified in Douglas (2018): Bora et

al., (2014), Bora et al., (2015), Lee et al., (2015), and Gupta and Trifunac (2017). In the short time since the Douglas (2018) catalog release, an FAS model by Bora et al., (2018) was also accepted for publication. Both Bora et al., (2014), and Bora et al., (2015) are developed using data from Europe, the Middle-East and the Mediterranean regions. Lee et al., (2015) uses data from Serbia and Gupta and Trifunac (2017) uses data from the Himalaya and northeastern India regions.

Bora et al., (2018) uses more recent data from shallow crustal earthquakes recorded globally (from the United States, Taiwan, Japan, and Italy). This model is the closest analog to the model developed as part of this dissertation research. However, the Bora et al., (2018) FAS model is very simple and emphasizes fitting the data to the functional form rather than model extrapolation to areas not well-constrained by the data. The median FAS model is developed in parallel with a model for ground motion duration, and these are combined to compute response spectra using random vibration theory. Since the main objective of Bora et al., (2018) is to develop a response spectrum model, a model for the aleatory variability of the FAS is not developed.

Inter-Frequency Correlation GMMs

For modern GMMs, models of the inter-period correlation of ϵ are commonly created for PSA (e.g. Baker and Cornell, 2006; Baker and Bradley, 2017; Baker and Jayaram, 2008; Cimellaro 2013; Goda and Atkinson, 2009; Abrahamson et al., 2014). If not modeled, the correlation has been saved as tables (e.g. Abrahamson et al., 2013; Al Atik, 2011; Akkar et al., 2014; Azarbakht et al., 2014; Jayaram et al., 2011). The Baker and Jayaram (2008) inter-period correlation model for within-event ϵ is based on PSA from crustal earthquakes. Using an updated database, Baker

and Bradley (2017) confirmed that the updated correlations were largely consistent with the Baker and Jayaram (2008) model.

Stafford (2017) developed FAS-based ρ_ϵ models for the between-event, between-site and within-site components of residuals based on the NGA-West1 database (Chiou et al., 2008). This study used unsmoothed FAS ordinates and used both as-recorded horizontal components of the ground-motions. Due to these differences in the smoothing of the FAS and the treatment of the two horizontal components, the resulting correlation models are not directly comparable. The differences between the Stafford model and the model developed here are discussed in Chapter 3.

Validation of the Inter-Frequency Correlation and Variability of Simulations

Recent validation efforts by Burks and Baker (2014) and Luco et al., (2016) are described previously. Bijelic et al., (2018) performed assessments of building performance using sets of recorded and SCEC simulated motions with matching spectral shape and duration. They found a bias in the response of structures under the simulated ground motions caused by the lack of inter-period correlation of the simulations; this conclusion is expanded upon in Chapter 4 of this dissertation.

Wang and Jordan (2014) applied a technique named Average-Based Factorization (ABF) to compare simulation-based and GMM-based seismic hazard models. ABF uses a hierarchical averaging scheme to separate the simulated ground-motions into relative (dimensionless) excitation fields representing site, path, directivity, and source effects. ABF partitions the variance of each of these effects into uncorrelated components, which allows for a component-wise

comparison between the variability of CyberShake simulations and empirical GMMs. Wang and Jordan (2014) found that for a large ensemble of CyberShake simulations (prototype version CS11), the total CS11 PSA variance is about 60% higher than the NGA-West1 GMMs (Abrahamson et al., 2008) at 2s and almost 30% lower at 10s. This study falls under the category of validation against empirical models.

Organization

This dissertation is organized into six chapters. Following this introduction, there are four main chapters. The dissertation culminates with a chapter summarizing the results and recommending future research areas. The content of the four body chapters are described below. Chapters 2 and 3 have been submitted for publication and Chapter 4 has been accepted for publication; these chapters underwent minor cosmetic modifications from their published versions in order to maintain consistency with the other dissertation chapters.

Chapter 2 describes the development of a ground-motion model for smoothed Fourier amplitude spectra using data recorded in California and Nevada. Generating this model served two main purposes. First, it can be used by others in future applications. Second, a natural result of ground-motion modeling is the residuals, which are used to develop a model for the correlation of the residuals between frequencies. This correlation model is the foundation of the following chapters. This chapter is modified from the paper entitled "An empirical model for Fourier amplitude spectra using the NGA-West2 database", authored by Jeff Bayless and N.A. Abrahamson, has been submitted for publication in the journal *Bulletin of the Seismological Society of America,* and is currently under review.

Chapter 3 describes the development of the model for the correlation of Fourier amplitude spectra residuals between frequencies, based off the EAS residuals from Chapter 2. This chapter is modified from the paper entitled "An empirical model for the inter-frequency correlation of epsilon for Fourier amplitude spectra", authored by Jeff Bayless and N.A. Abrahamson, which has been submitted for publication in the journal *Bulletin of the Seismological Society of America,* and is currently under review.

Chapter 4 is composed of two parts. First, the inter-frequency correlation is demonstrated to be a critical feature which should be considered as a validation parameter in ground-motion simulations, because it relates to the variability of dynamic structural response which controls seismic risk. Second, the inter-frequency correlations in multiple established simulation methods are evaluated to provide guidance for future calibration. This chapter is modified from the paper entitled "Evaluation of the inter-period correlation of ground motion simulations", authored by Jeff Bayless and N.A. Abrahamson, and has been accepted for publication in the journal *Bulletin of the Seismological Society of America.* As this paper was designed to be a standalone article, some material from this introduction chapter is repeated in Chapter 4.

Chapter 5 focuses on techniques to adjust the inter-frequency correlation in simulations to be consistent with the empirical model developed in Chapter 4. The simulation method EXSIM (Aktinson and Assatourians, 2014) is used as an example application of the inter-frequency correlation model. The challenges associated with this implementation are documented and recommendations are provided for future calibration efforts.

Chapter 2:

An empirical model for Fourier amplitude spectra using the NGA-West2 database

Abstract

An empirical ground-motion model (GMM) for shallow crustal earthquakes in California and Nevada based on the NGA-West2 database (Ancheta et al., 2014) is presented. Rather than the traditional response spectrum GMM, this model is developed for the smoothed effective amplitude spectrum (EAS), as defined by PEER (Goulet et al., 2018). The EAS is the orientation-independent horizontal component Fourier amplitude spectrum (FAS) of ground acceleration. The model is developed using a database dominated by California earthquakes, but takes advantage of crustal earthquake data worldwide to constrain the magnitude scaling and geometric spreading. The near-fault saturation is guided by finite-fault numerical simulations and non-linear site amplification is incorporated using a modified version of Hashash et al., (2018). The model is applicable for rupture distances of 0 – 300 km, $\boldsymbol{M}$ 3.0 – 8.0, and over the frequency range 0.1 – 100 Hz. The model is considered applicable for V_{s30} in the range 180 – 1500 m/s, although it is not well constrained for V_{s30} values greater than 1000 m/s. Models for the median and the aleatory variability of the EAS are developed. Regional models for Japan and Taiwan will be developed in a future update of the model. A MATLAB program that implements the EAS GMM is provided in Appendix B of this dissertation.

Introduction

The traditional approach for developing ground-motion models (GMMs) for engineering applications is to use response spectral values for a range of spectral periods. The response spectra GMMs can be used in either deterministic or probabilistic seismic hazard analyses to develop design response spectra. The response spectral values represent the response of a simple structure to the input ground motion and does not directly represent the ground motion itself. As an alternative, Fourier spectral values can be used instead of response spectral values. There are several advantages to using Fourier spectra in place of response spectra: (1) the scaling of Fourier spectra in the GMM is easier to constrain using seismological theory, (2) linear site response remains linear at all frequencies and does not depend on the spectral content of the input motion, as is the case for response spectra (Bora et al., 2016), and (3) for calibrating input parameters and methods for finite-fault simulations based on comparisons with GMMs, Fourier spectra are more closely related to the physics in the simulations.

An empirical Fourier spectrum GMM for shallow crustal earthquakes in California and Nevada based on the Pacific Earthquake Engineering Research Center (PEER) Next Generation Attenuation-West 2 (NGA-West2) database (Ancheta et al., 2014) is developed. The ground-motion parameter used in the GMM is the smoothed effective amplitude spectrum (EAS), as defined by PEER (Goulet et al., 2018). The EAS is the orientation-independent horizontal component Fourier amplitude spectrum (FAS) of ground acceleration that can be used with random vibration theory to estimate the response spectral values.

This paper describes the development of the empirical model using ground-motion data as the foundation, along with finite-fault simulations computed using the SCEC Broadband Platform (Maechling et al., 2015) to constrain the near-fault large-magnitude scaling, and the analytical site response modeling to capture the nonlinear site amplification (Hashash et al., 2018). Rather than simply fitting the empirical data, emphasis is placed on building the model using both the empirical data and analytical results from these seismological and geotechnical models so that the GMM extrapolates in a reasonable manner. A MATLAB program that implements the EAS GMM is provided in Appendix B of this dissertation. A model for the inter-frequency correlation of residuals derived from this GMM is presented in Chapter 3.

EAS Ground Motion Intensity Measure

The Effective Amplitude Spectrum (EAS), defined in Kottke et al., (2018) and used in the PEER NGA-East project (PEER, 2015; Goulet et al., 2018), can be calculated from an orthogonal pair of Fourier Amplitude Spectra (FAS) using Equation 2-1:

$$EAS(f) = \sqrt{\frac{1}{2}[FAS_{HC1}(f)^2 + FAS_{HC2}(f)^2]} \qquad (2-1)$$

where FAS_{HC1} and FAS_{HC1} are the FAS of the two orthogonal horizontal components of the ground motion and f is the frequency in Hz. The EAS is independent of the orientation of the instrument. Using the average power of the two horizontal components leads to an amplitude spectrum that is compatible with the use of RVT to convert Fourier spectra to response spectra. The EAS is

smoothed using the Konno and Ohmachi (1998) smoothing window, which has weights and window parameter defined by:

$$W(f) = \left(\frac{\sin(b\log(f/f_c))}{b\log(f/f_c)}\right)^4 \qquad (2-2)$$

$$b = {}^{2\pi}/_{b_w} \qquad (2-3)$$

The smoothing parameters are described in Kottke et al., (2018): "W is the weight defined at frequency *f* for a window centered at frequency f_c and defined by the window parameter b. The window parameter b can be defined in terms of the bandwidth, in $\log_{10}$ units, of the smoothing window, b_w." The Konno and Ohmachi smoothing window was selected by PEER NGA-East because it led to minimal bias on the amplitudes of the smoothed EAS when compared to the unsmoothed EAS. The bandwidth of the smoothing window, $b = 188.5$, was selected such that the RVT calibration properties before and after smoothing were minimally affected (Kottke et al., 2018). For consistency with the PEER database used to develop empirical FAS models, the smoothed EAS is used with the same smoothing parameters as described in Kottke et al. (2018).

On The Selection of Fourier Amplitudes

In seismic hazard and earthquake engineering applications, the pseudo-spectral acceleration (PSA) of a 5% damped single degree of freedom oscillator is a commonly used IM. PSA is useful for many applications; however it has drawbacks which are discussed here. The EAS component of the FAS is used as the IM for this study, because the FAS is a more direct representation of the frequency content of the ground motions than PSA and is better understood by seismologists. This

leads to several advantages, both in the empirical modeling and in forward application. The reasoning behind these claims is explained in this section.

The PSA calculation involves solving the differential equation for the response of an SDOF oscillator (with given damping) due to a specified forcing function, selecting the peak response of the oscillator, and scaling the peak oscillator displacement by the square of the oscillator natural frequency, ω. This calculation can be repeated for a range of oscillators with different natural frequencies to develop a response spectrum. The elastic SDOF oscillator response is described by the following second order, linear, inhomogeneous differential equation:

$$m * a(t) + c * v(t) + k * u(t) = p(t) \qquad (2-4)$$

where m is the SDOF lumped mass, $a(t)$ denotes the SDOF lateral acceleration, c denotes the viscous damping coefficient, $v(t)$ denotes the SDOF lateral velocity, k denotes the lateral stiffness, $u(t)$ denotes the SDOF lateral displacement relative to the ground, and $p(t)$ denotes the time-dependent forcing function due to the earthquake ground motion (Chopra, 2007).

Duhamel's convolution integral, also known as the unit impulse response procedure, is one approach to solving a linear differential equation, such as the one given by Equation 2-4. With this method, the response of the system (initially at rest) to a unit impulse force is shown (e.g. in Chopra, 2007) to be:

$$h(t-\tau) = \frac{1}{m\omega_d} e^{-\zeta\omega(t-\tau)} \sin[\omega_d(t-\tau)], t \geq \tau \qquad (2-5)$$

where τ is the time instance of the impulse, ω_d is the damped natural frequency, and ζ is the fraction of critical damping. The entire loading history (such as that due to ground acceleration) can then be represented as a succession of infinitesimally short impulses, each producing its own response of the form of Equation 2-5. Since the system is linearly elastic, the total response is the superposition of the responses to all impulses which make up the entire loading history. Taking the limit of the sum as the width of the impulse approaches zero leads to the general expression of Duhamel's integral for an arbitrary forcing function:

$$u(t) = \frac{1}{m\omega_d}\int_0^t p(\tau)e^{-\zeta\omega(t-\tau)}\sin[\omega_d(t-\tau)]\,d\tau = \int_0^t p(\tau)h(t-\tau) = h(t)\otimes p(t) \quad (2-6)$$

where $\otimes$ is the convolution operator. Equation 2-6 is called the convolution integral because convolution is performed in the time domain between the unit impulse response (h), and the force due to ground acceleration (p). Then, by the convolution property of the Fourier transform, the time-domain convolution of h and p can be expressed in the frequency domain as the point-wise multiplication of the Fourier transforms of h and p.

In Figure 2-1, these steps are shown using an example recorded acceleration time history. In the figure, the thin solid black line is the FAS of the recorded acceleration time history, or $|F\{p\}|$, where F denotes the Fourier transform operator. The solid heavy lines are the FAS of the SDOF oscillator impulse response, or $|F\{h\}|$. $|F\{h\}|$ is plotted for three different oscillator frequencies: 0.5, 2.0, and 10.0 Hz, as identified in the figure legend. The dashed lines are the FAS of the SDOF response to the ground motion, $|F\{u\}|$, at the same three frequencies. By Equation 2-4, and the

convolution property of the Fourier transform, for a given oscillator frequency, $|F\{u\}| = |F\{p\}| * |F\{h\}|$. This result can be confirmed qualitatively in Figure 2-1.

Figure 2-1 illustrates that oscillators with different natural frequencies are controlled by different frequency ranges of the ground motion. At relatively higher oscillator frequencies (e.g. 10 Hz; green lines in Figure 2-1), where there is little energy left to resonate the oscillator, the PSA ordinates are dominated by a wide frequency band of the ground motion that ultimately equals the integration over the entire spectrum of the input ground motion (Bora at al., 2016). This can be observed in Figure 2-1, where the dashed green line traces the ground motion FAS for frequencies less than about 4 Hz. The short period PSA is then controlled by the dominant period of the input ground motion, rather than the natural period of the oscillator.

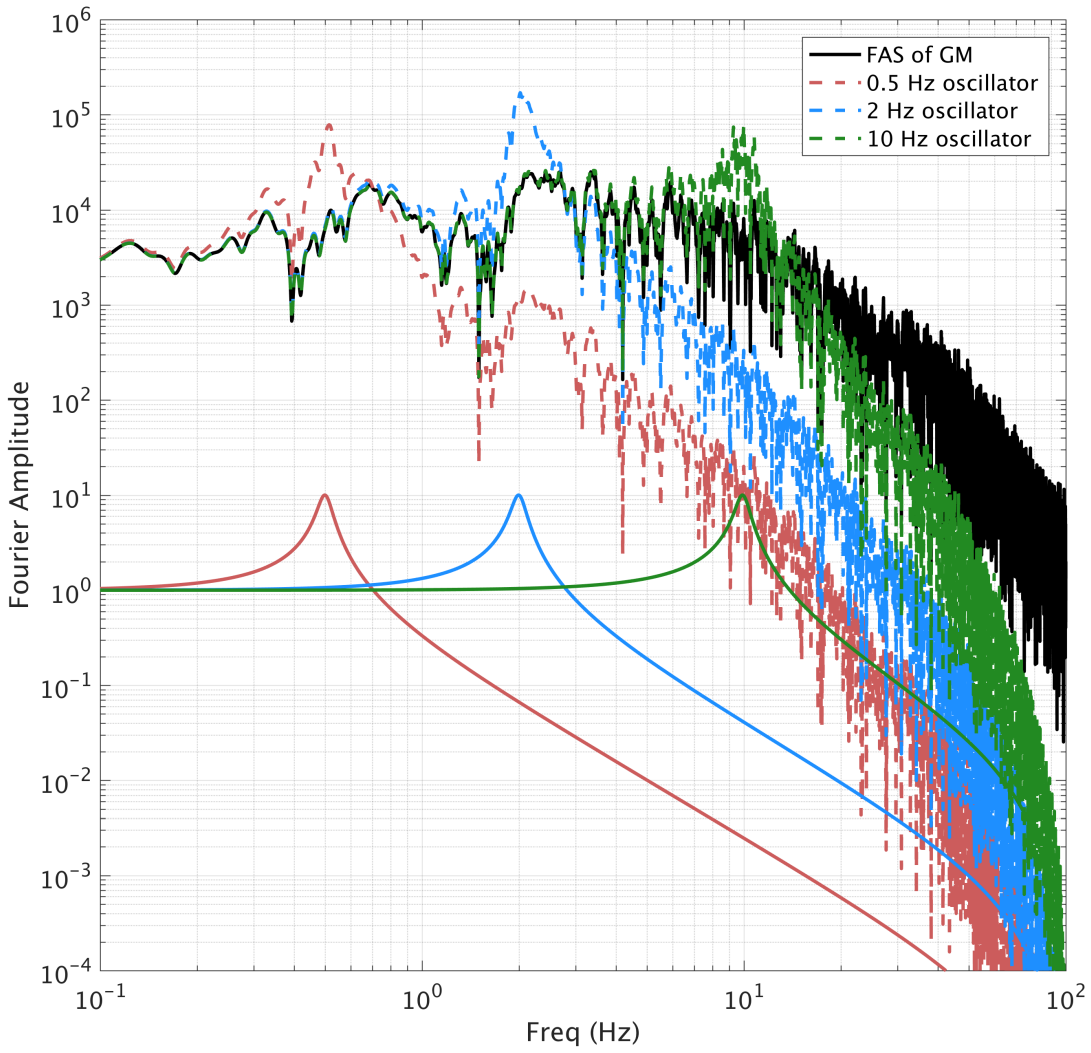

Figure 2-1. Fourier amplitudes developed from an example ground motion recording and SDOF oscillator response, illustrating the range of frequencies contributing to the response spectrum calculation.

In summary, PSA provides the spectrum of peak response from a SDOF system, which is influenced by a range of frequencies, and the breadth of that range is dependent on the oscillator period. The FAS provides a more direct representation of the frequency content of the ground motions, and since the Fourier transform is a linear operation, the FAS is a much more

straightforward representation of the ground motion. As a result, recordings from small earthquakes can be used to constrain path and site effects without dependence on response spectral shape. Numerous seismological models of the FAS are available (e.g. Brune 1970; Boore et al., 2014) to provide a frame of reference during model development. Additionally, using FAS more easily facilitates future calibration of the inter-frequency correlation of ground-motion simulation methods because there is not a strong reversal of the correlation coefficients at high frequencies, as described in Chapter 3.

Ground Motion Data

The PEER NGA-West2 strong-motion database includes over 21,000 three-component strong-motion records recorded worldwide from shallow crustal earthquakes, including aftershocks, in active tectonic regimes since 2003 (Ancheta et al, 2014). Earthquake magnitudes in the full database range from 3 to 7.9 and rupture distances extend to over 1,500 km. Earthquakes and recordings identified as questionable in quality or with undesirable properties are excluded; see Abrahamson et al., (2014) for a complete list of criteria for exclusions. At distances under 100 km, recordings from crustal earthquakes worldwide are retained to constrain the magnitude scaling and geometric spreading. At the larger distances (up to 300 km), region-specific anelastic attenuation and linear site effects due to the regional crustal structure are accounted for by including recordings only from California and Nevada. Only events with at least five recordings per earthquake are included.

The EAS has been calculated for each record in the database up to the Nyquist frequency by PEER (Kishida et al., 2016). The usable frequency range limitations of each record are accounted for by

applying the recommended lowest and highest usable frequencies for response spectra determined from Abrahamson and Silva (1997) as:

$$Lowest\ Usable\ Frequency\ (LUF) = 1.25 * \max(HPF_{HC1}, HPF_{HC2}) \qquad (2-7)$$

$$Highest\ Usable\ Frequency\ (HUF) = \frac{1}{1.25} * \min(\mathrm{LPF_{HC1}}, \mathrm{LPF_{HC2}}) \qquad (2-8)$$

where HPF is the record high-pass filter frequency, LPF is the record low-pass filter frequency, and $HC1$ and $HC2$ are the two horizontal components of a three component time series. The factors of 1.25 in Equations 2-7 and 2-8 were originally used by Abrahamson and Silva (1997) to ensure that the filters did not have a significant effect on the response spectral values. By limiting the usable period range using these factors, the frequency interval of the impulse response of a 5% damped oscillator will not exceed the filter values. And retaining this usable frequency range maintains consistency with the response spectrum calculations. Based on inspection of the usable frequency range of the data, the LUF was restricted to a minimum value of 0.1 Hz, and the HUF was restricted to a maximum value of 24 Hz for all recordings. Therefore, the regressions were performed between 0.1-24 Hz.

After screening for record quality, recording distance, minimum station requirements, and frequency limitations, the final dataset consists of 13,346 unique records from 232 earthquakes, both of which vary as a function of frequency. Figure 2-2 shows the frequency dependence of the number of earthquakes and recordings used in regressions steps 1 and 3 (listed in Table 2 and explained below.) Figure 2-3 shows a magnitude versus rupture distance scatterplot of the NGA-West2 database subsets used in regression step 1 at f = 0.2 and 10 Hz.

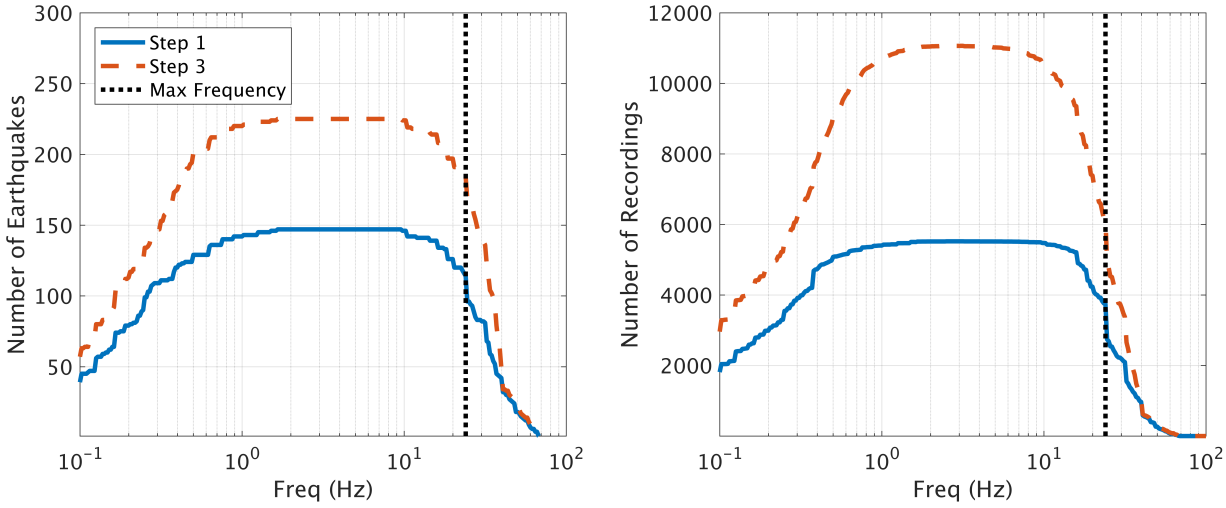

Figure 2-2. Number of earthquakes and recordings from the NGA-West2 EAS database used in the regression steps 1 and 3, versus frequency. The regressions were performed between 0.1-24 Hz, and higher frequencies are included in this figure only to display the rapid reduction of available data with increasing frequency.

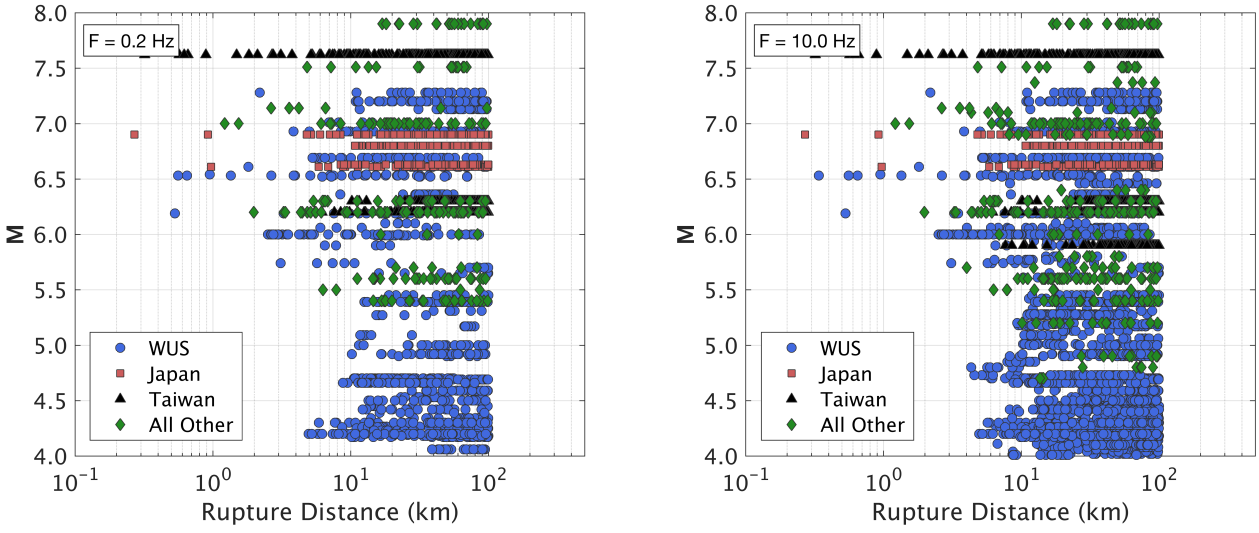

Figure 2-3. Magnitude vs. rupture distance pairs of the NGA-W2 EAS database subset used in regression step 1, at 0.2 and 10.0 Hz.

Median Model Functional Form

The model parameters are defined in Table 2-1. The scaling of the source is primarily described by moment magnitude (***M***). Source effects are also modeled using the depth to the top of the rupture plane (Z_{tor}), and a style-of-faulting flag for normal faults (F_{NML}). These source effects can be considered as proxies for stress drop scaling. The the closest distance to the rupture plane, R_{rup}, is used as the distance measure for path scaling. The linear and nonlinear site effects are parameterized using V_{s30}, the time-averaged shear-wave velocity in the top 30 m of the soil column below the site. Use of V_{s30} does not imply that 30 m is the key depth range for the site response, but rather that V_{s30} is correlated with the entire soil profile (Abrahamson and Silva, 2008). The scaling with respect to soil depth is parameterized by the depth to shear-wave velocity of 1 km/s, Z_1.

Table 2-1. Model parameter definitions.

Parameter	Definition
$\boldsymbol{EAS}$	Effective amplitude spectrum (g-sec). The EAS is the orientation-independent horizontal component Fourier amplitude spectrum (FAS) of ground acceleration, defined in Goulet et al., (2018).
$\boldsymbol{M}$	Moment magnitude
$\boldsymbol{Z_{tor}}$	Depth from the surface to the top of the rupture plane (km)
$\boldsymbol{F_{NM}}$	Style of faulting flag. 1 for Normal faulting earthquakes, 0 for all others.
$\boldsymbol{R_{rup}}$	Rupture distance (km)
$\boldsymbol{V_{S30}}$	Time averaged shear wave velocity in the upper 30 meters (m/s)
$\boldsymbol{Z_1}$	Depth from the surface to shear wave velocity horizon of at least 1 km/s (km)
$\boldsymbol{I_r}$	Peak ground acceleration for the $V_{s30} = 760$ m/s condition (g)

The model prediction for the EAS (units g-sec) ground motion is given by Equation 2-9:

$$ln\ EAS\ = ln\ EAS_{med}\ + \epsilon\sigma \qquad (2-9)$$

where σ is the total aleatory variability, and the standard-normal random variable ϵ is the number of standard deviations above or below the median. The median estimate of the EAS (EAS_{med}, with units g-sec) can be calculated from the general equation:

$$ln\ EAS_{med}\ = f_M + f_P + f_S + f_{Ztor} + f_{NM} + f_{Z1} \qquad (2-10)$$

where each of the model components in Equation 2-10 are described in the following sections.

Magnitude Scaling, $\boldsymbol{f_M}$

To capture the effects of energy radiated at the source, the formulation of the magnitude scaling is adopted from the Chiou and Youngs (2014) and Chiou and Youngs (2008) GMMs for response spectra. A polynomial magnitude scaling formulation was tested (e.g. Abrahamson et al., 2014), and after evaluating the data found that both formulations fit the data well, but the Chiou and Youngs (2014) formulation would extrapolate more reasonably. Additionally, the Chiou and Youngs (2014) formulation has undergone several years of testing and refinement and is based on seismological models for the source FAS (Chiou and Youngs, 2008), which translates directly to this application. The expression for the magnitude scaling is given by:

$$f_M = c_1 + c_2(\boldsymbol{M} - 6) + c_3 ln\ (1 + e^{c_n(c_M - \boldsymbol{M})}) \qquad (2-11)$$

The components of f_M are described in Chiou and Youngs (2008). To recap, the formulation captures approximately linear magnitude scaling at low frequencies (well below the source corner) and high frequencies (well above the source corner) with a non-linear transition in between, where the transition shifts to lower frequencies for larger magnitudes. The coefficient c_1 works jointly with the c_2 and c_3 terms to approximately represent the mean spectral shape after correcting for all other adjustments. The coefficient c_2 is the frequency independent linear $\boldsymbol{M}$ scaling slope for frequencies well above the theoretical corner frequency. The term with coefficient c_3 captures both the approximately linear scaling of the FAS below the theoretical corner frequency, and the non-linear transition to that scaling. The coefficient c_n controls the width of the magnitude range over which the transition between low- and high- frequency linear scaling occurs, and the coefficient c_M is the magnitude at the midpoint of this transition. All of the magnitude scaling terms were determined in the regression.

Path Scaling, $\boldsymbol{f_P}$

Together with the magnitude scaling, the extensively-tested path scaling formulation of Chiou and Youngs (2014) is utilized:

$$f_P = c_4\, ln\left(R_{rup} + c_5 \cosh(c_6 \max(\boldsymbol{M} - c_{hm}, 0))\right) + (-0.5 - c_4)\, ln\left(\hat{R}\right) + c_7 R_{rup} \quad (2-12)$$

where $\hat{R} = \sqrt{{R_{rup}}^2 + 50^2}$. The components of Equation 2-12 are described in Chiou and Youngs (2008). To recap, the term with coefficient c_4 captures near-source geometric spreading, which is magnitude and frequency dependent. The magnitude and frequency dependence on the geometric

spreading is introduced by adding a term to the rupture distance inside the log-distance term, expressed by the term with coefficient c_5. This additive distance is designed to capture the near-source amplitude saturation effects of the finite-fault rupture dimension. This term is a frequency-dependent constant for small magnitudes, and transitions to be proportional to $\exp(\boldsymbol{M})$ for large magnitudes, with the largest additive distance at high frequencies. Since the hyperbolic cosine is a monotonically increasing function, the coefficient c_5 controls the scaling of this term, and coefficients c_6 and c_{hm} control the gradient.

Since the coefficients c_5, c_6 and c_{hm} are multiplied by c_4, there is potential for trade-off between them. The regression procedure is started with the values for coefficients c_5, c_6 and c_{hm} from Chiou and Youngs (2014) to obtain c_4 from the data, ensuring the model did not over-saturate. Using Equations 2-11 and 2-12, the full saturation condition (no magnitude scaling at zero distance) leads to the following constraint on the coefficients: $c_2 = -c_4 c_6$. For c_2 values larger than the full saturation value, there will be a positive magnitude scaling at zero distance (i.e. not full saturation). It is reasonable for the EAS to have some scaling at zero distance even though the PSA is nearly fully saturated at high frequencies. The PSA saturates in part because the procedure involves selecting the peak response of the oscillator over all time, meaning it is not affected by duration. Conversely, the EAS is not a peak response operator, and so it will continue to scale for large magnitudes at short distance due to the longer source durations. This is the contribution of the lower amplitudes over the duration of the signal.

The near-source saturation of magnitude scaling is checked against the data and against finite-fault simulations (see Model Summary section of this paper for more details) and the EAS saturation in

this model does not disagree with those from the simulations. In later stages of the regression, the coefficients c_5, c_6 and c_{hm} are also determined empirically. The values from the regression do not change enough to impact the model, so coefficient values are fixed from Chiou and Youngs (2014) for c_5, c_6 and c_{hm} in the final model. Thus, the coefficients c_2 and c_4 control the saturation in the model development.

Following Chiou and Youngs (2014), at large distances, the distance scaling smoothly transitions to be proportional to $R^{-0.5}$ to model surface wave rather than body wave geometric spreading effects. This effect is introduced with the $ln(\hat{R})$ term, which controls at distances greater than 50 km by subtracting the c_4 coefficient and imposing a -0.5 slope. Effects of crustal anelastic attenuation (Q) are captured through the term with the frequency-dependent coefficient c_7. The Q scaling does not require magnitude dependence for the EAS.

Site Response, $\boldsymbol{f_S}$

The V_{s30} (m/s) dependence of site amplification is modeled using the form:

$$f_S = f_{SL} + f_{NL} \qquad (2-13a)$$

$$f_{SL} = c_8\, ln\left(\frac{min(V_{s30}, 1000)}{1000}\right) \qquad (2-13b)$$

$$f_{NL} = f_2 ln\left(\frac{I_R + f_3}{f_3}\right) \qquad (2-13c)$$

$$f_2 = f_4\left(e^{f_5(min(V_{s30},V_{ref})-360)} - e^{f_5(V_{ref}-360)}\right) \qquad (2-13d)$$

$$ln(I_R) = 1.238 + 0.846\, ln(EAS_{ref}(f = 5\, Hz)) \qquad (2-13e)$$

where the linear site amplification is given by f_{SL}, and the nonlinear site amplification is given by f_{NL}, which is the analytical site amplification function for FAS in the western United States (WUS) modified from Hashash et al. (2018).

The linear site term, f_{SL}, is formulated as a linear function of $ln(V_{s30})$ and is centered on the reference V_{s30} of 1000 m/s. The f_{SL} term is determined in the regression analysis. Abrahamson et al. (2014) observed that at long periods, the scaling of PSA with V_{s30} became weaker for higher V_{s30} values, and, therefore, selected a model that does not scale with V_{s30} above some maximum value, $V_1 = 1000$ m/s. Inclusion of this feature is based on evaluation of the data (Figure 2-4), which implies that above 1000 m/s the correlation between V_{s30} and the deeper profile no longer holds. Below 1000 m/s, the linear site amplification terms approximately scales linearly with $ln(V_{s30})$, so the regional linear V_{s30}-based site amplification is modeled with a single frequency-dependent coefficient, c_8.

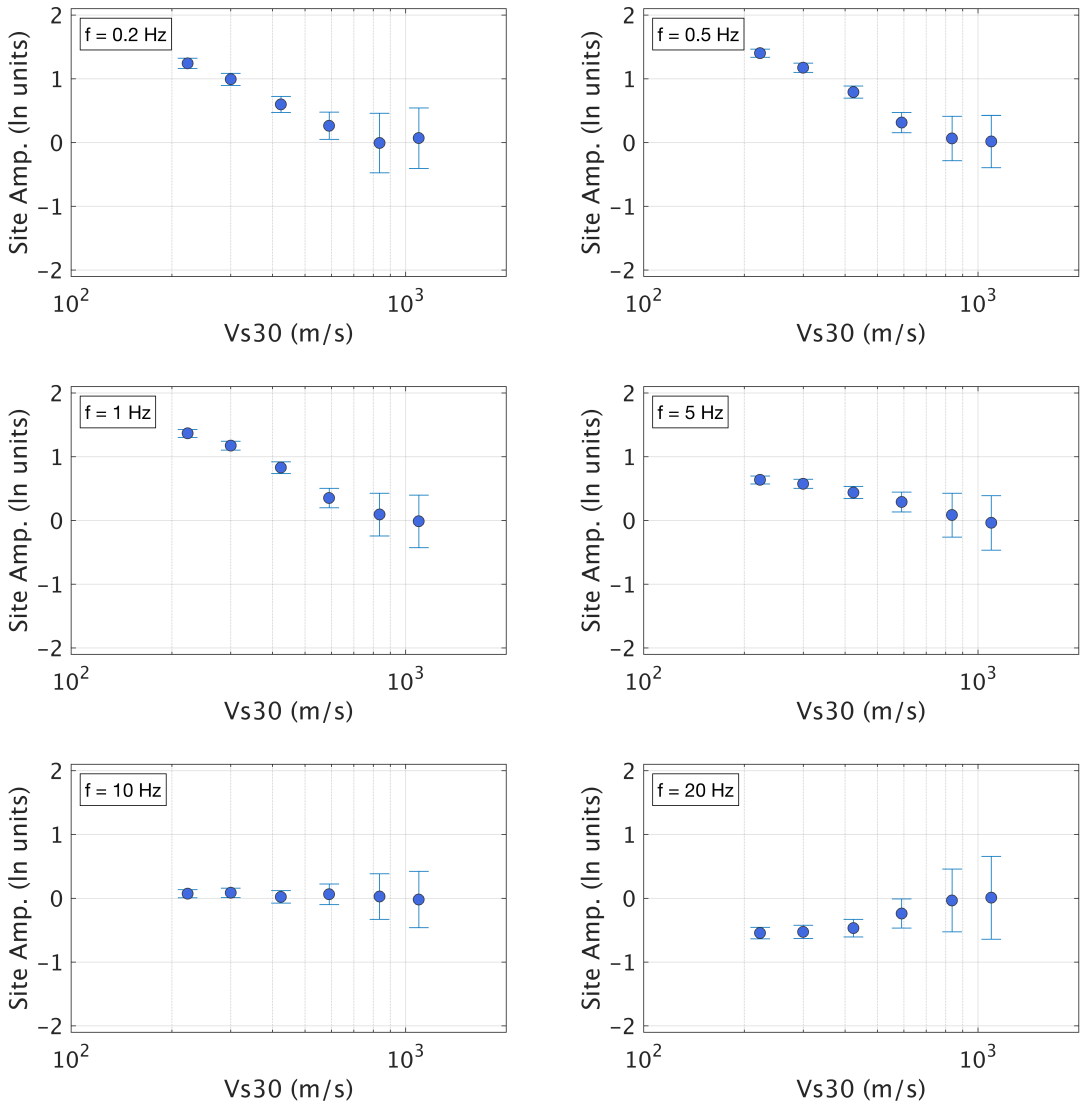

Figure 2-4. V_{s30} scaling of the linear site amplification terms, at $f = 0.2, 0.5, 1, 5, 10,$ and 20 Hz.

The nonlinear site amplification, f_{NL}, is constrained using a purely analytical model rather than obtaining it from the data. Empirical evaluations of the nonlinear effects are limited by the relatively sparse sampling of ground motions expected to be in the nonlinear range in the NGA-

West2 database (Kamai et al., 2014). Therefore, the Hashash et al. (2018) nonlinear site amplification term, f_{NL}, is adopted to model nonlinear soil amplification. This model was developed analytically by performing large-scale 1D site response simulations of input rock motions propagated through soil columns representative of WUS site conditions. Hashash et al. (2018) produced linear and nonlinear site amplification models for the PSA and FAS. Equations 2-13c and 2-13d are the nonlinear FAS amplification components of the Hashash et al. (2018) model developed for the WUS. In these equations, f_3, f_4 and f_5 are frequency-dependent coefficients, I_R is the peak ground acceleration (PGA, in units g) at rock outcrop, and V_{ref} is the limiting velocity beyond which there is no amplification relative to the reference rock condition, set to 760 m/s (Hashash et al., 2018). In this model, almost no nonlinearity is applied at frequencies below 1.0 Hz and the modification approaches zero for small values of the input motion (I_R) and as V_{s30} approaches V_{ref}.

To ensure smooth spectra in the GMM, a smoothed version of the Hashash et al. (2018) nonlinear site amplification model is implemented. The smoothing of coefficients f_3, f_4, and f_5 in frequency space are shown in Figure 2-5. The maximum frequency of the Hashash et al. (2018) model is 13.3 Hz, and the coefficients of the model reduce the nonlinear effect to zero for frequencies greater than this value simply due to the lack of FAS values at higher frequencies. Physically, this is not realistic behavior. To include nonlinear effects at the higher frequencies, the Hashash et al. (2018) model is modified by taking the minimum value of f_{NL} over all frequencies and constrain all higher frequencies to take the same value. An example of this method (for input values of $V_{s30} = 300$ m/s and $I_R = 0.8$ g) is shown in Figure 2-5.

To utilize the Hashash et al. (2018) nonlinear model requires the PGA on rock. Since the model is for the EAS, an estimate of the PGA (in units g) for the reference site condition is developed as a function of the EAS for the reference site condition at $f = 5$ Hz (in units g-sec), given by Equation 2-12e. The EAS at $f = 5$ Hz is used to estimate PGA because this is approximately the predominant frequency of the ground motions and should correlate strongly with the PGA. In Figure 2-6, the data used to develop the I_R - $EAS_{ref}(f = 5\,Hz)$ relationship are shown. Ground motions with $I_R > 0.01$g are included, with symbols identifying data within unit $\boldsymbol{M}$ bins. In Figure 2-6, I_R is corrected to the reference site condition using the Abrahamson et al. (2014) linear site amplification model, and the EAS is corrected the reference V_{s30} condition using the linear site amplification model from this study. The least squares fit given by Equation 2-12e is shown with the dashed line. Different $\boldsymbol{M}$ and distance ranges were evaluated similarly, with minimal differences in the slope of the relationship.

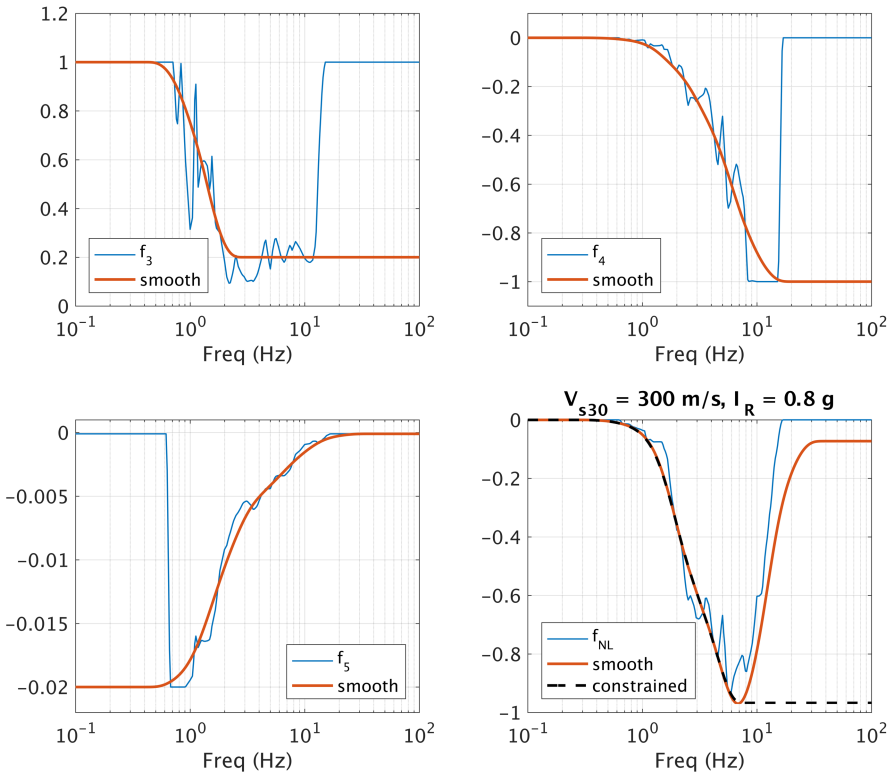

Figure 2-5. Smoothing of the Hashash et al. (2018) coefficients f_3, f_4 and f_5, and the smoothing procedure of term f_{NL} for example values of $V_{s30} = 300$ m/s and $I_R = 0.8$ g.

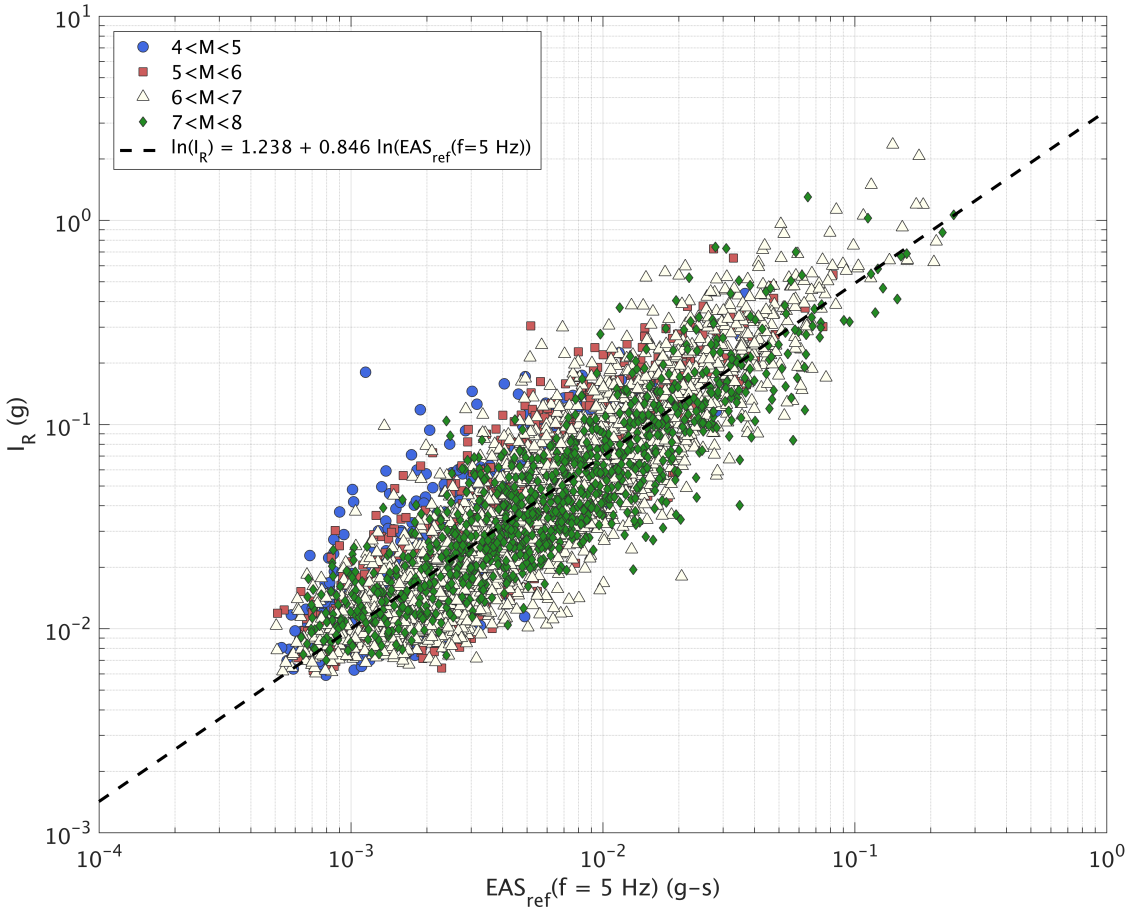

*Figure 2-6. Data used to develop the I_R - $EAS_{ref}(f = 5\ Hz)$ relationship, where I_R is the peak ground acceleration on rock and $EAS_{ref}(f = 5\ Hz)$ is the 5 Hz EAS on rock. Ground motions with $I_R > 0.01g$ are included, with symbols identifying **M** bins. I_R is corrected to the reference site condition using the Abrahamson et al. (2014) linear site amplification model, and the EAS is corrected the reference V_{s30} condition using the linear site amplification model from this study.*

Depth to Top of Rupture Scaling, $\boldsymbol{f_{Ztor}}$

To model differences in the ground motions for surface and buried ruptures, the depth to the top of rupture scaling model takes the form:

$$f_{Ztor} = c_9 \min(Z_{tor}, 20) \quad (2-14)$$

where c_9 is frequency dependent and Z_{tor} is non-negative and measured in km. The Z_{tor} scaling is capped at 20 km to prevent unbounded scaling with Z_{tor}.

Normal Style of Faulting Effects, $\boldsymbol{f_{NM}}$

To model the differences in ground motions for normal style faults, the normal faulting term is:

$$f_{NM} = c_{10} F_{NM} \quad (2-15)$$

where F_{NM} is 1 for normal style faults and 0 for all others, and c_{10} is determined in the regression. A style of faulting term for reverse events was considered but not included, because this term was highly correlated with Z_{tor}. Therefore, the reverse style of faulting scaling is captured in f_{Ztor}.

Soil Depth Scaling, $\boldsymbol{f_{Z1}}$

To model the scaling with respect to sediment thickness, the Abrahamson et al., (2014) formulation is adopted, which is parameterized by the depth to shear wave velocity horizon of 1.0 km/s, Z_1 (units of km). This model takes the form:

$$f_{Z1} = c_{11} \, ln\left(\frac{\min(Z_1, 2.0) + 0.01}{Z_{1Ref} + 0.01}\right) \quad (2-16a)$$

$$c_{11} = \begin{cases} c_{11a} & for\ V_{s30} \leq 200\ m/s \\ c_{11b} & for\ 200 < V_{s30} \leq 300\ m/s \\ c_{11c} & for\ 300 < V_{s30} \leq 500\ m/s \\ c_{11d} & for\ V_{s30} > 500\ m/s \end{cases} \quad (2-16b)$$

$$Z_{1Ref} = \frac{1}{1000}\exp\left(\frac{-7.67}{4}\ln\left(\frac{{V_{s30}}^4 + 610^4}{1360^4 + 610^4}\right)\right) \qquad (2-16c)$$

where Z_{1Ref} is the reference Z_1 for the regional model for California and Nevada. Equation 2-16c was developed by Chiou and Youngs (2014) to account for regional differences in the $V_{s30} - Z_1$ relationships in the data. Abrahamson et al., (2014) showed that the Z_1 scaling is dependent on the V_{s30} value and used the V_{s30} bins in Equation 2-16b to model this dependence. The soil depth scaling is capped to $Z_1 = 2$ km based on the range of the data and to avoid unconstrained extrapolation.

Regression Analysis

The random-effects model is used for the regression analysis following the procedure described by Abrahamson and Youngs (1992). This procedure leads to the separation of total residuals into between-event residuals (δB) and within-event residuals (δW), following the notation of Al Atik et al., (2010). For large numbers of recordings per earthquake, the between-event residual is approximately the average difference in logarithmic-space between the observed Intensity Measure (IM) from a specific earthquake and the IM predicted by the GMM. The within-event residual (δW) is the difference between the IM at a specific site for a given earthquake and the median IM predicted by the GMM plus δB. By accounting for repeatable site effects, δW can further be partitioned into a site-to-site residual ($\delta S2S$) and the single-station within-event residual (δWS, also called the within-site residual) (e.g. Villani and Abrahamson, 2015). Using this notation, the residuals take the following form:

$$Y = g(X_{es}, \theta) + \delta B_e + \delta S2S_s + \delta WS_{es} \quad (2-17)$$

$$\delta_{total} = Y - g(X_{es}, \theta) = \delta B_e + \delta S2S_s + \delta WS_{es} \quad (2-18)$$

where Y is the natural log of the recorded ground motion IM, $g(X_{es}, \theta)$ is the median GMM, X_{es} is the vector of explanatory seismological parameters (magnitude, distance, site conditions, etc.), θ is the vector of GMM coefficients, and δ_{total} is the total residual for earthquake e and site s.

The residual components δB, $\delta S2S$ and δWS are well-represented as zero-mean, independent, normally distributed random variables with standard deviations τ, ϕ_{S2S} and ϕ_{ss}, respectively (Al Atik et al., 2010). The total standard deviation, σ, is expressed as:

$$\sigma = \sqrt{\tau^2 + \phi_{S2S}^2 + \phi_{ss}^2} \quad (2-19)$$

The regression is performed in a series of steps to prevent trade-off of correlated model coefficients and to constrain different components of the model using the data relevant to each piece. These steps are given in Table 2-2, along with the data used and parameters determined from each step. In Step 1-a, a data set consisting of larger magnitudes and shorter distances is used to constrain the large magnitude scaling and near-source finite-fault saturation, using data from all regions. In Steps 1-b through 1-d, the same data set is used, and the remaining source effects are determined. In Step 2, the regionalized linear site amplification parameters are determined using the data from California and Nevada at distances within 100 km. In Steps 3-a through 3-c, data from California and Nevada are included out to 300 km distance. In these regression steps, the regional soil depth scaling, anelastic attenuation, and mean spectral shape coefficients are determined. For all steps

the regression is performed independently at each of 239 log-spaced frequencies spanning 0.1-24 Hz.

Table 2-2. Regression steps.

Step	Data Used	Parameters Free in the Regression	Parameters Smoothed after the Regression
1-a	$\boldsymbol{M} > 4, R_{rup} \leq 100\ km$, all regions	$c_1, c_2, c_3, c_n, c_M, c_4, c_7, c_8, c_9, c_{10}, c_{11}$	c_2, c_4 ($\boldsymbol{M}$, path)
1-b	Same as 1-a	$c_1, c_3, c_n, c_M, c_7, c_8, c_9, c_{10}, c_{11}$	c_3, c_n, c_M ($\boldsymbol{M}$)
1-c	Same as 1-a	$c_1, c_5, c_6, c_{hm}, c_7, c_8, c_9, c_{10}, c_{11}$	c_5, c_6, c_{hm} (path)
1-d	Same as 1-a	$c_1, c_7, c_8, c_9, c_{10}, c_{11}$	c_9 (Z_{tor})
1-e	Same as 1-a	$c_1, c_7, c_8, c_{10}, c_{11}$	c_{10} (F_{NM})
2	$\boldsymbol{M} > 4, R_{rup} \leq 100\ km$ from CA/Nevada	c_1, c_7, c_8, c_{11}	c_8 (V_{s30})
3-a	$\boldsymbol{M} > 3, R_{rup} \leq 300\ km$ from CA/Nevada	c_1, c_7, c_{11}	c_{11} (Z_1)
3-b	Same as 3-a	c_1, c_7	c_7 (Q)
3-c	Same as 3-a	c_1	c_1

Smoothing

The model coefficients are smoothed in a series of steps as outlined in Table 2-2. Smoothing of the coefficients is performed to assure smooth spectra and, in some cases, to constrain the model

to a more physical behavior where the data are sparse (Abrahamson et al., 2014). Tables of the values of the final smoothed coefficients are available in Appendix B.

Figure 2-7 through Figure 2-16 show the regressed model coefficients plotted versus frequency, before and after smoothing. The coefficients c_2 and c_4 are frequency independent and are determined from regressions in the high frequency range. The coefficients c_3, c_n, and c_M require only minor smoothing to assure smooth spectra in the final model, including extrapolation outside the ranges well constrained by data. The smoothing of c_7 (the anelastic attenuation term) is constrained to be nonpositive at all frequencies so that the model does not unintentionally increase in amplitude at very large distances. Minimal smoothing is required for the coefficient c_8 (the linear V_{s30} term). The coefficient c_9 (the Z_{tor} term) takes on negative values at low frequencies implying small de-amplification of low frequency ground motions with increasing Z_{tor}. The data lead to a large drop in c_{10} (the normal faulting term) at low frequencies but this is not included in the model because the theoretical basis is not clear; instead a frequency-independent constant is used (uniform scaling across frequencies) for normal style-of-faulting earthquakes. The c_{11} terms are smoothed as shown in Figure 2-14, where the uncertainty is largest for c_{11a}, which corresponds to the lowest V_{s30} bin with relatively fewer data.

The c_1 coefficient works collectively with the c_3 term to represent the mean spectral shape after correcting for all other adjustments. In the regression, unexpected behavior of c_1 at low frequencies is observed, as shown in Figure 2-16. At frequencies below about 0.3 Hz, the regressed coefficient values are equal to or larger than the 0.3 Hz value. If unmodified and combined with the c_3 term, this would lead to an irregular spectral "bump" at $f < 0.3$ Hz. Following Aki (1967) the mean

spectrum should be approximately linear with a 2-slope in this frequency range. Therefore, the c_1 coefficient is modified at low frequencies by constraining the slope from $f \approx 1.0$ Hz down to 0.1 Hz, as shown in Figure 2-16. The difference between the regressed values of c_1 and the constrained values of c_1 is denoted c_{1a}; this adjustment coefficient is plotted in the lower portion of Figure 2-16. By introducing the c_{1a} term, the model predicts smooth, theoretically appropriate spectra at low frequencies. This also allows for residuals which are zero-centered, which is required for computing the correlations of the residuals between frequencies. To account for this modification, the c_{1a} term must be added to the total standard deviation using Equation 2-21. The standard deviation model is discussed further below.

This unexpected behavior of c_1 may be due to bias in the data. At low frequencies, the signal to noise ratio is commonly low (Douglas and Boore, 2011). This contributes to the drop off in data at low frequencies shown in Figure 2-2. Additionally, at low frequencies, the large epsilon (above average) ground motions are more likely to be above the signal to noise ratio, and therefore, be included in the database. Likewise, the below average ground motions are more likely to be below this ratio and be excluded. The net effect may be that, for the FAS at low frequencies, the database is biased towards higher ground motions. Observing the data, the mean spectra for certain binned magnitude and distance ranges contain this feature. As an example, Figure 2-17 shows the geometric mean spectra of a subset of the data used in the analysis. This figure is created using recordings from strike-slip earthquakes with $R_{rup} < 50$ km, for $\boldsymbol{M}$ bins one unit wide, and adjusted to the reference V_{s30} condition. Below about 0.3 Hz, the bump in the spectral shape in the data that causes the increase of c_1 is evident, especially for the data with $\boldsymbol{M} > 7$ and $\boldsymbol{M} < 5$.

Other physical explanations of the cause of the increase in coefficient c_1 are not apparent. To check that long period basin effects are not the cause, the mean spectra are examined in the same way, but only including records with $Z_1 < 0.15$ km, and the same behavior is observed. To further test if basin effects are not adequately captured by the model, c_1 is fixed to the constrained shape and the residuals are mapped. These residuals do not have regional or spatial trends, implying that basin effects are not the culprit. Understanding the physical cause of the long-period shape of the spectrum will be evaluated further in a future study.

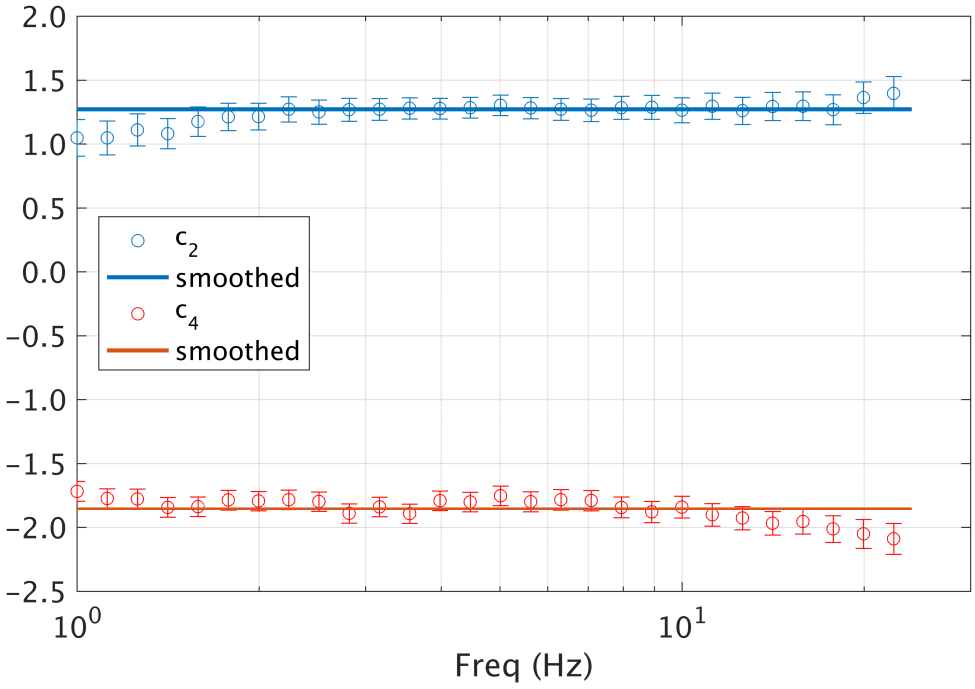

Figure 2-7. Smoothing of source scaling (c_2) and near source geometric spreading coefficients (c_4)

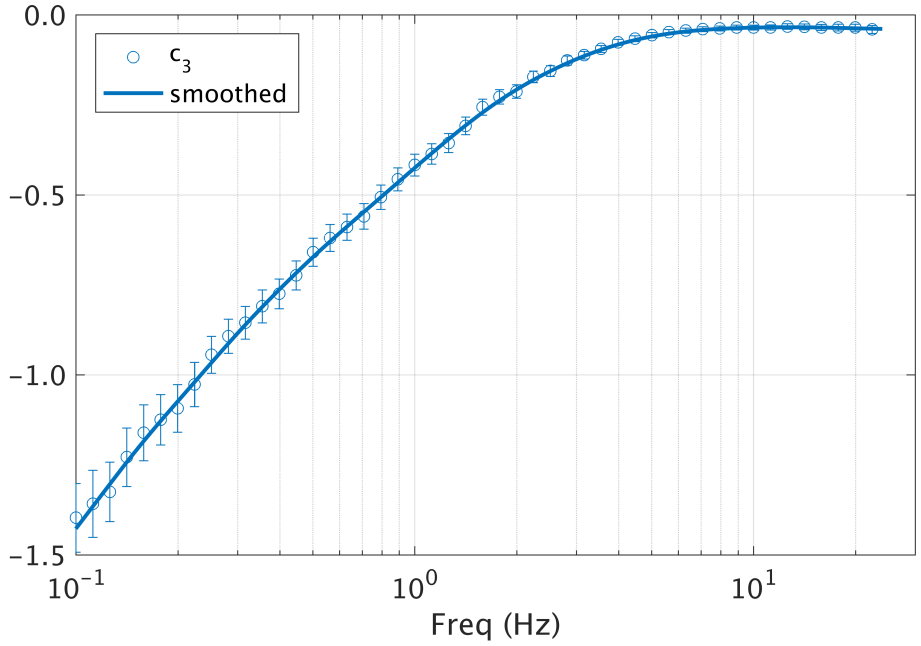

Figure 2-8. Smoothing of the source scaling coefficient, c_3.

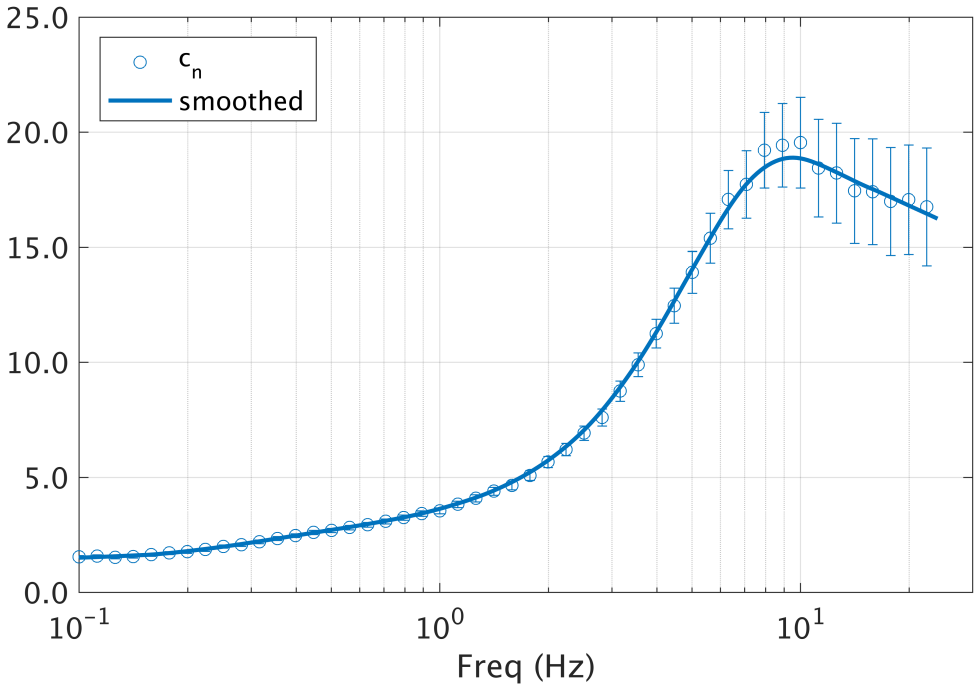

Figure 2-9. Smoothing of the source scaling coefficient, c_n.

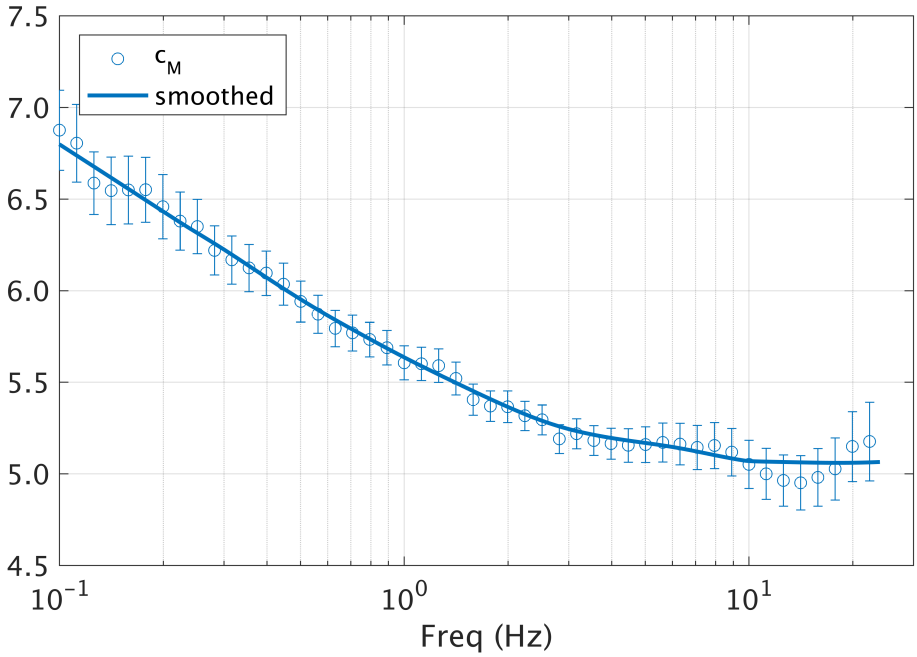

Figure 2-10. Smoothing of the source scaling coefficient, c_M.

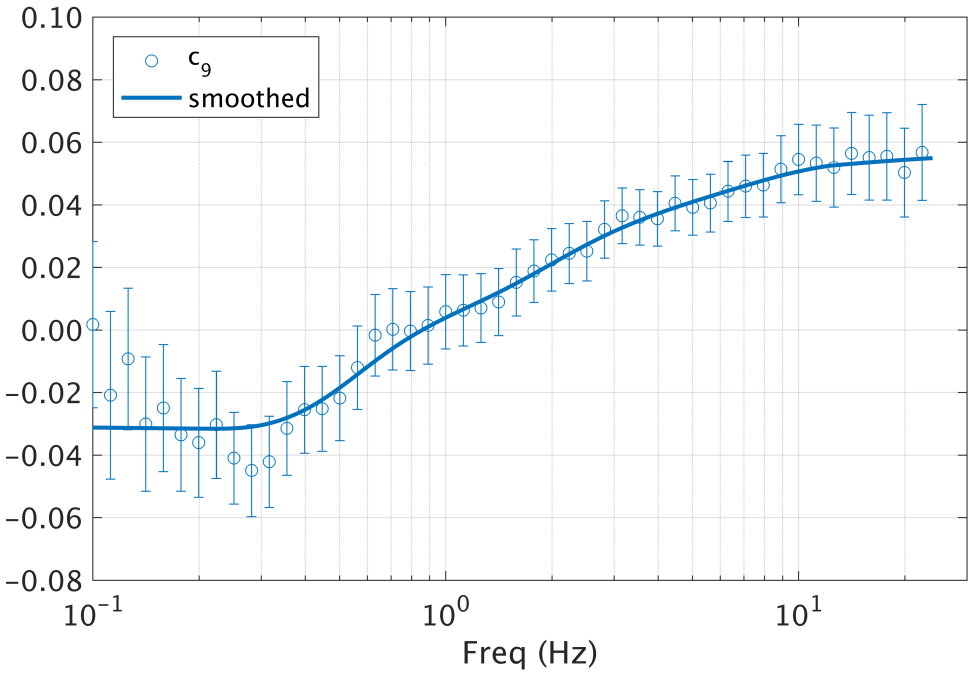

Figure 2-11. Smoothing of the Z_{tor} scaling coefficient, c_9.

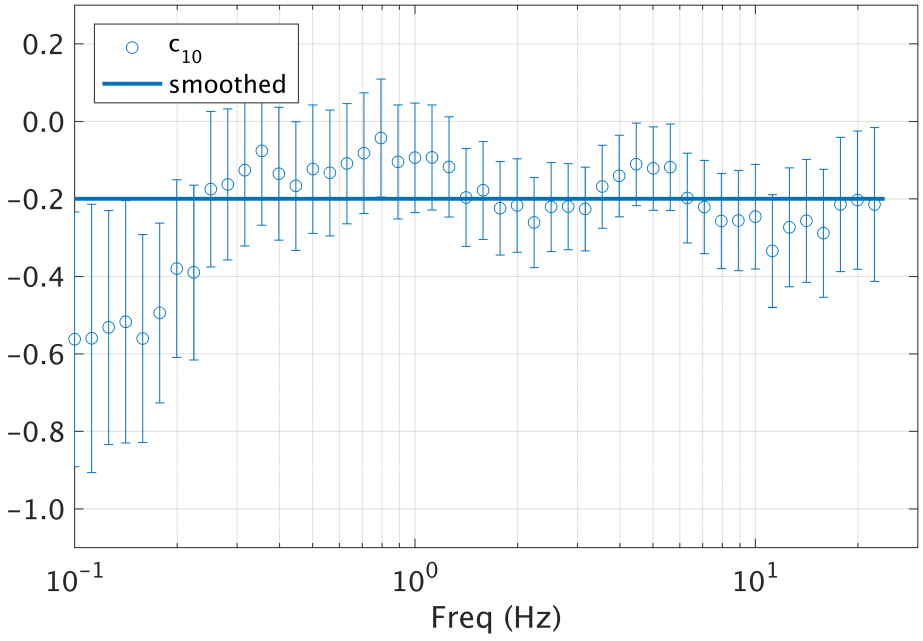

Figure 2-12. Smoothing of the F_{NM} style of faulting coefficient, c_{10}.

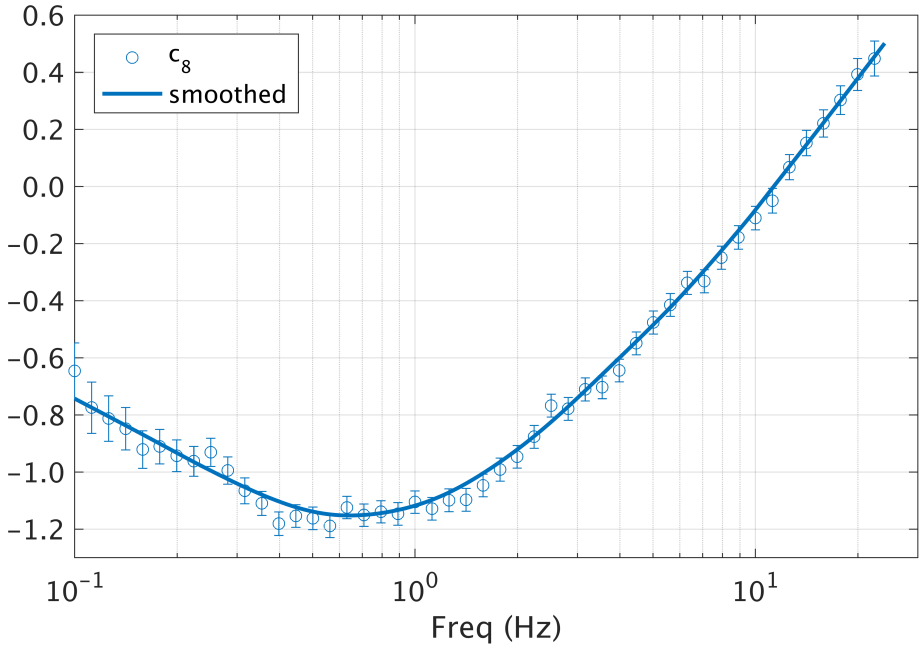

Figure 2-13. Smoothing of the linear V_{s30} scaling coefficient, c_8.

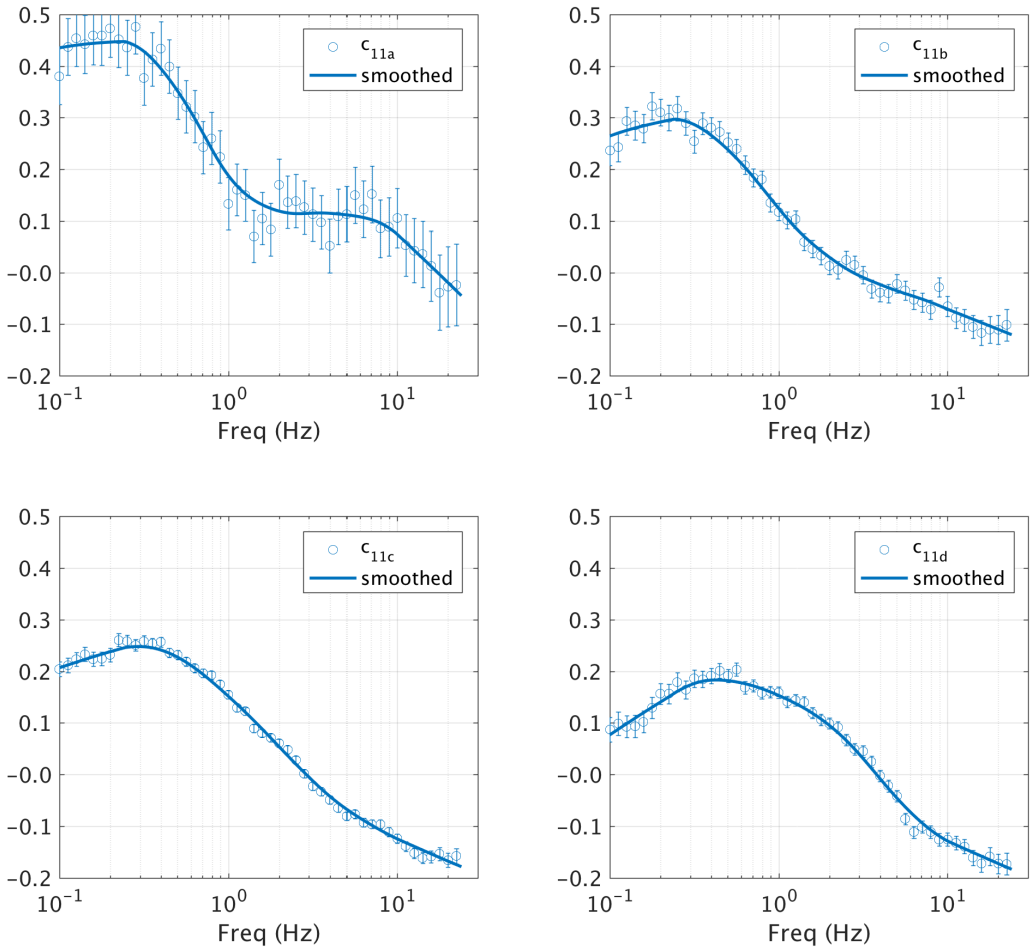

Figure 2-14. Smoothing of the Z_1 scaling coefficients, c_{11}.

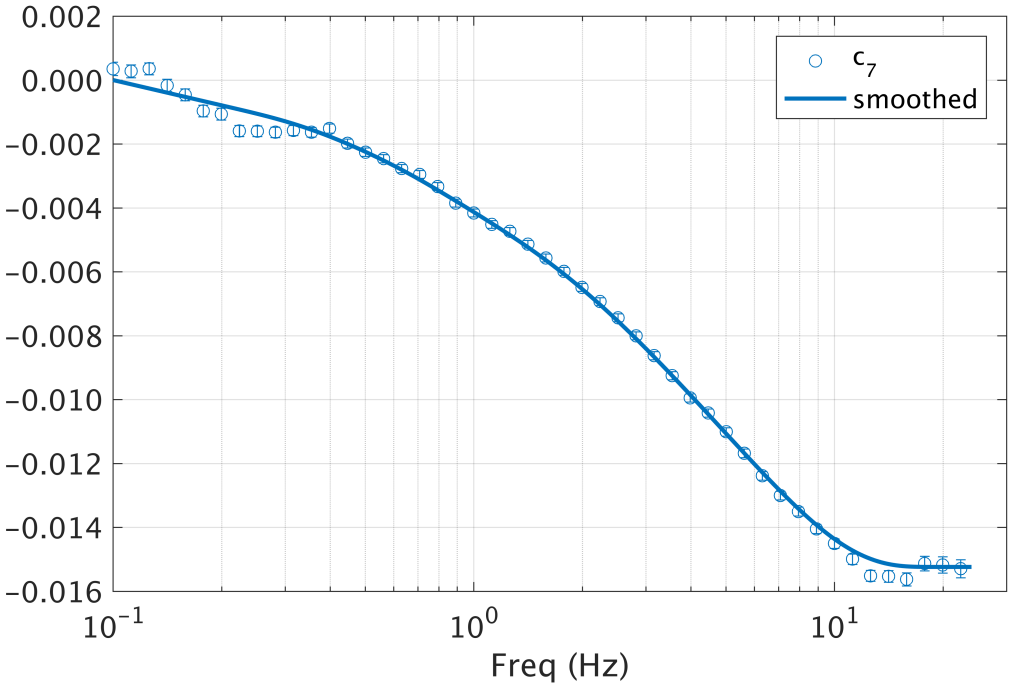

Figure 2-15. Smoothing of the anelastic attenuation coefficient, c_7.

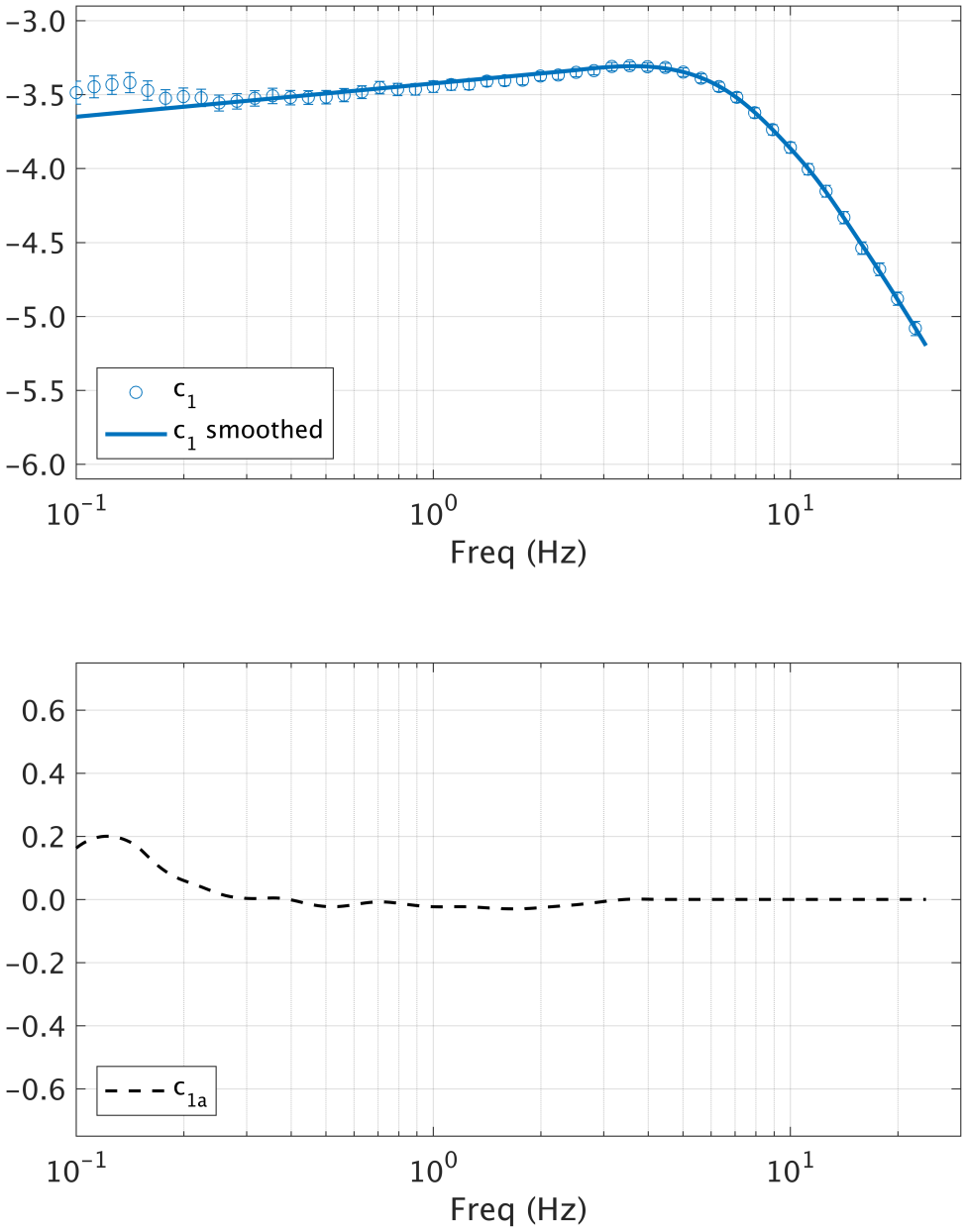

Figure 2-16. Smoothing of the coefficient, c_1, and adjustment coefficient c_{1a}.

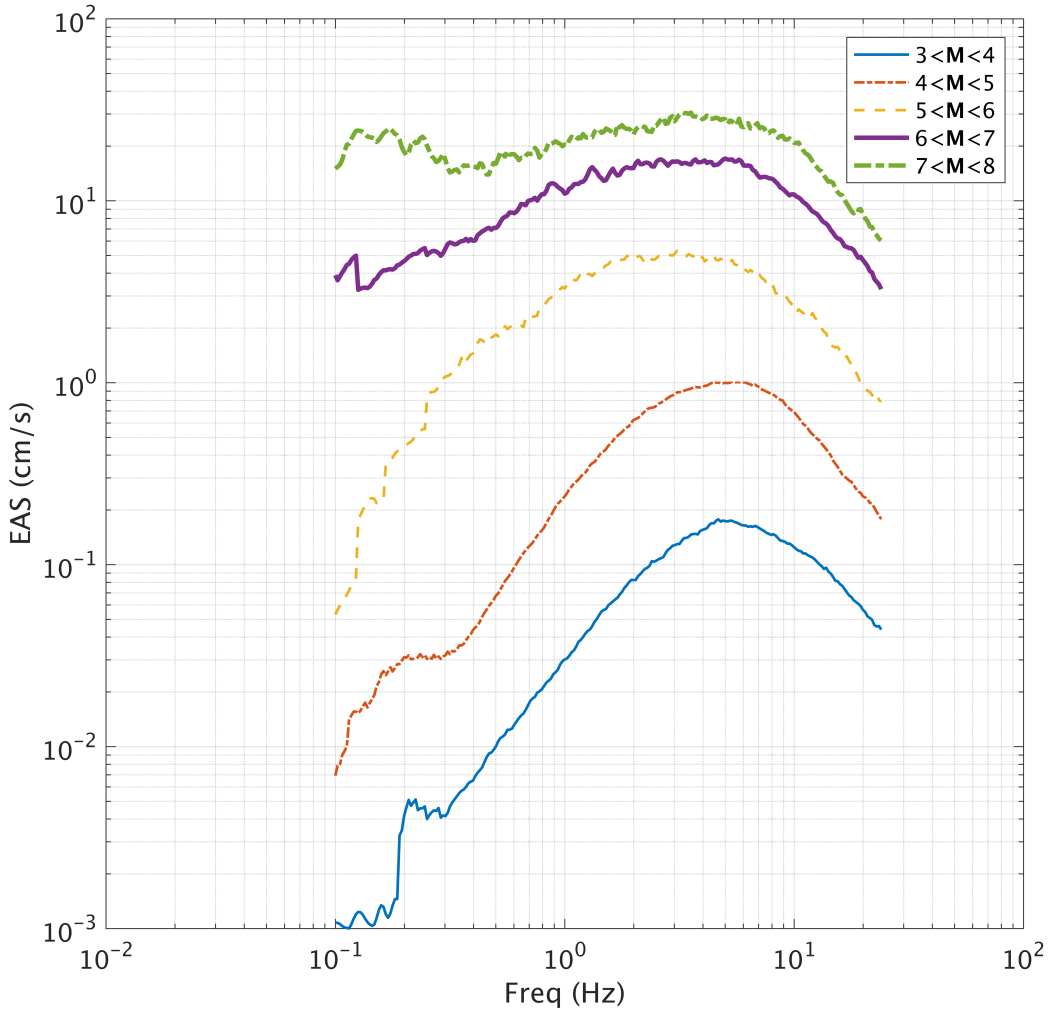

*Figure 2-17. The geometric mean EAS spectra of the data used in the analysis, calculated using recordings from strike-slip earthquakes with $R_{rup} < 50$ km, for **M** bins one unit wide, and adjusted to the reference V_{s30} condition.*

Extrapolation to 100 Hz

Model coefficients are obtained by regression for frequencies up to 24 Hz. At high frequencies, the FAS decays rapidly (Hanks 1982; Anderson and Hough, 1984). Anderson and Hough (1984) introduced the spectral decay factor kappa (κ) to model the rate of the decrease, where the

amplitude of the log(FAS) decays linearly versus frequency (linear spaced), and κ is related to the slope. The total site amplification is the combined effect of crustal amplification and damping (κ and Q), but the effect of κ is so strong that it controls the spectral decay of the FAS at high frequencies and is the only parameter specified in the extrapolation. The model is extrapolated using Equation 2-20:

$$D(\kappa, f) = \exp(-\pi\kappa f) \qquad (2-20a)$$

$$ln(\kappa) = -0.4 * ln\left(\frac{V_{s30}}{760}\right) - 3.5 \qquad (2-20b)$$

$$EAS(f > f_{max}) = EAS(f_{max}) * D(\kappa, f - f_{max}) \qquad (2-20c)$$

where $D(\kappa, f)$ is the Anderson and Hough (1984) diminution operator and f_{max} is the frequency beyond which the extrapolation occurs; $f_{max} = 24$ Hz. The parameter κ is estimated from V_{s30} using the relationship given by Equation 2-20b. This relationship is selected based on the range of $\kappa_0 - V_{s30}$ correlation models presented in Figure 2 of Ktenidou et al., (2014). The scatter observed in these correlations is large, as described in Ktenidou et al., (2014).

Residuals

The model is evaluated by checking the residuals from the regression analysis as functions of the main model parameters. Example figures are included below, and a larger set of residual figures are available in Appendix A.

Between-event and Between-site Residuals

Examples of the dependence on the source parameters of the between-event residuals at $f = 0.2$, 1.0, and 5.0 Hz are given in Figure 2-18 through Figure 2-20. In these figures, the diamond shaped

markers represent events from California and Nevada, and circles represent events from all other regions. There is not a strong magnitude dependence of the δB. For Z_{tor}, there is no trend in the residuals at high frequencies, where the model increases the ground motion with increasing Z_{tor}. There is a potential difference in Z_{tor} scaling between regions at low to moderate frequencies, an effect which should be evaluated further in the future. For F_{NM}, there is also no trend in the residuals at high frequencies, but at the lower frequencies, potential regional differences exist. The normal faulting term is constrained by sparse data (10 events at 0.2 Hz, including 6 from Italy), so this term is not refined further. Figure 2-18 through Figure 2-20 also show the dependence of the between-site residuals on V_{s30}. Overall, there is no trend in $\delta S2S$ versus V_{s30}. The standard deviation of these residuals (ϕ_{S2S}) is comparable to τ at frequencies greater than about 2 Hz.

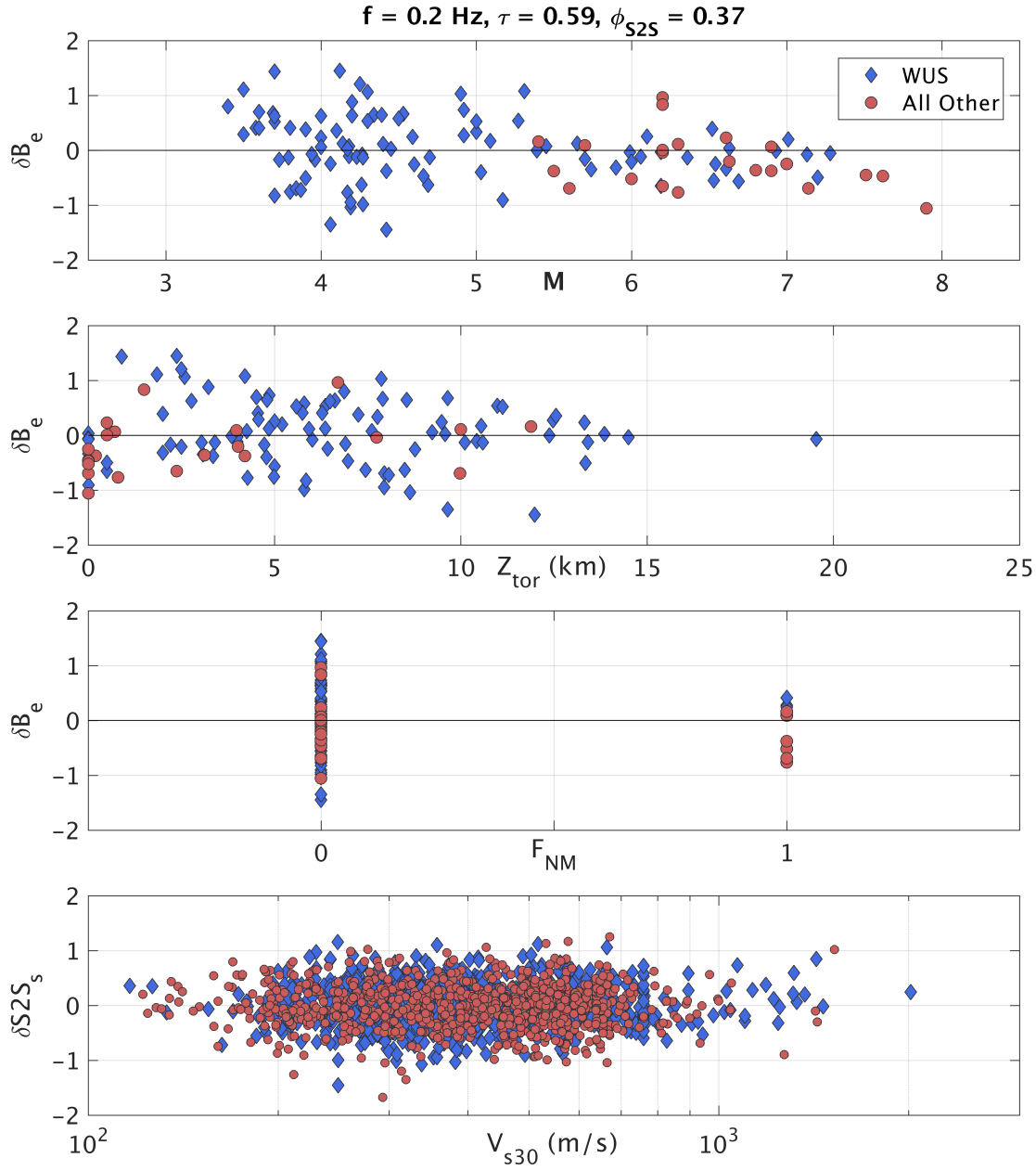

*Figure 2-18. Between-event residuals (δB_e) versus **M**, Z_{tor}, and F_{NM} and between-site residuals ($\delta S2S_s$) versus V_{s30}, for $f = 0.2$ Hz.*

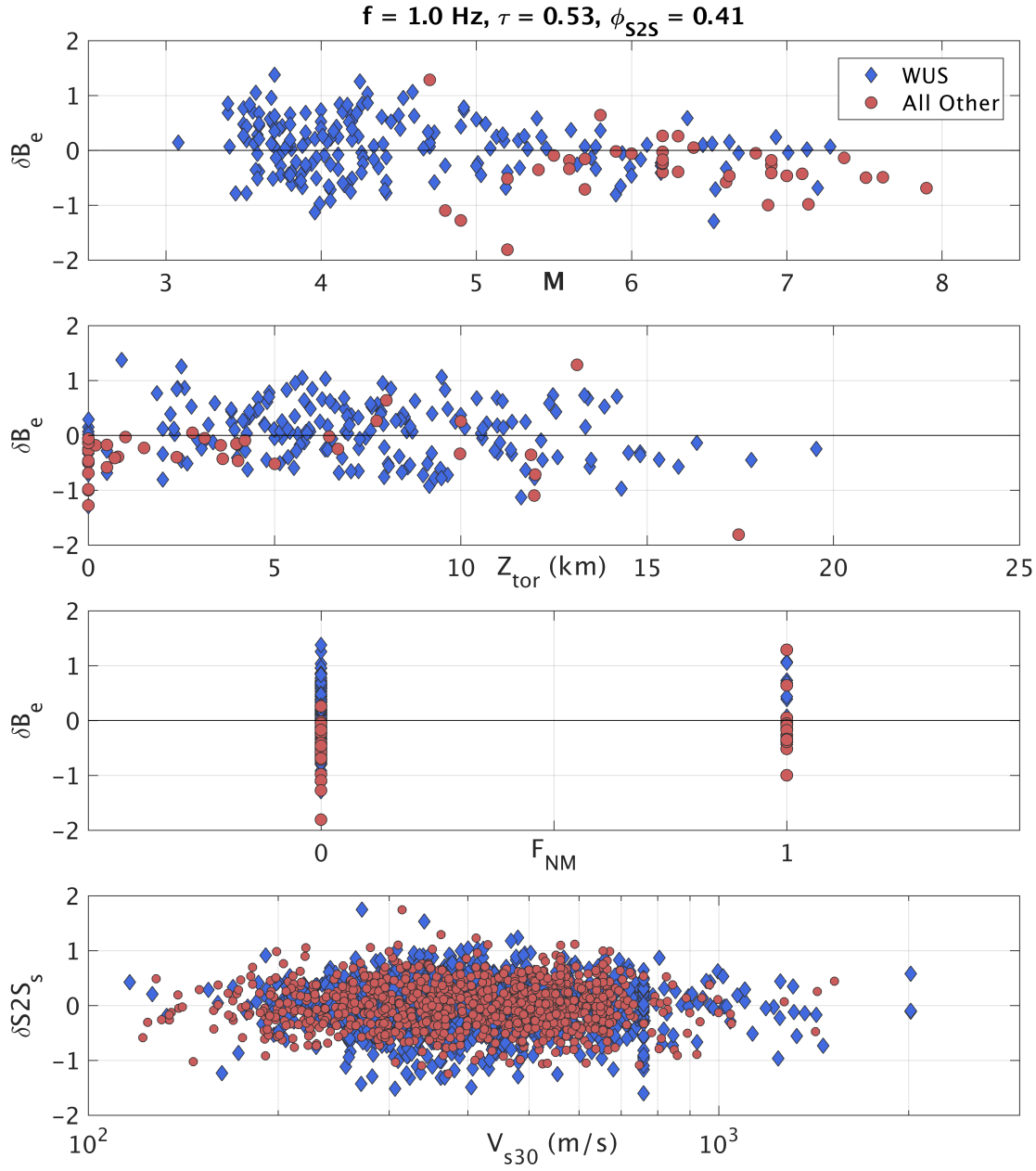

*Figure 2-19. Between-event residuals (δB_e) versus **M**, Z_{tor}, and F_{NM} and between-site residuals ($\delta S2S_s$) versus V_{s30}, for $f = 1$ Hz.*

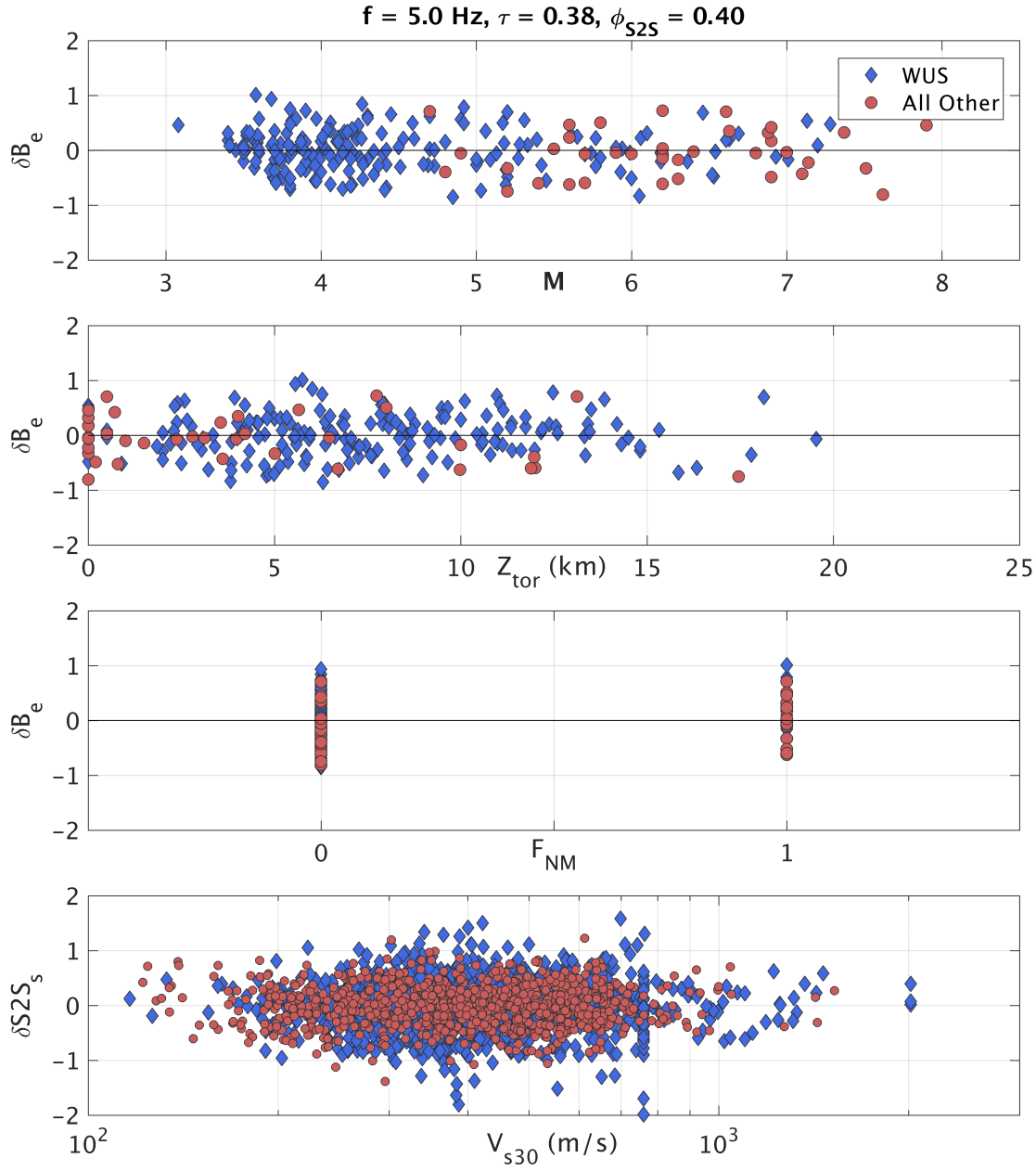

*Figure 2-20. Between-event residuals (δB_e) versus **M**, Z_{tor}, and F_{NM} and between-site residuals ($\delta S2S_s$) versus V_{s30}, $f = 5$ Hz.*

Within-site Residuals

Examples of the dependence on the model parameters of the within-site residuals at $f = 0.2$, 1.0, and 5.0 Hz are given in Figure 2-21 through Figure 2-23. The filled circles are individual residuals, and the black diamonds with whiskers represent the mean and 95% confidence interval of the mean for binned ranges of the model parameter. Overall, there is no trend observed in δWS versus moment magnitude. The linear site response model is evaluated through the V_{s30} and Z_1 dependence of the residuals. Overall, no strong trends are observed against V_{s30}, except for the highest V_{s30} values at low frequencies, where the residuals are slightly positive, indicating model under-prediction. The data are very sparse in this range (6 records with V_{s30} >1500 m/s and 106 records with V_{s30} >1200 m/s). No strong Z_1 dependencies on the residuals are observed.

The distance scaling of the model is evaluated using the distance-dependence of δWS as shown in Figure 2-21 through Figure 2-23. Additionally, the distance dependence is evaluated using magnitude binned residuals. Examples of the distance dependence binned by magnitude are shown in Figure 2-24 through Figure 2-26, where the magnitude bin ranges are given in the figure legends. In the distance range of about 5 – 100 km, there are no strong trends or biases of the residuals. At low frequencies, for distances beyond 100 km and in the $\boldsymbol{M}$5.5-6.5 bin, the δWS residuals are biased positive. This is likely due to the relatively limited data within this bin, and that the model scaling is appropriate even though these particular residuals are not zero-centered. Thus, neither the magnitude nor distance scaling are adjusted to center these residuals. At distances shorter than 1 km and for frequencies greater than about 2 Hz, there is a small systematic negative bias in the residuals (Figure 2-23). This means the near-fault saturation in this model is not as strong as

indicated by the data. Graizer (2018) chose to incorporate oversaturation (a peak in the distance scaling at about 5 km) into his ground motion models. The oversaturation of distance scaling is intentionally avoided in this model. Because the available ground-motion data is extremely sparse at such close distances, this model is compared with the saturation from finite-fault earthquake simulations (see Model Summary section of this paper for more details). Based on these results, and on the sparsity of the data, the small bias in the short-distance residuals is accepted.

The distance dependence of the model is also compared with data from four well-recorded WUS earthquakes in Figure 2-27 through Figure 2-30: 1989 $\boldsymbol{M}$6.9 Loma Prieta, 2010 $\boldsymbol{M}$7.2 El Mayor-Cucapah, 1992 $\boldsymbol{M}$7.3 Landers, and 1994 $\boldsymbol{M}$6.7 Northridge. In these figures, the top panels compare the recorded EAS with the model-predicted EAS at each site, including the event term for that earthquake. The lower panels show the within-event residuals for the same sites versus R_{rup}. Residuals for El Mayor-Cucapah, the most well-recorded large earthquake in California, show no bias or trend at either frequency. Besides a few outliers, the remaining three events have attenuation which does not disagree with the median model and is captured on average.

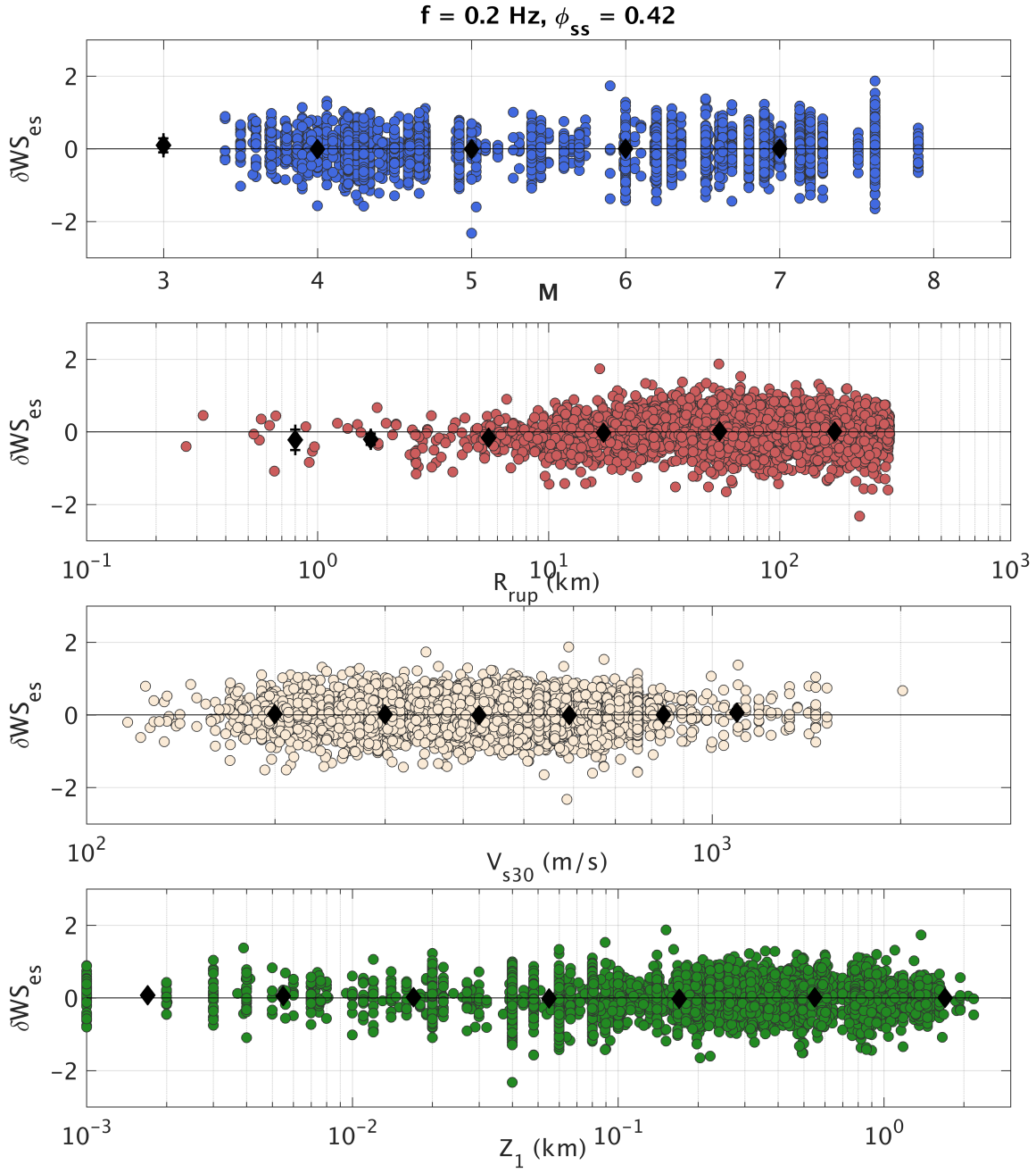

*Figure 2-21. Within-site residuals (δWS_{es}) versus **M**, R_{rup}, V_{s30}, and Z_1 for $f = 0.2$ Hz.*

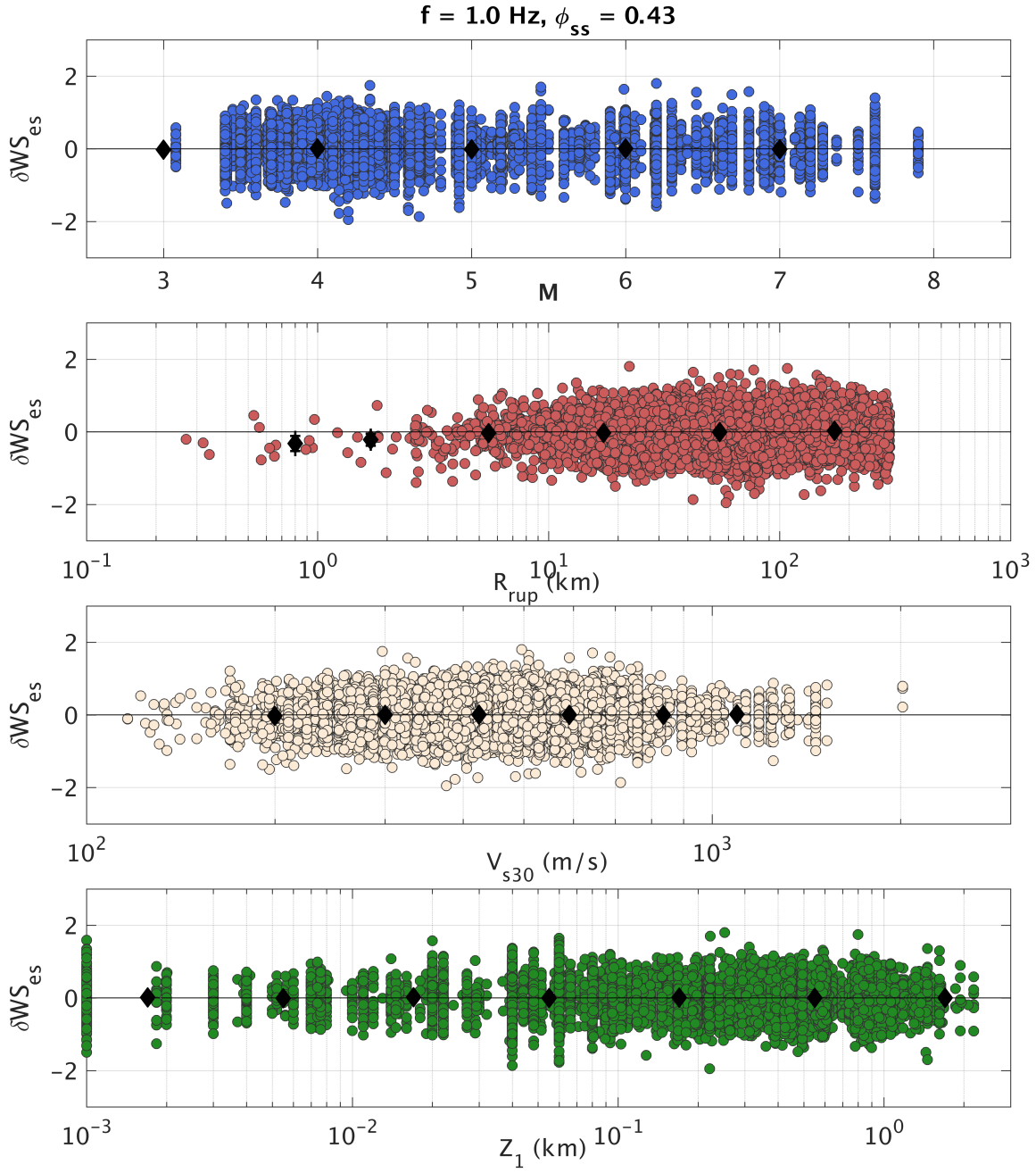

*Figure 2-22. Within-site residuals (δWS_{es}) versus **M**, R_{rup}, V_{s30}, and Z_1 for $f = 1$ Hz.*

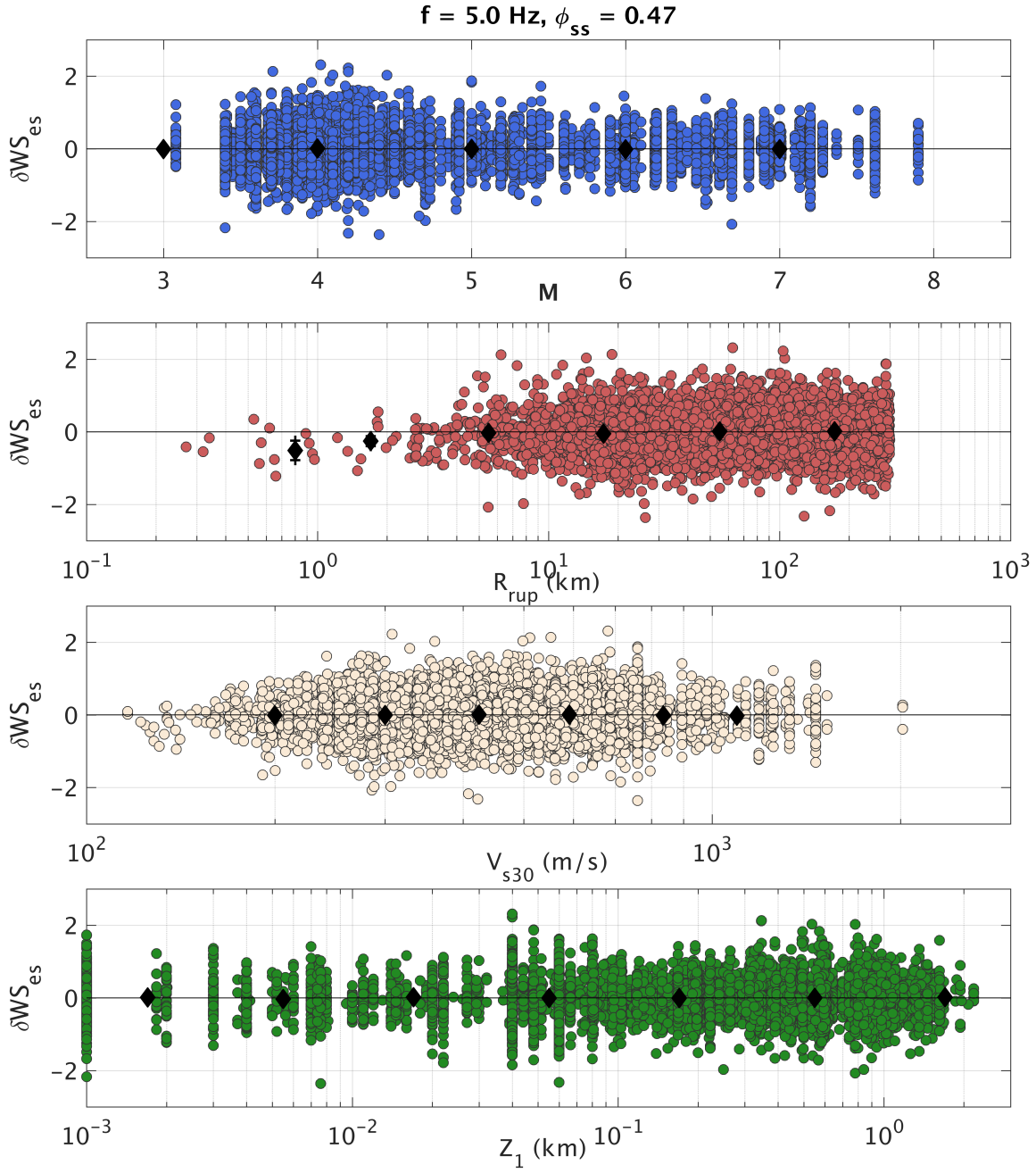

*Figure 2-23. Within-site residuals (δWS_{es}) versus **M**, R_{rup}, V_{s30}, and Z_1 for $f = 5$ Hz.*

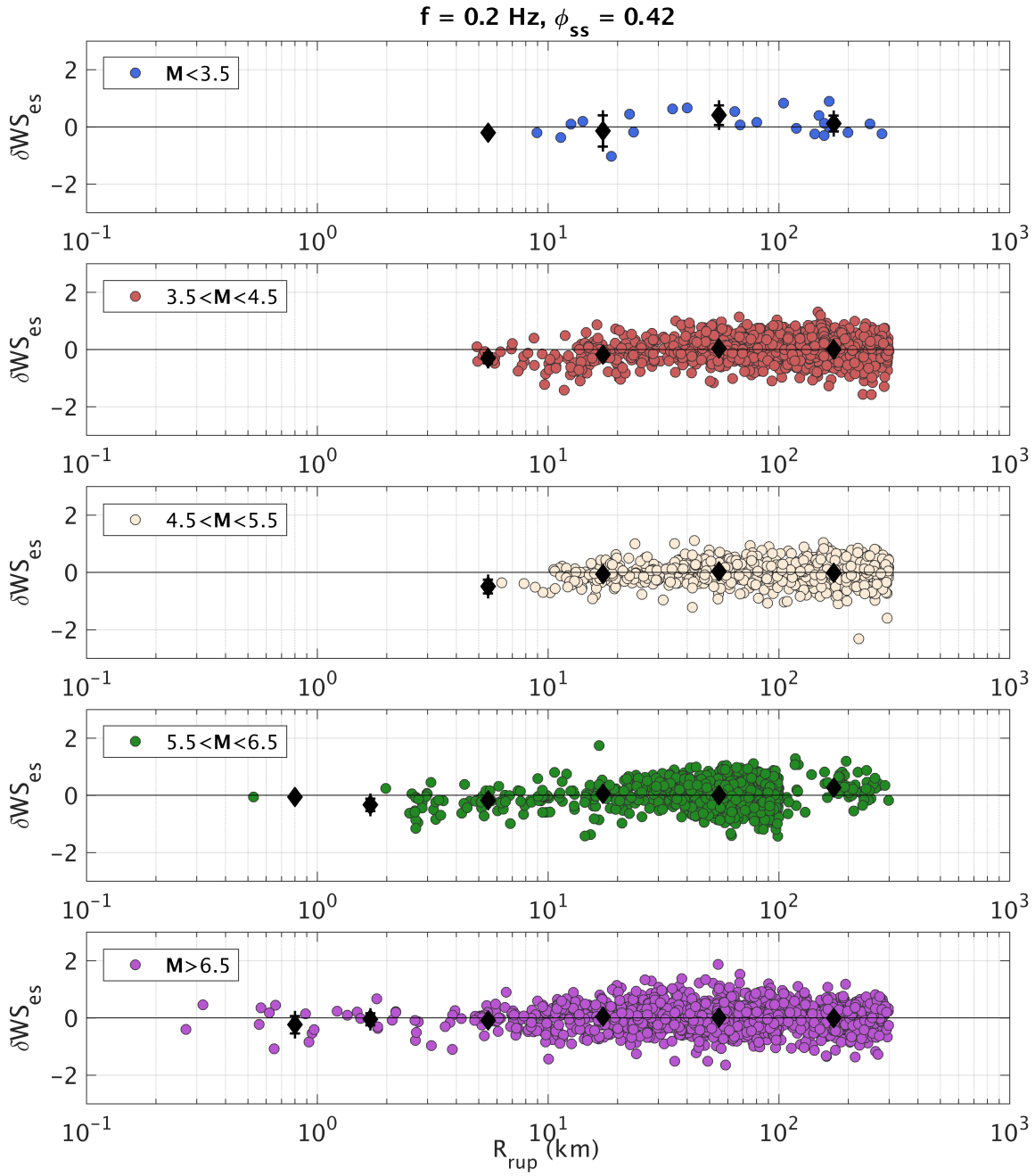

*Figure 2-24. Within-site residuals (δWS_{es}) versus R_{rup}, binned by **M** for $f = 0.2$ Hz.*

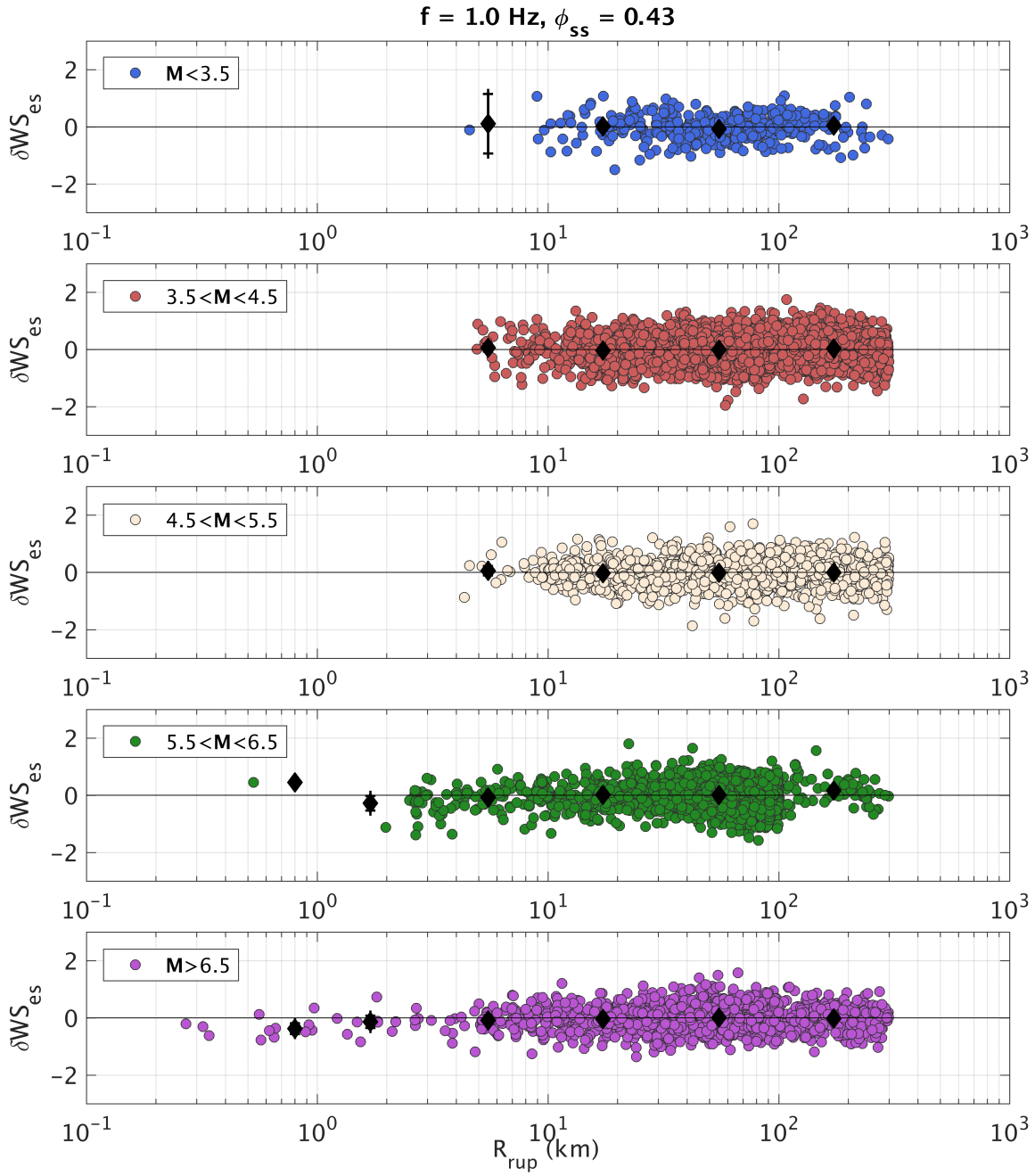

*Figure 2-25. Within-site residuals (δWS_{es}) versus R_{rup}, binned by **M** for $f = 1$ Hz.*

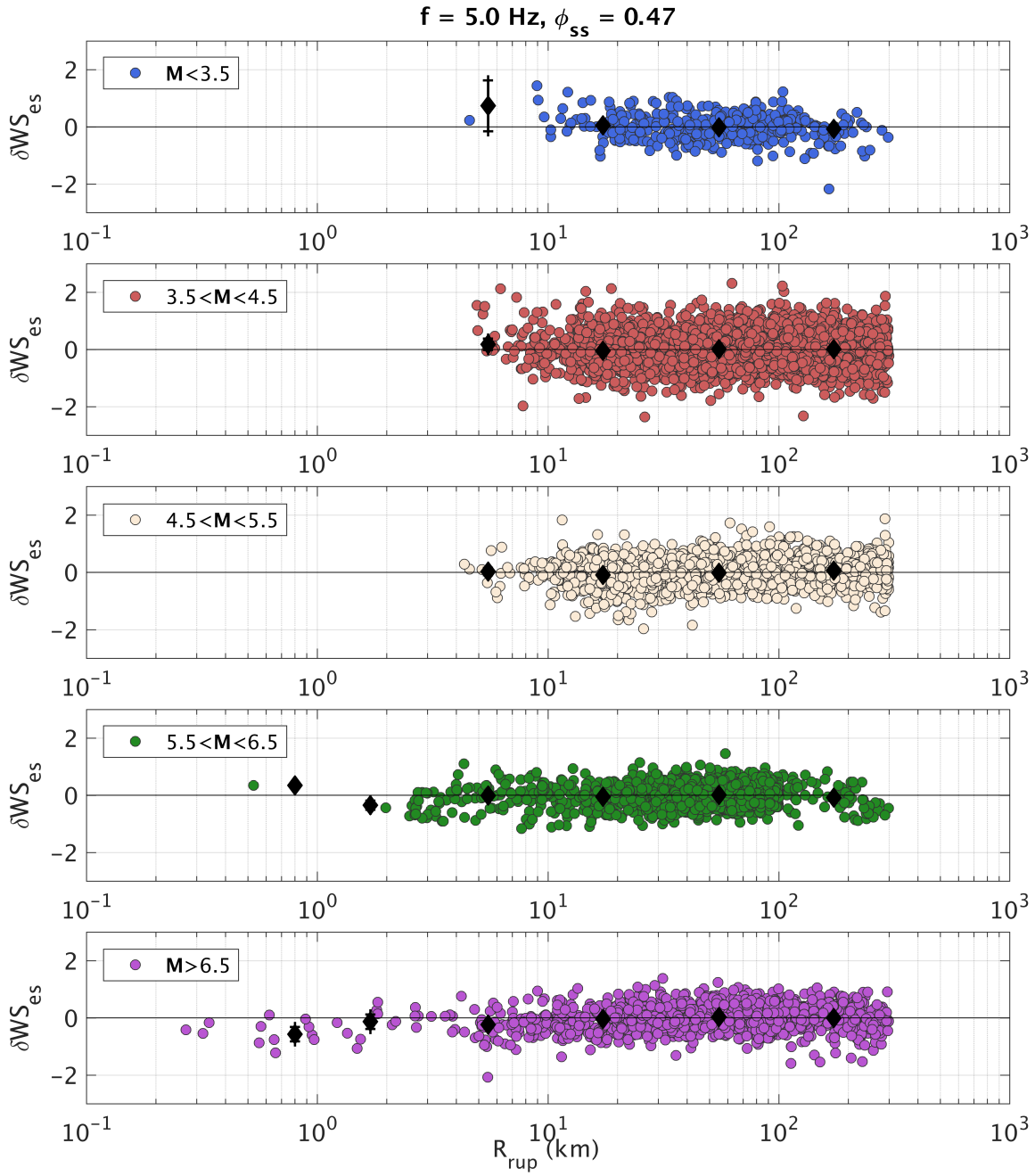

*Figure 2-26. Within-site residuals (δWS_{es}) versus R_{rup}, binned by **M** for $f = 5$ Hz.*

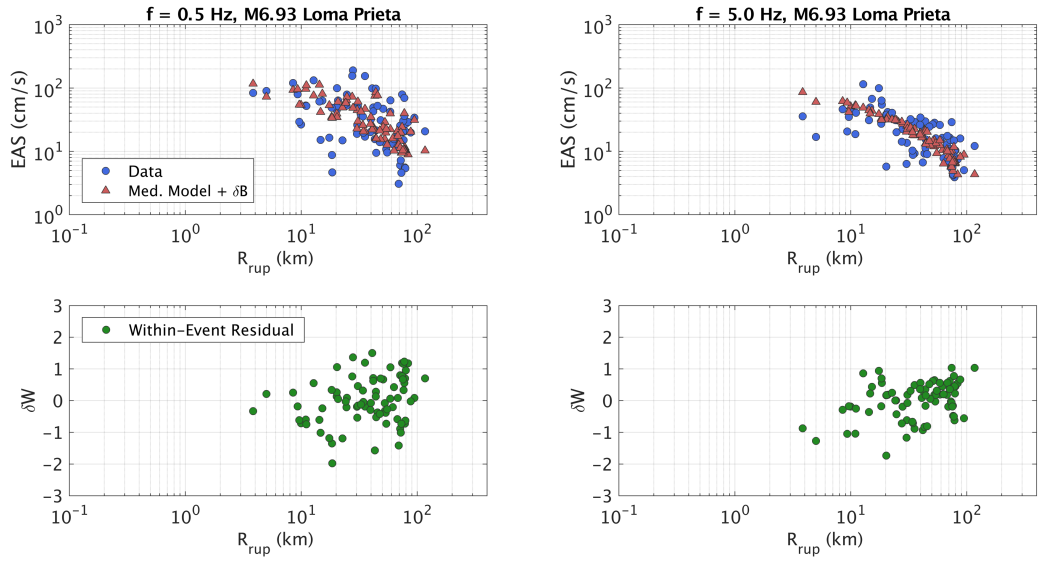

Figure 2-27. Comparison of the model distance attenuation with the ***M****6.93 Loma Prieta data for* $f = 0.5$ *Hz (left) and 5 Hz (right).*

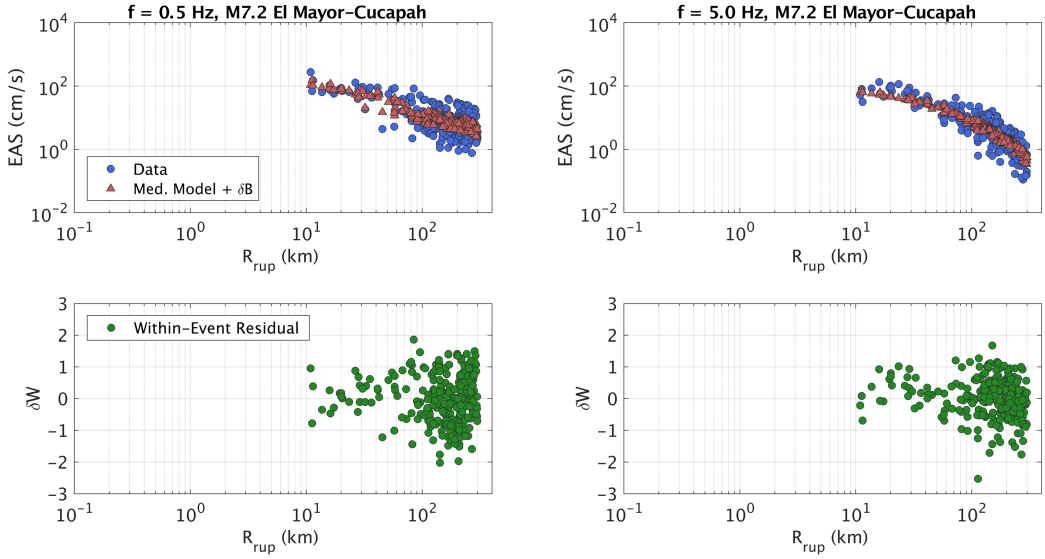

Figure 2-28. Comparison of the model distance attenuation with the ***M****7.2 El Mayor-Cucapah data for* $f = 0.5$ *Hz (left) and 5 Hz (right).*

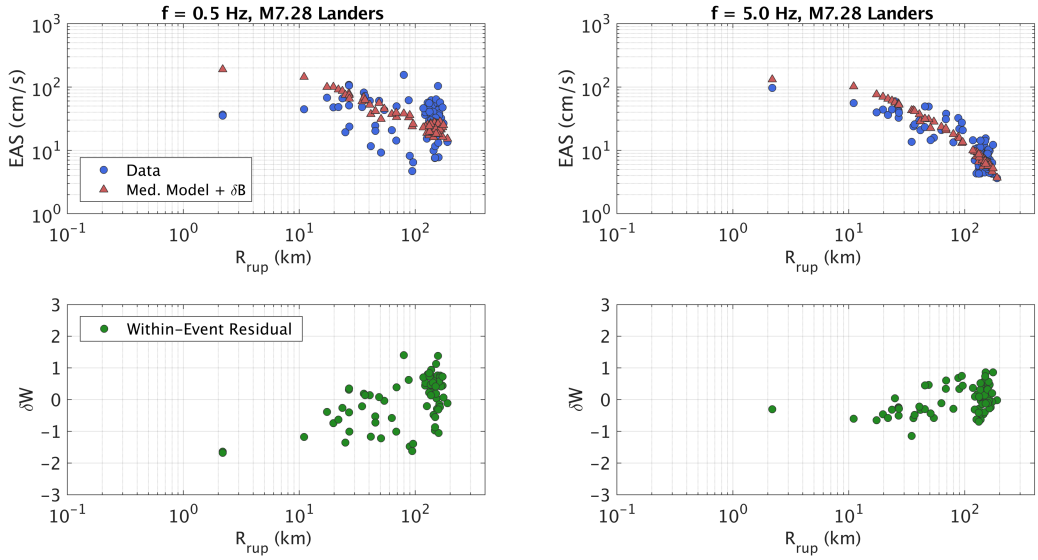

Figure 2-29. Comparison of the model distance attenuation with the ***M****7.28 Landers data for* $f = 0.5$ *Hz (left) and 5 Hz (right).*

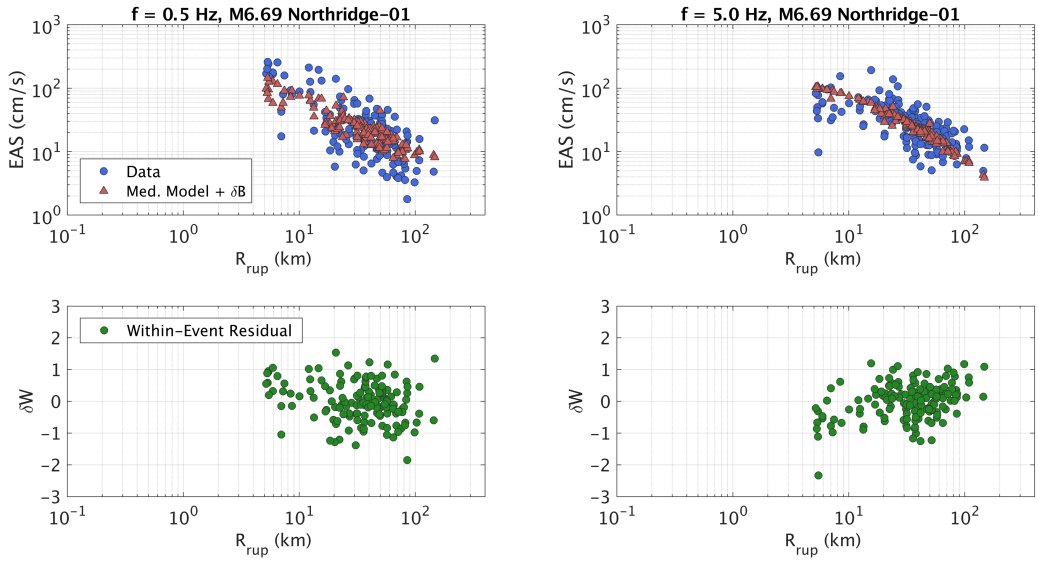

Figure 2-30. Comparison of the model distance attenuation with the ***M****6.69 Northridge data for* $f = 0.5$ *Hz (left) and 5 Hz (right).*

Model Summary

Median Model

In this section, the median model behavior is summarized. In Figure 2-31, the median EAS spectra from this model (solid lines) are compared with spectra from the additive double-corner-frequency source spectral model (dashed lines) described in Boore et al., (2014). The double-corner-frequency spectra are computed using typical parameters for the WUS given by Boore (2003), including shear-wave velocity = 3.5 km/s, density = 2.72 gm/cm^3, stress parameter $\Delta\sigma = 50$ bars, $\kappa = 0.025$ sec, the Boore and Thompson (2015) finite fault distance adjustment, the Boore and Thompson (2014) path duration for western North America, and the Boore (2016) crustal amplification model. The point-source spectral models are calculated using the software package SMSIM (Boore, 2005). The median model spectra are computed for a strike-slip scenario at $R_{rup} = 30$ km, with $Z_{tor} = 0$ km, and with the reference V_{s30} and Z_1 conditions. Figure 2-31 shows overall good agreement between the median model and the additive double-corner-frequency source spectral model with typical WUS parameters, including a well-defined decrease in corner frequency with increasing $\boldsymbol{M}$. At frequencies well below the corner frequency, the spectra should be directly proportional to seismic moment (M_0), and since $M_0 = 10^{1.5\boldsymbol{M}-16.05}$, the spectra in this range should scale by $10^{1.5} \approx 31.6$ for one magnitude unit. This approximate scaling is evident in Figure 2-31. At frequencies between 10 – 30 Hz, there is a dip in the model spectra compared with the point source spectra. This may be related to the region-specific attenuation parameters (geometric spreading and Q), where the point source spectra use generalized models for these attenuation parameters. The κ-based extrapolation in the model spectra begins at 24 Hz.

In Figure 2-32, the median EAS spectra from this model are shown for a set of scenarios. Panels (a) and (b) show the spectra for a vertical strike slip scenario at $R_{rup} = 30$ km with $V_{s30} = 1000$ and 500 m/s, respectively. In (c) and (d) are the spectra for the same V_{s30} but at $R_{rup} = 1$ km.

In Figure 2-33, the distance scaling of the median model is shown for $f = 0.2$, 1, 5, and 20 Hz. All spectra in this figure are from a strike-slip earthquake rupturing the ground surface with reference V_{s30} and Z_1 conditions. The distance scaling is compared with the Chiou and Youngs (2014) model for PSA (dashed lines) by scaling the PSA values to the $R_{rup} = 0.1$ km EAS values. At 0.2 Hz, where the Q term coefficient (c_7) is very small, the distance scaling is controlled by the geometric spreading terms, which includes a transition to $R^{-0.5}$ scaling to model surface wave geometric spreading at larger distances. At increasing frequencies, the effect of the Q term becomes more pronounced. In Figure 2-33(d), the distance scaling is shown to deviate significantly from the Chiou and Youngs (2014) model, which has a magnitude dependence on Q. This difference can be explained by the differences between EAS and PSA. At high frequencies, the PSA is strongly influenced by the predominant ground-motion frequency, as discussed above. Because of this, the PSA scaling at 20 Hz and 5 Hz are similar, but since the EAS at 20 Hz is directly representative of the ground motions in that frequency range, the distance scaling is much stronger for 20H than for 5 Hz.

The $\boldsymbol{M}$ scaling of the median EAS is shown in Figure 2-34 for a strike-slip surface rupturing scenario with reference V_{s30} and Z_1 conditions, for $f = 0.2$, 1, 5, and 20 Hz. In Figure 2-35 through

Figure 2-37, the median $\boldsymbol{M}$ scaling is compared with that from a set of broadband finite-fault simulations. The simulations were performed on the SCEC Broadband Platform, (Maechling et al., 2015) version 17.3, using simulation methods Graves and Pitarka (2015, also known as GP) and Atkinson and Assatourians (2015, also known as EXSIM). Both simulation methods were used to develop broadband time histories for vertical strike slip scenarios with a range of $\boldsymbol{M}$ from M6.5 to 8 and with stations arranged on constant R_{rup} bands. In these figures, the $\boldsymbol{M}$ scaling is shown for $R_{rup} = 3$, 10, 20, and 30 km for the median EAS model, the GP simulations, the EXSIM simulations, and for the Chiou and Youngs (2014; CY14 hereafter) model for PSA. For the CY14 PSA, the amplitudes are scaled to the EAS model values at $\boldsymbol{M}6.5$ for this comparison. The symbols identified in the legend represent the mean simulated EAS over all stations on a given R_{rup} band, and the standard error of the mean.

The simulations are used to evaluate the near-source saturation of the $\boldsymbol{M}$ scaling and to compare with the scaling implied by the data. Overall, there is less saturation in this GMM than there is in CY14 at all frequencies. At very close distances, there is stronger high-frequency saturation in EXSIM than in GP. Interestingly, this relationship is inverted at low frequencies. Based on these and other comparisons, it is determined the EAS saturation in this model is not inconsistent with the saturation from the simulations. The EAS should have some scaling at zero distance even though the PSA is nearly fully saturated at high frequencies because the PSA procedure involves selecting the peak response of the oscillator over all time, meaning it is not affected by duration. Conversely, the EAS will continue to scale for large magnitudes at short distance due to the longer source durations.

The site response scaling of the median model is summarized for a set of example scenarios in Figure 2-38. Panel (a) shows the V_{s30} scaling of the median model for a $\boldsymbol{M}7$ strike-slip earthquake rupturing the surface with reference Z_1 conditions at $R_{rup} = 30$ km. The solid lines represent the total (linear and nonlinear) V_{s30} scaling and the dashed lines represent only the linear portion of the V_{s30} scaling. Panel (b) shows the Z_1 scaling of the median model for the same scenario with $V_{s30} = 300$ m/s. Panel (c) shows the scaling of the modified Hashash et al. (2018) nonlinear site term with $\boldsymbol{M}$, for a scenario with $R_{rup} = 30$ km and $V_{s30} = 300$ m/s. Similarly, panel (d) shows the scaling of the modified Hashash et al. (2018) nonlinear site term with R_{rup}, for a scenario with $\boldsymbol{M}7$ and $V_{s30} = 300$ m/s.

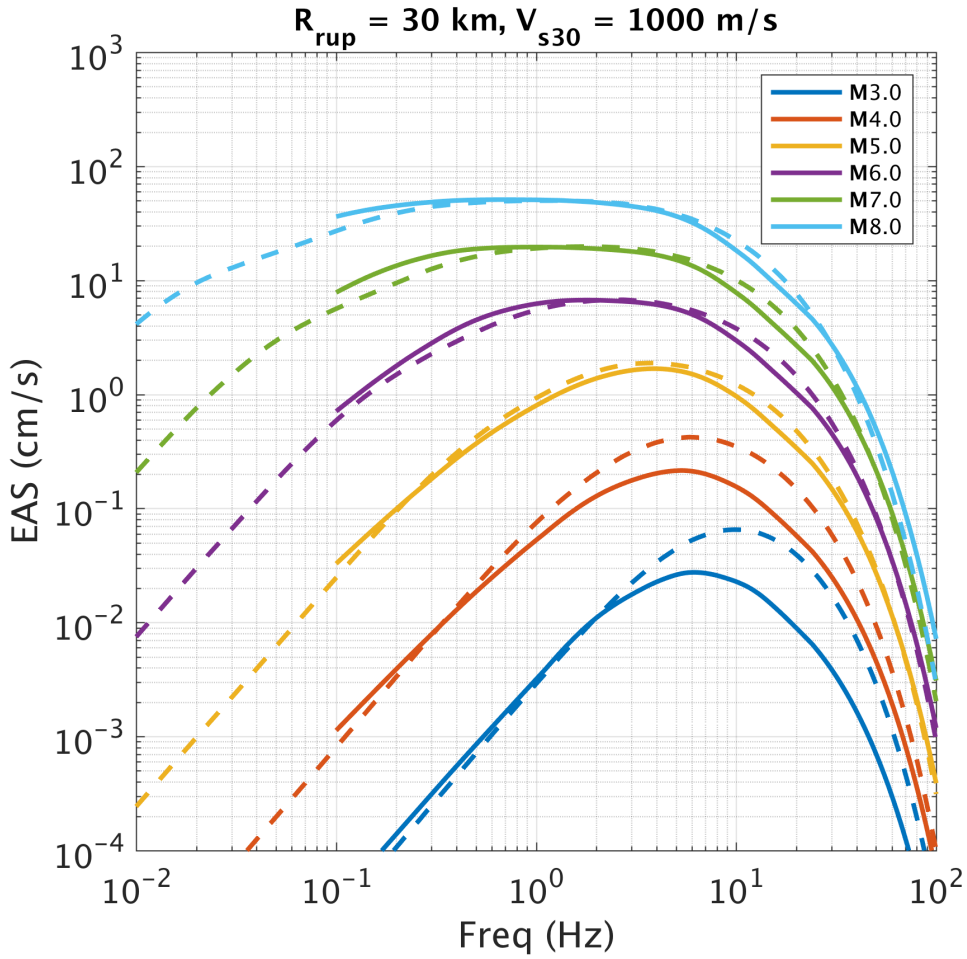

Figure 2-31. Median model spectra for a strike-slip scenario at $R_{rup} = 30$ km, with $Z_{tor} = 0$ km, and with the reference V_{s30} and Z_1 conditions (solid lines) compared with the additive double-corner frequency source spectral model with typical WUS parameters (dashed lines).

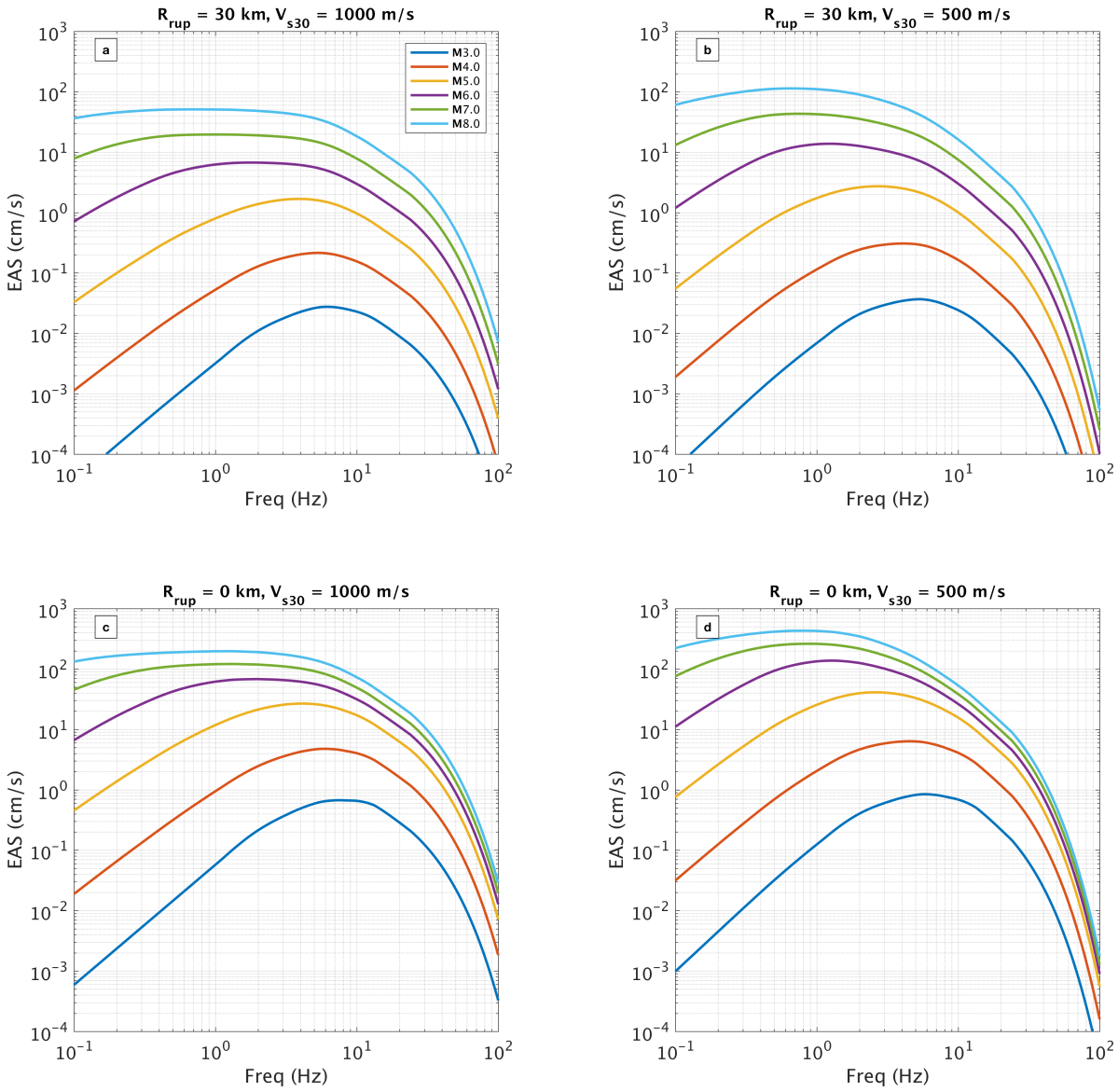

Figure 2-32. Median model EAS spectra for a set of scenarios described by the parameters in each title.

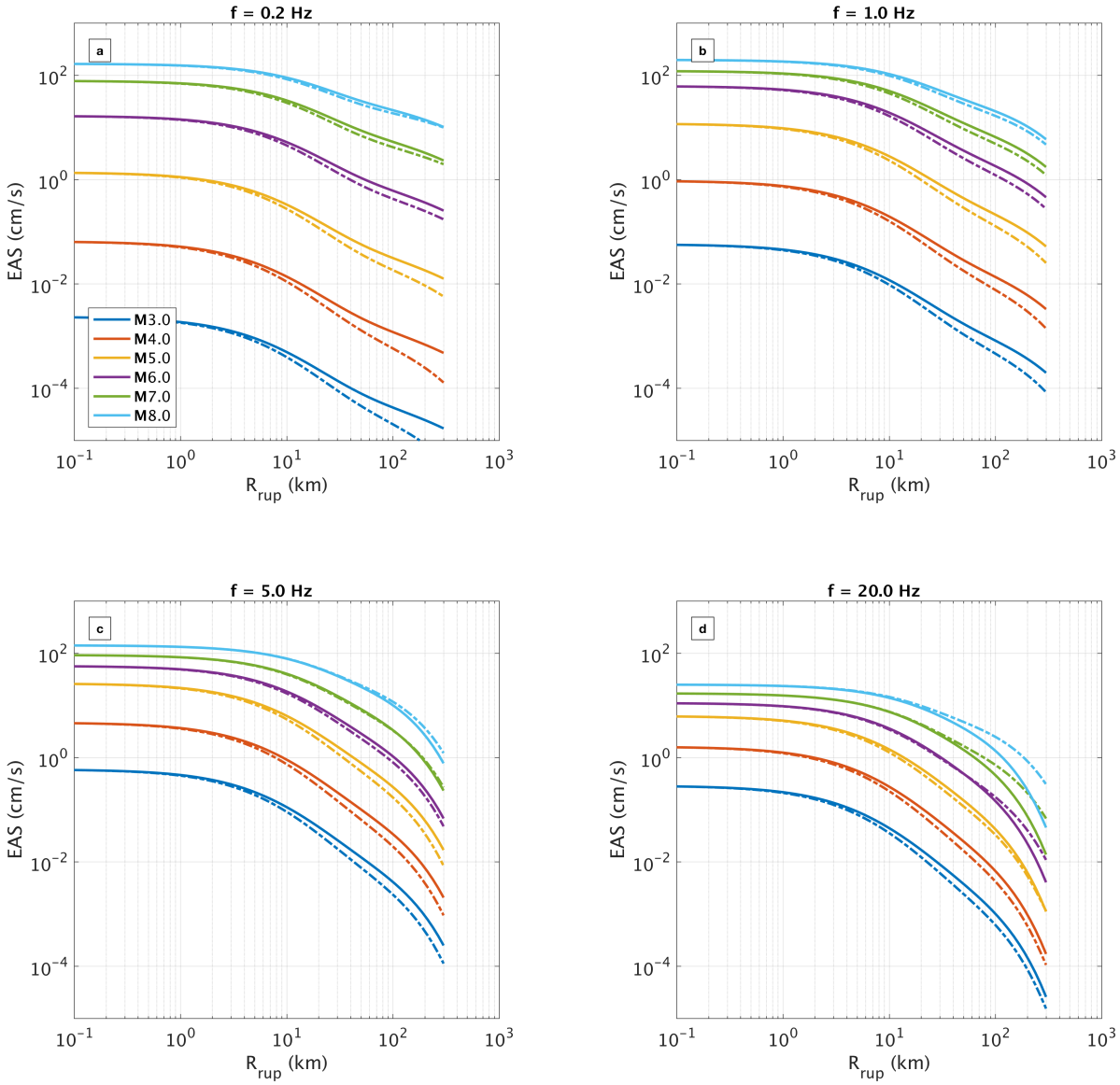

Figure 2-33. Distance scaling of the median EAS (solid lines) for a strike-slip scenario with reference V_{s30} and Z_1 conditions, for four frequencies. For reference, the distance scaling of the Chiou and Youngs (2014) model for PSA is shown for the same scenarios with the dash-dotted lines, where the PSA values have been scaled to the $R_{rup} = 0.1$ km EAS values.

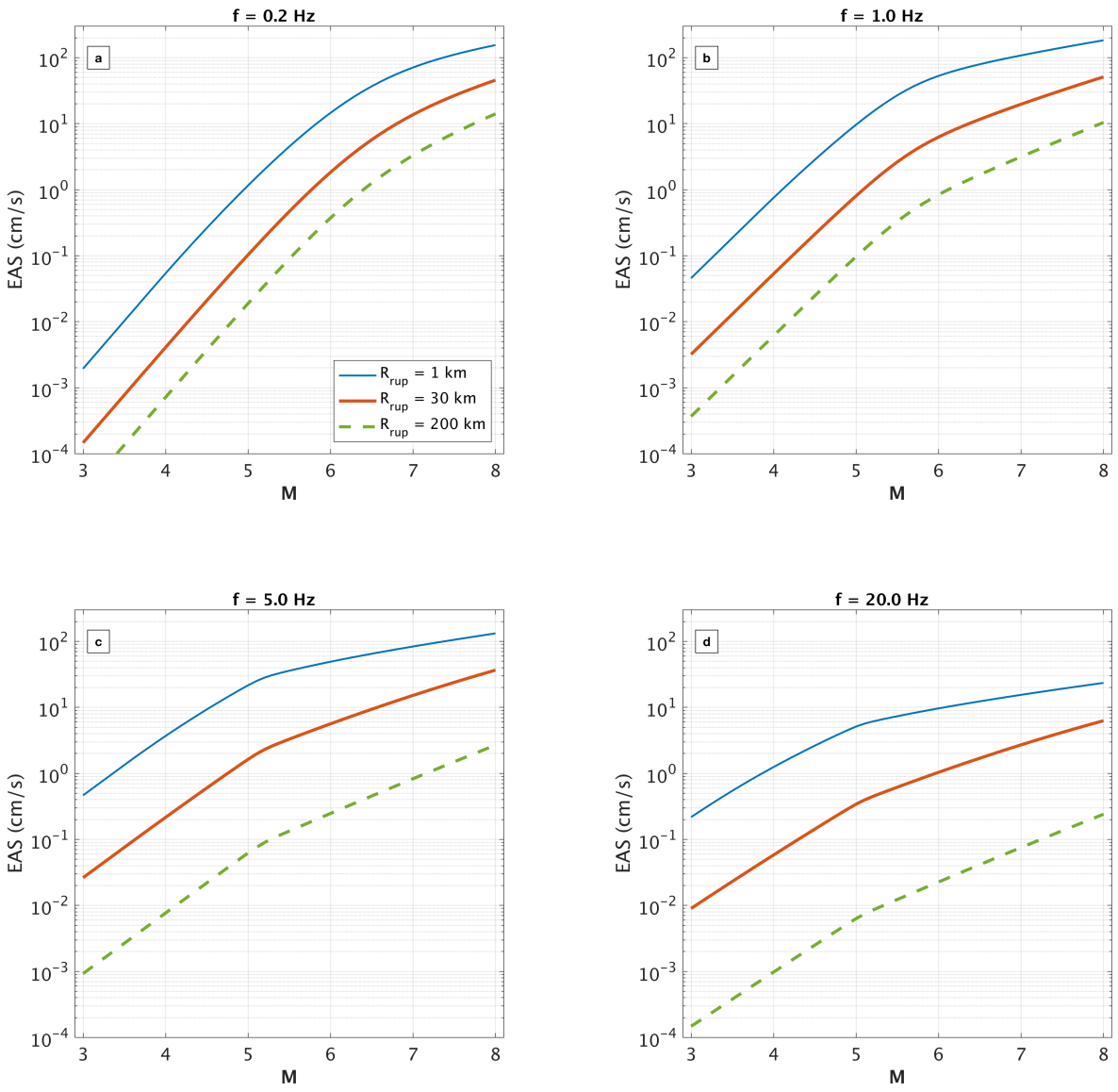

Figure 2-34. ***M*** *scaling of the median EAS for a strike-slip surface rupturing scenario with reference* V_{s30} *and* Z_1 *conditions, for* $f = 0.2$*, 1, 5, and 20 Hz.*

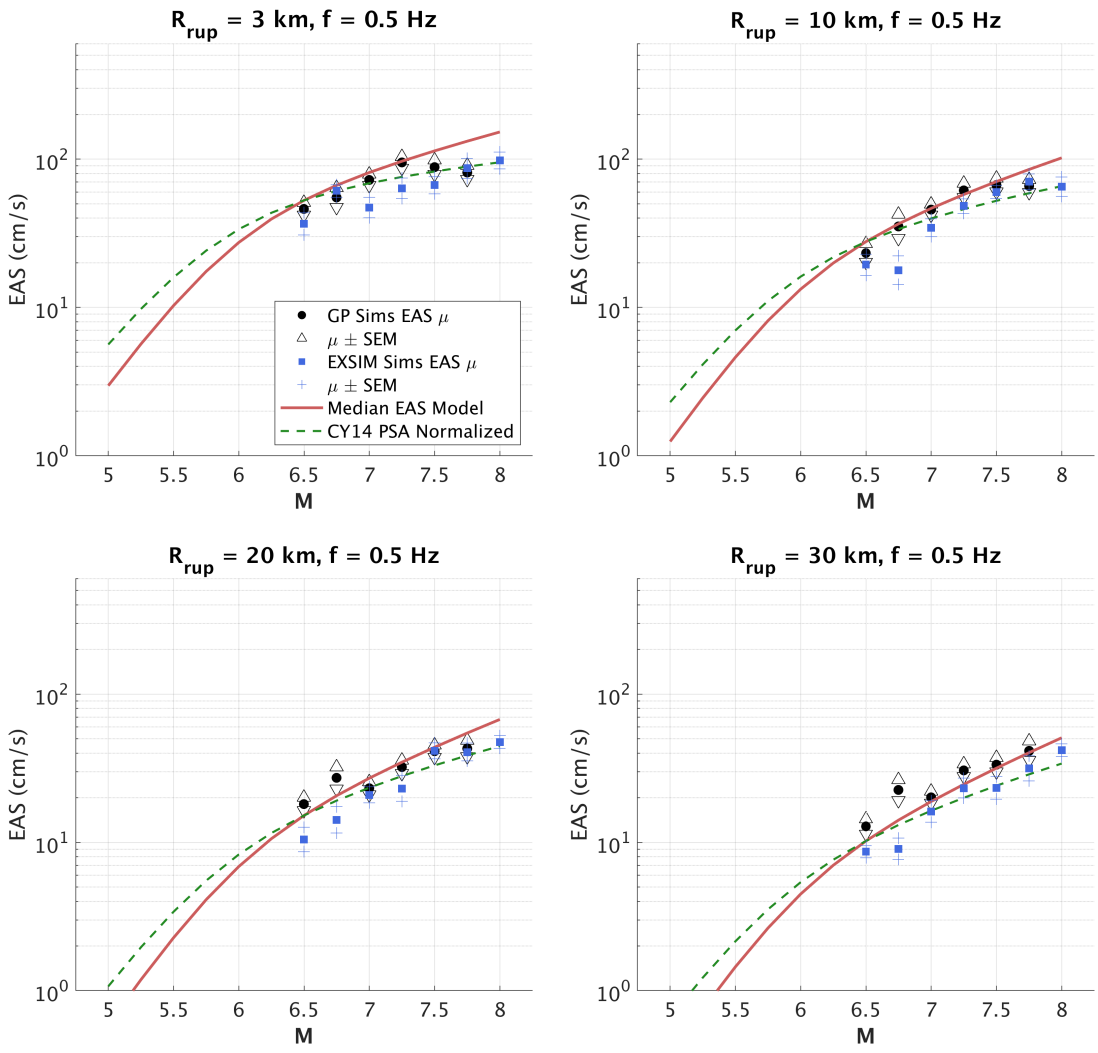

Figure 2-35. ***M*** *scaling of the median model for four distances, at* $f = 0.5$ *Hz for a strike-slip earthquake rupturing the surface with reference* V_{s30} *and* Z_1 *conditions, compared with results from finite-fault simulations.*

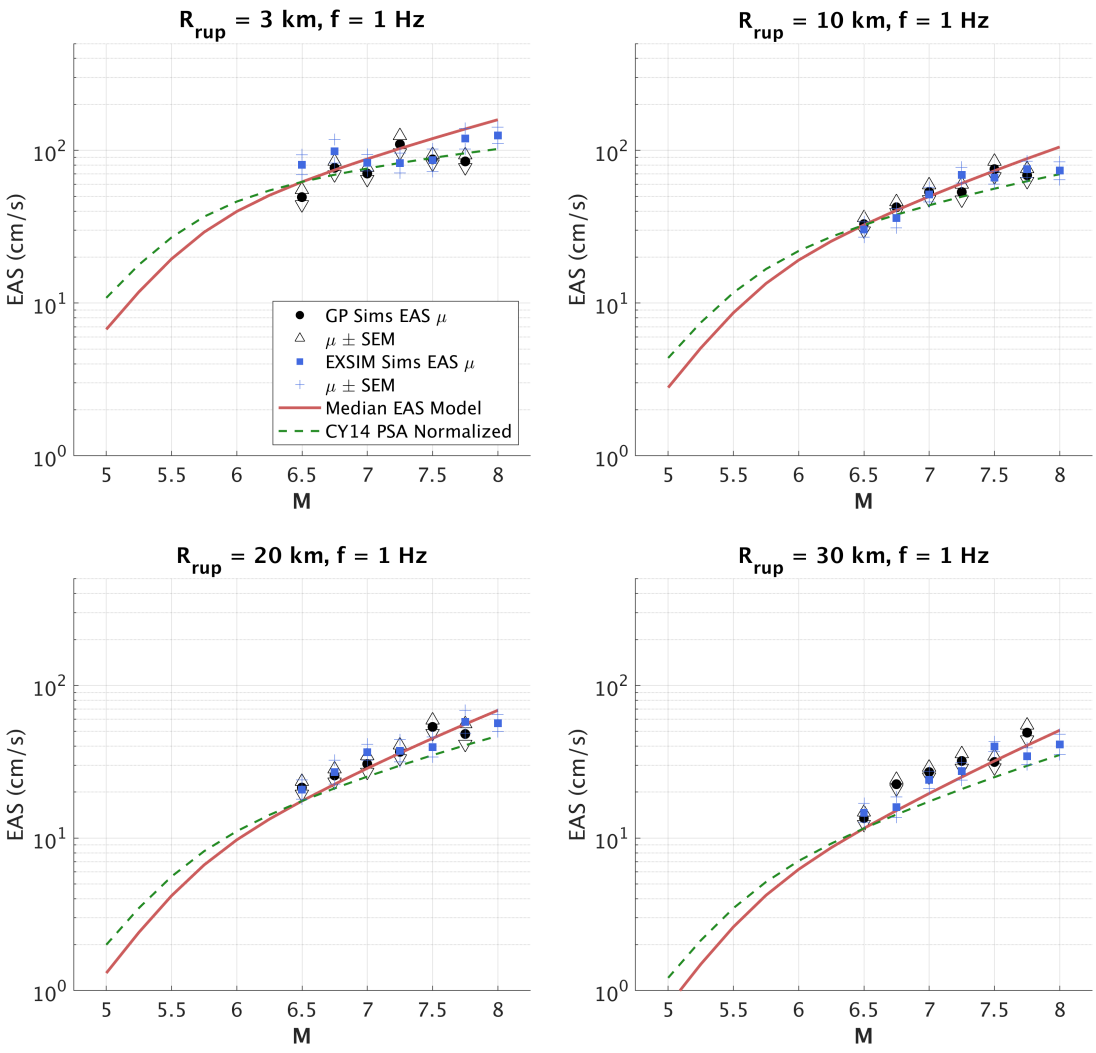

*Figure 2-36. **M** scaling of the median model for four distances, at $f = 1$ Hz for a strike-slip earthquake rupturing the surface with reference V_{s30} and Z_1 conditions, compared with results from finite-fault simulations.*

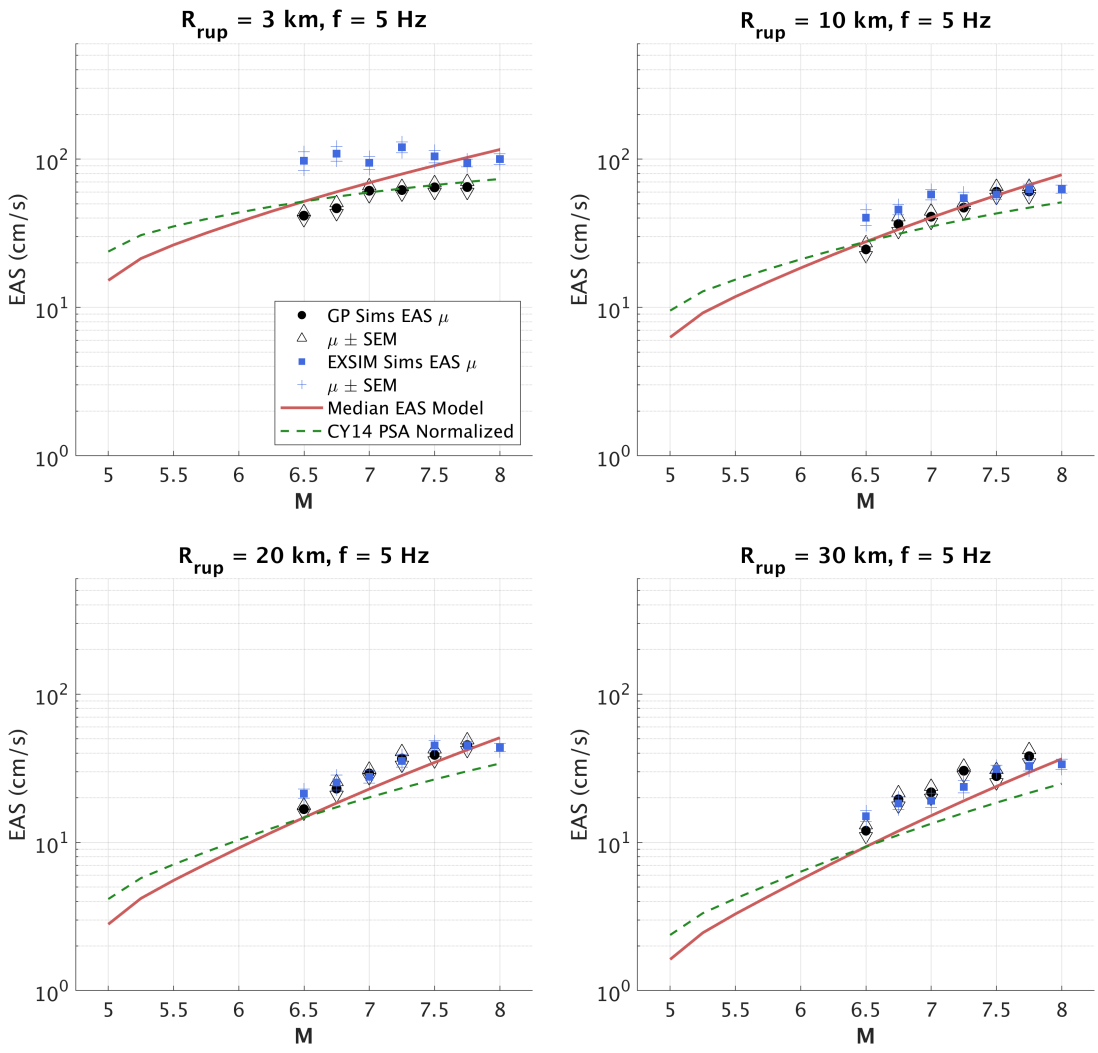

*Figure 2-37. **M** scaling of the median model for four distances, at $f = 5$ Hz for a strike-slip earthquake rupturing the surface with reference V_{s30} and Z_1 conditions, compared with results from finite-fault simulations.*

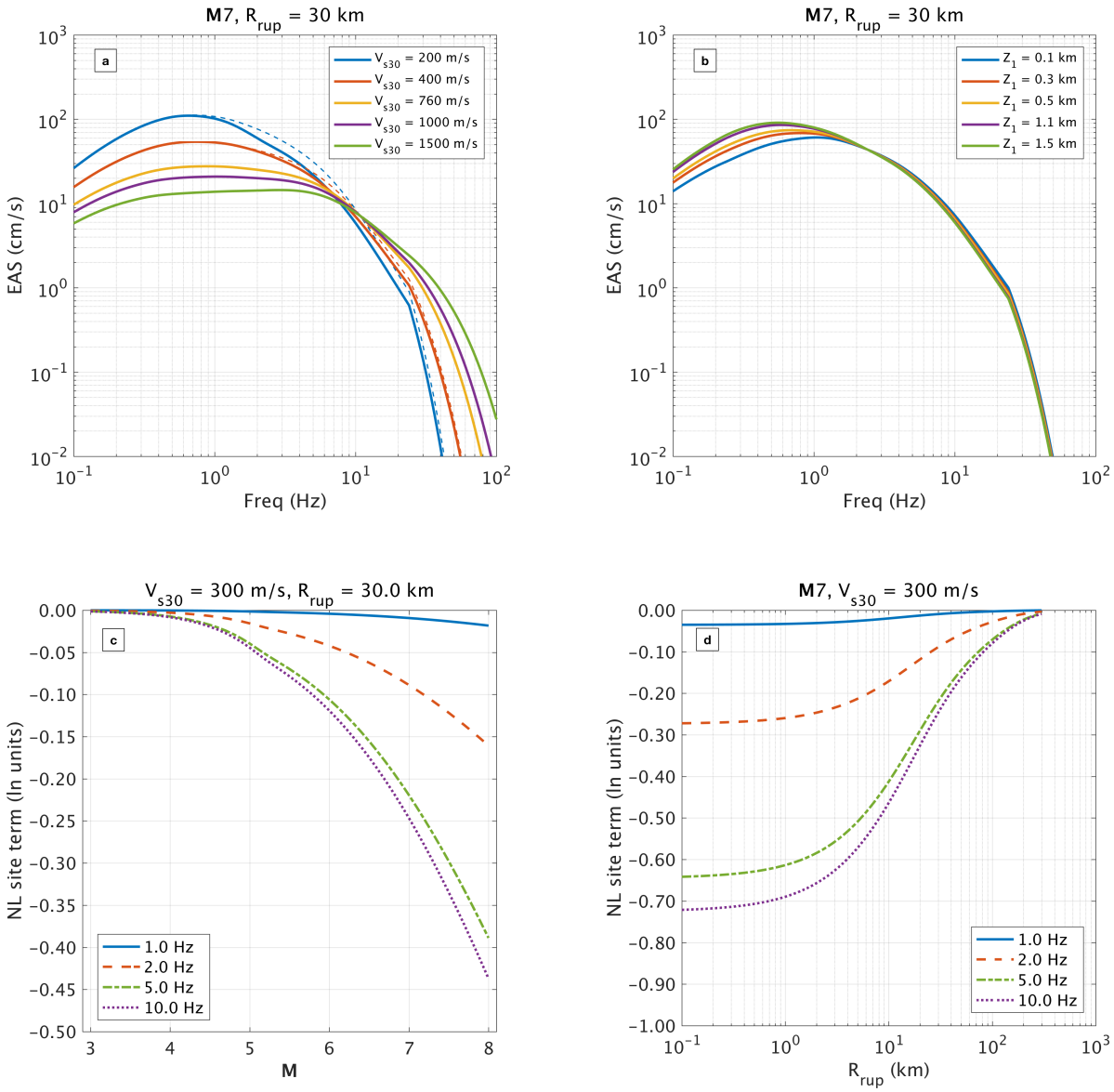

*Figure 2-38. (a) V_{s30} scaling of the median model for a **M**7 strike-slip earthquake rupturing the surface with reference Z_1 conditions at $R_{rup} = 30$ km. The solid lines represent the total (linear and nonlinear) V_{s30} scaling and the dashed lines represent only the linear portion of the V_{s30} scaling. (b) Z_1 scaling of the median model for the same scenario with $V_{s30} = 300$ m/s. (c) scaling of the modified Hashash et al. (2018) nonlinear site term with **M**, for $R_{rup} = 30$ km and $V_{s30} = 300$ m/s. (d) scaling of the modified Hashash et al. (2018) nonlinear site term with R_{rup}, for **M**7 and $V_{s30} = 300$ m/s.*

Standard Deviation Model

Prediction of the EAS (Equation 2-9) requires a model for the aleatory variability. The random-effects method employed leads to the separation of total residuals into between-event residuals (δB) site-to-site residuals ($\delta S2S$) and single-station within-event residuals (δWS), which have variance components τ^2, ϕ_{S2S}^2, and ϕ_{ss}^2, respectively. The total standard deviation model (natural logarithm units) is given by Equation 2-21.

$$\sigma = \sqrt{\tau^2 + \phi_{S2S}^2 + \phi_{ss}^2 + c_{1a}^2} \qquad (2-21)$$

Where c_{1a} is the spectral shape adjustment coefficient (Figure 2-16) which has been added to the total standard deviation, as described previously. Figure 2-39 shows the standard deviations for each component of Equation 2-21a, as calculated directly from the regression analysis (all magnitudes). The increase observed in τ at frequencies greater than about 3 Hz is consistent with the behavior of response spectrum models (e.g. Abrahamson et al., 2014, Chiou and Youngs, 2014). This is believed to be the effect of κ, which is related to regional crustal damping, being mapped into the between-event terms. For a given earthquake, recordings in close proximity to the source will have similar κ, and the high frequencies of these recordings may be systematically above or below average. If there is a regional difference in kappa, then the regression treats this as an event-specific variation, which artificially increases τ. Stafford (2017) also observed an increase in the variance components of the FAS with increasing frequency and hypothesized that the increase of ϕ_{S2S} reflects variations in κ across different sites.

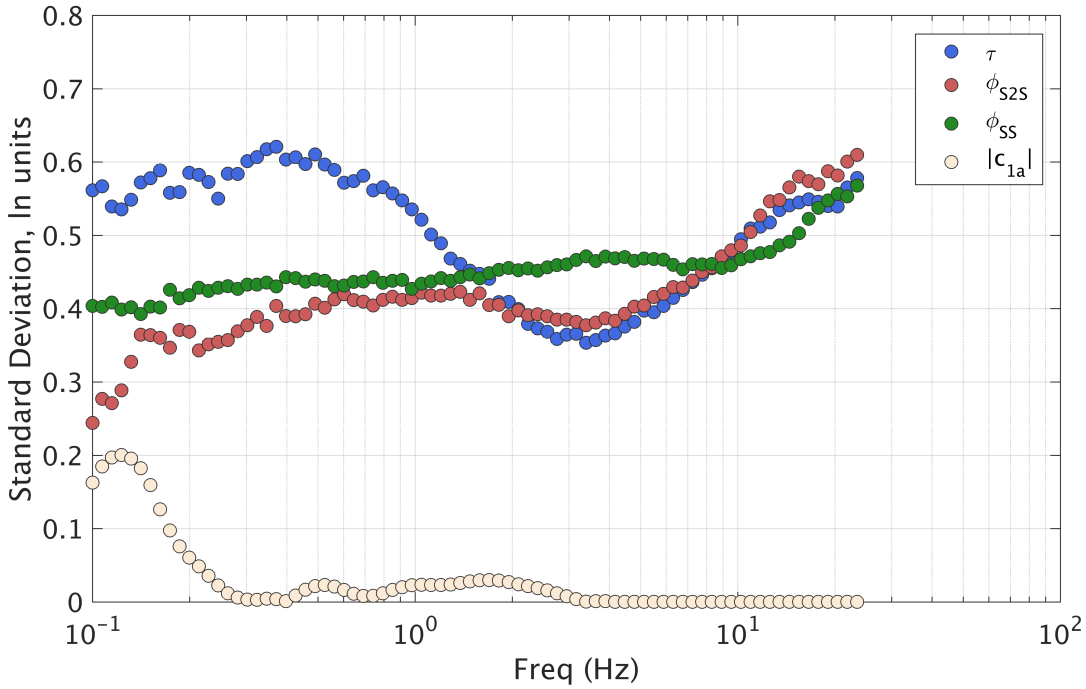

Figure 2-39. Standard deviation components calculated directly from the regression analysis, for all magnitudes.

The magnitude dependence of each aleatory term is fit as shown in Figure 2-40 and is given by Equations 22a-c. At low frequencies, the small-magnitude data have higher between-event standard deviation. This is also consistent with the Abrahamson et al., (2014) response spectrum model, and could be related to the steeper magnitude scaling slope at low magnitudes and the uncertainty in small-magnitude source measurements (Abrahamson et al., 2014). The standard deviations of the two within-event residuals do not have strong magnitude dependence at low frequencies. At higher frequencies, τ does not show strong magnitude dependence, but ϕ_{S2S} and ϕ_{ss} are larger for the small-magnitude data, which is again consistent with the Abrahamson et al., (2014) and Chiou and Youngs, (2014) models. Higher within-event variability for small

magnitudes may be related to the increased effect of the high-frequency radiation pattern, which is reduced for larger magnitude events due to destructive interference (Abrahamson et al., 2014).

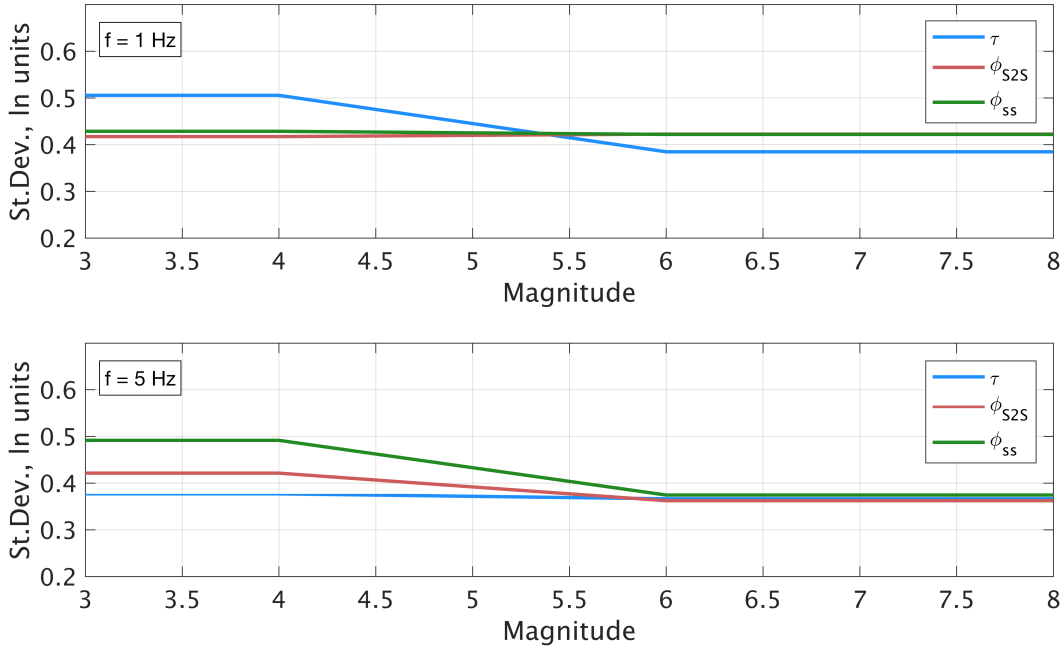

Figure 2-40. Magnitude scaling of the standard deviation terms for $f = 1$ and 5 Hz.

$$\tau = \begin{cases} s_1 & for\ \boldsymbol{M} < 4.0 \\ s_1 + \dfrac{s_2 - s_1}{2}(\boldsymbol{M} - 4) & for\ 4.0 \leq \boldsymbol{M} \leq 6.0 \\ s_2 & for\ \boldsymbol{M} > 6.0 \end{cases} \quad (2-22a)$$

$$\phi_{S2S} = \begin{cases} s_3 & for\ \boldsymbol{M} < 4.0 \\ s_3 + \dfrac{s_4 - s_3}{2}(\boldsymbol{M} - 4) & for\ 4.0 \leq \boldsymbol{M} \leq 6.0 \\ s_4 & for\ \boldsymbol{M} > 5.5 \end{cases} \quad (2-22b)$$

$$\phi_{ss} = \begin{cases} s_5 & for\ \boldsymbol{M} < 4.0 \\ s_5 + \dfrac{s_6 - s_5}{2}(\boldsymbol{M} - 4) & for\ 4.0 \leq \boldsymbol{M} \leq 6.0 \\ s_6 & for\ \boldsymbol{M} > 6.0 \end{cases} \quad (2-22c)$$

At frequencies above approximately 20 Hz, the model is constrained to smoothly transition to be flat in frequency space for all components of σ. The frequency dependence of the standard deviation model is shown in Figure 2-41, and examples of the total standard deviation model for a set of scenarios are shown in Figure 2-42. Coefficients s_1 through s_6 are given in Appendix B. In Figure 2-43, the components of the standard deviation model are compared with those from Bora et al., (2015) and Stafford (2017). The Bora et al., (2015) model was developed for smoothed FAS from data in Europe, the Mediterranean, and the Middle-East and the Stafford (2017) model was developed for unsmoothed FAS from a subset of the NGA-West1 database (Chiou et al., 2008).

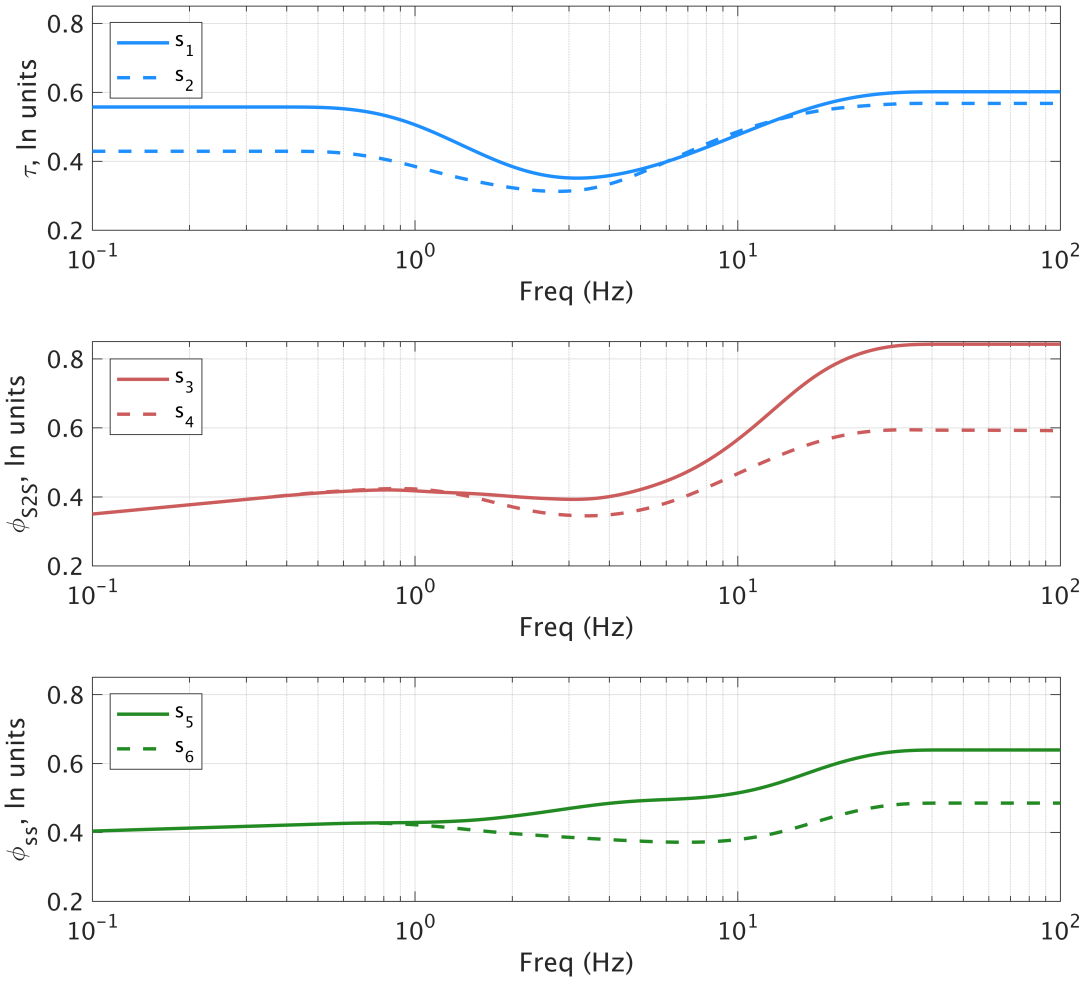

Figure 2-41. Frequency dependence of the standard deviation model.

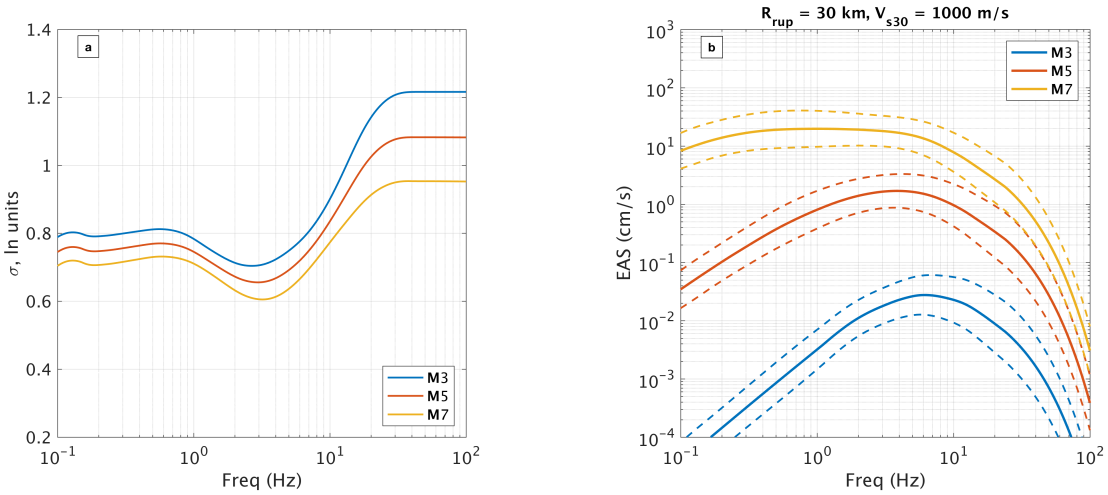

*Figure 2-42. (a) The total standard deviation model for **M**3, 5, and 7. (b) The median (solid lines) and median plus and minus one σ (dashed lines) EAS spectra for **M**3, 5, and 7 scenarios.*

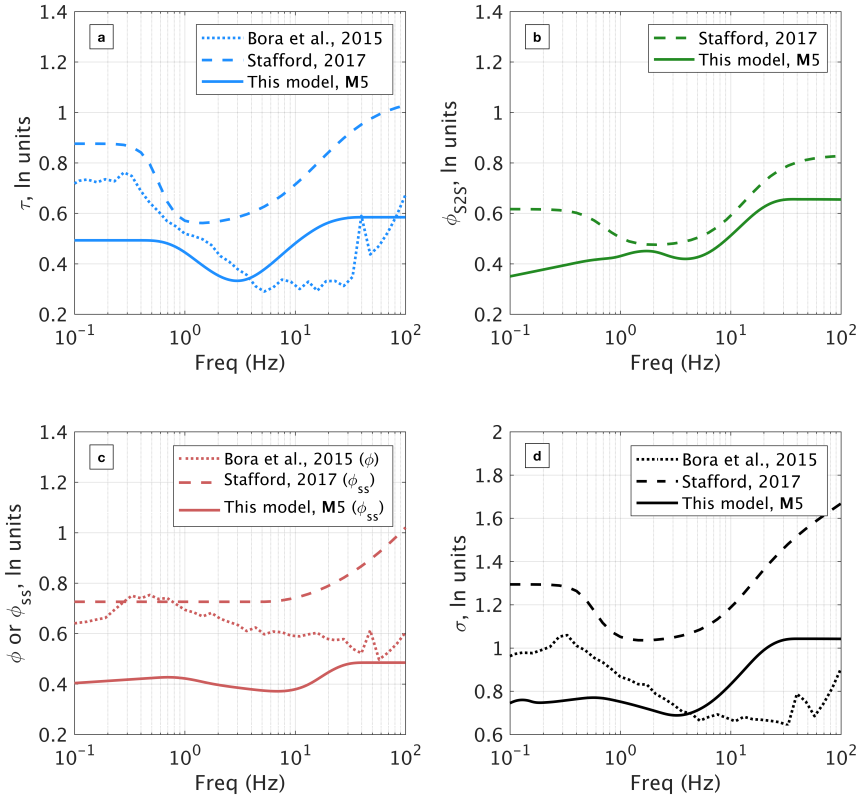

*Figure 2-43. Comparison of the standard deviation components between the Bora et al., (2015), Stafford (2015) models and this model, for a **M**5 earthquake. Panels (a) through (d) show the comparison of τ, ϕ_{S2S}, ϕ_{SS}, and σ, respectively.*

The standard deviation model developed here is linear, meaning it does not account for the effects of nonlinear site response. As discussed in Al Atik and Abrahamson (2010) and Abrahamson et al., (2014), the nonlinear effects on the standard deviation are influenced by the variability of the rock motion, leading to a reduction in the soil motion variability at high frequencies. In Abrahamson et al., (2014), the standard deviation of the rock motion is estimated by removing the site amplification variability (determined analytically) from the surface motion, and the variability of the soil motion is computed using propagation of errors. In a future update of the model, similar steps will be taken to account for the effects of nonlinear site response on the standard deviation.

Range of Applicability

The model is applicable for shallow crustal earthquakes in California and Nevada. The model is developed using a database dominated by California earthquakes, but uses data worldwide to constrain the magnitude scaling and geometric spreading. The model is applicable for rupture distances of 0 – 300 km, $\boldsymbol{M}$ 3.0 – 8.0, and over the frequency range 0.1 – 100 Hz. The V_{s30} range of applicability is 180 – 1500 m/s, although the model is not well constrained for V_{s30} values greater than 1000 m/s. Models for the median and the aleatory variability of the EAS are developed. Regional models for Japan and Taiwan will be developed in a future update of the model. A model for the inter-frequency correlation of ϵ_{EAS} is presented in Chapter 3.

Limitations and Future Considerations

The model presented uses the ergodic assumption, as introduced by Anderson and Brune (1999). This means that the variability in the data from a broad geographic region (in this case, globally

for the magnitude scaling and geometric spreading, and over the California and Nevada for the remaining parameters) are assumed to represent the variability of the ground motions over time for a given site in the target region. With this approach, the model is expected to be appropriate for general use in California and Nevada but will be biased for a particular site. In an ergodic model, systematic site, path, and source effects are the dominant parts of the aleatory variability, making fully or partially non-ergodic models attractive (Abrahamson, 2017). Developing a partially non-ergodic model requires repeated observations of source, path, or site effects. For example, in this model, with multiple recordings at a site, the median site-specific amplification for the site is separated and the intra-event residual is partitioned, shifting that component of aleatory variability into an epistemic uncertainty (Walling, 2009). To get a fully non-ergodic model, all of the components of the total ground-motion variability that are not representative of the variability of future observations of ground motion at a single site must be removed (Abrahamson and Hollenback, 2012).

Incorporating regional differences into a GMM is a first step towards a partially non-ergodic assumption (Kuehn and Scherbaum, 2016). To account for the known differences in regional crustal structure, regionalized models for Japan and Taiwan can be developed in a future model update. This will involve regionalizing the linear V_{s30} scaling (c_8), soil depth scaling (c_{11}), anelastic attenuation (c_7) and spectral shape (c_1) coefficients.

At frequencies above 24 Hz, this model uses a κ-based extrapolation. This approach required selecting a $\kappa - V_{s30}$ relationship from the literature. Future improvements to the model may

include explicit data regression at higher frequencies, developing a region-specific $\kappa - V_{s30}$ relationship, or calculating one directly from the database used.

The effects of rupture directivity and hanging-wall scaling are not explicitly included in the model. Therefore, these effects are accounted for in the total aleatory variability. The hanging-wall effect, characterized by increased ground motion amplitudes on the hanging-wall side of dipping ruptures, is not well constrained by the data. For NGA-West2, Donahue and Abrahamson (2013) investigated these effects for response spectra using finite-fault simulations, and the results were incorporated in the Abrahamson et al., (2014) model. In a future update, a similar study for the EAS could be incorporated into this model. The effects of rupture directivity on the EAS is also a potential future research topic. Finally, the effects of nonlinear site response on the standard deviation are not accounted for in this model, which can be addressed in a future update.

Chapter 3:

An empirical model for the inter-frequency correlation of epsilon for Fourier amplitude spectra

Abstract

An empirical ground motion model (GMM) for the inter-frequency correlation of epsilon (ρ_ϵ) for smoothed Fourier amplitude spectra (FAS) is presented. This model is developed for the smoothed effective amplitude spectrum (EAS), as defined by PEER (Goulet et al., 2018). The EAS is the orientation-independent horizontal component FAS of ground acceleration. Ground-motion data are from the Pacific Earthquake Engineering Research Center (PEER) Next Generation Attenuation-West 2 (NGA-West2) database (Ancheta et al., 2014), which includes shallow crustal earthquakes in active tectonic regions. The normalized residuals (ϵ) are obtained from the Bayless and Abrahamson (2018a) GMM, are partitioned into between-event, between-site, and within-site components, and a model is developed for the total correlation between frequencies. The total correlation model features a two-term exponential decay with the natural logarithm of frequency. At higher frequencies, the model differs substantially from previously published models, where the ground-motion smoothing technique employed has a large effect on the resulting correlations. The empirical ρ_ϵ are not found to have statistically significant magnitude, distance, site parameter, or regional dependence. The model is applicable for crustal earthquakes in active tectonic regions worldwide, for rupture distances of 0 – 300 km, $\boldsymbol{M}$ 3.0 – 8.0, and over the frequency range 0.1 – 24 Hz. Tables for the total correlation model coefficients and covariance matrices are provided in the electronic supplement to this dissertation.

Introduction

Residuals from empirical ground-motion models (GMMs, also known as ground-motion prediction equations, GMPEs) are typically partitioned into between-event residual (δB), and within-event residuals (δW), following the notation of Al Atik et al., (2010). For large number of recordings per earthquake, the between-event residual is approximately the average difference between the observed Intensity Measure (IM) from a specific earthquake and the IM predicted by the GMM. The within-event residual (δW) is the difference between the IM at a specific site for a given earthquake and the median IM predicted by the GMM plus δB. By accounting for repeatable site effects, δW can further be partitioned into a site-to-site residual ($\delta S2S$) and the single-station within-event residual (δWS; also called the within-site residual) (e.g. Villani and Abrahamson, 2015). Using this notation, the residuals take the following form:

$$Y_{es} = g(X_{es}, \theta) + \delta B_e + \delta S2S_s + \delta WS_{es} \qquad (3-1)$$

$$\delta_{total,es} = Y_{es} - g(X_{es}, \theta) = \delta B_e + \delta S2S_s + \delta WS_{es} \qquad (3-2)$$

where Y_{es} is the natural logarithm of the recorded ground motion IM for earthquake e and site s, $g(X_{es}, \theta)$ is the median GMM, X_{es} is the vector of explanatory seismological parameters (magnitude, distance, site conditions, etc.), θ is the vector of GMM coefficients, and $\delta_{total,es}$ is the total residual.

The residual components δB, $\delta S2B$ and δWS are well-represented as zero-mean, independent, normally distributed random variables with standard deviations τ, ϕ_{S2S} and ϕ_{ss}, respectively (Al Atik et al., 2010). GMM residual components are converted to epsilon (ϵ_B, ϵ_{S2S}, and ϵ_{WS}) by

normalizing the residuals by their respective standard deviations. Because of the normalization, the random variables ϵ_B, ϵ_{S2S}, and ϵ_{WS} are represented by standard-normal distributions (mean=0, variance=1). If the total residual is used, then the resulting ϵ_{total} will, in general, not have zero mean due to the uneven sampling of recordings per earthquake in the data set.

For a given recording, the values of ϵ at neighboring periods (T) are generally correlated. For example, if a ground motion is stronger than average at T=1.0 s, then it is likely to also be stronger than expected at nearby periods, e.g. T=0.8 s or T=1.2 s; however, for a widely-spaced period pair (e.g. T=10.0 s compared with T=1.0 s), the ϵ values will be weakly correlated. The inter-period (or equivalently, inter-frequency) correlation coefficient, ρ, quantifies the relationship of ϵ values between periods for a given recording.

An empirical GMM is presented for the inter-frequency correlation of epsilon (ρ_ϵ) for smoothed Fourier amplitude spectra (FAS). The correlation model is based on recordings from the Pacific Earthquake Engineering Research Center (PEER) Next Generation Attenuation-West 2 (NGA-West2) database (Ancheta et al., 2014), which includes shallow crustal earthquakes in active tectonic regions. The normalized residuals (ϵ) are obtained from the GMM described in Chapter 2. Rather than the traditionally used response spectrum, the GMM from Chapter 2 is developed for the median and variance of the smoothed effective amplitude spectrum (EAS), as defined by PEER (PEER, 2015). The EAS is the orientation-independent horizontal component FAS of ground acceleration, described below.

Chapter Organization

In this chapter, the correlation of epsilon is briefly reviewed, the ground motion intensity measure (IM) used is described, the reasoning behind selecting Fourier amplitudes as the IM is given, the development of the correlation model and the sensitivity of the correlation to database subsets is described, and the model is compared with other published correlation models.

Review of the Correlation of ϵ

The correlation coefficient of two random variables is a measure of their linear dependence. In this case, ϵ calculated from a large set of ground motions at different frequencies (f) are random variates. The correlation coefficient between $\epsilon(f_1)$ and $\epsilon(f_2)$ can be estimated using a maximum likelihood estimator, the Pearson-product-moment correlation coefficient, ρ (Fisher, 1958). The correlation coefficient for a sample of ϵ at frequencies f_1 and f_2 is given by Equation 3-3:

$$\rho_{\epsilon(f_1),\epsilon(f_2)} = \frac{cov\big(\epsilon(f_1),\epsilon(f_2)\big)}{\sigma_{\epsilon(f_1)}\sigma_{\epsilon(f_2)}} = \frac{\sum_{i=1}^{n}\big(\epsilon_i(f_1)-\overline{\epsilon(f_1)}\big)\big(\epsilon_i(f_2)-\overline{\epsilon(f_2)}\big)}{\sqrt{\sum_{i=1}^{n}\big(\epsilon_i(f_1)-\overline{\epsilon(f_1)}\big)^2}\sqrt{\sum_{i=1}^{n}\big(\epsilon_i(f_2)-\overline{\epsilon(f_2)}\big)^2}} \quad (3-3)$$

where cov is the covariance, σ is the standard deviation, n is the total number of observations, i is the i^{th} observation of ϵ, and $\overline{\epsilon(f_1)}$ and $\overline{\epsilon(f_2)}$ are the sample means of ϵ at frequencies f_1 and f_2, respectively. In our applications, $\bar{\epsilon}$ is equal to zero, indicating that the GMM is unbiased. The relation for $\rho_{\epsilon(f_1),\epsilon(f_2)}$ given in Equation 3-3 is reciprocal; the correlation coefficient between two given frequencies is the same regardless of which frequency is the conditioning frequency.

The total residuals are correlated for a single earthquake, and this effect is removed by separating the residual components. To account for all residual terms, the total correlation is calculated as Equation 3-4:

$$\rho_{total}(f_1, f_2) = \frac{\rho_B(f_1, f_2)\tau(f_1)\tau(f_2) + \rho_{S2S}(f_1, f_2)\phi_{S2S}(f_1)\phi_{S2S}(f_2) + \rho_{WS}(f_1, f_2)\phi_{ss}(f_1)\phi_{ss}(f_2)}{\sigma(f_1)\sigma(f_2)} \quad (3-4)$$

where $\rho_B(f_1, f_2)$ is the correlation of the normalized between-event residuals, $\rho_{S2S}(f_1, f_2)$ is the correlation of the normalized site-to-site residuals, $\rho_{WS}(f_1, f_2)$ is the correlation of the normalized single-station within-event residuals, and σ is the total standard deviation. Confidence bounds on ρ are based on a variance stabilizing transformation of of ρ, given in Equation 3-5 (Kutner et al., 2004). The variance z is given by Equation 3-6, assuming that n is large enough so that z has an approximately normal distribution. The convergence of z to a normal distribution is very rapid as n increases (Bradley, 2011).

$$z = tanh^{-1}(\rho) = \frac{1}{2} ln\left(\frac{1+\rho}{1-\rho}\right) \quad (3-5)$$

$$Var(z) = \frac{1}{n-3} \quad (3-6)$$

Using a database of partitioned residuals, the calculation of $\rho_{\epsilon(f_1),\epsilon(f_2)}$ can be repeated for every frequency pair of interest. Figure 3-1 shows a graphical representation of this step at three example frequency pairs. The resulting correlation coefficients for each pair of frequencies can be saved as tables (e.g. Abrahamson et al., 2014; Al Atik, 2011; Akkar et al., 2014; Azarbakht et al., 2014; Jayaram et al., 2011), or can be empirically modeled. For modern GMMs, models of the correlation

of ϵ are commonly created for the acceleration response spectrum (PSA; e.g. Baker and Cornell, 2006; Baker and Bradley, 2017; Baker and Jayaram, 2008; Cimellaro 2013; Goda and Atkinson, 2009; Abrahamson et al., 2014). Recently, Stafford (2017) developed a correlation model for ϵ from FAS. This model, and the development methodology, is summarized and compared with the developed model in the Model Comparison section.

The physical meaning of ρ_ϵ and its relevance for structural response is described in Chapter 4. In summary, the parameter ϵ is an indicator of the peaks and troughs at a given frequency in a spectrum, and ρ_ϵ characterizes the relative width of these extrema. The width of peaks and troughs in ground-motion spectra have relevance in risk because the variability in the dynamic structural response can be under-estimated if the correlation in simulated ground motions is too low.

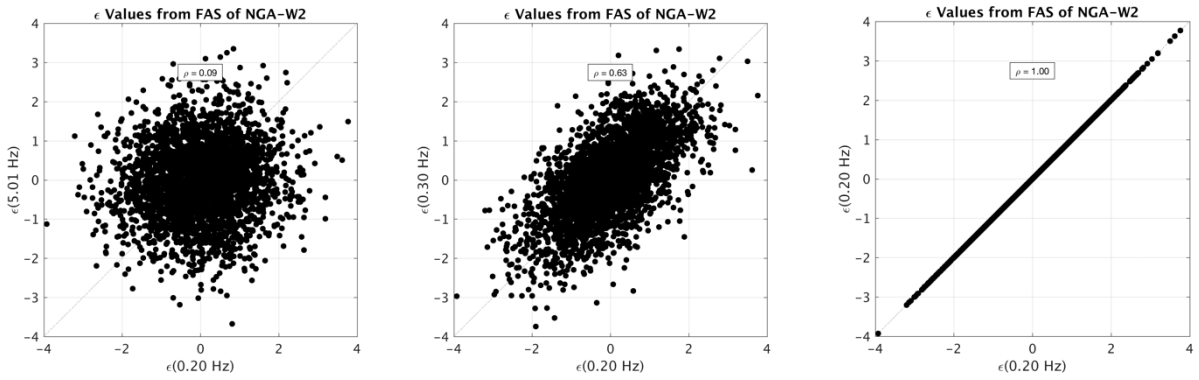

Figure 3-1. ϵ values at pairs of frequencies, exhibiting the correlation dependent on frequency spacing. Left: f_1 = 0.2 Hz and f_2 = 5.0 Hz. Middle: f_1 = 0.2 Hz and f_2 = 0.3 Hz. Right: f_1 = 0.2 Hz and f_2 = 0.2 Hz

EAS Ground Motion Intensity Measure

The EAS is defined in Goulet et al., (2018) and is calculated for an orthogonal pair of FAS using Equation 3-7:

$$EAS(f) = \sqrt{\frac{1}{2}[FAS_{HC1}(f)^2 + FAS_{HC2}(f)^2]} \qquad (3-7)$$

where FAS_{HC1} and FAS_{HC1} are the FAS of the two orthogonal horizontal components of a three component time series, and f is the frequency in Hz. The EAS is independent of the orientation of the instrument, and in this way, is compatible with the input required to use random vibration theory to compute the orientation-independent PSA from the FAS (Goulet et al., 2015). The EAS is smoothed using the $\log_{10}$-scale Konno and Ohmachi (1998) smoothing window, which has weights and window parameter values described in Kottke et al., (2018). The smoothing of the EAS has a direct impact on ρ_ϵ. By using the smoothed EAS, consistency is maintained with the PEER database and with other PEER projects, including the NGA-East empirical FAS models (Goulet et al., 2018) and the EAS model described in Chapter 2. The EAS are processed by PEER following the procedure of Kishida et al., (2016).

The correlation model developed here is based on the residuals and variance for the GMM described in Chapter 2, therefore, the correlation model is for the inter-frequency correlation of epsilon for the smoothed EAS ($\rho_{\epsilon,EAS}$). For notational brevity, the EAS subscript is dropped hereafter and is implied unless noted otherwise. Similarly, if not stated explicitly, the term 'inter-

frequency' is implied in all uses of the word 'correlation' in this chapter, as this is the only type of correlation evaluated.

On the Selection of Fourier Amplitudes

In seismic hazard and earthquake engineering applications, the pseudo-spectral acceleration of a 5% damped single degree of freedom oscillator (also referred to as an acceleration response spectrum, or PSA) is a commonly used IM. PSA is useful for many applications; however, it has drawbacks. The FAS is a more direct representation of the frequency content of the ground motions than PSA and is better understood by seismologists. This leads to several advantages, both in the empirical modeling and in forward application.

Chapter 2 illustrates that oscillators with different natural frequencies are controlled by different frequency ranges of the ground motion. At relatively higher oscillator frequencies, where there is little energy left to resonate the oscillator, the PSA ordinates are dominated by a wide frequency band of the ground motion that ultimately equals the integration over the entire spectrum of the input ground motion (Bora at al., 2016). The short-period PSA is then controlled by the dominant period of the input ground motion, rather than the natural period of the oscillator. Therefore, as recognized by Carlton and Abrahamson (2014), at periods smaller than the peak period (T_p), the ϵ_{PSA} values will be more correlated with the ϵ_{PSA} values of T_p than for other periods with similar spacing. This effect can be observed as the reversal and increase in the Baker and Jayaram (2008) PSA correlation coefficients at short periods, which is discussed further in the section titled Model Comparison.

In summary, PSA provides the spectrum of peak response from a SDOF system, which is influenced by a range of frequencies, and the breadth of that range is dependent on the oscillator period. The FAS provides a more direct representation of the frequency content of the ground motions, and because the Fourier transform is a linear operation, the FAS is a more straightforward representation of the ground motion. Additionally, using FAS more easily facilitates future calibration of the inter-frequency correlation of ground-motion simulation methods (e.g. Chapters 3 and 4) because there is not a reversal of the correlation coefficients at high frequencies.

Inter-Frequency Correlation Model

The subset of the NGA-West2 ground-motion database used to develop the model is described in Chapter 2; the data used is dominated by California earthquakes, but takes advantage of crustal earthquake data worldwide to constrain the magnitude scaling and geometric spreading. Additionally, a broader subset of data is used for testing regional variations of the correlation, as described further in the section titled Dependence of the Correlation on Data Subsets. The partitioned EAS residuals are used over the empirical frequency range of the EAS model; 0.1-24 Hz. The database accounts for the usable frequency range limitations of each record, and for each frequency pair, the records are only utilized in the correlation calculation if both frequencies fall within the usable range. The contour plot shown in Figure 3-2 displays the amount of records (i.e. ϵ's) used at each pair of regression frequencies.

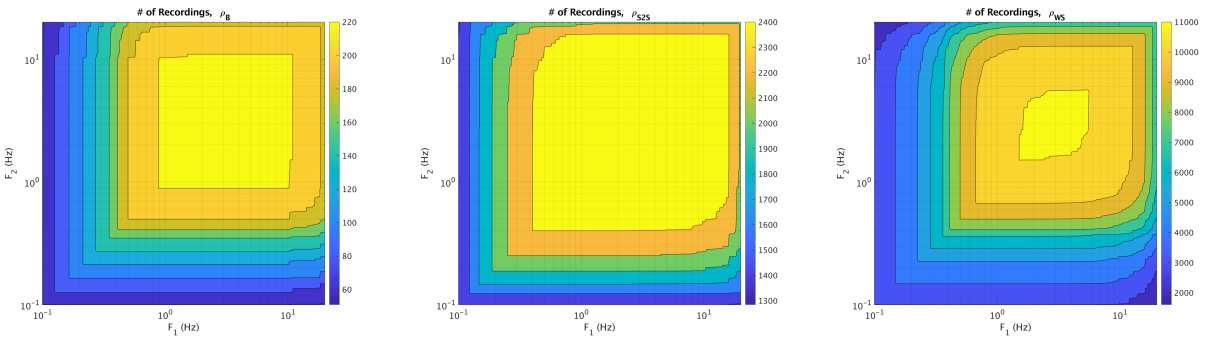

Figure 3-2. Number of recordings (ϵ) used at each pair of frequencies for the correlation calculations, (left) the between-event component, (middle) the between-site component, (right) the within-site component.

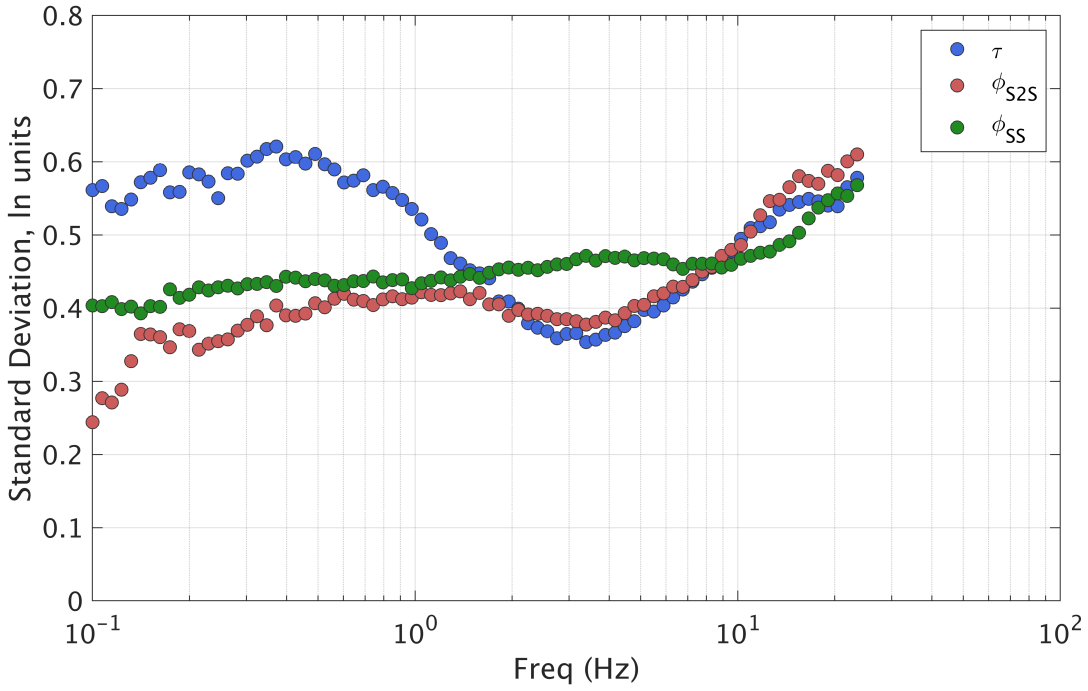

Figure 3-3. Standard deviation components of the Bayless and Abrahamson (2018a) EAS GMM.

To begin, the correlation coefficient, ρ_ϵ, is calculated for each of the normalized residual components ($\epsilon_B, \epsilon_{S2S}$ and ϵ_{WS}) at each pair of modeled frequencies. The total correlation (Equation

3-4) is calculated using ρ_ϵ of each residual component and with the component standard deviations shown in Figure 3-3. Figure 3-3 shows that the between-event residual standard deviation (τ) is larger than the other to standard deviation components at frequencies below 1 Hz, and above 1 Hz, the values of all three components are comparable. As a result, the between-event correlation contributes significantly to the total correlation (Equation 3-4). This is different from response spectra, where the within-event standard deviation is often significantly larger than the between-event standard deviation, so the total correlations mostly reflect the within-event correlations (Stafford, 2017). The resulting correlations are presented as contours in Figure 3-4. These figures are symmetric about the 1:1 line because correlation coefficient between two frequencies is the same regardless of which frequency is the conditioning frequency. The four correlation coefficient matrices shown in Figure 3-4 are provided in the electronic supplement to this article.

To help visualize these results, Figure 3-5 deconstructs the ρ_ϵ contours from Figure 3-4 into five cross-sections at conditioning frequencies: 0.2, 0.5, 2, 5, and 15 Hz. In this figure, the solid lines are the ρ_ϵ cross-sections and the dashed lines represent the 95% confidence interval of ρ_ϵ (Kutner et al., 2004).

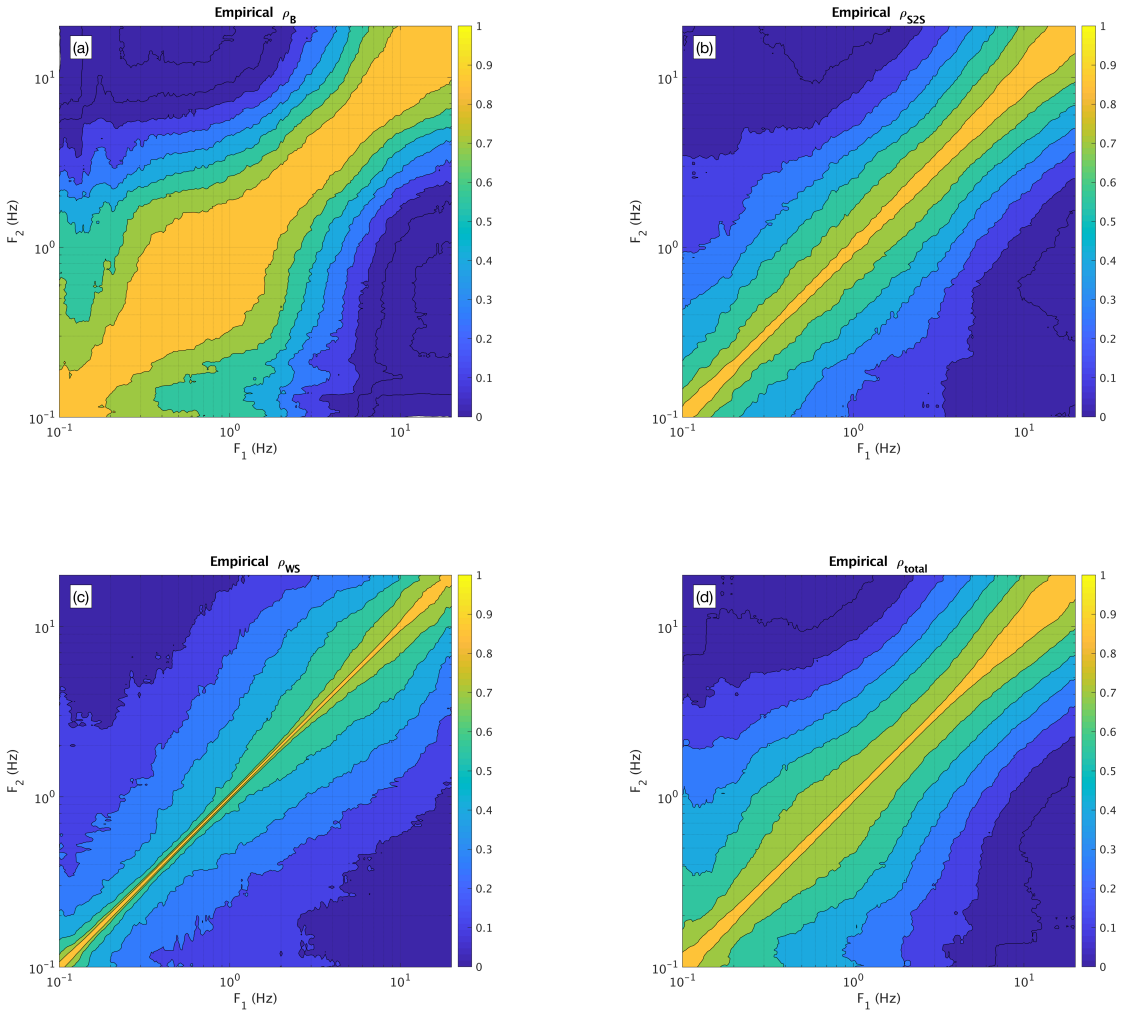

Figure 3-4. Empirical ρ_ϵ contours, showing (a) the between-event component, (b) the between-site component, (c) the within-site component, and (d) the total.

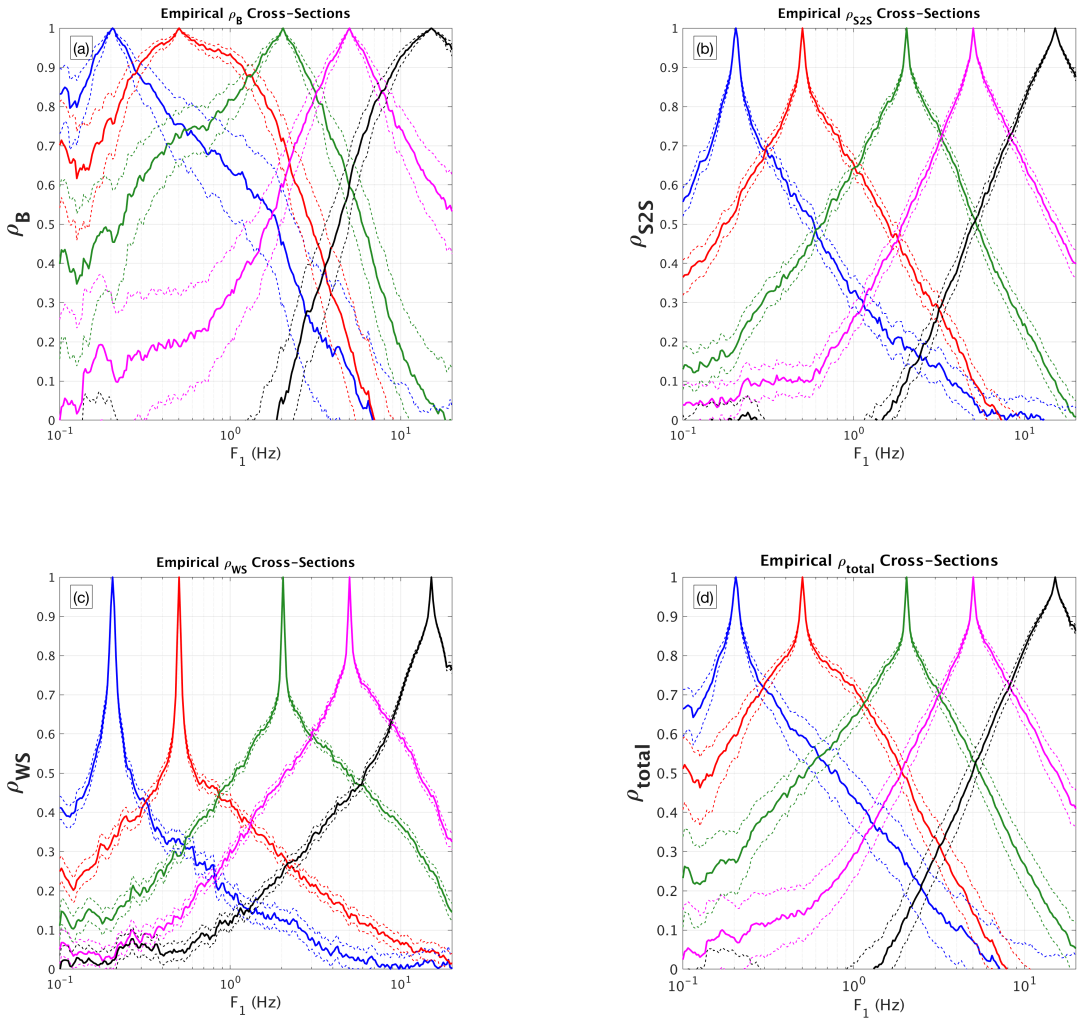

Figure 3-5. Empirical ρ_ϵ cross-sections versus frequency at conditioning frequencies 0.2, 0.5, 2, 5, and 15 Hz (solid lines), with 95% confidence bounds on ρ (dashed lines), for (a) the between-event component, (b) the between-site component, (c) the within-site component, and (d) the total correlation.

Between-event empirical correlation

The between-event empirical ρ_ϵ cross-sections are displayed in Figure 3-5a. Of the residual components, the confidence intervals on these correlation coefficients are the widest because there are the fewest samples of the between-event terms (earthquakes) for calculating ρ_ϵ. Figure 3-5a shows that the between-event ρ_ϵ contributes significantly to the $\rho_{\epsilon,total}$ and that some frequency dependence exists. The between-event ρ_ϵ physically relates to source effects (e.g. stress drop) which drive ground motions over a broad frequency range and thus lead to relatively broad inter-frequency ρ_ϵ.

Stafford (2017) observed minor magnitude dependence of the between-event empirical ρ_ϵ, and attributed these to the variations in the source corner frequency for events of the same magnitude, concluding that larger magnitude events should exhibit stronger inter-frequency correlations over a broader range of frequencies than smaller magnitude events. The ρ_ϵ model developed here does not depend on magnitude; the reasoning behind this decision is described in the section titled Dependence of the Correlation on Data Subsets.

Between-site empirical correlation

The between-site residual represents the systematic deviation of the observed amplification at a site from the median amplification predicted by the model using a V_{s30}-based site classification (Al Atik et al., 2010). Therefore, the between-site ρ_ϵ represents the inter-frequency correlation of the systematic site amplification deviations. The between-site empirical ρ_ϵ cross-sections are displayed in Figure 3-5b. These correlations are generally not as strong as the between-event

empirical ρ_ϵ, but still contribute significantly to the total correlation. The shape of the ρ_ϵ cross-sections does not vary strongly with conditioning frequency, especially below 5 Hz. At frequencies above 5 Hz, the ρ_ϵ cross-sections broaden mildly.

Within-site empirical correlation

The within-site residual component represents the remaining residual after partitioning the random effects for the event and the site. The within-site empirical ρ_ϵ cross-sections are shown in Figure 3-5c. The confidence intervals on these correlation coefficients are close-fitting because there are many samples of the within-site residuals for calculating ρ_ϵ. The within-site ρ_ϵ cross-sections are characterized by a steep decay at frequencies very close to the conditioning frequency, followed by a relatively flat slope at frequencies farther away from the conditioning frequency. In general, the strength of the within-site component inter-frequency correlations are substantially lower than the other residual components.

Total correlation model

The total inter-frequency ρ_ϵ cross-sections, calculated using Equation 3-4, are shown in Figure 3-5d. Some frequency dependence is observed; if the correlation were independent of the conditioning frequency, all the contour lines on Figure 3-4d would be parallel. The contours are not parallel, indicating a minor frequency dependence of the inter-period correlations. For example, the 0.2 Hz correlation cross-section in Figure 3-5d drops off more rapidly moving away from the conditioning frequency and has a different overall shape than the cross-section conditioned at 15 Hz. The broader correlations at high frequencies are the result of the log-scale

smoothing window used on the EAS. Initially, the correlations were modeled independently of the conditioning frequency with an exponential drop off in log-frequency space. The simplicity of this approach had a few advantages. First, it guarantees to produce a positive definite covariance matrix, which is a favorable feature for simulating realizations of ground motions. Second, a simple model was a good starting point for evaluating the correlation in ground-motion simulations. The frequency-independent model was a good fit to the empirical correlations on average, but was generally too broad at low frequencies, and too narrow at high frequencies; therefore, the total inter-frequency ρ_ϵ are fit with a slightly more complex, frequency-dependent model. The frequency-dependent model allows for more robust evaluations of the simulations, and for future applications of the model to incorporate correlations as similar to the data as possible.

Figure 3-6 shows the total ρ_ϵ contours (Figure 3-4d) in yet another manner; only the upper triangular part of the symmetric correlation matrix is plotted. Each line in the top panel is the empirical total correlation coefficients for one of 239 conditioning frequencies, indicated by the frequency with correlation value 1. Each of these correlation contours are fit independently to develop the correlation model. The bottom panel of Figure 3-6 show a subset of the total empirical correlation coefficients, along with the empirical model. The model contours in the bottom panel of Figure 3-6 are assigned different line weights subjectively to identify frequency ranges with significantly different shapes.

The total ρ_ϵ empirical model takes the form given in Equations 3-8 through 3-11,

$$\rho_{\epsilon,total,Model}(f_1, f_2) = tanh\,[\mathrm{A}(f_m)e^{B(f_m)*f_r} + \mathrm{C}(f_m)e^{D(f_m)*f_r}] \quad (3-8)$$

$$f_r = \left|ln\left(\frac{f_1}{f_2}\right)\right| \quad (3-9)$$

$$f_m = min(f_1, f_2) \quad (3-10)$$

$$if\ f_1 = f_2,\ \ \rho_{\epsilon,total,Model}(f_1, f_2) = 1 \quad (3-11)$$

where f_1 and f_1 are the two frequencies considered, $tanh$ is the hyperbolic tangent, A, B, C, and D are frequency-dependent constants, f_r is the absolute value of the natural log-ratio of the two frequencies, and f_m is the minimum of the two frequencies. The model in Equation 3-8 is a two-term exponential decay with the natural logarithm of frequency. Two exponential terms are required to model the shape of the correlation cross-sections (e.g. Figure 3-5d) which starts off with a steep decay at frequencies very close to the conditioning frequency, and then flattens as the log ratio of frequencies increases. Equation 3-8 includes the hyperbolic tangent operator because the regression is performed on Fisher-transformed values of the correlation (Equation 3-5), which results in approximately normally distributed variables, z. This transformation emphasizes the fit to the higher correlation values, which are the priority for model accuracy. The Fisher transformation is undefined for $\rho_\epsilon = 1$, so the correlation model is set to be unity when $f_1 = f_2$ (Equation 3-11). The frequency dependence of coefficients A, B, C, and D is shown in Figure 3-7 and values are given in the electronic supplement to this dissertation.

The total ρ_ϵ empirical model contours and cross-sections are shown in Figure 3-8. The empirical model compares favorably with the empirical correlations, especially at high correlation values which are emphasized in the regression using the Fisher-transformation (Equation 3-5).

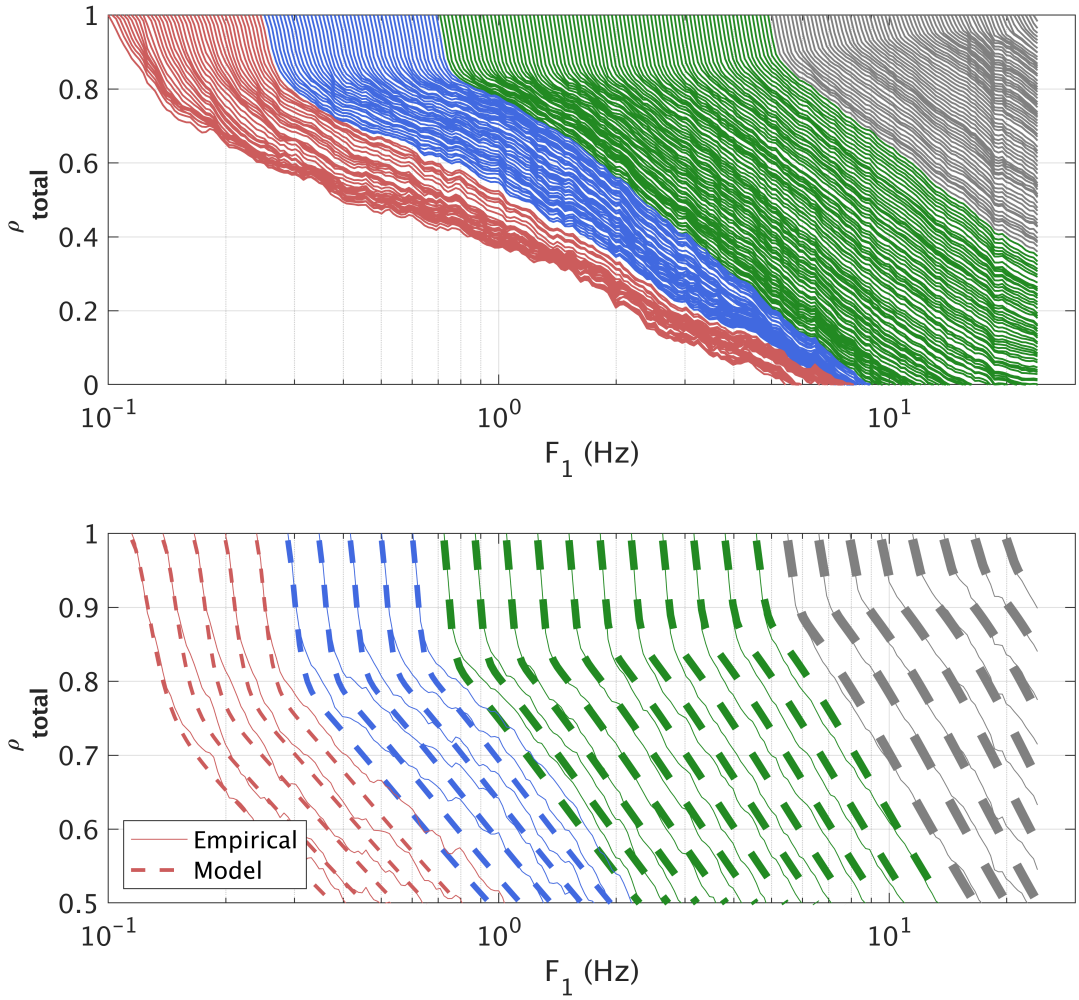

Figure 3-6. Top: Empirical total correlation coefficients for 239 conditioning frequencies. Bottom: A subset of the total empirical correlation coefficients (solid lines), along with the model (dashed lines).

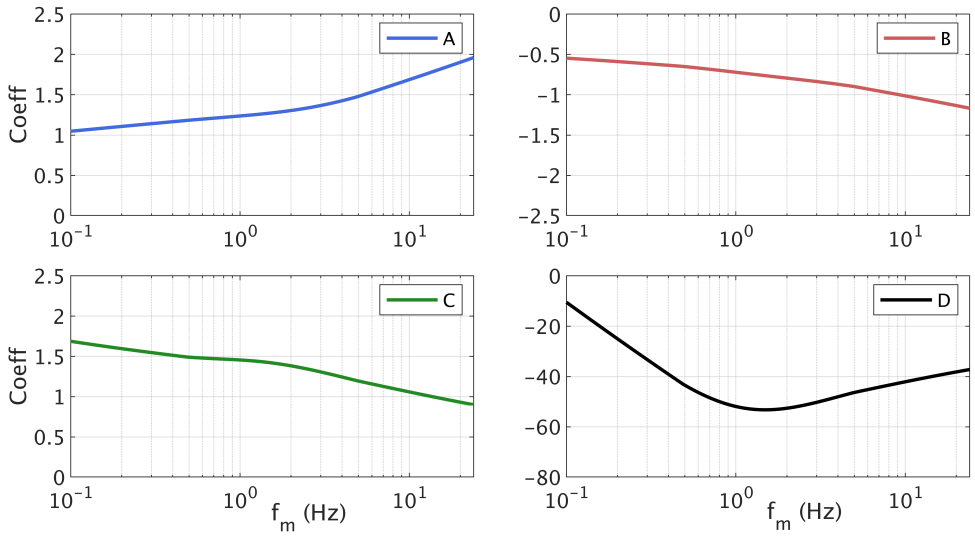

Figure 3-7. Frequency dependence of the $\rho_{\epsilon,total}$ empirical model coefficients.

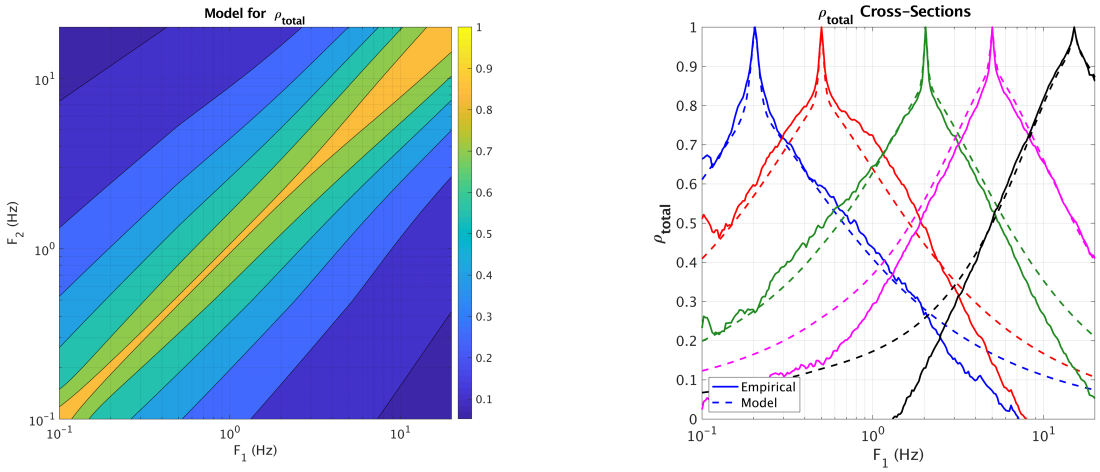

Figure 3-8. Left: Empirical model $\rho_{\epsilon,total}$ contours. Right: Empirical model $\rho_{\epsilon,total}$ cross-sections (dashed lines), compared with empirical cross-sections (solid lines).

Model Application

The total ρ_ϵ empirical model is developed using the PEER NGA-West2 EAS database (Ancheta et al., 2014), and is not found to have strong magnitude, distance, site parameter, or regional dependence (discussed further below). Therefore, the model is applicable for crustal earthquakes in active tectonic regions worldwide. The model is applicable for rupture distances of 0 – 300 km, $\boldsymbol{M}$ 3.0 – 8.0, and over the frequency range 0.1 – 24 Hz. At frequencies outside this range, the model has not been tested. If extrapolation is required, using the values for coefficients A, B, C, and D at either $f = 0.1$ or $f = 24$ Hz is recommended, for extrapolating to lower and higher frequencies, respectively. Tables for the total ρ_ϵ model coefficients and covariance matrices are provided in the electronic supplement to this dissertation.

Model Comparison

In this section, the model is compared with two other empirical models for ρ_ϵ.

Comparison with Baker and Jayaram (2008)

Baker and Jayaram (2008) developed an inter-period correlation model for within-event ϵ based on PSA. Using an updated database, Baker and Bradley (2017) confirmed that the updated correlations were largely consistent with the Baker and Jayaram (2008) model. In PSA GMMs, the within-site and between-site residuals are usually combined when within-event correlations are computed, and the within-event standard deviation is often significantly larger than the between-event standard deviation, so the total correlations mostly reflect the within-event correlations (Stafford, 2017). The Baker and Jayaram (2008) contours derived from within-event ϵ for PSA are

shown in Figure 3-9. An important difference between the contours derived from EAS (Figure 3-4) and those from PSA is the behavior at high frequencies. The PSA contours in Figure 3-9 broaden substantially at high frequencies (short periods); this is because of the wide frequency range that influences the short-period PSA, as discussed previously. The EAS contours do not behave this way because the Fourier transform operation at each frequency bin is independent of neighboring bins. For frequencies below about 10 Hz, the Baker and Jayaram (2008) model is independent of the conditioning frequency.

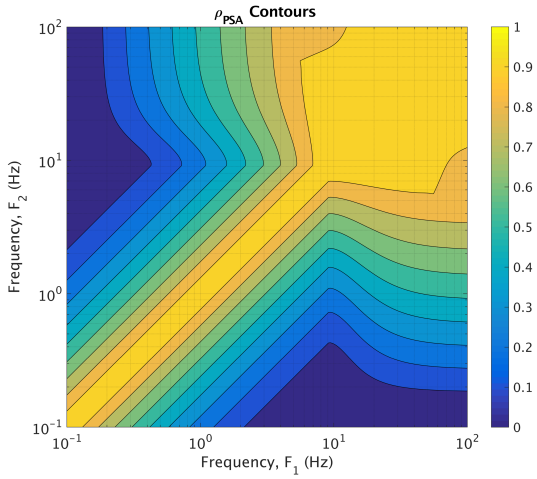

Figure 3-9. Baker and Jayaram (2008) PSA correlation model contours, developed from the within-event residuals of NGA-West GMMs.

Comparison with Stafford (2017)

Stafford (2017; S17 hereafter) used a subset of the NGA-West1 database to develop models for the inter-frequency ρ_ϵ and variance of FAS. S17 modeled the FAS using two approaches: first by adapting the Yenier and Atkinson (2015) FAS model to the data, and second, by performing a regression to the data with a simple GMM at each frequency independently. Like this study, S17

partitioned the residuals into between-event, between-site and within-site components. S17 used unsmoothed FAS ordinates in the model development, which is an important distinction from the approach presented here and has an effect on the resulting models, as shown below. Additionally, the S17 model used both as-recorded horizontal components of the ground-motions, as opposed to an orientation-independent horizontal component, such as the EAS used here.

Figure 3-10 summarizes the S17 model for the total ρ_ϵ of the unsmoothed FAS over the frequency range 0.1 – 24 Hz, assuming a source corner frequency of 0.08 Hz. In panel (b), the S17 total ρ_ϵ model cross-sections are compared with the total ρ_ϵ model developed here. The S17 total ρ_ϵ model features more frequency dependence and at high frequencies, has a much stronger decay of the correlations in the vicinity of the conditioning frequency than the model developed here. The large differences in high frequency ρ_ϵ models are likely the result of the different smoothing techniques employed. The smoothing averages the EAS in log-spaced frequency bands, which increases the correlation between frequencies. As mentioned previously, the smoothing is done to maintain consistency with the PEER database and with models developed in other studies using the PEER database. At frequencies below 0.2 Hz, the S17 exponential decay near the conditioning frequency is slightly weaker than the model developed here, but the differences are smaller. These differences can be attributed to the combination of differences described above: ground-motion component, database, smoothing technique, and ground-motion model used for computing the residuals.

S17 observed minor magnitude dependence of the between-event ρ_ϵ, and attributed these to the variations in the source corner frequency for events of the same magnitude, concluding that larger magnitude events should exhibit stronger inter-frequency correlations over a broader range of

frequencies than smaller magnitude events. Magnitude dependence is not incorporated into the total correlation model developed here; the reasoning behind this is described in the following section.

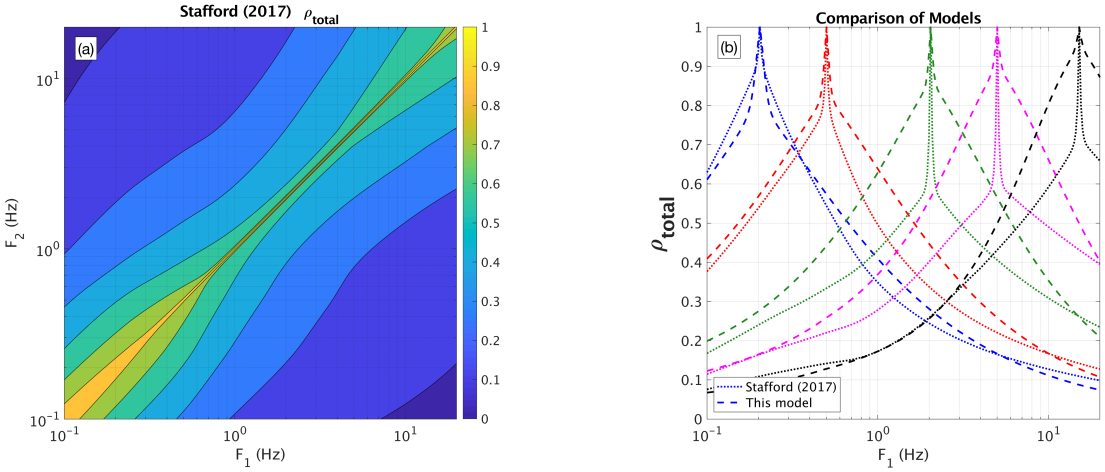

Figure 3-10. Left: Stafford (2017) $\rho_{\epsilon,total}$ contours using $f_c = 0.08$ Hz. Right: Comparison of the two $\rho_{\epsilon,total}$ model cross-sections at five conditioning frequencies.

Dependence of the Correlation on Data Subsets

There have been conflicting conclusions published about the sensitivity of response spectra correlation coefficients to the ground-motion database subsets. Azarbakht et al. (2014), using PSA and the NGA-W1 database, concluded that the within-event correlation coefficients had meaningful dependencies on the causal magnitudes and distances of the recordings. This conclusion differs from those made by several other published studies, including Baker and Cornell (2005), Baker and Jayaram (2008), Baker and Bradley (2017), and Carlton and Abrahamson (2014). Baker and Bradley (2017) investigated the dependence of PSA inter-period correlations on binned data subsets of the PEER NGA-West2 database. They concluded that the

correlations show no systematic trends with causal magnitude, distance, or V_{s30}. This was the same conclusion made by Baker and Jayaram (2008), which was developed using the NGA-West1 database. Carlton and Abrahamson (2014) concluded that the robustness of generic correlation models for PSA is a result of their dependence on spectral shape rather than tectonic region. Stafford (2017), working with unsmoothed FAS, found weak magnitude dependence on the between-event inter-period correlations, attributing these to the variations in the source corner frequency for events with the same magnitude. Stafford (2017) did not observe systematic dependence of the between-site or within-site residual correlations on causal magnitude or distance.

To investigate the dependence of the correlations on different seismological parameters, the total ρ_ϵ of the EAS is recalculated for subsets of the data. The subsets are created by binning residuals based on magnitude, distance, V_{s30}, and earthquake region. The complete list of residual subsets analyzed is given in Table 3-1. For each data subset listed in Table 3-1, ρ_ϵ for each component of the residuals is calculated and the ρ_ϵ contours and cross-sections are reviewed. As expected, deviations from the full database ρ_ϵ occur, but no systematic differences are found based on this qualitative assessment.

Table 3-1. Data subsets analyzed to investigate ρ_ϵ dependence on seismological parameters.

Parameter	Bins
M	< 4.0, 4.0-5.0, 5.0-6.0, 6.0-7.0, > 7.0
R_{rup} (km)	0-15, 15-30, 30-50, 50-75, 75-100
V_{s30} (m/s)	< 300, 300-500, 500-700, > 700
Region	Western North America (WNA; primarily California), All non-WNA, Japan, Taiwan, China, Mediterranean

The dependence is also investigated more methodically by following the procedure taken by Baker and Bradley (2017). With this routine, the total ρ_ϵ from each data subset is calculated using the GMM residuals from that subset. The total ρ_ϵ for the subset is then compared with the ρ_ϵ from the full database. The results of this procedure are summarized in Figure 3-11, where the total empirical ρ_ϵ for four frequency pairs are shown for the 20 subsets from Table 3-1. In Figure 3-11, the full database total ρ_ϵ for each frequency pair is shown with the solid, horizontal line, with dashed lines representing the lower and upper bounds for 95% confidence intervals of these coefficients (Kutner et al., 2004). The solid circles are the total ρ_ϵ calculated for each indicated data subset, and the triangles indicate 95% confidence intervals of those coefficients. The 95% confidence intervals represent the statistical uncertainty in the correlation coefficients due to the finite number of samples, and the standard deviation of the samples. If the confidence intervals of two groups do not overlap, then the differences in the correlation coefficients of the two groups are statistically significant at the 95% confidence level.

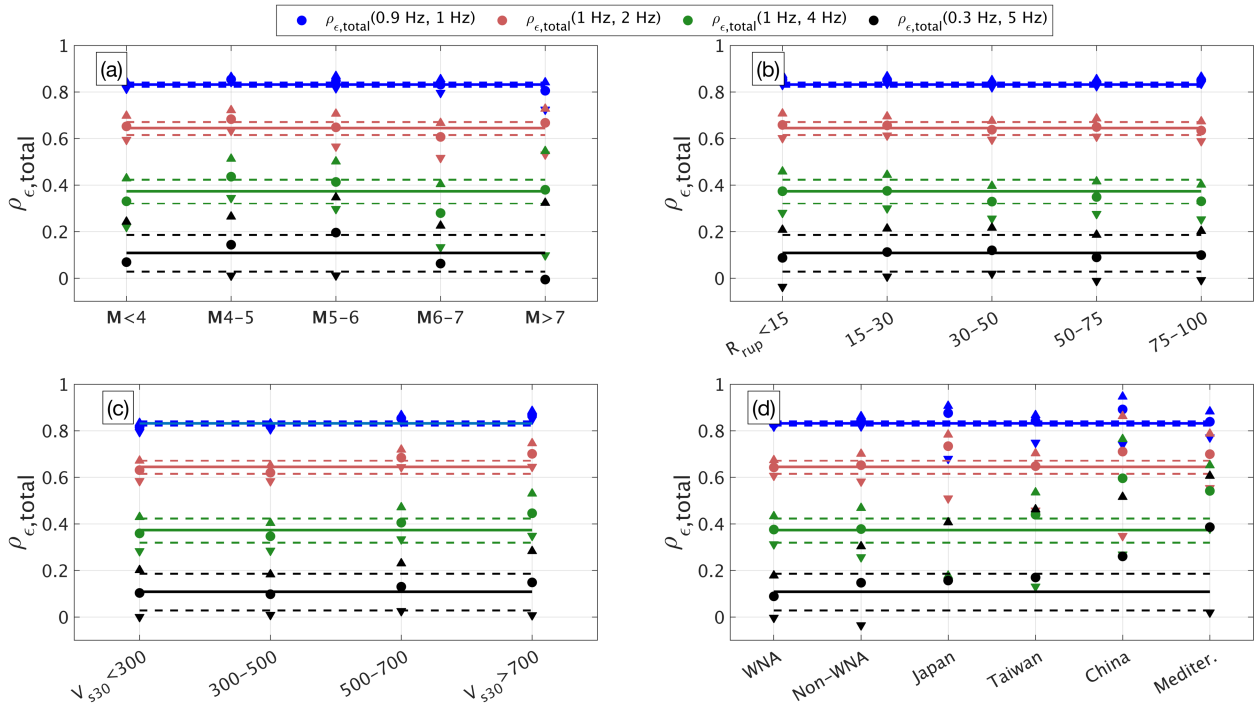

Figure 3-11. Total ρ_ϵ for four frequency pairs (identified in the legend) for the 20 data subsets from Table 1. The full database total ρ_ϵ for each frequency pair is shown with the solid, horizontal line, and dashed lines represent the lower and upper bounds for 95% confidence intervals of these coefficients (Kutner et al., 2004). The solid circles are the total ρ_ϵ calculated for each indicated data subset, and the triangles indicate 95% confidence intervals of those coefficients.

Figure 3-11 panel (a) shows the magnitude binned results, which reveal no systematic trends. The largest magnitude bin suffers from the smallest sample size, especially for the between-event terms, and has the largest variations from the full database ρ_ϵ. But at each frequency pair the 95% confidence intervals for the binned data overlap with those for the full database, indicating that the two are not statistically significantly different for this bin. Panel (b) shows the distance binned results, which also have overlapping confidence intervals for each frequency pair and bin, revealing no apparent dependence of ρ_ϵ on distance. Panel (c) shows the V_{s30} binned results. The $V_{s30} > 700$ m/s bin has the largest deviations from the full database, but no systematic, statistically

significant dependencies are observed. Panel (d) shows the results for the regional data subsets, where deviations from the full database are stronger than any of the other data subsets examined. Panels a, b, and c from Figure 3-11 are from the CA model residuals, but correlations in panel d are from residuals for a larger subset of the full NGA-West2 database. The regional subsets have overlapping confidence intervals with the full database for each frequency pair except for the Japan subset coefficient at 1 and 4 Hz. The WNA, all non-WNA, Japan, and Taiwan regions contain a substantial number of events and recordings in this analysis. The China and Mediterranean regions have the smallest sample sizes, as indicated by the wide confidence intervals, such that their deviations from the full database correlation coefficients are likely not significant, but this should be investigated in the future using more data for each region.

Based on this analysis of the data subsets, no conclusive, systematic relationships are detected between ρ_ϵ and the seismological parameters reviewed. The largest differences in correlation coefficients occur at widely spaced frequencies, when ρ_ϵ themselves are low. This is an expected feature, because of the heteroskedastic (non-constant standard deviation) nature of the correlation coefficients. Correlation coefficients with values close to zero have a larger standard deviation than coefficients with values close to one, meaning that the confidence intervals for low correlation coefficients are wider. This effect can be observed in Figure 3-11 panel (a), where the 95% confidence intervals are tight for the 0.9 and 1 Hz pair coefficient, and wide for the 0.3 and 5 Hz pair coefficient. As a result, differences between ρ_ϵ at low values are not usually significant. Additionally, in practice, the frequency ranges with high correlations are the most important, since these are related to the width of peaks and troughs in the spectra, and the wider frequency pairs with low correlations are not as impactful. Therefore, it is neither practical nor necessary to include

dependencies on the reviewed seismological parameters in the inter-frequency EAS correlation model developed here. This conclusion agrees with the Baker series of conclusions for PSA (Baker and Cornell, 2005; Baker and Jayaram, 2008; Baker and Bradley, 2017) and with Carlton and Abrahamson (2014).

Correlation of select well-recorded events

Since no systematic relationships between ρ_ϵ and magnitude, distance, or site parameter are observed, the inter-frequency correlation should approximately agree with the empirical model for a given event or set of events. To test this, the residuals from nine events identified by the SCEC BBP validation project (Dreger et al., 2015) are used to calculate the inter-frequency ρ_ϵ and compare with the empirical model. The SCEC BBP is a collaborative software development project, with the objective to integrate complex scientific codes for generating broadband ground-motion simulations for earthquakes. A key part of the SCEC process is to validate the simulations against data from well-recorded earthquakes, as described in the Dreger et al. (2015) validation exercise. The nine events from active crustal regions for validating the simulations against data are: 2008 Chino Hills, 2007 Alum Rock, 1987 Whittier Narrows, 1986 North Palm Springs, 1994 Northridge, 1989 Loma Prieta, 1992 Landers, 2000 Tottori, and 2004 Niigata (Goulet et al., 2015).

Figure 3-12a shows the $\rho_{\epsilon,total}$ contours derived from residuals for these nine events, and Figure 3-12b compares the $\rho_{\epsilon,total}$ cross-sections with the empirical model. Figure 3-12 supports the hypothesis that $\rho_{\epsilon,total}$ should approximately agree with the empirical model for a given event or set of events. In this case, departures from the model are observed, especially for the cross-section

conditioned at 0.2 Hz, but the 95% confidence bounds on $\rho_{\epsilon,total}$ indicate that differences are not statistically significant because these enclose the model over most frequencies.

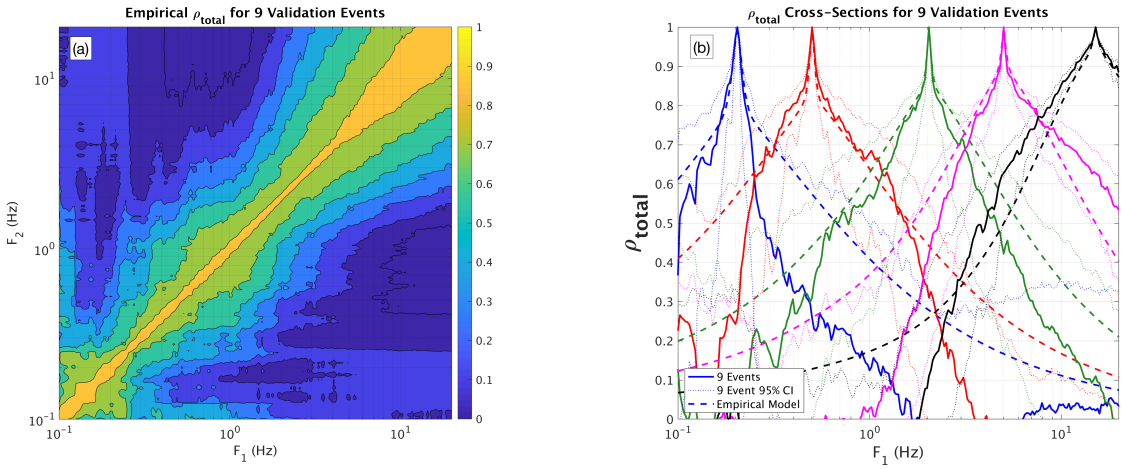

Figure 3-12. Left: Empirical $\rho_{\epsilon,total}$ contours derived from the nine SCEC validation events (Goulet et al., 2015). Right: $\rho_{\epsilon,total}$ cross-sections from the SCEC events (solid lines), with 95% confidence intervals for $\rho_{\epsilon,total}$ (dotted lines) compared with empirical model for $\rho_{\epsilon,total}$ (dashed lines).

Conclusions

The empirical model for the inter-frequency correlation of the *EAS* developed in this study is applicable to shallow crustal earthquakes in active tectonic regions worldwide, for rupture distances of 0 – 300 km, magnitude of 3.0 – 8.0, and frequency of 0.1 – 24 Hz. This correlation model can be used to define the inter-frequency correlation in stochastic ground-motion simulation methods. It is also appropriate for use in evaluation and validation studies of the inter-frequency correlations from numerical simulations for ground motions that also use the standard *EAS* approach for smoothing the *FAS*. These are the topics of Chapters 4 and 5 of this dissertation.

Chapter 4:

Evaluation of the inter-frequency correlation of ground motion simulations

Abstract

It is shown that the inter-frequency correlation of epsilon (ρ_ϵ) is an essential component of ground motions for capturing the variability of structural response that is needed in seismic fragility and seismic risk studies. To perform this demonstration, large suites of scenario ground motion simulations are generated using the point source stochastic method. Two compatible suites of simulations are developed; one suite without any imposed inter-frequency correlation, and one with Fourier amplitude ϵ sampled from a multivariate normal distribution with covariance specified by the empirical model developed in Chapter 3. It is illustrated how the effect of ρ_ϵ propagates through the structural response and into to seismic risk calculations. Without the adequate inter-frequency correlation of ground motions, variability in the structural response may be under-estimated. This leads to structural fragilities which are too steep (under-estimated dispersion parameter β) and propagates through to non-conservative estimates of seismic risk.

To assess the current state of multiple existing ground motion simulation methods, their inter-frequency correlations are compared with empirical models. None of the six finite-fault simulation methods tested adequately capture the inter-period correlations over the entire frequency range evaluated, although several of the methods show promise, especially at low frequencies. Using the correlation of the Fourier spectra provides the developers of the simulation methods better feedback in terms of how they can modify their methods that is not clear when using response spectra comparisons. Based on the relative differences in the correlations of the Song (2016) source method, it appears that changes to the rupture generator may be the most promising approach to modifying the long period inter-period correlations.

Introduction

Ground-motion models (GMMs, also known as ground-motion prediction equations, GMPEs, or attenuation models) are used for estimating the level of ground shaking at a site, including the uncertainty in that level, based on earthquake magnitude, source-to-site distance, local site conditions, and other seismological parameters. Among other applications, GMMs are often used in probabilistic seismic hazard analyses (PSHA), including those performed to develop the U.S. Seismic Design Maps (ASCE, 2016). GMMs can be developed using recorded ground-motions, using numerical earthquake simulations, or a combination of both approaches.

Empirical GMM residuals are the difference, in logarithmic space, between the recorded ground shaking and the median ground shaking predicted by the GMM. These residuals are typically partitioned into between-event residual (δB), and within-event residuals (δW), following the notation of Al Atik et al., (2010). For large numbers of recordings per earthquake, the between-event residual is approximately the average difference in logarithmic-space between the observed Intensity Measure (IM) from a specific earthquake and the IM predicted by the GMM. The within-event residual (δW) is the difference between the IM at a specific site for a given earthquake and the median IM predicted by the GMM plus δB. By accounting for repeatable site effects, δW can further be partitioned into a site-to-site residual ($\delta S2S$) and the single-station within-event residual (δWS) (e.g. Villani and Abrahamson, 2015).

The residual components δB, $\delta S2S$ and δWS are well-represented as zero-mean, independent, normally distributed random variables with standard deviations τ, ϕ_{S2S} and ϕ_{ss}, respectively (Al Atik et al., 2010). These GMM residual components are converted to epsilon (ϵ_B, ϵ_{S2S}, and ϵ_{WS}) by normalizing the residuals by their respective standard deviations. Because of the normalization, the random variables ϵ_B, ϵ_{S2S}, and ϵ_{WS} are represented by standard-normal distributions (mean=0, variance=1). If the total residual is used, then the resulting ϵ_{total} will, in general, not have zero mean due to the uneven sampling of recordings per earthquake in the data set.

For a given recording, the values of ϵ at neighboring periods (T) are correlated. For example, if a ground motion is stronger than average at T=1.0 s, then it is likely to also be stronger than expected at nearby periods, e.g. T=0.8 s or T=1.2 s; however, for a widely-spaced period pair (e.g. T=10.0 s compared with T=1.0 s), the ϵ values will be weakly correlated. The inter-period correlation coefficient, ρ, quantifies the relationship of ϵ values between periods for a given recording.

The correlation coefficient of two random variables is a measure of their linear dependence. In this case, ϵ calculated from a large set of ground motions at different frequencies (f) are random variates. The correlation coefficient between $\epsilon(f_1)$ and $\epsilon(f_2)$ can be estimated using a maximum likelihood estimator, the Pearson-product-moment correlation coefficient, ρ (Fisher, 1958). The correlation coefficient for a sample of ϵ at frequencies f_1 and f_2 is given by Equation 4-1,

$$\rho_{\epsilon(f_1),\epsilon(f_2)} = \frac{cov\big(\epsilon(f_1),\epsilon(f_2)\big)}{\sigma_{\epsilon(f_1)}\sigma_{\epsilon(f_2)}} = \frac{\sum_{i=1}^{n}\big(\epsilon_i(f_1)-\overline{\epsilon(f_1)}\big)\big(\epsilon_i(f_2)-\overline{\epsilon(f_2)}\big)}{\sqrt{\sum_{i=1}^{n}\big(\epsilon_i(f_1)-\overline{\epsilon(f_1)}\big)^2}\sqrt{\sum_{i=1}^{n}\big(\epsilon_i(f_2)-\overline{\epsilon(f_2)}\big)^2}} \quad (4-1)$$

where cov is the covariance, σ is the standard deviation, n is the total number of observations, i is the i^{th} observation of ϵ, and $\overline{\epsilon(f_1)}$ and $\overline{\epsilon(f_2)}$ are the sample means of ϵ at frequencies f_1 and f_2, respectively. $\bar{\epsilon}$ equal to zero indicates that the GMM is unbiased. The relation for $\rho_{\epsilon(f_1),\epsilon(f_2)}$ given in Equation 4-1 is reciprocal; the correlation coefficient between two given frequencies is the same regardless of which frequency is the conditioning frequency. To account for all residual terms, the total correlation is calculated as Equation 4-2,

$$\rho_{\epsilon,total}(f_1,f_2) = \frac{\rho_B(f_1,f_2)\tau(f_1)\tau(f_2) + \rho_{S2S}(f_1,f_2)\phi_{S2S}(f_1)\phi_{S2S}(f_2) + \rho_{WS}(f_1,f_2)\phi_{ss}(f_1)\phi_{ss}(f_2)}{\sigma(f_1)\sigma(f_2)} \quad (4-2)$$

where $\rho_B(f_1,f_2)$ is the correlation of the normalized between-event residuals, $\rho_{S2S}(f_1,f_2)$ is the correlation of the normalized site-to-site residuals, and $\rho_{WS}(f_1,f_2)$ is the correlation of the normalized single-station within-event residuals.

Using a database of residuals, the calculation of $\rho_{\epsilon(f_1),\epsilon(f_2)}$ can be repeated for every frequency pair of interest. Figure 4-1 shows a graphical representation of this step at three example frequency pairs. The resulting correlation coefficients for each pair of frequencies can be saved as tables (e.g. Abrahamson et al., 2013; Al Atik, 2011; Akkar et al., 2014; Azarbakht et al., 2014; Jayaram et al., 2011), or can be empirically modeled. For modern GMMs, models of the correlation of ϵ are commonly created for PSA (e.g. Baker and Cornell, 2006; Baker and Bradley, 2017; Baker and Jayaram, 2008; Cimellaro 2013; Goda and Atkinson, 2009; Abrahamson et al., 2013). Recently, correlation models for ϵ from Fourier amplitude spectra (FAS) have also been developed (e.g. Stafford, 2017; and Chapter 3 of this dissertation).

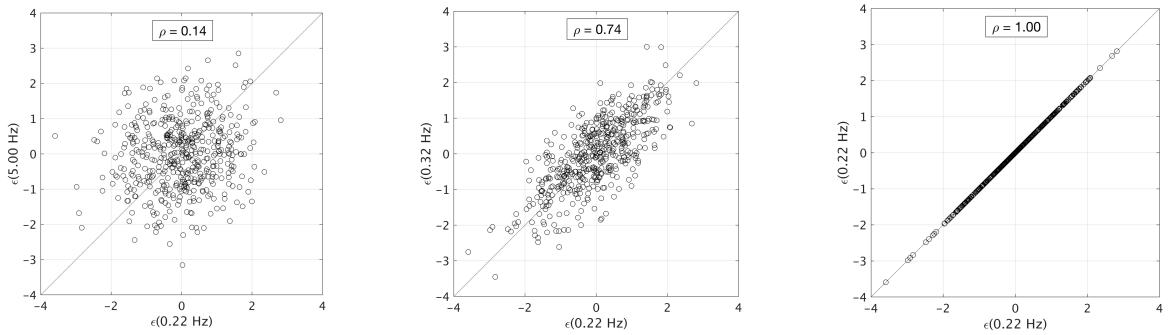

Figure 4-1. ϵ values at pairs of frequencies calculated from a database of ground motions, exhibiting the correlation dependent on frequency spacing. Left: f_1 = 0.2 Hz and f_2 = 5.0 Hz. Middle: f_1 = 0.2 Hz and f_2 = 0.3 Hz. Right: f_1 = 0.2 Hz and f_2 = 0.2 Hz

Physical Meaning and Relevance of ρ_ϵ

Because larger than average ground motions tend to be from local spectral peaks and lower than average ground motions tend to be from local spectral troughs, the parameter ϵ is an indicator of the peaks and troughs at a given frequency in a spectrum. And since ρ_ϵ is a measure of the linear dependence of ϵ between two frequencies, it follows that ρ_ϵ characterizes the relative width of these extrema. For example, very high ρ_ϵ (values close to one) over broad frequency pairs indicate wide peaks and troughs in the spectra; leading to smoother undulating spectra. Conversely, very low ρ_ϵ (values close to zero) between neighboring frequency pairs indicate very narrow peaks and troughs; leading to 'noisy' looking spectra.

The generic term 'spectra' can refer to either PSA or FAS. PSA spectra are the peak response from a single degree of freedom oscillator system. PSA spectra are influenced by a range of frequencies, and the breadth of that range is dependent on the oscillator period (Chapter 2) and on the damping.

The FAS provides a more direct representation of the frequency content of the ground motions, and because the Fourier transform is a linear operation, the FAS is a much more straightforward representation of the ground motion and is better understood by seismologists. This simpler behavior makes the FAS preferable over PSA for incorporating inter-period correlation into numerical methods for ground-motion simulations, and it is the IM adopted in this study.

Since ρ_ϵ is a measure of the width of spectral peaks, it has relevance in dynamic structural response. For linear response, a structure will be sensitive to the frequency content over a range of frequencies about the natural frequency of the structures. For the uncorrelated case, if the ϵ value at the natural frequencies is a high positive value (corresponding to a peak), the values of ϵ at the nearby frequencies will be randomly high or low so the response of the structure will increase a small factor; however, for the correlated case, the values of ϵ at the nearby frequencies will tend to also be positive values so the response of the structure will increase a larger factor relative to the uncorrelated case. During nonlinear seismic response, the effect of the correlation can be even greater than for linear response. For nonlinear response, structures can experience softening characterized by elongation of their natural vibration period (Lin et al., 2008; Bradford 2007). This occurs when damage to the structural elements leads to large strains which reduce the effective stiffness and increases effective damping. As a structure softens, its effective fundamental period increases and the response will depend on if the structure is softening into a peak or a trough in the spectrum. For the correlated case, the chance of softening into a peak or a trough will depend on the breadth of a ground motion spectral peak or trough, thereby affecting the structural response. The aggregate effect is the variability in structural response is higher for ground motions with

realistic ρ_ϵ than for ground motions with unrealistically low ρ_ϵ; this point is demonstrated in the following sections of this chapter.

Chapter Organization

In this chapter, the effect on structural fragilities of ρ_ϵ is demonstrated, and the ρ_ϵ in existing ground-motion simulation methods is evaluated. First, a short summary of the four main components of Pacific Earthquake Engineering Research Center's (PEER) Performance Based Earthquake Engineering (PBEE) framework is presented, and this framework is used to define structural risk in terms of structural fragility and seismic hazard. A method for developing structural fragilities from ground motion simulations is described, and using a generic example, ρ_ϵ is shown to be a critical feature of ground motions that should be considered as a validation parameter for numerical simulations. A method is developed for generating simulated ground motions with appropriate ρ_ϵ. An example of seismic risk for a generic site in southern California using this ground-motion simulation method is presented and compared with results using the same simulation method but without the correlation. For this example, the propagation of ρ_ϵ to the structural response variability and then into seismic risk is illustrated. Finally, the inter-frequency correlations of multiple existing ground-motion simulation methods are evaluated and compared with empirical models for the correlation.

Structural Risk in Performance Based Earthquake Engineering

Following Moehle and Deierlein (2004), PEER's probabilistic framework for PBEE is separated into four main analysis steps: hazard analysis (characterized by a ground motion Intensity

Measure, IM), structural analysis (characterized by an Engineering Demand Parameter, EDP), damage analysis (characterized by Damage Measure, DM), and loss analysis (characterized by a Decision Variable, DV). Using this framework, one can focus solely on the first two analysis steps to estimate the EDP hazard, defined as the mean annual rate of exceeding a given structural response level. The EDP hazard is given by Equation 4-3,

$$\lambda(EDP > z) = \int_x P(EDP > z|IM = x) \left|\frac{d\lambda(IM>x)}{dx}\right| dx \qquad (4-3)$$

where $\lambda(EDP > z)$ is the mean annual rate of exceeding EDP value z. $P(EDP > z|IM = x)$ is the structural fragility, which is the probability of exceeding EDP value of z given IM $= x$. $\lambda(IM > x)$ is the mean annual rate of exceeding IM value x, and $d\lambda$ is the rate of occurrence of IM value x, which is the slope of the IM hazard curve. Therefore, the EDP hazard for exceeding a specified value z is comprised of two quantities: the structural fragility, and the ground motion hazard, integrated over all relevant IM levels, x.

In this chapter, the selected IMs are 5% damped pseudo-spectral acceleration (PSA) and Fourier amplitude spectra (FAS), and the selected EDP is the maximum interstory drift ratio (MIDR), but it is noted that the EDP risk framework (Equation 4-2) is applicable to other appropriate IMs and EDPs. As interstory drift is commonly adopted as the EDP, it is common to refer to the EDP hazard as drift hazard.

Structural Risk using Ground Motion Simulations

Fragilities Developed from Simulations

A fragility function specifies the probability of a structural consequence (EDP) as a function of the ground motion intensity (IM). Fragility functions can be obtained using the Incremental Dynamic Analysis (IDA) procedure as a means of integrating structural simulations and ground motions (Moehle and Deierlein, 2004; Baker, 2013). With this procedure, using a suite of ground motions, structural response calculations are carried out in which the building is subjected to the input ground motions having a specified IM amplitude, and the fraction of the ground motions exceeding the specified EDP are counted. The process is repeated at increasing IM levels to obtain the probability of exceeding the EDP at discrete IM amplitudes. A lognormal cumulative distribution function can be fit to the probabilities, e.g Equation 4-4,

$$P_{fit}(EDP > z|IM = x) = \Phi[\frac{\ln(x) - \ln(\alpha)}{\beta}] \qquad (4-4)$$

where $P_{fit}(EDP > z|IM = x)$ is the fitted fragility function, Φ is the CDF of the standard normal distribution, α is the IM with median fragility, β is the logarithmic standard deviation of the CDF, and α and β are estimated from the IDA results. This method is demonstrated in this chapter. An alternative to IDA is the Multiple Stripe Analysis (MSA) method, where ground motions selected specifically for the IM amplitude are analyzed, instead of scaling one set of ground motions for multiple IM amplitudes (Baker, 2013). MSA uses scenario-specific ground motions for each IM level, but because the hazard at long return periods is usually driven by increasing epsilon, not

magnitude, the IDA approach has merit. The fundamental impact of the correlation can be demonstrated using an IDA, so this is the approach taken in the following example.

Incorporating ρ_ϵ into Ground Motion Simulations

The point source (PS) stochastic method for simulating earthquake ground motions, which is based on the pioneering work of Brune (1970), Hanks and McGuire (1981) and Boore (1983), among others, has been developed and refined over several decades. David Boore formalized the method and extended it to the simulation of acceleration time series (Boore, 1983; Boore, 2003). With the Boore (2003) method (Boore03 hereafter), a simulated time series is produced using a seismological model of the Fourier amplitude spectrum, and assuming the spectrum is distributed with random phase angles over a time duration related to the earthquake magnitude and the distance between the source and site. Boore (2003) gives a comprehensive description of the method; only a brief summary is provided here.

The classic procedure starts by generating normally distributed noise (Figure 4-2a) and applying a time-domain taper with duration consistent with the scenario being considered (Figure 4-2b). The tapered noise is transformed into the frequency domain (Figure 4-2c), and the FAS of the noise is normalized by the square root of the mean power, such that the FAS has mean power of one (Figure 4-2d, showing the natural logarithm of these values). The normalized FAS is then shaped to the PS Fourier amplitude spectrum of the considered scenario (Figure 4-2e), and inverse transformed to the time domain using the phase angles from the tapered time domain noise (Figure 4-2f).

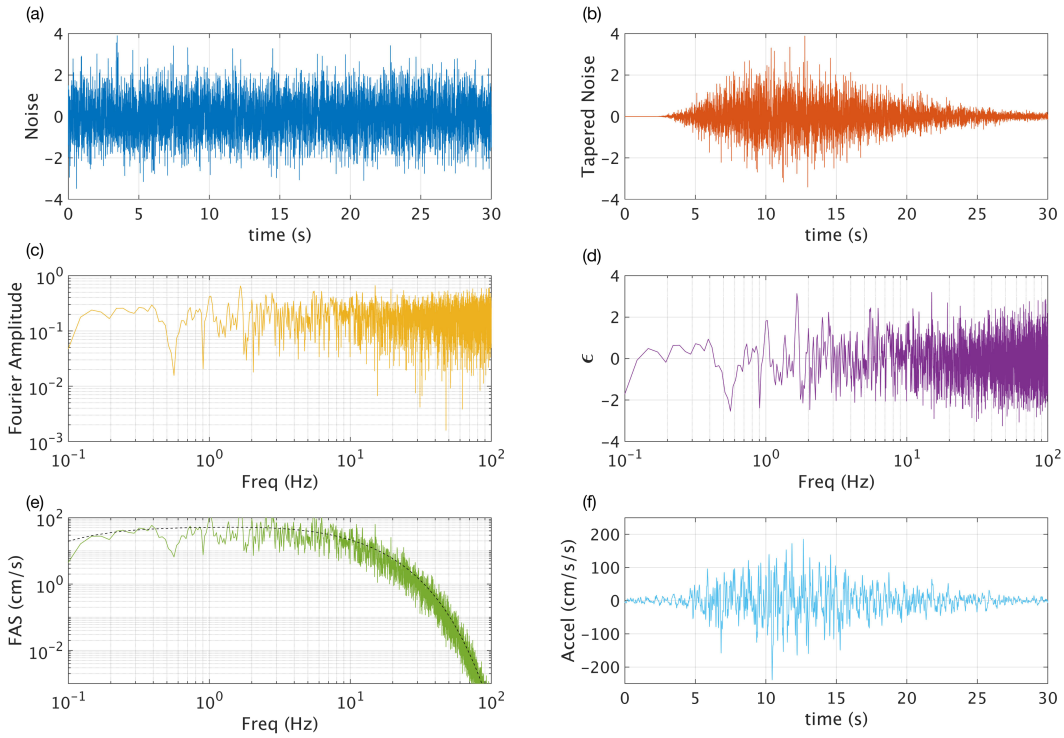

Figure 4-2. Illustration of the Boore (2003) procedure for simulating acceleration time series using the point-source stochastic method. Each sub-panel is described in the text.

The Boore03 procedure filtered white noise in the time-domain, resulting in ϵ with no correlation between frequencies. To generate a simulated time series with realistic inter-period correlation, the Boore03 procedure can be modified as follows. First, a symmetric, positive definite covariance matrix (Σ) for the inter-frequency $\rho_{\epsilon,total}$ of FAS is needed (e.g. the one from Chapter 3). This matrix is factorized using the Cholesky decomposition $\Sigma = LL^T$, where L is a lower triangular matrix (Seydel, 2012). Then the zero-mean correlated random variables Y can be calculated as $Y = LZ$, where Z are independent random variables drawn from a standard normal distribution. The random variables Y are then normally distributed with zero mean and covariance matrix Σ. In

step d from Figure 4-2, ϵ values are replaced with correlated random numbers sampled in this fashion. The sample ϵ is scaled by a standard deviation equal to 0.65 (ln units). The value of 0.65 is consistent with the standard deviation of the FAS that results from the Boore03 procedure (Figure 4-2d), which is not sensitive to the time-domain variance of input white noise (Figure 4-2b). The scaled ϵ are converted to normalized FAS by taking their natural exponent. The correlated ϵ are standard-normally distributed in natural logarithm space, so the normalized FAS are log-normally distributed. For a log-normally distributed variable X, the first moment (mean) is given by Equation 4-5 (Kenney and Keeping, 1951):

$$E[X] = e^{\mu_\epsilon + \frac{1}{2}\sigma_\epsilon^2} \qquad (4-5)$$

where μ_ϵ and σ_ϵ are the mean and standard deviation of the natural logarithm X. In this application, $\mu_\epsilon = 0$. The normalized FAS need to have unit mean so that implementing the correlation does not change the mean amplitude of the simulations (over a suite of realizations) with respect to the unmodified simulation method. Therefore, to get normalized FAS with mean equal to one, these must be scaled by the adjustment factor given in Equation 4-6.

$$SF = \frac{1}{e^{\frac{1}{2}\sigma_\epsilon^2}} \qquad (4-6)$$

With the imposed value of $\sigma_\epsilon = 0.65$, the adjustment factor $SF = 0.8096$. Finally, the normalized and adjusted FAS are scaled by the Fourier amplitude spectrum of the considered scenario (Figure 4-2e), and the Boore03 recipe is continued to generate time series with realistic inter-frequency ρ_ϵ

of FAS. This procedure for creating simulated time series with realistic inter-period correlation is similar to the method described in Stafford (2017).

Using these modifications, two simulation procedures arise: the original Boore03 method and the Boore03 method modified to include the inter-period correlation of epsilon. An individual realization of each procedure results in a pair of compatible acceleration time series. Both have similar phasing, duration, frequency content, and amplitudes. Individual realizations of correlated ϵ may be positive or negative for frequency bands, but as the sample size is increased, the sampled ϵ have the intended standard-normal parameter values. Therefore, with a sufficient sample size, the median FAS or PSA of a simulated scenario should be the same for both procedures.

Example Application

In the following example, structural fragilities are developed using an IDA with two sets of ground motions created using the two simulation procedures described in the previous section. The first set of ground motions has near zero inter-period correlation and the second set has realistic inter-period correlation. Suites of 500 uncorrelated and correlated ground motions are developed using the same point source Fourier amplitude spectrum as the basis for the ground motion amplitudes.

Both suites of simulations have similar ground motion distributions in FAS space (approximately 0.65 ln units), as shown in Figure 4-3 and Figure 4-4, respectively. The PSA is calculated directly from the acceleration time histories, which are obtained by performing the inverse Fourier transform. On the right side of Figure 4-3 and Figure 4-4, the random vibration theory (RVT) spectrum derived from seismological parameters consistent with the point source spectrum is

plotted (Boore and Thompson, 2012). The median PSA of the suite of 500 ground motions closely matches the RVT spectrum in both cases.

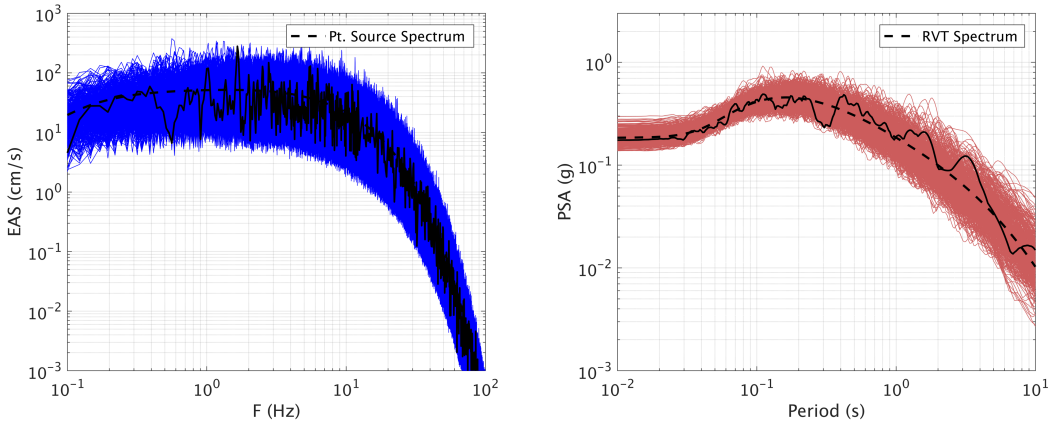

*Figure 4-3. A suite of 500 uncorrelated ground motion simulations for a **M**7.0 scenario at 30 km. Left: FAS realizations in blue, and the point source scenario spectrum in black. Right: PSA spectra realizations in red, and the RVT spectrum in black. One realization is identified with bold line type.*

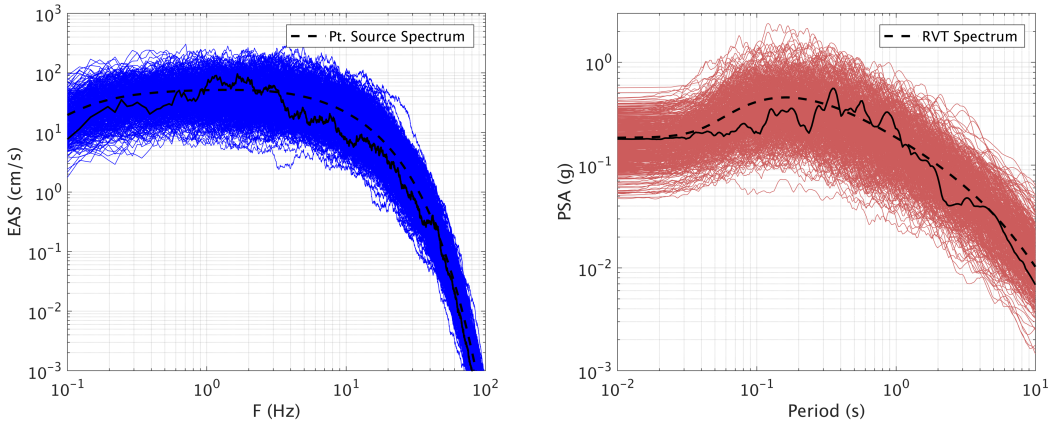

Figure 4-4. Like Fig. 3, but using the correlated ground motion simulations procedure.

Although they have the same median, Figure 4-3 and Figure 4-4 illustrate the substantial differences in the distribution of PSA between the uncorrelated and correlated ground motion sets.

This happens because PSA spectra are influenced by a range of frequencies. As described previously, considering broad (highly correlated) spectra, the ground motions with extreme FAS ϵ at given period generally stay extreme over the range of periods influenced by the response spectrum calculation (i.e. troughs remain in troughs, and peaks remain in peaks). The aggregate effect is the variability in PSA is higher for ground motions with realistic ρ_ϵ than for ground motions with low ρ_ϵ. The response spectrum is a simplified version of a real structure, and therefore its behavior mimics the expected response of a complete structural analysis.

As a verification check, the ρ_ϵ of FAS is back-calculated from the suite of 500 simulated time histories, using the point source spectrum as the reference model for calculating residuals. These ρ_ϵ are summarized for the two suites of ground motions in Figure 4-5. These figures are symmetric about the 1:1 line because the correlation coefficient between two frequencies is the same regardless of which frequency is the conditioning frequency. As shown in Figure 4-5a, the Boore03 procedure (uncorrelated) simulations exhibit near-zero correlation between frequencies. The correlated set of ground motions (Figure 4-5b) have ρ_ϵ of FAS consistent with the model imposed on the Fourier amplitudes, as expected.

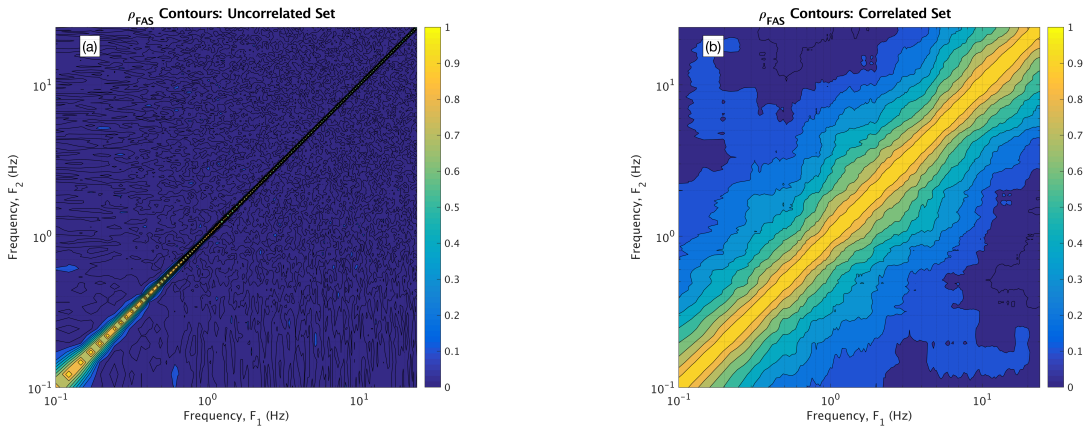

Figure 4-5. ρ_ϵ of FAS contours over 01.1-24 Hz from (a) the suite of 500 uncorrelated ground motion simulations and (b) the suite of 500 correlated ground motion simulations.

Example Application: Structural Models

The open source finite-element platform, OpenSees (McKenna et al., 2010), is used to model the structures and to perform the dynamic nonlinear structural analyses. The fragility results presented in this chapter are for the 6-story steel special moment-resisting frame (SMRF) building model described in Kalkan and Kunnath (2006). Since the impact of the correlation is related to structural softening, structures with varying fundamental periods are analyzed to confirm that the observations are not specific to just one type of structure or fundamental period. In addition to the 6-story steel building, a 12-story reinforced concrete building, (Heo, 2009) and a typical California Department of Transportation highway overcrossing (Kunnath et al., 2008) are tested. These alternate structures give similar results to the Kalkan and Kunnath (2006) model.

The Kalkan and Kunnath (2006) building model is based on an existing building located in Burbank, California. The existing building was designed as described by Kalkan and Kunnath

(2006), “in accordance with UBC (ICBO 1973) requirements. The rectangular plan of the building measures 36.6 m by 36.6 m with an 8.2 cm thick lightweight concrete slab over 7.5 cm metal decking. The primary lateral load-resisting system is a moment frame around the perimeter of the building. Interior frames are designed to carry only gravity loads. All columns are supported by base plates anchored on foundation beams, which in turn are supported on a pair of 9.75 m, 0.75 m diameter concrete piles.” The building was instrumented by the California Strong Motion Instrumentation Program (CSMIP) and recorded the response of the 1987 Whittier Narrows, 1991 Sierra Madre, and 1994 Northridge earthquakes.

The OpenSees computer models of this building were previously developed by Kunnath et al., (2004) and Kalkan and Kunnath (2006), including calibration of the models to match the observed response with the simulated response. The two-dimensional frame model used here is summarized by Kalkan and Kunnath (2006): “A force-based nonlinear beam-column element that utilizes a layered “fiber” section is utilized to model all components of the frame model. A fiber section model at each integration point, which in turn is associated with uniaxial material models and enforces Bernoulli beam assumptions for axial force and bending, represents the force-based element. Centerline dimensions were used in the element modeling. One half of the total building mass was applied to the frame distributed proportionally to the floor nodes. Modeling of the members and connections was based on the assumption of stable hysteresis derived from a bilinear stress-strain model. The columns were assumed to be fixed at the base level.” For additional model properties, the reader is referred to Kalkan and Kunnath (2006).

Example Application: Results

Following the IDA approach, these sets of ground motions are scaled and numerical structural simulations are carried out using OpenSees. The IDA results for the 6-story steel SMRF building model are presented in Figure 4-6, where blue symbols and lines represent data from the uncorrelated simulations and the red symbols and lines represent the correlated simulations. For each PSA level (at the fundamental structural period; T=1.38 s), the fraction of the ground motions exceeding 4% MIDR are counted. The process is repeated over multiple IM levels to obtain the probability of exceeding 4% MIDR at the discrete IM amplitudes. The lognormal CDF parameters α and β are optimized to fit these probabilities in log-space. The least-squares fit is performed in logarithmic space in order to focus the fit on the low-end tail of the CDF, which controls the risk.

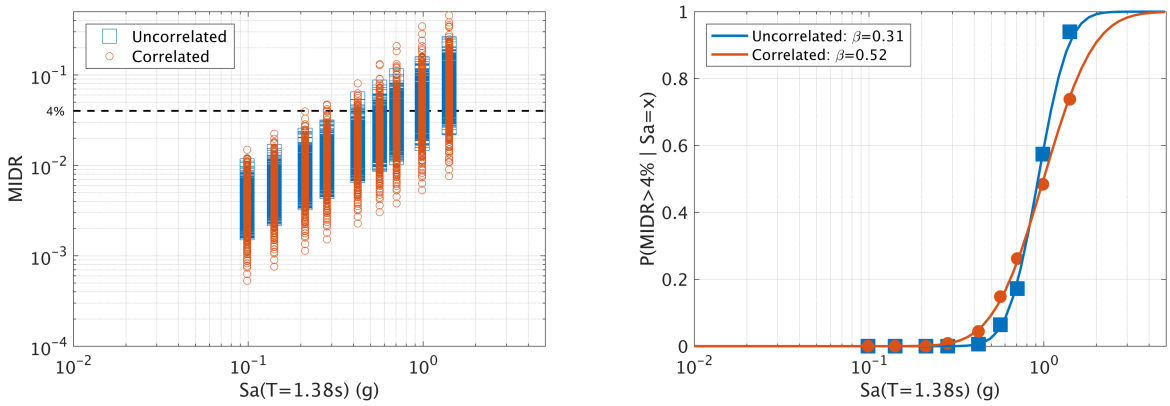

Figure 4-6. Left: MIDR results of the structural analysis for suites of 500 ground motions at. Right: MIDR>4% probabilities (symbols) and the fitted CDF fragility functions (lines).

As expected, the median structural response is similar between the correlated and uncorrelated ground motions sets, but the standard deviations of the structural responses are significantly different. For the presented results, the lognormal CDF dispersion parameter β is 0.31 for the

uncorrelated ground motions and 0.52 for the correlated ground motions (comparable to the building code value 0.6; ASCE, 2016). Larger β values mean flatter fragility curves with higher probabilities of failure at the lower IM levels.

The structural fragilities are combined with the seismic hazard to calculate the EDP hazard, using Equation 4-3. The results are shown in Figure 4-7, where the left panel compares the structural fragilities and marginal risk on a logarithmic vertical axis. Plotting them this way illustrates the consequential differences between them at moderate IM levels, where the hazard is higher, and the risk is sensitive to the fragility. To calculate the risk from the EDP hazard, a step function of the DMs (usually collapse) as a function of EDP fragility is assumed. The right panels of Figure 4-7 compare the marginal and cumulative marginal risk on a linear scale for the two ground motion sets. For this case, the highest marginal risk comes from PSA(T=1.38 s) levels less than 1g. Structural risk is calculated for four damage states using MIDR exceedances of 0.5%, 1%, 2%, and 4% (Table 4-1). For the MIDR>4% case, the structural risk calculated using the ground motions with realistic inter-period correlations is a factor of 1.43 higher than the risk calculated using uncorrelated ground motions, which corresponds to approximately the difference between a 4,000- and 2,800-year return period.

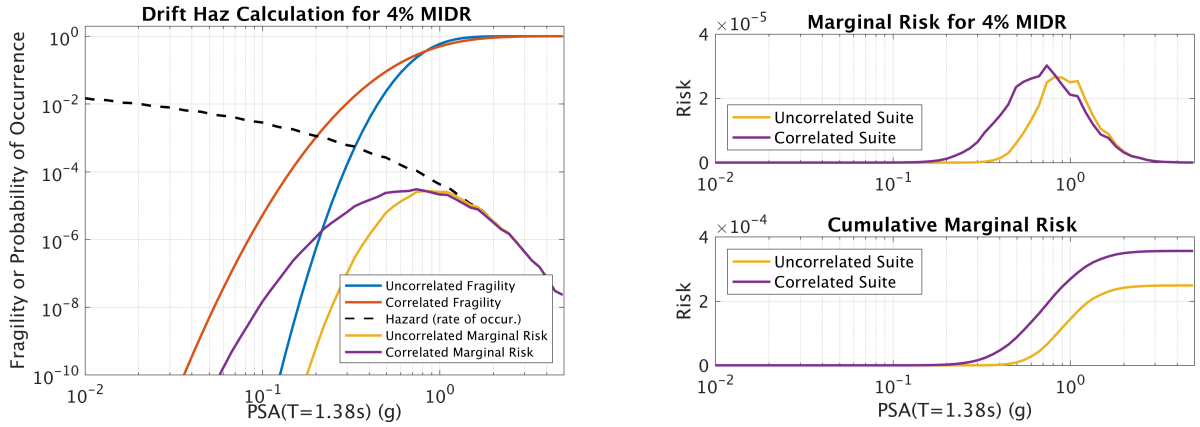

Figure 4-7. Left: Combining the seismic hazard occurrence and MIDR>4% fragilities to get the EDP hazard. Right: the marginal risk and cumulative marginal risk on linear scales.

Table 4-1. Structural risk for damage states with MIDR exceedances of 0.5%, 1%, 2%, and 4%.

GM Suite	MIDR ≥ 0.5%	MIDR ≥ 1%	MIDR ≥ 2%	MIDR ≥ 4%
Correlated	1.44E-02	5.12E-03	1.42E-03	3.56E-04
Uncorrelated	1.25E-02	4.26E-03	1.11E-03	2.49E-04
Ratio	1.15	1.20	1.28	1.43

Evaluating the Correlation of Existing Ground Motion Simulations

In the previous section, the inter-frequency correlation of simulated ground motions is demonstrated to be an important feature for capturing the variability of structural response, and therefore impacts the risk. In this section, the inter-frequency correlations of multiple existing ground-motion simulation methods are evaluated and compared with empirical models. The procedure to calculate the correlations is outlined and applied to suites of ground motion simulations calculated using several established simulation methods. The simulations used are from the Southern California Earthquake Center (SCEC) Broadband Platform (BBP, Maechling et al., 2015) and from the Lawrence Livermore National Laboratory (LLNL).

Simulation Methods Evaluated

The SCEC BBP is a collaborative software development project, with the objective to integrate complex scientific codes for generating broadband ground motions for earthquakes. Contributions come from many scientific groups including researchers, practitioners, and software development. On the BBP, the modular components include rupture generation, low- and high-frequency seismogram synthesis, non-linear site effects, and visualization (Maechling et al., 2015). Collections of these modules by different groups form alternate simulation methods. All of the BBP simulations evaluated here are based on regionalized 1-D (plane layered) earth models with engineering bedrock surface conditions, and do not model near surface site effects. The currently implemented methods include EXSIM (Atkinson and Assatourians, 2015), GP (Graves and Pitarka, 2015), SDSU (Olsen and Takedatsu, 2015), and UCSB (Crempien and Archuleta, 2015).

The process described in Dreger et al., (2015) established that specific methods (over defined period and magnitude ranges) on the BBP produce median results suitable for use in engineering applications. This validation exercise, driven by the needs of two major ground motion hazard projects, evaluated the performance of the different simulation methods in matching median PSA (RotD50 component), using both recorded earthquakes and GMMs for validation. For validating the simulations against data, nine events in active crustal regions were considered: 2008 Chino Hills, 2007 Alumn Rock, 1987 Whittier Narrows, 1986 North Palm Springs, 1994 Northridge, 1989 Loma Prieta, 1992 Landers, 2000 Tottori, and 2004 Niigata (Goulet et al., 2015). These nine events are the simulations utilized herein, calculated with SCEC BBP version 16.5. The SONG (Song, 2016) method is also evaluated. Song (2016) is implemented on the SCEC BBP, but has not undergone the Dreger et al., (2015) validation exercise.

A set of simulations calculated by LLNL are also evaluated, which are described in Rodgers et al. (2018). LLNL simulated ground motions for an **M**7.0 scenario earthquake on the Hayward Fault using 3-D earth structure and surface topography, with the open source finite-difference wave propagation code SW4. These simulations span frequencies from 0 to 4 Hz and the computational domain covers a 120 by 80 km area surrounding the fault, with a dense grid of simulation sites (2,301 in total) at the ground surface throughout the domain. The deterministic source description was created using the GP rupture generator. For more details on the simulation method and assumptions, the reader is referred to Rodgers et al., (2018).

Previous Work

Others have studied the correlation of PSA of simulated ground motions (Burks and Baker, 2014), and the structural response of buildings to simulated and recorded ground motions, considering differences in ϵ (Tothong and Cornell, 2006). Tothong and Cornell concluded that the PSA for positive ϵ records (simulated using the point source stochastic method) drop off rapidly as the period ratio increases or decreases as compared to the as-recorded motions, resulting in an underestimation of the inelastic response of structures. This conclusion is consistent with the findings herein. More recently, Burks and Baker (2014) evaluated the inter-frequency correlations of response spectra using a subset of the Dreger et al. (2015) SCEC simulations, calculated using BBP version 11.2. Burks and Baker (2014) used simulations of the 1989 Loma Prieta earthquake (40 stations on rock site conditions), and obtained simulations performed by three groups: EXSIM, CSM (Anderson, 2015), and GP. The conclusions from Burks and Baker (2014) can be summarized as follows: the GP correlations were generally too low at short periods (the less theoretically rigorous, or stochastic portion) but had some correlation at long periods (the deterministic portion). The EXSIM method correlations were too low at all periods, and the CSM correlations were high at all periods relative to the empirical models and data. The Goulet et al., (2015) SCEC validation exercise did not evaluate the CSM method (Dreger and Jordan, 2014), so it is not included in this analysis. In future work, correlation of this method should be evaluated since the conclusions from Burks and Baker (2014) indicate this method could provide some insight on the features controlling the correlation. Following a description of the procedure for calculating the correlation, the Burks and Baker (2014) conclusions are compared with the results from this study.

Procedure

To calculate ρ_ϵ of the simulations, the first step is to calculate the FAS from the simulated acceleration time series. The Effective Amplitude Spectrum (EAS), defined in the PEER NGA-east project (Goulet et al., 2018), is calculated for each orthogonal pair of FAS using Equation 4-7,

$$EAS(f) = \sqrt{\frac{1}{2}[FAS_{HC1}(f)^2 + FAS_{HC2}(f)^2]} \quad (4-7)$$

where FAS_{HC1} and FAS_{HC1} are the FAS of the two orthogonal horizontal components of a three component time series. The EAS is independent of the orientation of the instrument, and in this way is compatible with the PEER RVT approach for developing orientation-independent PSA predictions (Goulet et al., 2018). The EAS are smoothed using the $\log_{10}$-scale Konno and Ohmachi (1998) smoothing window, which has weights and window parameter defined by Equations 4-8 and 4-9.

$$W(f) = \left(\frac{\sin(b\log(f/f_c))}{b\log(f/f_c)}\right)^4 \quad (4-8)$$

$$b = {}^{2\pi}/_{b_w} \quad (4-9)$$

The smoothing parameters (W, f_c, b, b_w) are described in Kottke et al., (2018). The Konno and Ohmachi (1998) smoothing window was selected by PEER NGA-East because it led to minimal bias on the amplitudes of the smoothed EAS when compared to the unsmoothed EAS. The

bandwidth of the smoothing window, $b = 188.5$, was selected such that the RVT calibration properties before and after smoothing were minimally effected (Kottke et al., 2018). This study uses smoothed EAS with the same smoothing parameters as described in Kottke et al. (2018), which has a direct impact on ρ_ϵ. Using the smoothed EAS maintains consistency with the PEER database and with other PEER projects; including the NGA-East empirical FAS models (Goulet et al., 2018) and the Bayless and Abrahamson (2018) EAS model (Chapter 2).

The simulation residuals are computed relative to the EAS ground motion model developed in Chapter 2. The simulation residuals are partitioned as given by Equation 4-10.

$$\ln(EAS\ Residual)_{es}\,(f) = \delta B_e(f) + \delta S2S_s(f) + \delta WS_{es}(f) + C(f) \qquad (4-10)$$

where $C(f)$ is the mean residual between the suite of simulations and the empirical EAS GMM. The overall bias exists because the median EAS from the simulations is different from the empirical model for a given scenario. The overall bias between the simulations and the empirical model is removed by accounting for $C(f)$. In order to avoid over-fitting the simulations, which would artificially decrease the computed correlations, the $C(f)$ is partitioned into two terms: $C_{fit}(f)$, the smooth linear fit in log-frequency space to $C(f)$, and $\Delta C(f)$, the remaining bias, termed the 'method-bias' (Equations 4-11 and 4-12).

$$\ln(EAS\ Residual)_{es}\,(f) = \delta B_e(f) + \delta S2S_s(f) + \delta WS_{es}(f) + C_{fit}(f) + \Delta C(f) \qquad (4-11)$$

$$C(f) = C_{fit}(f) + \Delta C(f) \qquad (4-12)$$

This procedure achieves the goal of fitting the simulation data in a way that is consistent with the procedure for developing an empirical GMM, and yields residuals from the simulations which are consistent with the empirical residuals (i.e. are approximately normally distributed with zero mean). The bias terms for the six simulation methods evaluated are summarized in Figure 4-8. The cause of the method-bias is not clear; it could result from the theoretical 1-D Green's functions, or it may be introduced by the source representation, for example. The correlation of this bias is included in the total correlation by modifying Equation 4-2 into Equation 4-13.

$$\rho_{\epsilon,total}(f_1,f_2) = \frac{\left[\begin{matrix}\rho_B(f_1,f_2)\tau(f_1)\tau(f_2) + \rho_{S2S}(f_1,f_2)\phi_{S2S}(f_1)\phi_{S2S}(f_2) + \\ \rho_{WS}(f_1,f_2)\phi_{ss}(f_1)\phi_{ss}(f_2) + \rho_{\Delta C}(f_1,f_2)\theta_{\Delta C}\theta_{\Delta C}\end{matrix}\right]}{\sigma_{total}(f_1)\sigma_{total}(f_2)} \qquad (4-13)$$

where $\rho_{\Delta C}$ and $\theta_{\Delta C}$ are the auto-correlation and standard deviation of the method-bias term, respectively, and σ_{total} is the total standard deviation including the contribution from ΔC (Equation 4-14).

$$\sigma_{total}^2 = \tau^2 + \phi_{S2S}^2 + \phi_{ss}^2 + \theta_{\Delta C}^2 \qquad (4-14)$$

Moving forward, the appropriate components of the correlation model must be selected carefully when making comparisons between the empirical ρ_ϵ and the ρ_ϵ of simulations, so that the conclusions drawn are meaningful. To facilitate this, comparisons between each of the available correlation components are provided. For the BBP simulations, which are based on regionalized 1-D earth models without site effects, the between-site component of the correlation is not captured. This is because of an inherent limitation of 1-D simulations, namely, that there is no

variability in the site response because all sites have the same site adjustment. This means the $\delta S2S$ term cannot be distinguished from the constant (Equation 4-15).

$$\ln(EAS\ Residual)_{es}\,(f) = \delta B_e(f) + \delta WS_{es}(f) + [\delta S2S_s(f) + C(f)] \qquad (4-15)$$

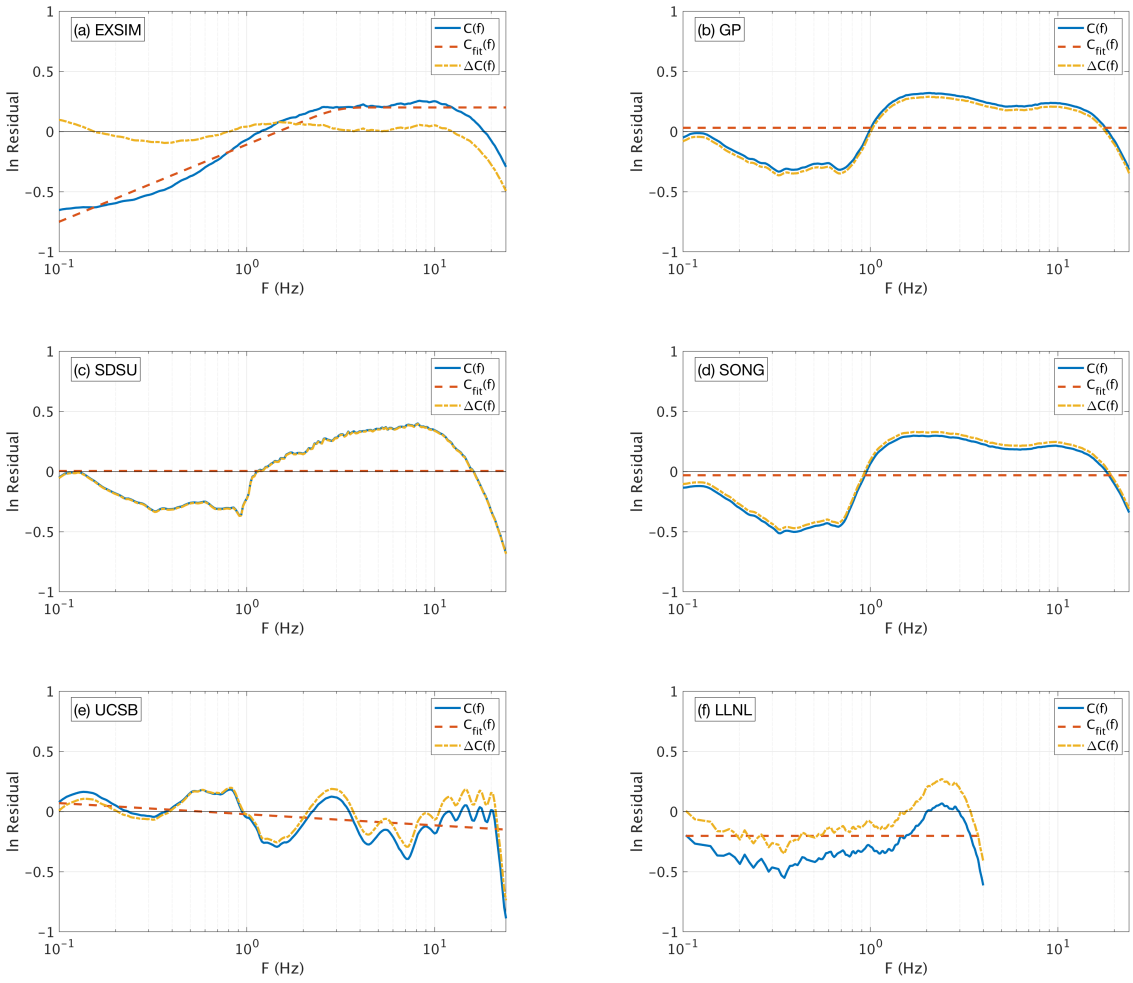

Figure 4-8. The overall bias between the simulations and the empirical model, $C(f)$, the smooth linear fit in log-frequency space, $C_{fit}(f)$, and the remaining model term bias $\Delta C(f)$ for the six simulation methods evaluated.

Stafford (2017) and Bayless and Abrahamson (2018; modified from Chapter 3) both found that a significant contribution to the total correlations comes from the between-site terms. As a result, the most appropriate comparison for tuning the methods based on a 1-D assumption is the correlation of the between-event and within-site terms, because they can be separated and compared directly. If these methods were tuned to the total correlation, the resulting within-site and between-event components would be over-estimated since the between-site correlation component is relevant but cannot be determined for a 1-D simulation.

The LLNL simulations, which use a 3-D earth structure including surface topography, have the potential to overcome this limitation of 1-D modeling; however, since the simulation data used for this study includes one realization of the source (e.g. one earthquake scenario and one simulated time history per site), the between-event correlations cannot be estimated or separated from the constant. Also, the $\delta S2S$ and δWS terms cannot be separated (Equation 4-16).

$$\ln(EAS\ Residual)_{es}\,(f) = [\delta S2S_s(f) + \delta WS_{es}(f)] + [\delta B_e(f) + C(f)] \qquad (4-16)$$

In this case, the method-bias term includes one realization of the between-event term. Because the residual components cannot be separated, the total correlation of these simulations is compared with the total correlation from the data. The conclusions drawn herein would be strengthened by having more earthquake simulation scenarios to evaluate the correlation components individually.

For both the SCEC and LLNL simulations, the quantity of simulation stations is large enough to robustly estimate the correlation coefficients for a given scenario. For the SCEC simulations, multiple source realizations of the same earthquake are utilized as separate events with respect to

calculating residuals. Two approaches for calculating ρ_ϵ from the simulations are tested. First, the correlations are calculated for individual validation events. Second, the residuals from the nine events are combined into one database before calculating ρ_ϵ. No systematic differences in the correlations are observed between these approaches, indicating that the correlation behavior of the simulations is not event specific. Results shown herein are for the combined database approach. Bayless and Abrahamson (2018, modified from Chapter 3) also showed that the inter-frequency EAS correlations calculated using recorded data from only the nine SCEC validation events did not vary systematically from the correlations calculated from the full database. This also indicates that the correlations are not event or magnitude specific and that using simulations from a small group of earthquake scenarios should still yield correlations which are broadly consistent with the ρ_ϵ empirical model.

The total correlation model for EAS developed in Chapter 3 is summarized in Figure 4-9a. The Baker and Jayaram (2008) model for inter-period correlation of ϵ for response spectra (ρ_{PSA}) from shallow crustal earthquakes is shown in Figure 4-9b. An important difference between the EAS and PSA correlations is the behavior at high frequencies. The PSA contours broaden substantially at high frequencies, this is because of the wide ground motion frequency range of influence on the short period PSA, as described in Chapter 2. The EAS contours do not exhibit this behavior since the Fourier transform operation at each frequency bin is independent of neighboring bins. Stafford (2017) also developed an inter-frequency correlation model for FAS. This model is based on different data and assumptions than the model developed in Chapter 3, including using the FAS without smoothing. These differences are discussed in detail in Chapter 3. The correlation model developed in Chapter 3 is consistent with the empirical EAS datasets developed at PEER and has

ρ_ϵ components for the three residual components described previously (δB, $\delta S2S$ and δWS), along with a total correlation model.

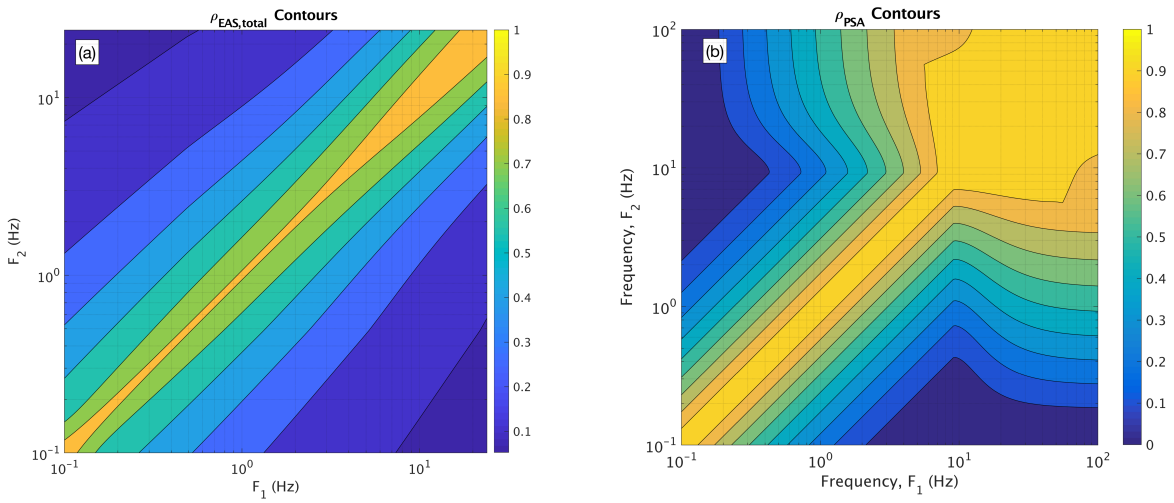

Figure 4-9. (a) Contours of the total EAS correlation model developed in Chapter 3. (b) Baker and Jayaram (2008) PSA correlation model contours.

Inter-Period Correlations

This section evaluates the current status of the correlation contained in the simulation methods described above. Evaluations are performed primarily in the frequency domain, so that shortcomings can be resolved by future improvement to the simulation methods. The specific parts of the simulation methods driving the correlation are yet to be determined, and although the results shown here provide some insights, more work is still needed to identify the causal features. Therefore, the focus here is on presenting the results without concluding which features of the simulations control the correlation.

Figure 4-10 through Figure 4-14 summarize the inter-period correlation of ϵ for EAS and response spectra (ρ_{EAS} and ρ_{PSA}) of the five BBP simulation methods evaluated. These are calculated using the nine validation event simulations described above, with residuals calculated using the GMM for EAS developed in Chapter 2, and using the NGA-West2 GMMs for PSA. These figures provide a visual means of subjectively comparing the correlations calculated from the simulation methods with the empirical correlations. Each figure shows cross-sections of the ρ_ϵ contours at conditioning frequencies 0.2, 0.5, 2, 5, and 15 Hz. Panels (a) through (c) of each figure compare the cross-sections of the between-event, within-site, and total ρ_{EAS} with empirical correlations, respectively. Panel (d) compares the ρ_{PSA} with the Baker and Jayaram model. The comparisons focus on correlations greater than 0.4, because it is expected that the correlation values greater than about 0.5 impact the structural response. As mentioned previously, the BBP simulations are based on regionalized 1-D earth models without site effects, so the between-site component of the correlation is not captured. Figure 4-15 presents the same summary of the correlations calculated from the LLNL simulations, where the empirical ρ_ϵ cross-sections represent the total correlation model.

EXSIM method results are shown in Figure 4-10. As expected, since EXSIM is based on the PS stochastic method, the within-site and total inter-period correlations for this method are lower than the empirical correlations and drop rapidly moving away from the conditioning frequency. The between-event correlation conditioned at 15 Hz (black line in panel a) is broad relative to other frequencies; similar relatively high between-event correlation at the higher frequencies are

observed for several of the simulation methods. The within-event ρ_{PSA} observed are generally consistent with the conclusions of Burks and Baker (2014).

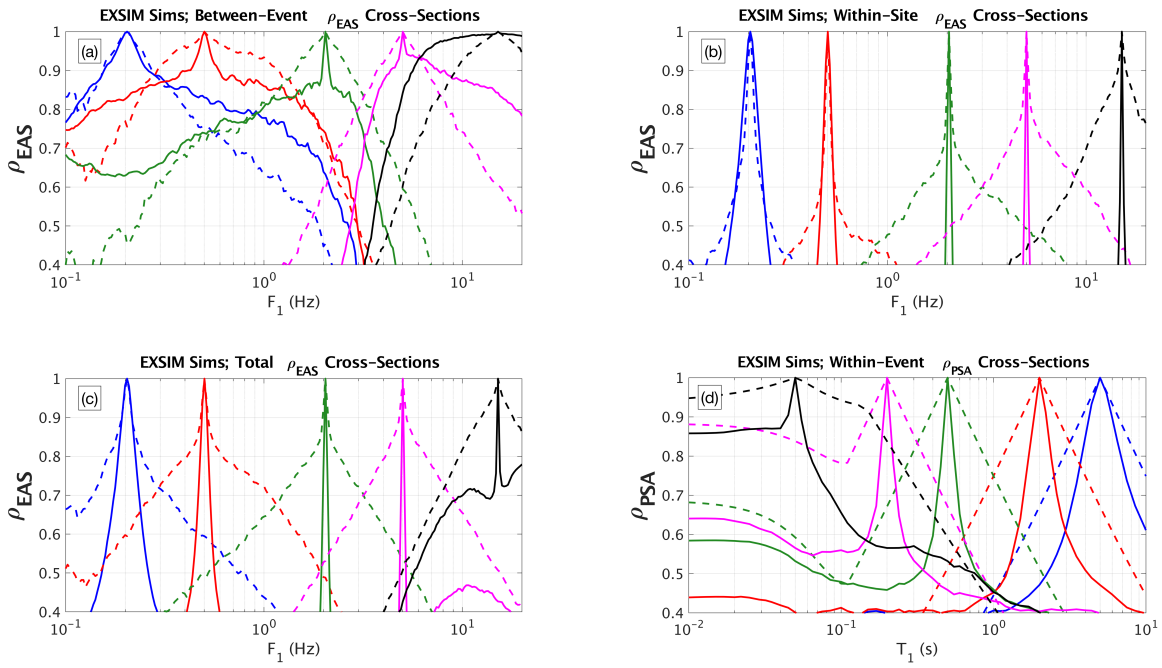

Figure 4-10. Summary of the correlations calculated from the Atkinson and Assatourians (2015) SCEC BBP validation simulations, compared with empirical correlations. (a) Between-event ρ_{EAS} cross-sections versus frequency at conditioning frequencies 0.2, 0.5, 2, 5, and 15 Hz (solid lines), compared with the empirical correlations from Bayless and Abrahamson (2018) (dashed lines). (b) Comparison of the within-site ρ_{EAS}. (c) Comparison of the total ρ_{EAS}. (d) Within-event ρ_{PSA} cross-sections versus period (solid lines), compared with the Baker and Jayaram (2008) model (dashed lines).

Figure 4-11 displays the GP method results. At frequencies above 1 Hz, this method is similar to EXSIM, and the within-site correlations are therefore similarly low. At frequencies below 1 Hz, the correlations generally show significant promise, but the total ρ_{EAS} values still drop of too quickly moving away from the conditioning frequency for most frequencies. At frequencies less than about 0.25 Hz, the total correlations are similar to the empirical correlations. By definition, the PSA correlations reflect the EAS correlations. This is evident for GP as the short period (<1

sec) PSA correlations are low, and the long period (>1 sec) ones are closer to the empirical model. The within-event ρ_{PSA} for the GP method are also generally consistent with those calculated by Burks and Baker (2014).

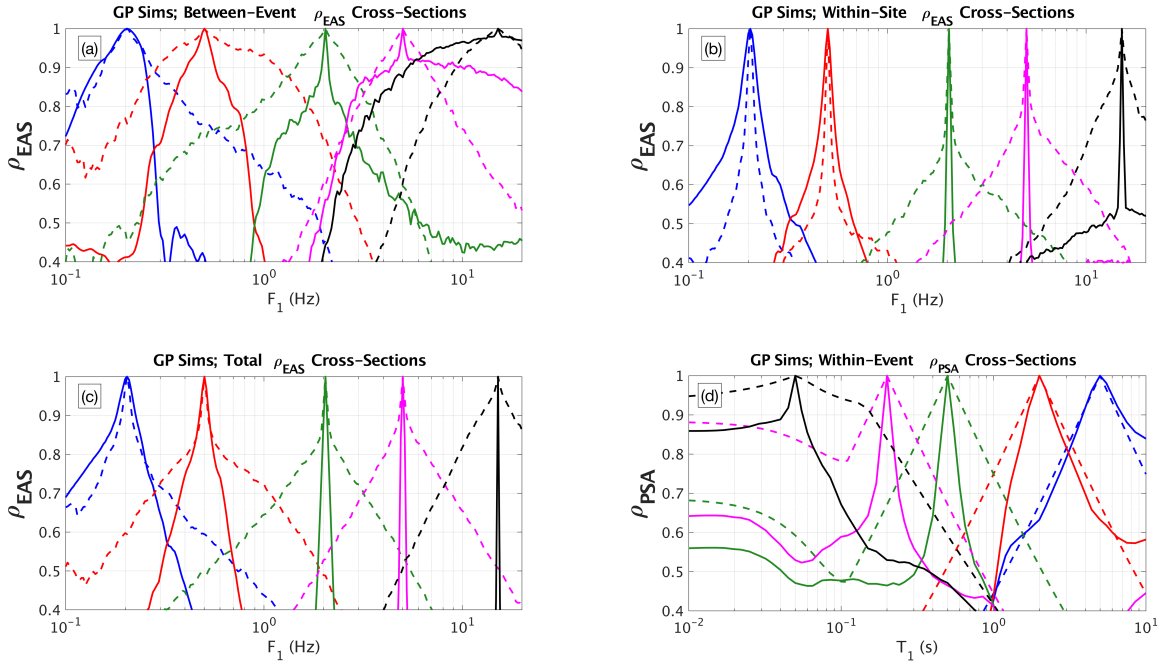

Figure 4-11. Summary of the correlations calculated from the Graves and Pitarka (2015) SCEC BBP validation simulations. See Figure 4-10 caption for a complete description of each panel.

SDSU method results are shown in Figure 4-12. At frequencies below 1 Hz, this method is identical to GP, and therefore the correlations are the same as GP. At higher frequencies, this method shows an abrupt drop of the within-site correlation away from the conditioning frequency, followed by moderately high correlation (between 0.7 and 0.95) over the entire frequency range greater than 1 Hz. The cause of this feature is currently not known and should be studied further.

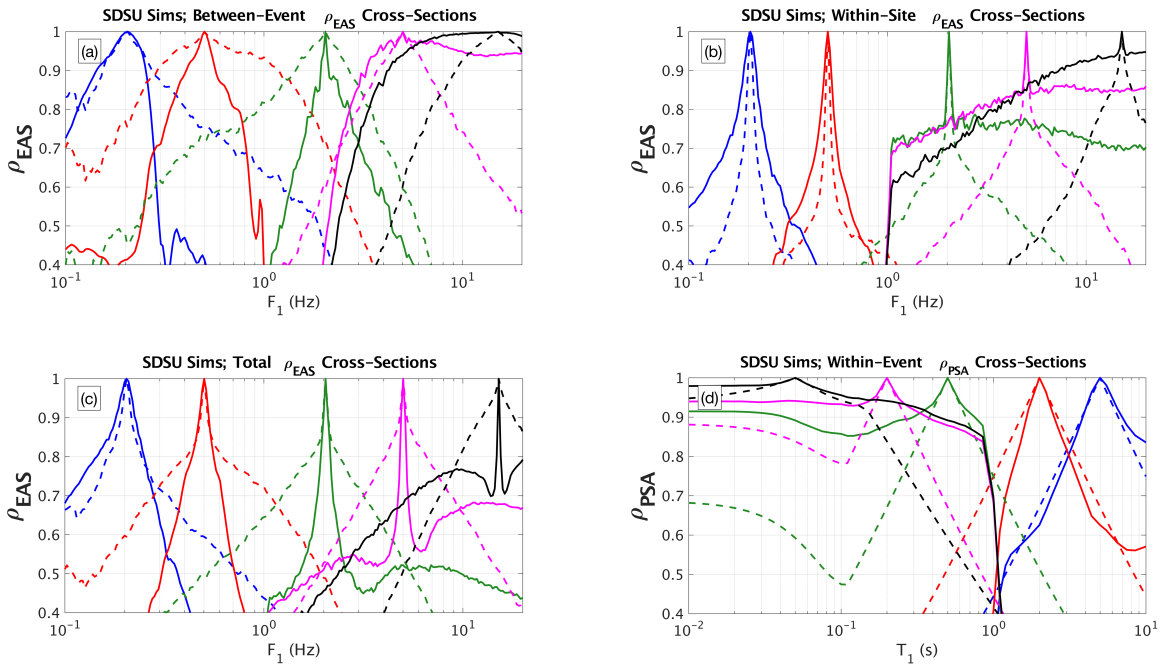

Figure 4-12. Summary of the correlations calculated from the Olsen and Takedatsu (2015) SCEC BBP validation simulations. See Figure 4-10 caption for a complete description of each panel.

Figure 4-13 displays the SONG method results. The SONG method uses the GP wave propagation and simulation code; the only differences are in the earthquake source. Including this method in the analysis is a convenient way to isolate the effects of the correlation of earthquake source parameters on the GP simulation method inter-frequency correlations. The SONG earthquake source method is characterized by kinematic source parameters (including slip, rupture velocity, peak slip velocity) with 1-point statistics (median and standard deviation) and 2-point statistics (autocorrelation in space and correlation between parameters) constrained by dynamic rupture modeling. Because the SONG low frequency correlations are significantly broader than the GP correlations, this indicates that correlation of these parameters in the source may have an important effect on modeling the low frequency inter-period correlations. Like GP, the SONG total correlations are closest to the empirical model at low frequencies, and actually exceed the

empirical correlations at frequencies very near the conditioning frequency. The total correlations are low at the high frequencies. This model is the only one evaluated which potentially over-estimates the total ρ_{EAS} over a wide range of frequencies (approximately 0.1 - 0.7 Hz).

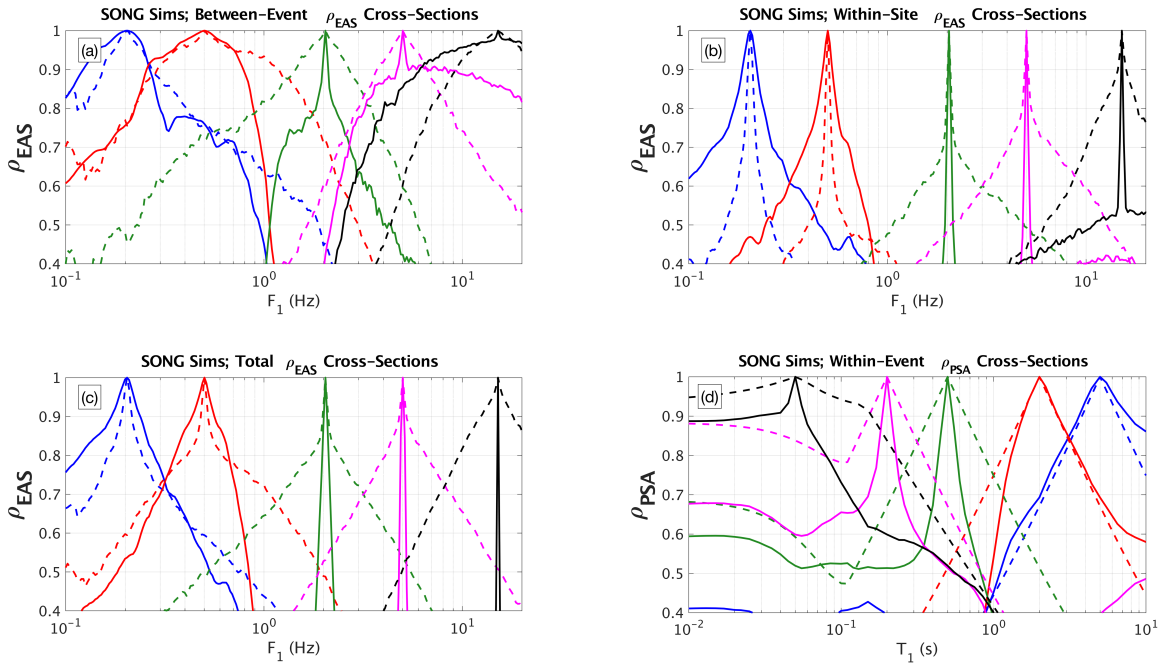

Figure 4-13. Summary of the correlations calculated from the Song (2015) SCEC BBP validation simulations. See Figure 4-10 caption for a complete description of each panel.

Figure 4-14 displays the UCSB method results. This model, like several others, has lower within-site correlation than the empirical models at frequencies above 1 Hz. Likewise, the low frequency total correlations are closer, but still slightly low, compared to the data, except for very low frequencies where they are similar to the empirical correlations. The between-event ρ_{EAS} at high frequencies is much broader than the empirical models, and this effect propagates through to the total ρ_{EAS}. An undulating pattern in the ρ_{EAS} is also observed, especially for low correlation values at frequencies far from the conditioning frequency. This pattern was not observed with the other

methods, but the higher correlation values will have the most effect on structural response, therefore the undulating feature at low correlation values is not a major concern with respect to validation.

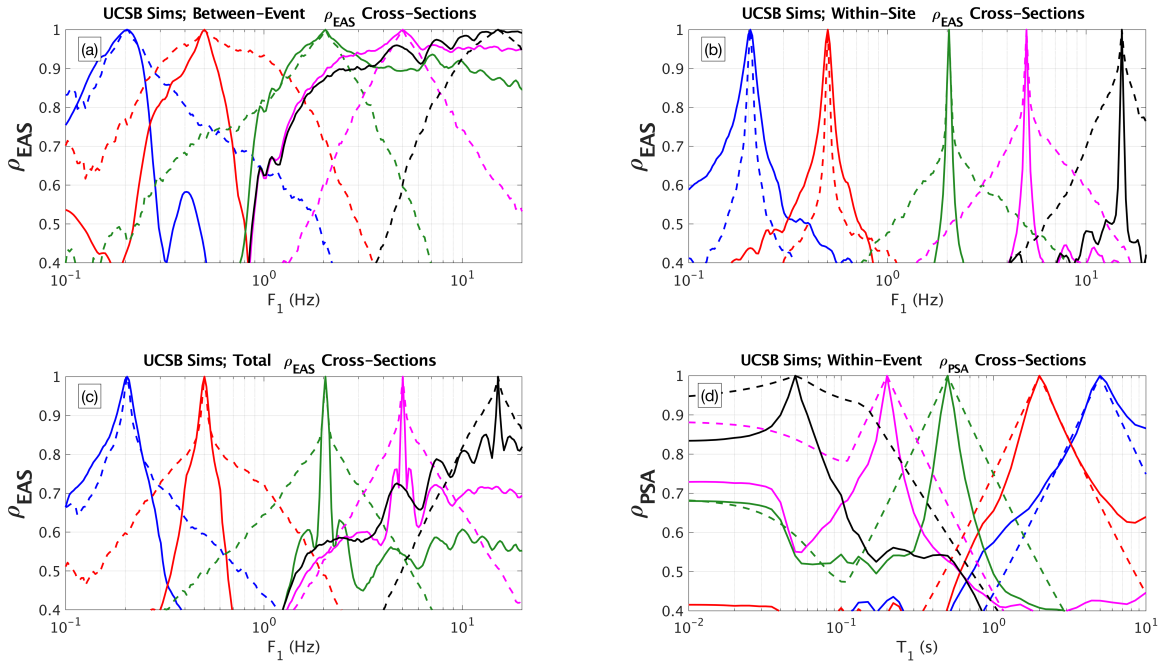

Figure 4-14. Summary of the correlations calculated from the Crempien and Archuleta (2015) SCEC BBP validation simulations. See Figure 4-10 caption for a complete description of each panel.

Figure 4-15 displays the LLNL method results over the frequency range 0.1 to 4 Hz. As described previously, these simulations are for one realization of the source, so the between-event and between-site correlations cannot be separated. Therefore, the correlations calculated include one realization of the between-event correlation in addition to the remaining correlation, and so they are compared with the total correlation model. These results show a similar trend to the other methods analyzed; the most broad correlations at lowest frequencies, with too steeply dropping correlations at higher frequencies. At the lowest frequencies, the total correlations are similar to

those from the data, but further refinements should be made to frequencies greater than about 0.25 Hz. These conclusions regarding the LLNL simulations would be strengthened by having more earthquake simulation scenarios to evaluate the correlation components individually.

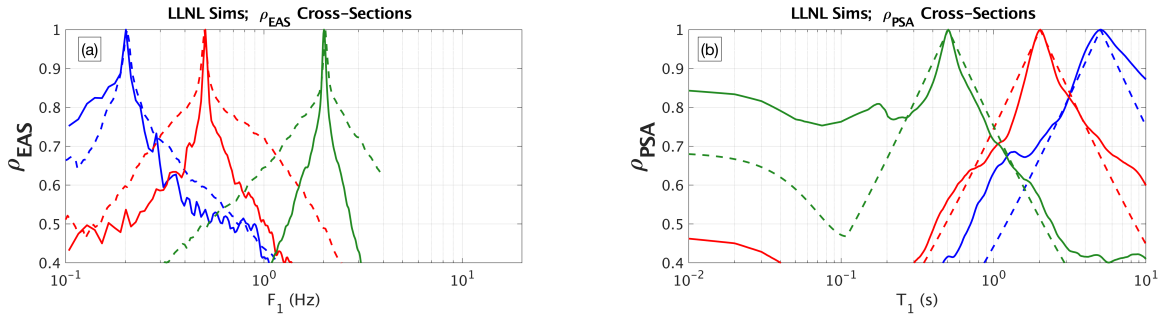

Figure 4-15. Summary of the correlations calculated from the Rodgers et al. (2018) Hayward fault scenario simulations at conditioning frequencies 0.2, 0.5, and 2 Hz. (a) Comparison of the total ρ_{EAS}. (b) Comparison with the Baker and Jayaram (2008) within-event ρ_{PSA} model.

Conclusions

The inter-period correlation of epsilon is an important component of ground motions for capturing the variability of structural response that is needed in seismic fragility and seismic risk studies. Without the adequate inter-period correlation of ground motions, variability in the structural response may be under-estimated. This leads to structural fragilities which are too steep (under-estimated dispersion parameter β) and propagates through to non-conservative estimates of seismic risk. The conclusions herein apply directly to structural fragility or risk assessments which are derived from ground motion simulations, commonly referred to as 'ruptures to rafters' simulations. These results are similar for the three structures analyzed: a 6-story steel special moment-resisting frame (SMRF), a 12-story reinforced concrete building, and a typical California Department of Transportation highway overcrossing.

None of the six finite-fault simulation methods tested adequately capture the inter-period correlations over the entire frequency range evaluated, although several of the methods show promise, especially at low frequencies. Using the correlation of the EAS provides the developers of the simulation methods better feedback in terms of how they can modify their methods that is not clear when using PSA comparisons. For the stochastic part of the simulation, adding the empirical correlation is relatively straight-forward, such as was done for the stochastic simulations used here. For the deterministic part of the simulation, capturing the correlation is more difficult as it requires modifying the rupture generator or the wave propagation parts of the simulation which have already been validated for the median ground motion. Based on the relative differences in the correlations of the SONG source method, it appears that changes to the rupture generator may be the most promising approach to modifying the long period inter-period correlations.

Chapter 5:

Calibrating the inter-period correlation of EXSIM finite-fault ground motion simulations

Abstract

In the previous chapter, the inter-frequency correlation of epsilon of Fourier amplitude spectra (ρ_ϵ) is shown to be an important ground-motion characteristic for capturing the variability of structural response that is needed in seismic fragility and seismic risk studies. Therefore, the inter-frequency correlation from numerical simulation methods needs to be tested and validated. The previous chapter also evaluated the ρ_ϵ of existing finite-fault ground-motion simulation methods. None of the six finite-fault simulation methods tested adequately capture the ρ_ϵ over the entire frequency range evaluated, although several of the methods show promise, especially at low frequencies. In this chapter, approaches are developed to incorporate the observed ρ_ϵ into the finite-fault simulation algorithm EXSIM (Atkinson and Assatourians, 2015). Incorporation of the correlation into the Fourier amplitude spectra of each EXSIM sub-source is tested, but the resulting correlations (of the FAS of the complete finite-fault simulation considering all sub-sources) are lower than desired, meaning there is destructive interference of the correlation between sub-sources. As an alternative, a method to implement the correlation as a post-processing modification is introduced, which achieves the short-term goal of being be able to prescribe the correlation of the full waveform seen in the data for other applications, e.g. structural risk. The implementation of the correlation into the sub-sources should be studied further in future work.

Introduction

The inter-period correlation of epsilon (ρ_ϵ) is an important component of ground motions for capturing the variability of structural response that is needed in seismic fragility and seismic risk studies. Without the appropriate inter-period correlation of ground motions, variability in the structural response may be under-estimated. This leads to structural fragilities which are too steep (under-estimated dispersion parameter β) and propagates through to non-conservative estimates of seismic risk. This is the motivation for calibrating the inter-frequency correlation of the finite fault simulations. In Chapter 4, current state of multiple existing ground motion simulation methods was assessed by evaluating the inter-frequency correlations from forward simulations and comparing with the correlation from empirical models. None of the six finite-fault simulation methods tested adequately capture the inter-period correlations over the entire frequency range evaluated, although several of the methods show promise, especially at low frequencies. Therefore, the inter-frequency correlation from numerical simulation methods needs to be calibrated. This chapter tests methods for calibrating the simulation method EXSIM (Atkinson and Assatourians, 2014).

Background on SMSIM and EXSIM

The point-source stochastic method for simulating ground motions, based on the pioneering work of Brune (1970), Hanks and McGuire (1981) and Boore (1983), among others, has been developed and refined over several decades. David Boore formalized the method, extended it to the simulation of acceleration time series, and developed a computer code named SMSIM for the implementation (Boore, 1983; Boore, 2003; Boore, 2005). An SMSIM simulated time series is produced using a

seismological model of the Fourier amplitude spectrum, and assuming the spectrum is distributed with random phase angles over a time duration related to the earthquake magnitude and the distance between the source and site. The Boore (2003) procedure starts by generating normally distributed noise (Figure 5-1a) and applying a time-domain taper with duration consistent with the scenario being considered (Figure 5-1b). The tapered noise is transformed into the frequency domain (Figure 5-1c), and the FAS of the noise is normalized by the square root of the mean power, such that the FAS has mean power of one (Figure 5-1d, showing the natural logarithm of these values). The normalized FAS is then shaped to the point-source Fourier amplitude spectrum of the considered scenario (Figure 5-1e), and inverse transformed to the time domain using the phase angles from the tapered time domain noise (Figure 5-1f).

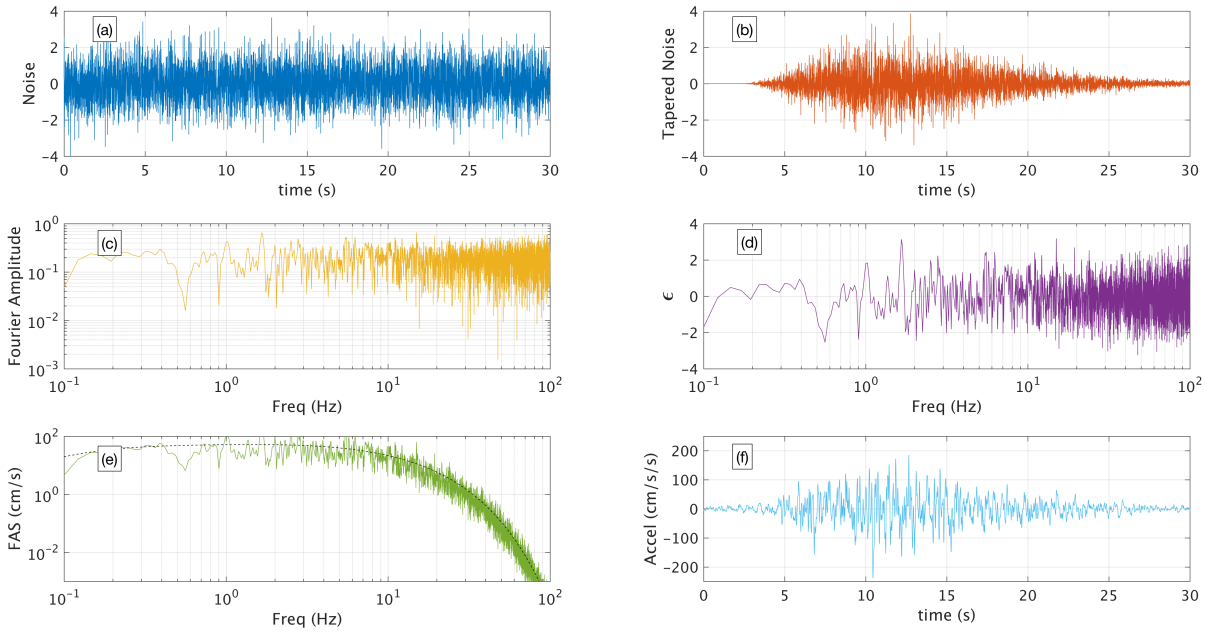

Figure 5-1. Illustration of the Boore (2003) procedure for simulating acceleration time series using the point-source stochastic method. Each sub-panel is described in the text.

EXSIM is the finite-fault extension of SMSIM. Like SMSIM, EXSIM is also an open-source simulation algorithm for generating time series of ground motion for earthquakes. EXSIM divides a finite-fault rupture into sub-sources with each sub-source modeled as a point source using the point-source stochastic method. The acceleration time series resulting from each sub-source is summed in the time domain after applying appropriate time delays for propagation of the rupture front (Atkinson and Assatourians, 2014). The version of EXSIM used here is described in Atkinson and Assatourians (2014) and is implemented as a FORTRAN code in the Southern California Earthquake Center (SCEC) Broadband Platform (BBP, Maechling et al., 2015) v17.3.

Implementing the Correlation

SMSIM

SMSIM uses filtered white noise in the time-domain, resulting in ϵ with no correlation between frequencies. To generate a simulated time series with realistic inter-period correlation of the epsilon, the SMSIM procedure can be modified as described below.

First, a symmetric, positive-definite covariance matrix (Σ) for the inter-frequency $\rho_{\epsilon,total}$ of FAS is needed (e.g. the one from Chapter 3). This matrix is factorized using the Cholesky decomposition $\Sigma = LL^T$, where L is a lower triangular matrix (Seydel, 2012). Then the zero-mean correlated random variables Y can be calculated as $Y = LZ$, where Z are independent random variables drawn from a standard normal distribution. The random variables Y are normally distributed with zero mean and covariance matrix Σ. In step d from Figure 5-1, ϵ values are replaced with correlated random numbers sampled in this fashion. The sample ϵ is scaled by a

standard deviation equal to 0.65 (ln units). The value of 0.65 is consistent with the standard deviation of the FAS that results from the SMSIM procedure (Figure 5-1d), which is not sensitive to the time-domain variance of input white noise (Figure 5-1b). The scaled ϵ are converted to normalized FAS by $\exp(\epsilon * \sigma)$. The correlated ϵ are standard-normally distributed in natural logarithm space, so the normalized FAS are log-normally distributed. For a log-normally distributed variable X, the first moment (mean) is given by Equation 5-1 (Kenney and Keeping, 1951):

$$E[X] = e^{\mu_\epsilon + \frac{1}{2}\sigma_\epsilon^2} \qquad (5-1)$$

where μ_ϵ and σ_ϵ are the mean and standard deviation of the natural logarithm X. In this application, $\mu_\epsilon = 0$. The normalized FAS need to have unit mean so that implementing the correlation does not change the mean amplitude of the simulations (over a suite of realizations) with respect to the unmodified simulation method. Therefore, to get normalized FAS with mean equal to one, these must be scaled by the adjustment factor given in Equation 5-2.

$$SF = \frac{1}{e^{\frac{1}{2}\sigma_\epsilon^2}} \qquad (5-2)$$

With the imposed value of $\sigma_\epsilon = 0.65$, the adjustment factor $SF = 0.8096$. Finally, the normalized and adjusted FAS are scaled by the Fourier amplitude spectrum of the considered scenario (Figure 5-1e), and the SMSIM recipe is continued to generate time series with realistic ρ_ϵ: $\text{SMSIM}_{\text{corr}}$ (Figure 5-2).

This $SMSIM_{corr}$ procedure is similar to the method described in Stafford (2017). Individual realizations of correlated ϵ may be positive or negative for frequency bands, but as the sample size is increased, the sampled ϵ have the intended standard-normal parameter values. Therefore, with a sufficient sample size, and with the adjustment factor given by Equation 5-2, the median FAS or spectral acceleration (PSA) of a simulated scenario should be the same as from the unmodified SMSIM procedure. In Figure 5-3, example smoothed FAS spectra from the SMSIM and $SMSIM_{corr}$ procedures are shown for one sample of ϵ.

In this implementation, the model for the inter-frequency ρ_ϵ of FAS developed in Chapter 3 is used to generate correlated ϵ. The model usable frequency range is $f = 0.1$-24 Hz and requires extrapolation for frequencies outside this range. The extrapolation is performed by using the values for model coefficients $\mathrm{A}, \mathrm{B}, C$, and D (Equation 3-8) at either $f = 0.1$ or $f = 24$ Hz, for extrapolating to lower and higher frequencies, respectively. The extrapolation is performed to generate correlated ϵ over the frequency range 0.01-100 Hz in the SMSIM and EXSIM (described below) implementation procedures. This extrapolation may introduce a bias in the correlations at very low and high frequencies, as discussed further below.

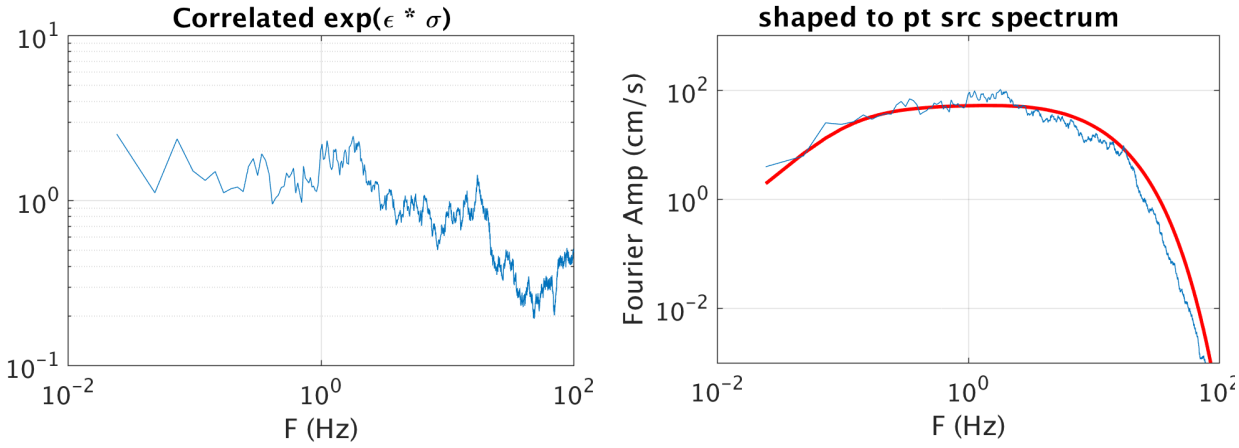

Figure 5-2. Left: An example realization of correlated ϵ. Right: The point source Fourier amplitude spectrum of the example scenario (heavy red line) and the correlated ϵ shaped to the spectrum (blue).

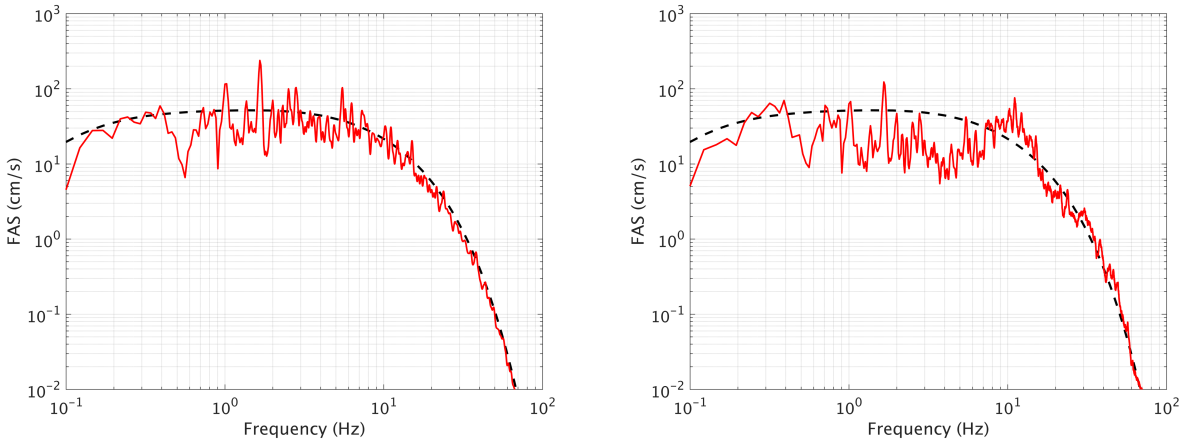

Figure 5-3. Left: An example smoothed FAS spectrum from the unmodified SMSIM procedure (low ρ_ϵ). Right: An example smoothed FAS spectrum from the SMSIM$_{corr}$ procedure. In both panels the point source scenario spectrum is given by the dashed line.

EXSIM: Sub-Sources

As described previously, EXSIM is the finite-fault extension of SMSIM. Ideally, implementing the inter-frequency correlation should involve following the SMSIM$_{corr}$ procedure for all the sub-sources, and the resulting finite-fault time series should also have the appropriate ρ_ϵ. In Chapter 3, it is shown that the total ρ_ϵ does not have a strong dependence on magnitude, so the small events

(the sub-sources) effectively have the same ρ_ϵ as the larger scenario. Thus, the summation of multiple sub-sources in the time domain should be equivalent to the summation of the sub-source Fourier amplitude spectra due to the linearity of the Fourier transform. This concept is tested in this section.

Each of the sub-source implementations are tested using 300 realizations of the same earthquake scenario for a single site. The scenario is the Northridge earthquake using the source as defined in Goulet et al. (2014) and the site is Sylmar Converter Station East (SCSE), which is located approximately 5km from the rupture plane. The sub-source implementation is tested using three approaches: Method 0, Method 1 and Method 2; these are described below.

Method 0

Method 0 is the unmodified version of EXSIM. Using Method 0, the smoothed FAS of the 300 simulated acceleration time series of the Northridge-SCSE scenario are calculated and shown in Figure 5-4a. The FAS are smoothed, and ϵ and ρ_ϵ are calculated using the mean of these spectra as a reference. Figure 5-4b shows the ρ_ϵ cross-sections at five conditioning frequencies calculated from these simulations, along with the ρ_ϵ model cross-sections (from Chapter 3) which are used to generate the correlated ϵ values (in Methods 1 and 2). As expected, there is effectively zero inter-period ρ_ϵ using unmodified EXSIM.

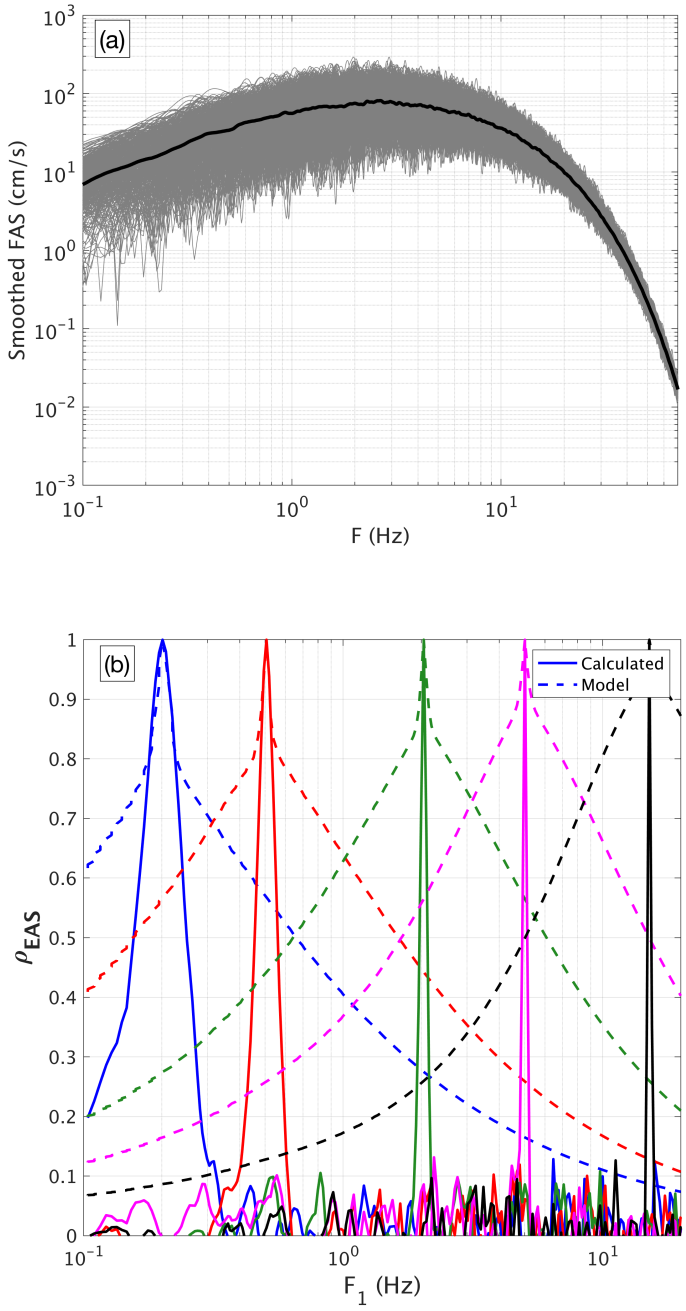

Figure 5-4. Results created using unmodified EXSIM (Method 0). (a) The smoothed FAS of the 300 realizations of the Northridge-SCSE scenario, with the geometric mean of these spectra (heavy line). (b) The ρ_ϵ at five conditioning frequencies calculated from these simulations (solid) along with the ρ_ϵ model from Chapter 3.

Method 1

For Method 1, the code is modified by following the $SMSIM_{corr}$ procedure with a different sample of correlated ϵ within each sub-source of the finite rupture. This means that for a given rupture, the different sub-sources will have correlated Fourier spectra with local peaks and troughs over different frequency ranges due to the random sampling of correlated ϵ.

The smoothed FAS of the 300 simulated acceleration time series of the Northridge-SCSE scenario are calculated and shown in Figure 5-5a. The FAS are smoothed, and ϵ and ρ_ϵ are calculated using the mean of these spectra as a reference. Figure 5-5b shows the ρ_ϵ cross-sections at five conditioning frequencies calculated from these simulations, along with the ρ_ϵ model cross-sections (from Chapter 3) which are used to generate the correlated ϵ values.

The ρ_ϵ cross-sections in Figure 5-5b are much weaker than the ρ_ϵ prescribed to each sub-source, meaning there is significant destructive interference of the correlation between sub-sources. This result led to the second method for sub-source implementation, Method 2.

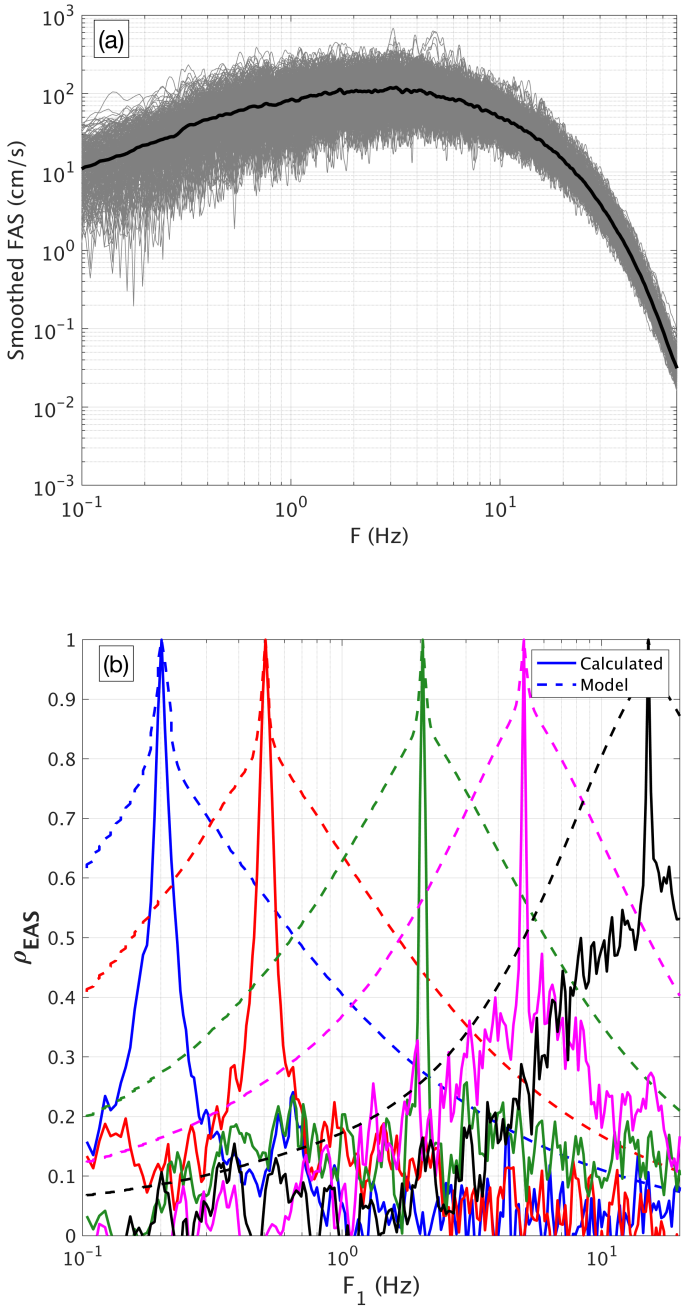

Figure 5-5. Results created using EXSIM with the SMSIM$_{corr}$ procedure applied to each sub-source, Method 1 (using a different sample of correlated ϵ within each sub-source for a given realization.)

Method 2

Method 2 is tested with the objective of avoiding the destructive interference of the correlation between sub-sources observed using Method 1. For Method 2, the $SMSIM_{corr}$ procedure is followed with the same sample of correlated ϵ within each sub-source of the finite rupture. In this case, for a given rupture realization, the different sub-sources will have correlated Fourier spectra with peaks and troughs in the same frequency ranges. Between alternate rupture realizations, the correlated ϵ samples vary. The simulation is repeated for the same Northridge-SCSE scenario 300 times and the smoothed FAS of the resulting acceleration time series are calculated and shown in Figure 5-6a. Figure 5-6b shows the ρ_ϵ cross-sections at five conditioning frequencies.

The ρ_ϵ cross-sections from Method 2 (Figure 5-6b) are stronger than from Method 1 but are still weaker than the ρ_ϵ prescribed to each sub-source. This means there is still destructive interference of the correlation between sub-sources. Since each sub-source is prescribed the same correlated ϵ values for a given realization, this was not the expected result.

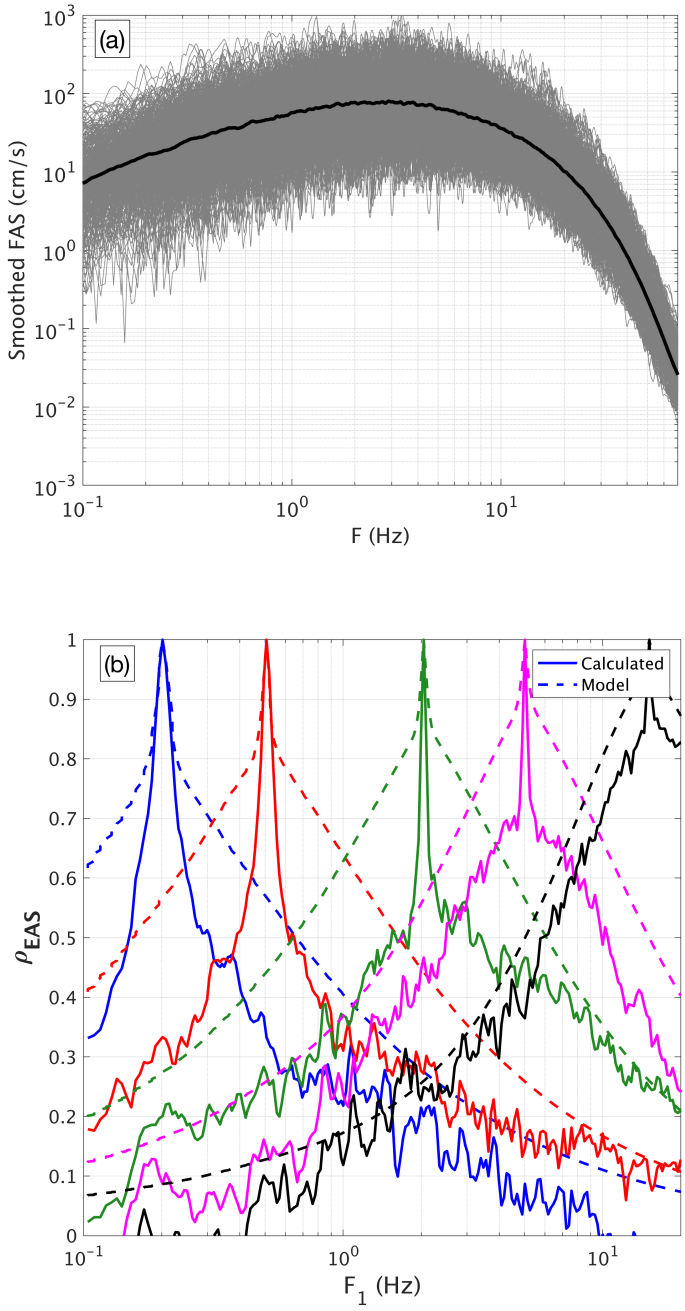

Figure 5-6. Results created using EXSIM with the SMSIM$_{corr}$ procedure applied to each sub-source, Method 2 (using the same sample of correlated ϵ within each sub-source for a given realization.)

In Chapter 3, it is shown that the total ρ_ϵ does not have a strong dependence on magnitude, so the small events (the sub-sources) effectively have the same ρ_ϵ as the larger scenario. Thus, the summation of multiple sub-sources in the time domain was expected to be equivalent to the summation of the sub-source Fourier amplitude spectra due to the linearity of the Fourier transform. Upon further inspection, this is not the case because the real and imaginary parts of the Fourier transform are individually linear, and so they possess the additive property of linearity as given by Equation 5-3 (Smith, 1997):

$$\begin{gathered} if\ f_1(t) + f_2(t) = f_3(t) \\ then\ \mathcal{F}_{1R}(s) + \mathcal{F}_{2R}(s) = \mathcal{F}_{3R}(s) \\ and\ \mathcal{F}_{1I}(s) + \mathcal{F}_{2I}(s) = \mathcal{F}_{3I}(s) \end{gathered} \qquad (5-3)$$

where $f(t)$ denotes a time-domain signal, $\mathcal{F}(s)$ denotes its Fourier transform, and subscripts R and I denote the real and imaginary parts of the transform. By Equation 5-3, the summing of time-domain signals from the sub-sources can contribute to the degradation of the inter-frequency correlation due to differences in the phasing. This effect can be understood by considering the most extreme case: two time-domain signals f_1 and f_2, where $f_2 = -f_1$, so it follows that $f_1 + f_2 = 0$ and the two signals are purely out of phase. In this case, the Fourier amplitude spectra (magnitude) of the two signals are identical, but the phase angles are shifted by π. The Fourier amplitude spectra of the quantity $f_1 + f_2$ is zero and is not equal to the sum of the Fourier amplitude spectra of both signals.

Figure 5-7 shows this effect for a less extreme case: two acceleration time histories f_1 and f_2 which represent the response from two EXSIM sub-sources for this example. In this case, $f_2(t) = 0.75 *$

$f_1(t-5)$ and $f_3 = f_1 + f_2$. On the right side of Figure 5-7, the FAS are shown over the frequency range 1-2 Hz. This figure shows that the additive property of the linearity of the Fourier transform, which applies to the real and imaginary parts, does not necessarily hold for the Fourier amplitudes (magnitudes). This is the effect of differences in phase angles on the finite-fault Fourier amplitude spectrum, which is causing the reduction in correlation between frequencies shown in Figure 5-6b. This effect should be studied further in the future with methods for generating partially correlated phase angles so that the correlation can be implemented at the sub-source level.

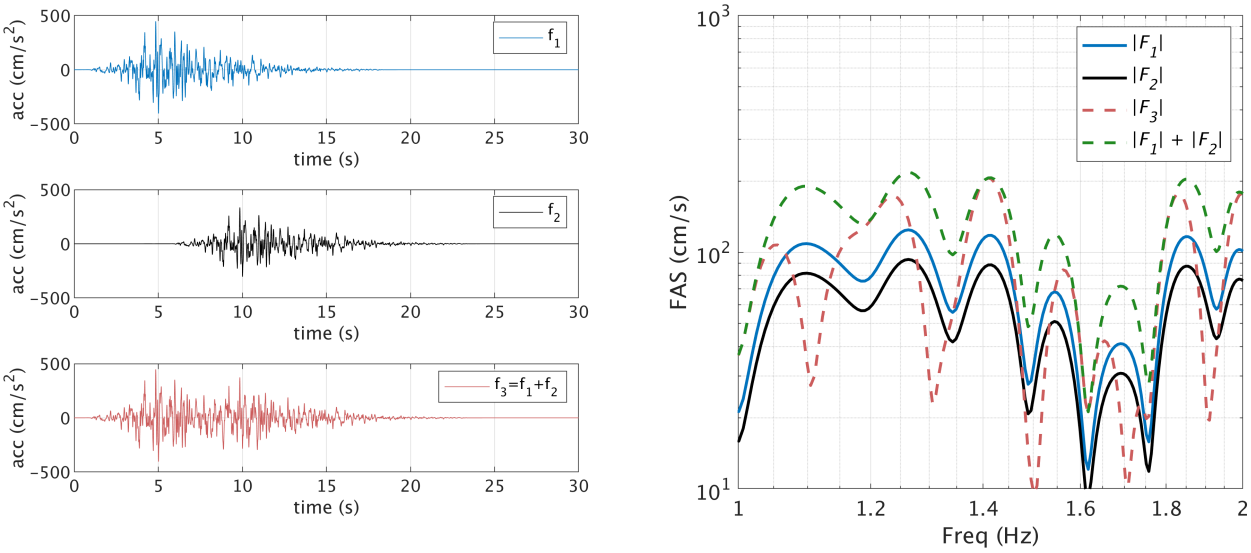

Figure 5-7. Left: Example acceleration time histories f_1 and f_2, which represent the response from two EXSIM sub-sources, plus their sum, f_3. Right: The FAS over the frequency range 1-2 Hz.

EXSIM: Post-Processing

Rather than incorporating ρ_ϵ into each EXSIM sub-source, another approach is to implement the ρ_ϵ as a post-processing step. For a given earthquake scenario and site, the post-processing method steps are:

- Run the unmodified EXSIM algorithm n times.
- Calculate the geometric mean FAS of the n simulated time series.
- Using the mean spectrum as the target (in place of the point source spectrum), shape the sample of correlated ϵ to the target spectrum.
- Perform the inverse Fourier transform using the phase angles from the tapered time domain noise from any of the i^{th} simulation realizations.

This method is tested using the same earthquake and site (Northridge-SCSE) and with $n = 300$. The resulting FAS and the ρ_ϵ are shown in Figure 5-8. In this case, the ρ_ϵ match the prescribed model well, and with increasing n, the match should also improve.

The post-processing method allows for full calibration of the correlation of the simulations, which has use in practice in the short-term (e.g. structural risk applications, such as those in Chapter 4), but it is not a desirable approach. The ρ_ϵ observed in the data is an important property of ground motions, and there is some physical reason for the existence of the correlation. The theoretical cause is currently not well understood (although the relative contributions of GMM components to the total correlation have been identified in Chapter 3), but the correlation must be introduced in some combination of the earthquake source, the travel path, and the local site response. Therefore, the preferable approach is to incorporate the correlation into seismological models (EXSIM, as well as others) through these foundational elements so that the models most closely represent the earthquake process. When the post-processing method is applied, the physical process built into the finite-fault simulation is ignored.

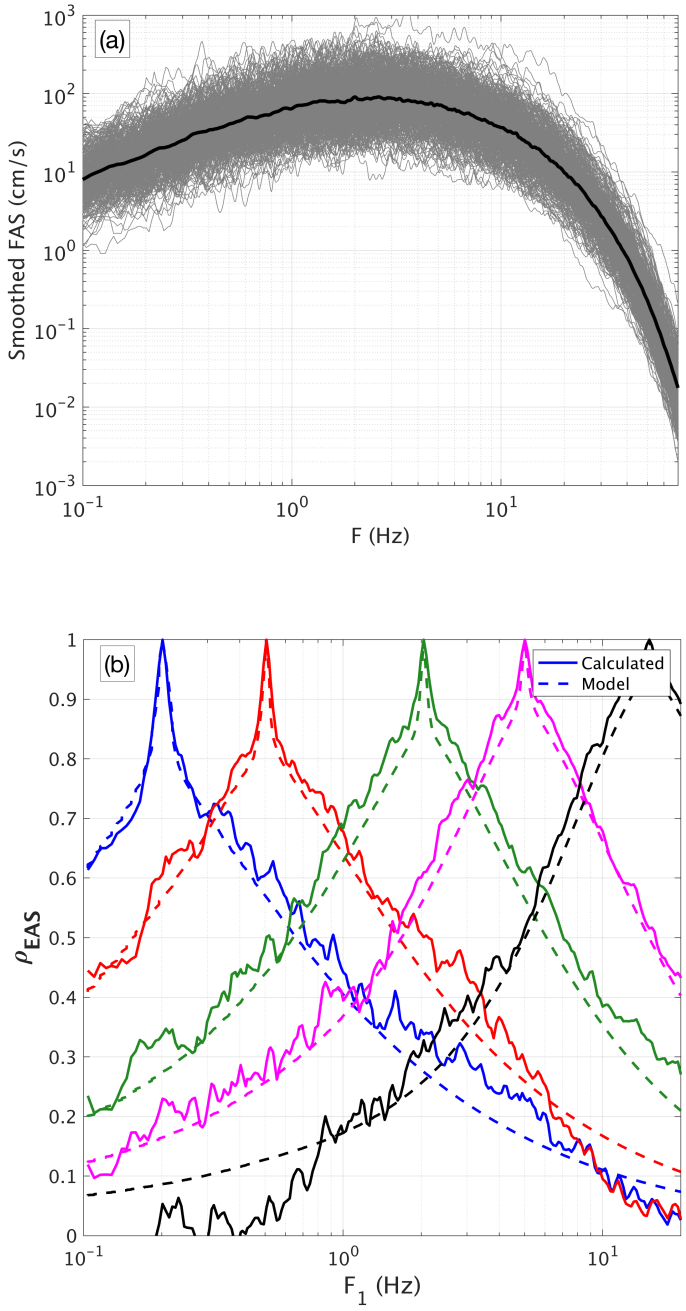

Figure 5-8. (a) The smoothed FAS of 300 realizations of the Northridge-SCSE scenario created using EXSIM with the post-processing ρ_ϵ procedure, with the geometric mean of these spectra (heavy line). (b) the ρ_ϵ at five conditioning frequencies calculated from these simulations (solid) along with the ρ_ϵ model from Chapter 3 used to generate correlated the ϵ values (dashed).

SCEC Broadband Platform Implementation

Due to the unresolved shortcomings of the sub-source method, the post-processing method is tested on the SCEC Broadband Platform v17.3. Simulations of seven of the Dreger et al. (2014) validation events are analyzed: Alum Rock, Chino Hills, Landers, Loma Prieta, North Palm Springs, Northridge, and Whittier Narrows. The simulations on the BBP use 50 realizations (each with a different random number generation seed) of each event and each earthquake simulates ground motions for approximately 45 sites.

The response spectra goodness-of-fit (GOF) is a summary of the logarithmic residuals of the simulated response spectra relative to the recorded ground motions. The GOF is calculated at each spectral period. The GOF plot is the primary evaluation tool used in the Goulet et al., (2015) validations of the SCEC BBP simulations. Figure 5-9 shows a GOF plot for simulations of the Loma Prieta earthquake. This plot is created using the combination of all 50 source realizations and all recording stations, where the solid black line is the mean GOF for all stations (with the average of all source realizations representing the PSA at a station). The pink band is the 90% confidence interval for the mean, and the purple band is the standard deviation centered around the mean (Goulet et al., 2014). Figure 5-10 shows the same summary plot for the Northridge earthquake simulations. In both figures, the top panel shows the GOF summary for unmodified EXSIM, and the bottom panel shows the GOF summary for EXSIM with the post-processing ρ_ϵ procedure.

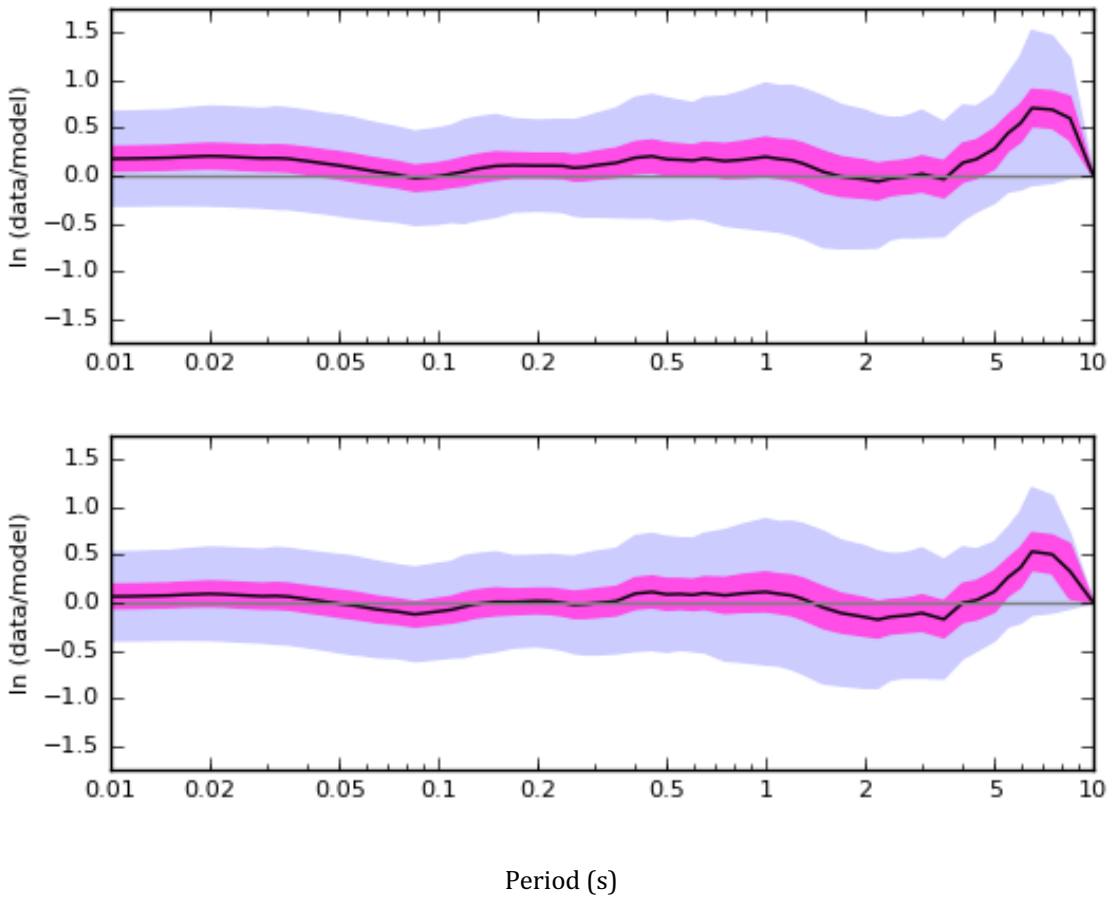

Figure 5-9. The goodness-of-fit (GOF) for response spectra, simulations of the Loma Prieta earthquake. Top: Unmodified EXSIM, Bottom: EXSIM with the post-processing ρ_ϵ procedure.

As shown in Figure 5-9 and Figure 5-10, the post-processing ρ_ϵ procedure does not introduce a significant bias in the mean residual. Minor shifts in the mean residuals are due to the random sampling of correlated ϵ over the 50 source realizations. The difference in the mean residual seen for the two earthquakes in Figure 5-9 and Figure 5-10 is similar because the same samples of ϵ were used in the 50 realizations of both earthquakes (a result of the same set of random number generator seeds). If different ϵ sets were used between earthquakes, then the two simulations would have different mean bias effects. Additionally, with more realizations, the mean bias will approach the unmodified EXSIM, so that validations for the median PSA do not need to be repeated.

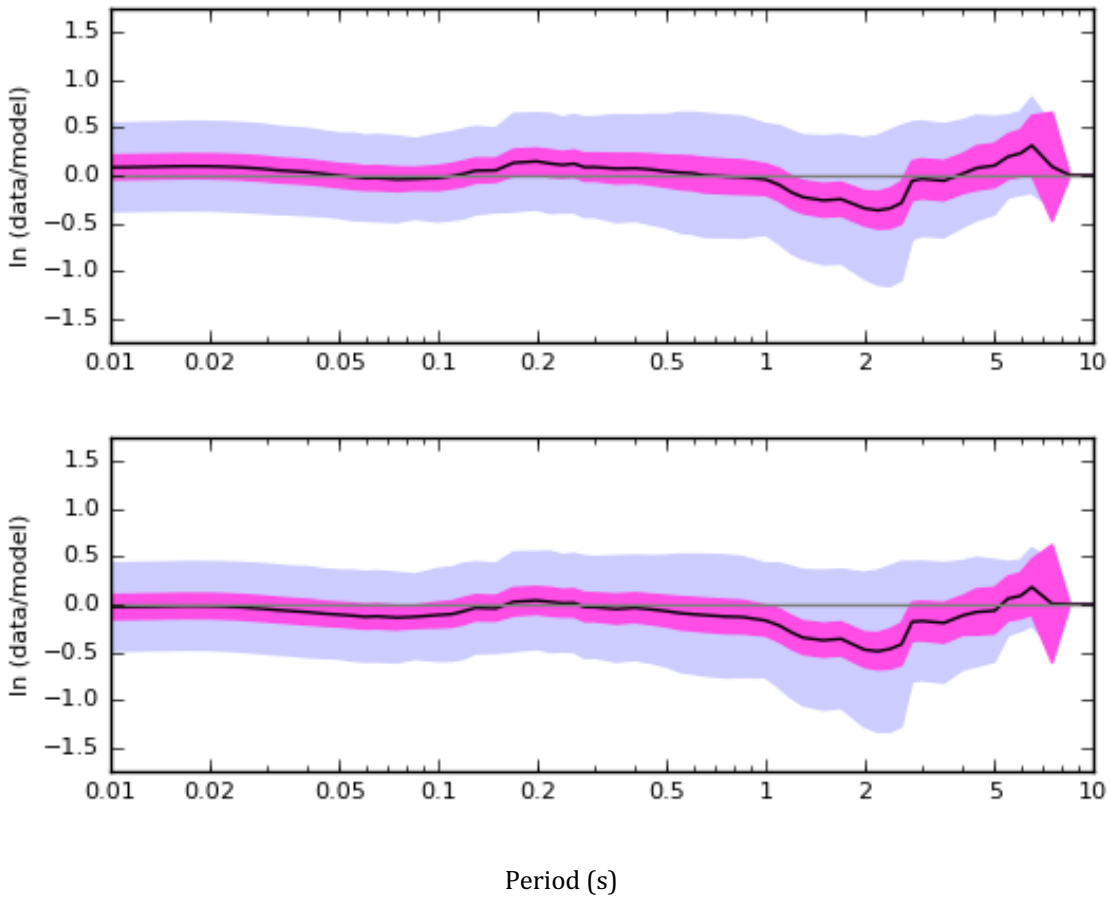

Figure 5-10. The goodness-of-fit (GOF) for response spectra, simulations of the Northridge earthquake. Top: Unmodified EXSIM, Bottom: EXSIM with the post-processing ρ_ϵ procedure.

Using the simulations, residuals are also calculated from the NGA-West2 GMMs for PSA. These models are smooth, so they produce residuals appropriate for back-calculating ρ_ϵ from the simulated time series. Using the seven validations events, with 50 source realizations of each event, and with approximately 45 stations per event, a database of 13,400 PSA residuals is developed. Figure 5-11b summarizes the within-event ρ_ϵ of these PSA residuals; panel (a) shows the within-event ρ_ϵ for the unmodified version of EXSIM. This figure indicates that the post-processing implementation of ρ_ϵ, applied to the FAS, performs quite well. The ρ_ϵ for PSA is significantly

improved relative to the unmodified EXSIM version. These correlations approximately match the Baker and Jayaram (2008) empirical model, except for the very long periods where the correlation is higher than the model. At long periods, the correlations may be biased due to the extrapolation of the FAS ρ_ϵ model to frequencies as low as $f = 0.01$ Hz. This effect should be studied further.

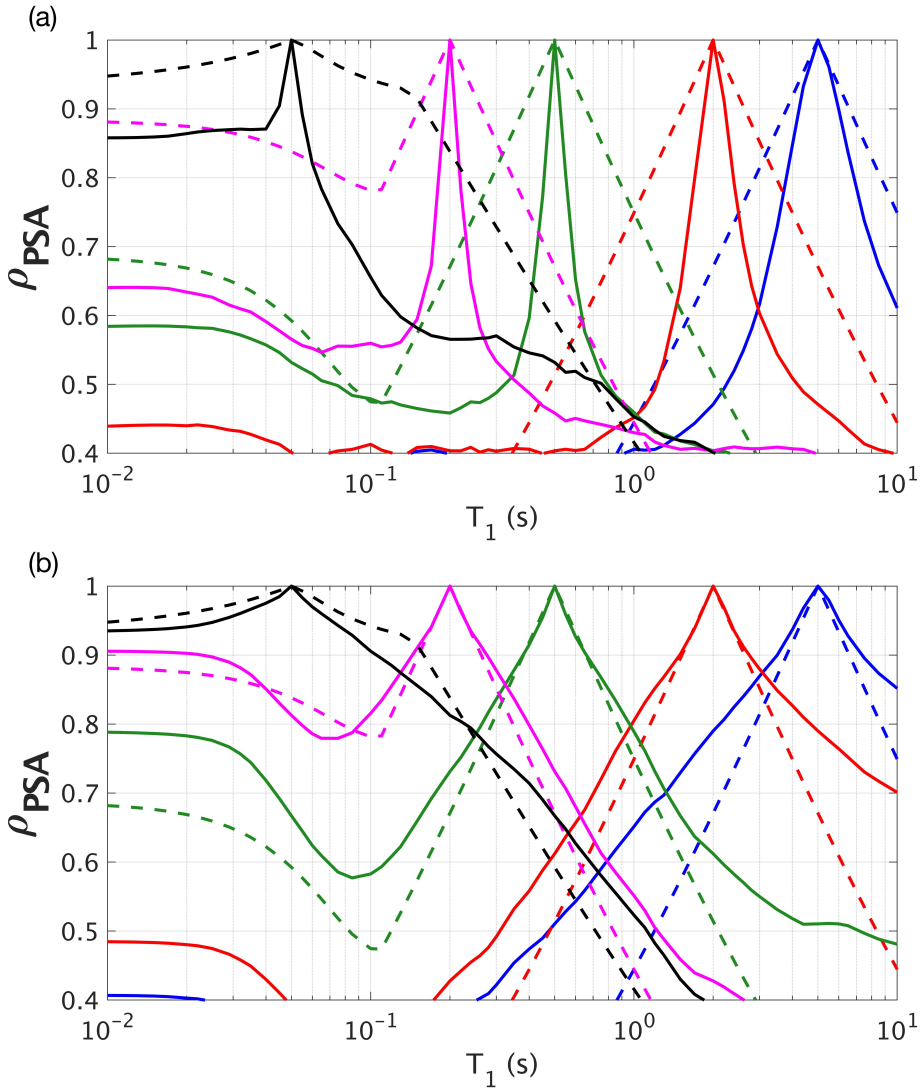

Figure 5-11. Comparison of within-event ρ_ϵ of PSA, (a) for unmodified EXSIM, and (b) for EXSIM with the post-processing ρ_ϵ procedure. Both plots show cross-sections of ρ_ϵ versus period at conditioning periods 0.05, 0.2, 0.5, 2, and 5 sec calculated from the simulations (solid lines), compared with the Baker and Jayaram (2008) model (dashed lines).

Conclusions and Recommendations for Future Work

The correlation incorporated into the Fourier amplitude spectra of each EXSIM sub-source results in lower than desired ρ_ϵ, meaning there is destructive interference of the correlation between sub-sources. EXSIM has been calibrated using no correlation between frequencies, and in order to incorporate the correlation on a sub-source level, these calibrations will need to change.

The ρ_ϵ can be calibrated as a post-processing modification, which is not preferable, but achieves the short-term goal of being be able to prescribe the total correlation of the full waveform seen in the data for other applications, e.g. structural risk. This method has been implemented and tested on the SCEC Broadband Platform. In the long term, preferable approach is to incorporate the correlation into seismological models (EXSIM, as well as others) through the foundational elements (source, path, site) so that the models most closely represent the earthquake process.

Chapter 6:

Summary and Recommendations

This dissertation makes progress towards improving the time series from ground-motion simulations in terms of adequately capturing the key features of empirical ground motions. Specifically, the dissertation addresses the inter-frequency correlation in the Fourier Spectra. The purpose of this research is three-fold: (1) to illustrate that the inter-period correlation in ground-motion simulations is a critical feature that affects the variability of the nonlinear structural response that should be included as a key validation parameter, (2) to develop an avenue for improving the correlation in the simulations, and (3) to provide an example application.

To achieve these goals, the research consists of four major components: (1) development of a ground motion model for smoothed Fourier amplitude spectra, (2) development of a ground motion model for the inter-frequency correlation of epsilon for smoothed Fourier amplitude spectra, (3) demonstration of the importance of the inter-frequency correlation in simulations for capturing the variability of structural response, and an assessment of the correlations in existing simulation methods, and (4) implementation of the correlation into the simulation method EXSIM.

This chapter summarizes each previous chapter, reviews the principal conclusions, and provides recommendations for future work.

Chapter 2

In this chapter, an empirical ground-motion model (GMM) is developed for shallow crustal earthquakes in California and Nevada based on the NGA-West2 database (Ancheta et al., 2014). Rather than the traditional response spectrum GMM, this model is developed for the smoothed effective amplitude spectrum (EAS), as defined by PEER (Goulet et al., 2018). The EAS is the

orientation-independent horizontal component Fourier amplitude spectrum (FAS) of ground acceleration. The model is developed using a database dominated by California earthquakes, but takes advantage of crustal earthquake data worldwide to constrain the magnitude scaling and geometric spreading. The near-fault saturation is guided by finite-fault numerical simulations and non-linear site amplification is incorporated using a modified version of Hashash et al., (2018). The model is applicable for rupture distances of 0 – 300 km, $\boldsymbol{M}$ 3.0 – 8.0, and over the frequency range 0.1 – 100 Hz. The model is considered applicable for V_{s30} in the range 180 – 1500 m/s, although it is not well constrained for V_{s30} values greater than 1000 m/s. Models for the median and the aleatory variability of the EAS are developed.

Recommendations for future work include:

1. Developing regionalized models for Japan and Taiwan to account for the known differences in regional crustal structure. The linear V_{s30} scaling (c_8), soil depth scaling (c_{11}), anelastic attenuation (c_7) and spectral shape (c_1) coefficients can all be regionalized.

2. Improving the scaling of the EAS at high frequencies. Improvements to the model may include explicit data regression to frequencies greater than 24 Hz, developing a region-specific $\kappa - V_{s30}$ relationship, or calculating one directly from the database used.

3. Adding hanging-wall effects to the model. The hanging-wall effect, characterized by increased ground motion amplitudes on the hanging-wall side of dipping ruptures, is not well constrained by the data. For NGA-West2, Donahue and Abrahamson (2013) investigated these effects for response spectra using finite-fault simulations, and the results

were incorporated in the Abrahamson et al., (2014) model. The EAS of the Donahue and Abrahamson (2013) simulations could be utilized to develop analytical constraints on the hanging-wall scaling for EAS.

4. Adding directivity effects to the model. Similarly, directivity effects are well-known but are not well constrained by the data and have been proven to be difficult to model. Using finite fault simulations to supplement the empirical data for modeling directivity effects in coordination with the EAS model is a future opportunity.

5. Adding nonlinear site effects into the standard deviation. The EAS GMM standard deviation model is linear, meaning it does not account for the effects of nonlinear site response. An improved formulation would involve estimating the standard deviation of the rock motion by removing the site amplification variability (which needs to be determined analytically) from the surface motion and computing the variability of the soil motion using numerical simulations, such as Hashhash et al. (2018) with propagation of errors.

Chapter 3

In this chapter, an empirical GMM for the inter-frequency correlation of epsilon (ρ_ϵ) for smoothed EAS is presented. Residuals from the GMM developed in Chapter 2 are partitioned into between-event, between-site, and within-site components, and a model is developed for the total correlation between frequencies. The total correlation model features a two-term exponential decay with the natural logarithm of frequency. At higher frequencies, the model differs substantially from previously published models, where the ground-motion smoothing technique used has a large

effect on the resulting correlations. The empirical ρ_ϵ are not found to have statistically significant magnitude, distance, site parameter, or regional dependence. The model is applicable for crustal earthquakes in active tectonic regions worldwide, for rupture distances of 0 – 300 km, $\boldsymbol{M}$ 3.0 – 8.0, and over the frequency range 0.1 – 24 Hz. This correlation model can be used to define the inter-frequency correlation in stochastic ground-motion simulation methods. It is also appropriate for use in validation studies of the inter-frequency correlations from physics-based numerical simulations for ground motions. To be consistent with the empirical EAS data, the standard EAS approach for smoothing the FAS needs to be used for the simulations.

Recommendations for future work include:

1. Developing models for the individual components of the inter-frequency correlation. Although a model for the total correlation is most practical, models for the individual correlation components may also be useful for improving ground motion simulations.
2. Evaluating the inter-frequency correlation for possible regional differences. The conclusions about the regional variations of the correlation were not strong, primarily because data outside the US is relatively limited, and because the GMM for non-CA regions was still under development at the time of writing. In a future update, regional variations in ρ_ϵ can be studied using more data and a polished non-CA region EAS GMM.

Chapter 4

In this chapter, two goals are achieved. First, ρ_ϵ is demonstrated to be an essential component of ground motions for capturing the variability of structural response that is needed in seismic

fragility and seismic risk studies. Namely, the effect of ρ_ϵ propagates through the structural response and into to seismic risk calculations. Without the adequate inter-period correlation of ground motions, variability in the structural response may be under-estimated. This leads to structural fragilities which are too steep (under-estimated dispersion parameter β) and propagates through to non-conservative estimates of seismic risk.

Second, multiple existing ground-motion simulation methods are evaluated by comparing their inter-frequency correlations with empirical models. None of the six finite-fault simulation methods tested adequately capture the inter-period correlations over the entire frequency range evaluated, although several of the methods show promise, especially at low frequencies. Using the correlation of the Fourier spectra provides better feedback in terms of how to modify simulation methods than when using response spectra comparisons because Fourier spectra are more closely related to the physics in the simulations.

Recommendations for future work include:

1. Further evaluating the causal features of the correlation in the deterministic (low-frequency) portion of the simulations. Sensitivity studies on the rupture characterization should be among the first tests, including the rupture initiation timing perturbations, spatial correlation of slip, slip-rate functions and rise time perturbations. Tests can also be performed using asperity-based source models.

2. Evaluating other 3D simulation methods, including SCEC CyberShake simulations.

3. Further evaluating the Rodgers et al., (2018) simulations, including multiple realizations

of the source, and potentially other scenarios, to distinguish the between-event and between-site correlation components.

Chapter 5

In this chapter, approaches are developed to incorporate the observed ρ_ϵ into the finite-fault simulation algorithm EXSIM (Atkinson and Assatourians, 2015). The correlation is incorporated into the Fourier amplitude spectra of each EXSIM sub-source, but this results in lower than desired ρ_ϵ, meaning there is destructive interference of the correlation between sub-sources. EXSIM has been calibrated using no correlation between frequencies, and to incorporate the correlation on a sub-source level, these previous calibrations of parameters will need to be updated. As an alternative, the ρ_ϵ can be added to the simulations as a post-processing modification. This approach is not preferable but achieves the short-term goal of being be able to prescribe the correlation of the full waveform seen in the data for other applications, e.g. structural risk. This method is implemented successfully on the SCEC Broadband Platform.

In the long term, the preferable approach is to incorporate the correlation into seismological models (EXSIM, as well as others) through the foundational elements (source, path, site) so that the models most closely represent the earthquake process.

Recommended future research topics include:

1. Calibrating the EXSIM sub-source implementation to match the observed ρ_ϵ.

2. Calibrating ρ_ϵ of other BBP finite-fault simulation methods.

3. Upon successful calibration of ρ_ϵ, performing validations of the simulation methods (median and standard deviation of response spectra) to confirm that the calibration does not introduce adverse effects into other features of the simulated time series.

References

Abrahamson, N.A., and Silva, W.J. (1997). Empirical response spectral attenuation relations for shallow crustal earthquakes, Seismol. Res. Lett., 68(1): 94–127.

Abrahamson, N.A., and Youngs, R.R. (1992). A stable algorithm for regression analyses using the random effects model, Bull. Seismol. Soc. Am., 82: 505-510.

Abrahamson, N.A., Atkinson, G., Boore, D., Bozorgnia, Y., Campbell, K., Chiou, B., Idriss, I.M., Silva, W., and Youngs, R. (2008). Comparisons of the NGA Ground-Motion Relations. *Earthquake Spectra*, 24: 45-66.

Abrahamson NA, Silva WJ, Kamai R. (2014). Summary of the ASK14 Ground Motion Relation for Active Crustal Regions. *Earthquake Spectra*, 3**0**:1025-1055.

Abrahamson, N. A., and Hollenback, J. C., (2012). Application of single-site sigma ground motion prediction equations in practice, Paper No. 2536, in Proceedings, 15th World Conference on Earthquake Engineering, 24–28 September 2012, Lisbon, Portugal.

Abrahamson, N.A. (2017). Recent Advances in Seismic Hazard. Presentation given at the Pacific Rim Forum, Jan 23-23, 2017.

Aki, K. (1967), Scaling Law of Seismic Spectrum, J. Geophys. Res. 72, 1217–1231.

Akkar S, Sandıkkaya MA, Ay BÖ (2014) Compatible ground-motion prediction equations for damping scaling factors and vertical-to-horizontal spectral amplitude ratios for the broader Europe region. Bull Earthq Eng 12:517–547. doi: 10.1007/s10518-013-9537-1

Al Atik L, Abrahamson NA, Cotton F, Scherbaum F, Bommer JJ, Kuehn N. (2010) The variability of ground-motion prediction models and its components. *Seismological Research Letters,* **81(5)**:794-801.

Al Atik, L. (2011). Correlation of spectral acceleration values for subduction and crustal models, in COSMOS Technical Session, Emeryville, California, 13 pp.

Al Atik, L., and Abrahamson, N. A., (2010). Nonlinear site response effects on the standard deviations of predicted ground motions, Bull. Seismol. Soc. Am. 100, 1288–1292.

Ancheta, T. D., Darragh, R. B., Stewart, J. P., Seyhan, E., Silva,W. J., Chiou, B. S.-J., Wooddell, K. E., Graves, R. W., Kottke, A. R., Boore, D. M., Kishida, T., and Donahue, J. L., (2014). NGA-West2 database, Earthquake Spectra 30, 989–1005.

Anderson, J. G (2015) The Composite Source Model for Broadband Simulations of Strong Ground Motions Seismological Research Letters, January/February 2015, v. 86, p. 68-74, First published on December 17, 2014, doi:10.1785/0220140098

Anderson, J. G., and J. N. Brune (1999). Probabilistic seismic hazard assessment without the ergodic assumption. Seismological Research Letters 70 (1), 19–28.

Anderson, J.G. and Hough, S.E. (1984) A Model for the Shape of the Fourier Amplitude Spectrum of Acceleration at High Frequencies, Bull. Seismol. Soc. Am. 74, 1969–1993.

ASCE. (2016). Minimum Design Loads for Buildings and Other Structures. ASCE/SEI Standard 7-16.

Atkinson, G. M., and Assatourians, K. (2015) Implementation and Validation of EXSIM (A Stochastic Finite-Fault Ground-Motion Simulation Algorithm) on the SCEC Broadband Platform Seismological Research Letters, January/February

Azarbakht A, Mousavi M, Nourizadeh M, Shahri M. Dependence of correlations between spectral accelerations at multiple periods on magnitude and distance. *Earthq Eng Struct Dyn* 2014; **43**:1193–1204.

Baker J.W., and Cornell C.A. (2006). Correlation of Response Spectral Values for Multi-Component Ground Motions, *Bulletin of the Seismological Society of America*, **96 (1),** 215-227.

Baker J.W., and Jayaram N. (2008) Correlation of spectral acceleration values from NGA ground motion models. *Earthq Spectra* 2008; **24**:299–317. doi: 10.1193/1.2857544

Baker, J.W., and Bradley, B.A. (2017). Intensity measure correlations observed in the NGA-West2 database, and dependence of correlations on rupture and site parameters. Earthquake Spectra, 33(1), 145–156.

Baker, JW. Trade-offs in ground motion selection techniques for collapse assessment of structures. Vienna Congress on Recent Advances in Earthquake Engineering and Structural Dynamics. Vienna, Austria. 2013.

Bayless J, and Abrahamson N.A. (2018a, in review) An empirical model for Fourier amplitude spectra using the NGA-West2 database.

Bayless J, and Abrahamson N.A. (2018b, in review). An empirical model for the inter-frequency correlation of epsilon for Fourier amplitude spectra.

Bayless J., and Abrahamson N.A. (2018c, in press). Evaluation of the inter-period correlation of ground motion simulations. Bull. Seismol. Soc. Am.

Bjelic, N., Lin, T., and Deierlein, G. (2018). Validation of the SCEC Broadband Platform simulations for tall building risk assessments considering spectral shape and duration of the ground motion. *Earthquake Engineering Structural Dynamics*, 47(11), 2233-2251.

Boore D.M. and Thompson EM. (2012). Empirical improvements for estimating earthquake response spectra with random-vibration theory, *Bull. Seismol. Soc. Am*; **102(2)**, 761-772

Boore D.M. (1983). Stochastic simulation of high-frequency ground motions based on seismological models of the radiated spectra, *Bull. Seismol. Soc. Am*; **73**, 1865–1894.

Boore, D.M. (2003). Simulation of ground motion using the stochastic method, *P&A Geophysics.* 160, 635-675.

Boore, D.M. (2005). SMSIM-Fortran Programs for Simulating Ground Motions from Earthquakes: Version 2.3—A Revision of OFR 96-80-A, U. S. Geol. Surv. Open-File Rept. 00-509, revised 15 August 2005, 55 pp.

Boore, D.M. (2016). Determining Generic Velocity and Density Models for Crustal Amplification Calculations, with an Update of the Boore and Joyner (1997) Generic Site Amplification for VS(Z)=760 m/s, Bull. Seismol. Soc. Am. 106, 316-320.

Boore, D.M. and E.M. Thompson (2014). Path durations for use in the stochastic-method simulation of ground motions, Bull. Seismol. Soc. Am. 104, 2541-2552.

Boore, D.M., C. Di Alessandro, and N.A. Abrahamson (2014). A generalization of the double-corner-frequency source spectral model and its use in the SCEC BBP Validation Exercise, Bull. Seismol. Soc. Am. 104, 2387-2398.

Boore, D.M. and E.M. Thompson (2015). Revisions to some parameters used in stochastic-method simulations of ground motion, Bull. Seismol. Soc. Am. 105, 1029-1041.

Bora, S.S., Scherbaum, F., Kuehn, N., Stafford, P. (2014): Fourier spectral- and duration models for the generation of response spectra adjustable to different source-, propagation-, and site conditions. *Bulletin of Earthquake Engineering*, 12, pp. 467—493

Bora, S.S., F. Scherbaum, N. Kuehn, P.J. Stafford, and B. Edwards (2015). Development of a response spectral ground-motion prediction equation (GMPE) for seismic hazard analysis from empirical Fourier spectral and duration models, Bull. Seismol. Soc. Am. 105, no. 4, 2192–2218.

Bora, S.S., F. Scherbaum, N. Kuehn, and P.J. Stafford (2016). On the relationship between Fourier and response spectra: Implications for the adjustment of empirical ground-motion prediction equations (GMPEs), Bull. Seismol. Soc. Am. 3, doi: 10.1785/0120150129.

Bora, S.S., Cotton, F., and Scherbaum, F. (2018, in press). NGA-West2 E,pirical Fourier and Duration Models to Generate Adjustable Response Spectra, *Earthquake Spectra*

Bradford SC. (2007). *Time-frequency analysis of systems with changing dynamic properties.* Dissertation (Ph.D.), California Institute of Technology.

Bradley B.A. (2011) Empirical correlation of PGA, spectral accelerations and spectrum intensities from active shallow crustal earthquakes. Earthq Eng Struct Dyn 40:1707–1721. doi: 10.1002/eqe.1110

Brune JN. (1970). Tectonic stress and spectra of seismic shear waves from earthquakes, *J. Geophys. Res*. **75**, 4997–5009.

Burks, L.S., and Baker, J.W. (2014). Validation of ground motion simulations through simple proxies for the response of engineered systems. *Bulletin of the Seismological Society of America*, 104(4) 1930-1946.

Burks, L.S. (2014). *Ground motion simulations : validation and application for civil engineering problems.* Thesis (PhD), Stanford University, Department of Civil and Environmental Engineering.

Carlton, B., and Abrahamson, N.A. (2014). Issues and Approaches for Implementing Conditional Mean Spectra in Practice. Bulletin of the Seismological Society of America ; 104 (1): 503–512. doi: https://doi.org/10.1785/0120130129

Chiou, B. S.-J., R. B. Darragh, N. Gregor, and W. J. Silva (2008). NGA project strong-motion database, Earthq. Spectra 24, no. 1, 23–44.

Chiou, B.S.-J., and Youngs, R. R., (2014). Update of the Chiou and Youngs NGA model for the average horizontal component of peak ground motion and response spectra, Earthquake Spectra 30, 1117–1153.

Chiou, B.S.-J., Youngs R.R. (2008). An NGA model for the average horizontal component of peak ground motion and response spectra, Earthq. Spectra, 24: 173–216.

Chopra, A.K. (2007) Dynamics of Structures, Theory and Applications to Earthquake Engineering. Higher Education Press, Beijing.

Cimellaro GP. (2013). Correlation in spectral accelerations for earthquakes in Europe. *Earthq Eng Struct Dyn*, **42**:623–633. doi: 10.1002/eqe.2248

Crempien, J. G. F., and Archuleta, R. J. (2015) UCSB Method for Simulation of Broadband Ground Motion from Kinematic Earthquake Sources Seismological Research Letters, January/February 2015, v. 86, p. 61-67, First published on December 17, 2014, doi:10.1785/0220140103

Donahue J.L., Abrahamson N.A. (2013). Hanging wall scaling using finite-fault simulations, PEER Report 2013/14, Pacific Earthquake Engineering Research Center, University of California, Berkeley, CA.

Douglas, J. (2018), Ground motion prediction equations 1964-2018, http://www.gmpe.org.uk.

Douglas, J. and D. M. Boore (2011). High-frequency filtering of strong-motion records, Bull. Earthquake Engineering 9 395-409.

Dreger, D. S., Beroza, G.C., Day, S. M., Goulet, C. A., Jordan, T. H., Spudich, P. A., and Stewart, J. P. (2015). Validation of the SCEC Broadband Platform V14.3 Simulation Methods Using Pseudospectral Acceleration Data, Seismol. Res. Lett., 86, no. 1, doi:10.1785/0220140118.

Dreger, D. S., Jordan, T. H. (2014). Introduction to the Focus Section on Validation of the SCEC Broadband Platform V14.3 Simulation Methods. Seismological Research Letters ; 86 (1): 15–16. doi: https://doi.org/10.1785/0220140233

Fisher, R.A. (1958). *Statistical Methods for Research Workers*, 13th Ed., Hafner.

Goda K, Atkinson GM. (2009). Probabilistic Characterization of Spatially Correlated Response Spectra for Earthquakes in Japan. *Bull Seismol Soc Am*; **99:**3003–3020. doi: 10.1785/0120090007

Goulet, C.A., Abrahamson, N.A., Somerville, P.G. and K, E. Wooddell (2015) The SCEC Broadband Platform Validation Exercise: Methodology for Code Validation in the Context of Seismic-Hazard Analyses, Seismol. Res. Lett., 86, no. 1, doi: 10.1785/0220140104

Goulet, C.A., Kottke, A., Hollenback, J., Kuehn, N., Kishida, T., Boore, D.M., Abrahamson, N.A., Bozorgnia, Y., Der Kiureghian, A., Ktenidou, O-J., Rathje, E.M., Silva, W.J., Thompson, E.M., Wang, X. (2018). Effective Amplitude Spectrum and Smoothing Optimization for the Development of Ground Motion Models Based on Fourier Amplitudes, Earthquake Spectra, in preparation.

Graizer, V. (2018). GK17 Ground-Motion Prediction Equation for Horizontal PGA and 5% Damped PSA from Shallow Crustal Continental Earthquakes. Bull. Seismol. Soc. Am. 108. No 1, pp 380-398. doi: 10.1785/0120170158.

Graves, R., Jordan, T.H., Callaghan, S., Deelman, E., Field, E., Juve, G., Kesselman, C., Maechling, P., Mehta, G., Milner, K., Okaya, D., Small, P., and Vahi, K. (2011). CyberShake: A Physics-Based Seismic Hazard Model for Southern California. Pure Appl. Geophys. 168: 367. https://doi.org/10.1007/s00024-010-0161-6

Graves, R., and Pitarka, A. (2015) Refinements to the Graves and Pitarka (2010) Broadband Ground-Motion Simulation Method Seismological Research Letters, January/February 2015, v. 86, p. 75-80, First published on December 17, 2014, doi:10.1785/0220140101

Gupta, D., and Trifunac, M.D. (2017). Scaling of Fourier spectra of strong earthquake ground motion in western Himalaya and northeastern India. Soil Dynamics and Earthquake Engineering, 102:137-159.

Hanks TC, and McGuire RK. (1981) The character of high-frequency strong ground motion, *Bull. Seismol. Soc. Am,* **71**, 2071–2095.

Hanks, T.C. (1982). fmax, Bull. Seismol. Soc. Am. 72, 1867–1879.

Hashash, Y.M.A., Harmon, J., Ilhan, O., Stewart, J.P., Rathje, E.M., Campbell, K.W., Silva, W.J., and Goulet, C.G. (2018, in press). Modelling of Site Amplification via Large Scale Nonlinear Simulations with applications to North America, paper presented to the Geotechnical Earthquake Engineering and Soil Dynamics Conference, 2018.

Heo YA. *Framework for Damage-Bassed Probabilistic Seismic Performance Evaluation of Reinforced Concrete Frames*. Dissertation (Ph.D.), UC Davis. 2009.

Irikura, K., and Miyake, H. (2011). Recipe for Predicting Strong Ground Motion from Crustal Earthquake Scenarios. *Pure and Applied Geophysics*, 168(2011), 85–104. doi: 10.1007/s00024-010-0150-9

Jayaram, N., J.W. Baker, H. Okano, H. Ishida, M.W. McCann Jr, Y. Mihara (2011). Correlation of response spectral values in Japanese ground motions. Earthquake and Structures 2 (4), 357-376

Kalkan E and Kunnath SK. (2006) Effects of Fling Step and Forward Directivity on Seismic Response of Buildings. *Earthquake Spectra*; **22**, No. 2, 367–390.

Kamai, R., Abrahamson, N. A., and Silva,W. J., (2014). Nonlinear horizontal site amplification for constraining the NGA-West2 GMPEs, Earthquake Spectra 30, 1223–1240.

Kenney, J.F. and Keeping, E.S. (1951). *Mathematics of Statistics, Pt. 2*, 2nd ed. Princeton, NJ: Van Nostrand, p. 123

Kishida, T., Ktenidou, O., Darragh, R.B., Silva, W.J. (2016). Semi-Automated Procedure for Windowing Time Series and Computing Fourier Amplitude Spectra for the NGA-West2 Database. PEER Report No. 2016/02, Pacific Earthquake Engineering Research Center, University of California, Berkeley, CA.

Konno, K. and Ohmachi, T., (1998). Ground-motion characteristics estimated from spectral ratio between horizontal and vertical components of microtremor, *Bull. Seismol. Soc. Am*. **88**: 228−241.

Kottke A., Rathje E., Boore D.M., Thompson E., Hollenback J., Kuehn N., Goulet C.A., Abrahamson N.A., Bozorgnia Y., Der Kiureghian A., Silva W.J., Wang X. (2018). Selection of random vibration procedures for the NGA East Project, PEER report #2018-05.

Ktenidou, O., Cotton, F., Abrahamson, N.A., Anderson, J.G. (2014). Taxonomy of kappa: A review of Definition and Estimation Approaches Targeted to Applications. *Seismol. Res. Lett*., 86, no. 1, doi: 10.1785/0220130027

Kuehn, N.M, and Scherbaum, F. (2016). A Partially Non-Ergodic Ground-Motion Prediction Equation for Europe and the Middle East. Bull Earthquake Eng. 14: 2629. https://doi.org/10.1007/s10518-016-9911-x

Kunnath SK, Erduran E, Chai YH, and Yashinsky M. (2008). Effect of Near-Fault Vertical Ground Motions on Seismic response of Highway Overcrossings. *J. Bridge Engineering*; **13(3)**, 282-290.

Kutner M, Nachtsheim C, Neter J, Li W. (2005). Applied Linear Statistical Models. McGraw-Hill/Irwin: New York, 1396.

Lee, V.W, Trifunac, M.D., Bulajic, B., and Manic, M. (2016). A preliminary empirical model for frequency-dependent attenuation of Fourier amplitude spectra in Serbia from the Vrancea earthquakes. Soil Dynamics and Earthquake Engineering, 83:167-179, Apr 2016.

Lin L, Naumoski N, Foo S, and Saatcioglu M. (2008). Elongation of the fundamental periods of reinforced concrete frame buildings during nonlinear seismic response, presented at the 14th World Conf Eqk Eng, Beijing.

Luco, N., Rezaeian, S., Goulet, C., Skarlatoudis, A., Bayless, J., Silva, F., and Maechling, P. (2016). Implementation of Ground Motion Simulation Validation (GMSV) Gauntlets on the Broadband Platform. Report for SCEC Award #15136, Submitted March 31, 2016.

Maechling, P. J., F. Silva, S. Callaghan, and T. H. Jordan (2015). SCEC Broadband Platform: System Architecture and Software Implementation, *Seismol. Res. Lett.*, 86, no. 1, doi: 10.1785/0220140125.

McKenna, F., Scott, M.H., and Fenves, G.L. (2010). "Nonlinear Finite Element Analysis Software Architecture Using Object Composition." Journal of Computing in Civil Engineering, 24(1):95-107.

Moehle JP, and Deierlein GG. (2004). A framework methodology for performance-based earthquake engineering. Paper presented at the 13th World Conference on Earthquake Engineering, Vancouver.

Olsen, K. B., and Takedatsu, R. (2015) The SDSU Broadband Ground-Motion Generation Module BBtoolbox Version 1.5. Seismological Research Letters, January/February 2015, v. 86, p. 81-88, First published on December 17, 2014, doi:10.1785/0220140102

PEER (2015) NGA-East: Median Ground-Motion Models for the Central and Eastern North America Region. PEER Report No. 2014/05, Pacific Earthquake Engineering Research Center, University of California, Berkeley, CA.

Rodgers, A.J., Pitarka, A., Petersson, N.A., Sjogree, B., and McCallen, D.B. (2018) Broadband (0-4 Hz) Ground Motions for a Magnitude 7.0 Hayward Fault Earthquake With Three-Dimensional Structure and Topography, *Geophysical Research Letters*, 45, 739-747. doi: 10.1002/2017GL076505

Seydel, R.U. (2012). *Tools for Computational Finance*, Universitext, Springer-Verlag London Limited

Smith, S.W. (1997). *The Scientist and Engineer's Guide to Digital Signal Processing*. First Edition. California Technical Publishing.

Song, S.G. (2016) Developing a generalized pseudo-dynamic source model of Mw 6.5-7.0 to simulate strong ground motions, *Geophysical Journal International*, 204, 1254-1265. doi: 10.1093/gji/ggv521

Stafford, P.J. (2017). Inter-frequency correlations among Fourier spectral ordinates and implications for stochastic ground-motion simulation, *Bulletin of the Seismological Society of America.* ISSN: 1943-3573

Taborda R., Roten D. (2015). Physics-Based Ground-Motion Simulation. In: Beer M., Kougioumtzoglou I., Patelli E., Au IK. (eds) Encyclopedia of Earthquake Engineering. Springer, Berlin, Heidelberg

Tothong, P., and C. A. Cornell (2006). An empirical ground-motion attenuation relation for inelastic spectral displacement, *Bull. Seismol. Soc. Am.* **96,** no. 6, 2146–2164.

Villani, M.A. and Abrahamson, N. (2015). Repeatable Site and Path Effects on the Ground-Motion Sigma Based on Empirical Data from Southern California and Simulated Waveforms from the CyberShake Platform. Bulletin of the Seismological Society of America. 105. 10.1785/0120140359.

Walling, M. A. (2009). Non-ergodic probabilistic seismic hazard analysis and spatial simulation of variation in ground motion. PhD diss., University of California, Berkeley.

Wang, F., and Jordan, T.H. (2014). Comparison of Probabilistic Seismic-Hazard Models Using Averaging-Based Factorization. *Bulletin of the Seismological Society of America*; 104 (3): 1230–1257. doi: https://doi.org/10.1785/0120130263

Yenier, E. and G.M. Atkinson (2015). An equivalent point-source model for stochastic simulation of earthquake ground motions in California, Bull. Seismol. Soc. Am. 105, no. 3, 1435–1455.

Appendix A:

EAS GMM Residual Figures

This appendix contains a set of residual figures from the EAS model developed in Chapter 2. Between-event, between-site, and within-site residuals are presented for the following frequencies: 0.1, 0.15, 0.2, 0.3, 0.5, 0.8, 1, 1.5, 2, 3, 5, 8, 10, 15, 20, and 24 Hz.

Between-event and Between-site Residuals

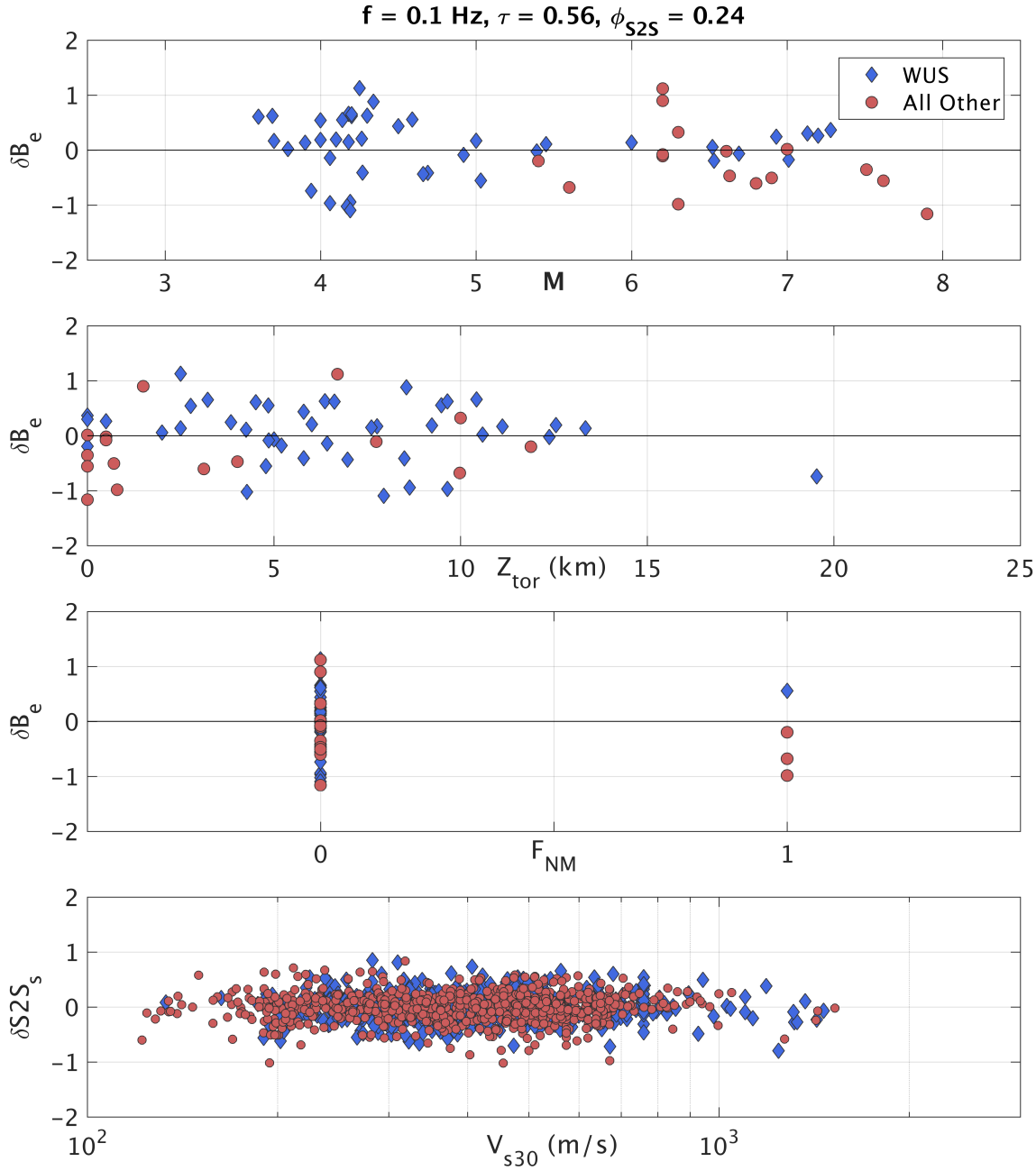

*Figure A-1. Between-event residuals (δB_e) versus **M**, Z_{tor}, and F_{NM} and between-site residuals ($\delta S2S_s$) versus V_{s30}, for $f = 0.1$ Hz.*

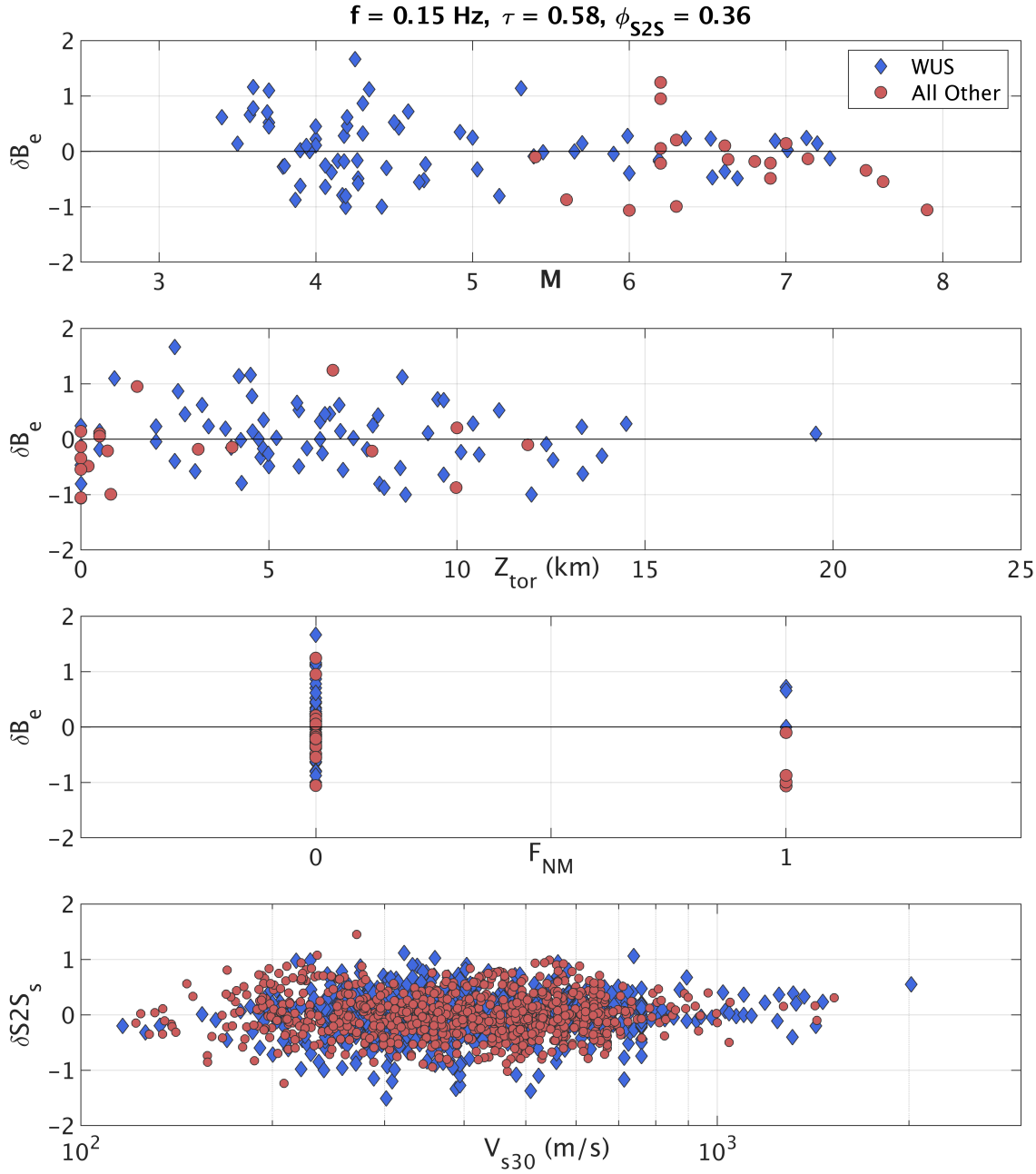

*Figure A-2. Between-event residuals (δB_e) versus **M**, Z_{tor}, and F_{NM} and between-site residuals ($\delta S2S_s$) versus V_{s30}, for $f = 0.15$ Hz.*

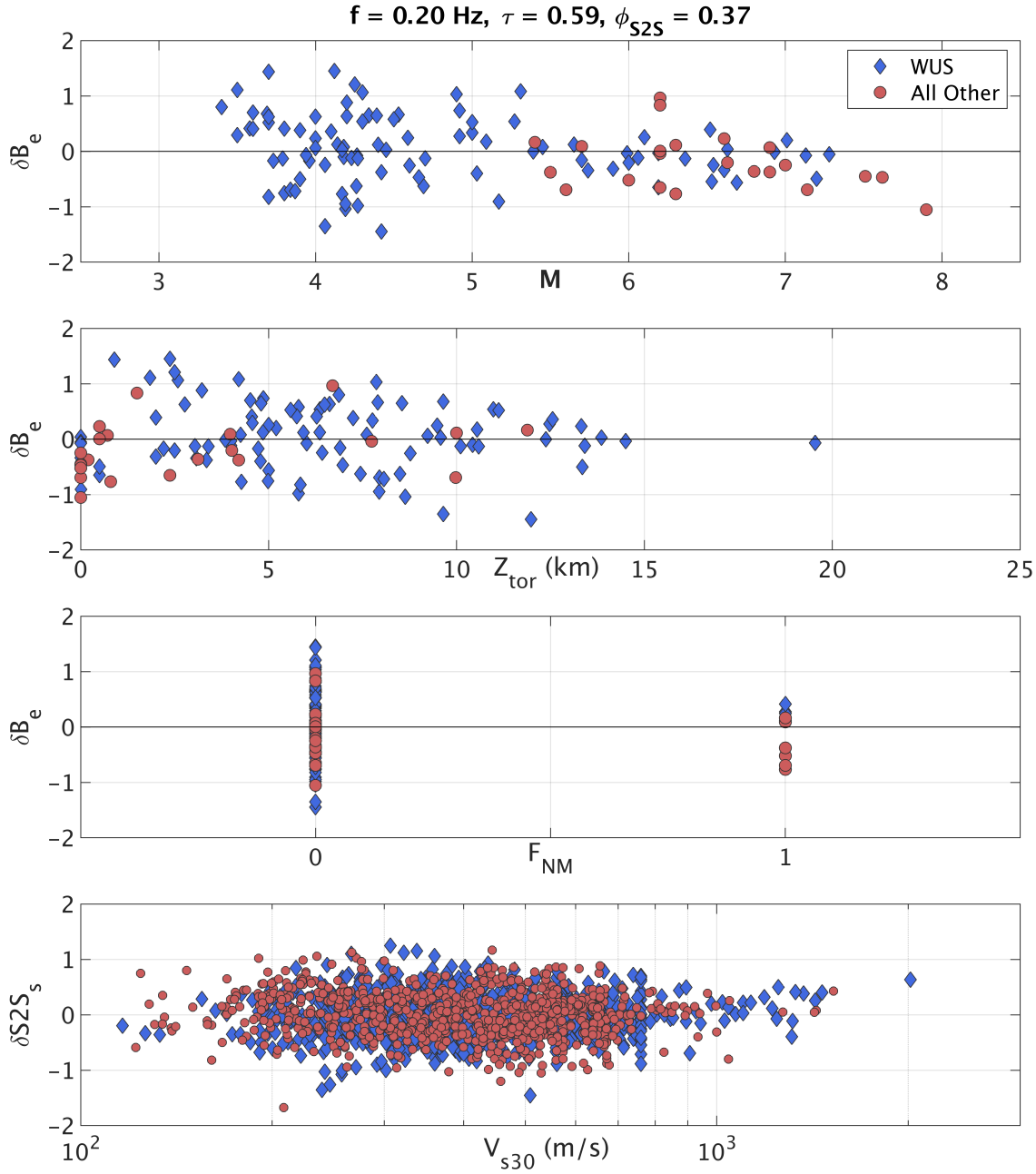

*Figure A-3. Between-event residuals (δB_e) versus **M**, Z_{tor}, and F_{NM} and between-site residuals ($\delta S2S_s$) versus V_{s30}, for $f = 0.2$ Hz.*

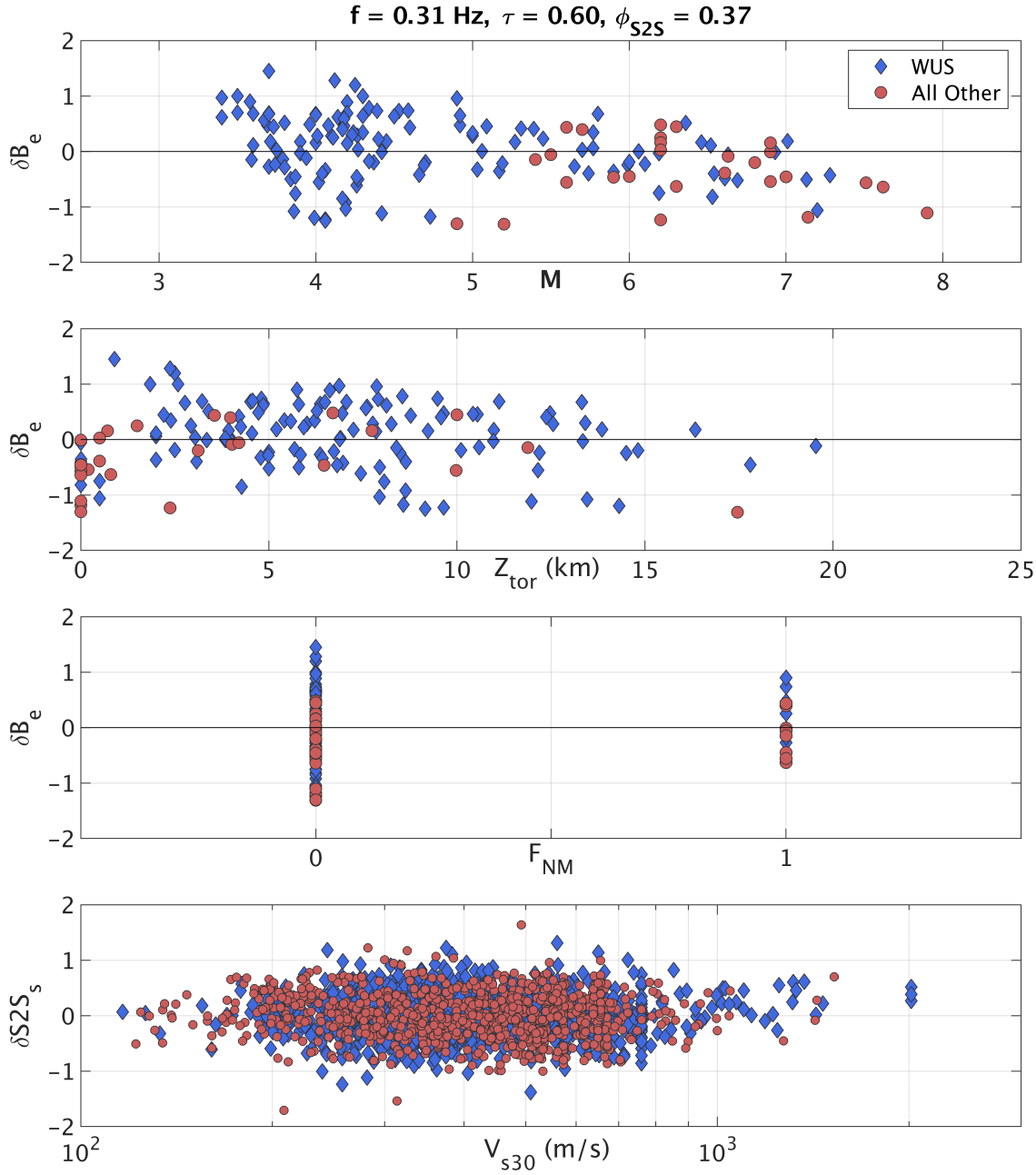

*Figure A-4. Between-event residuals (δB_e) versus **M**, Z_{tor}, and F_{NM} and between-site residuals ($\delta S2S_s$) versus V_{s30}, for $f = 0.3$ Hz.*

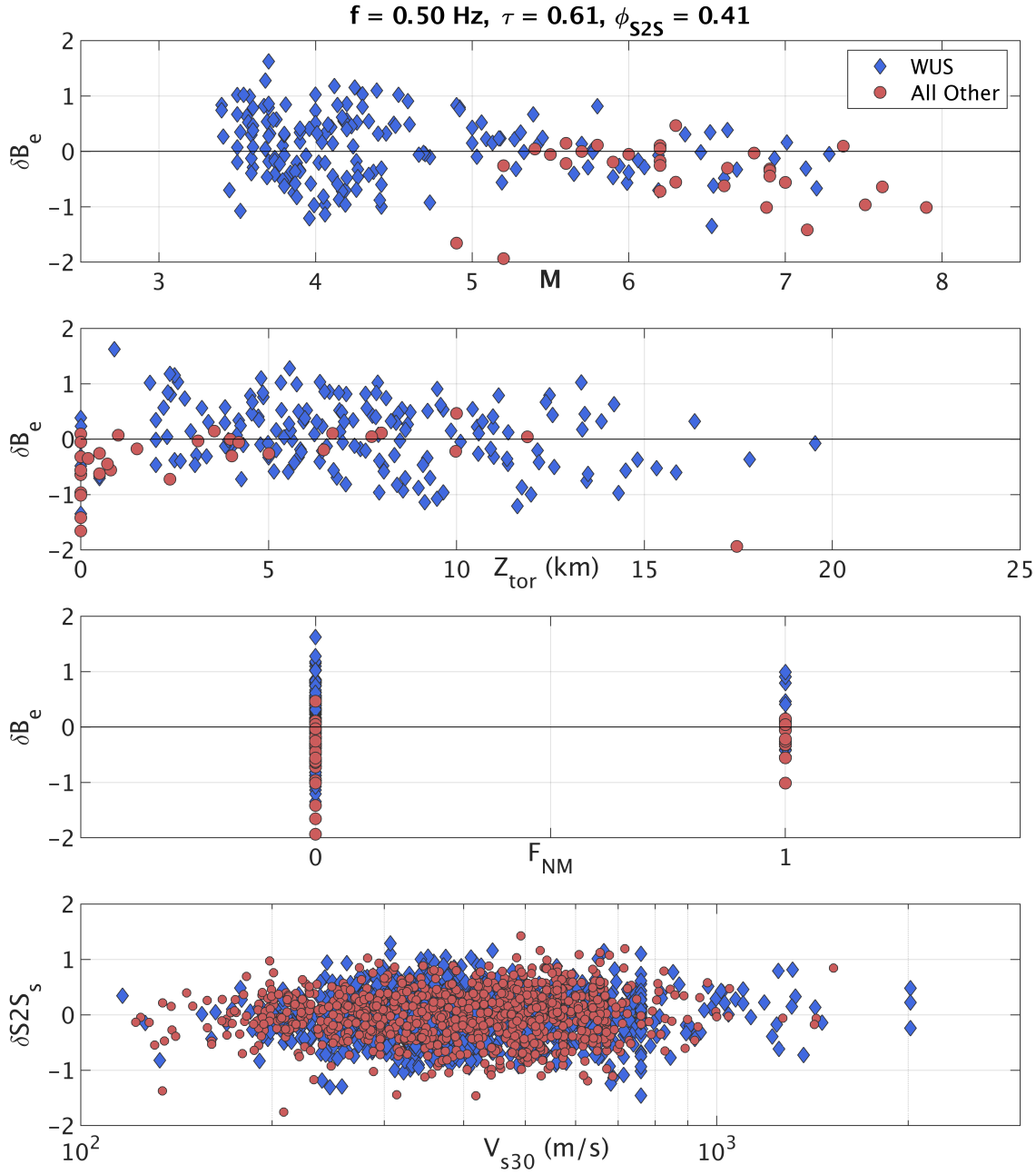

*Figure A-5. Between-event residuals (δB_e) versus **M**, Z_{tor}, and F_{NM} and between-site residuals ($\delta S2S_s$) versus V_{s30}, for $f = 0.5$ Hz.*

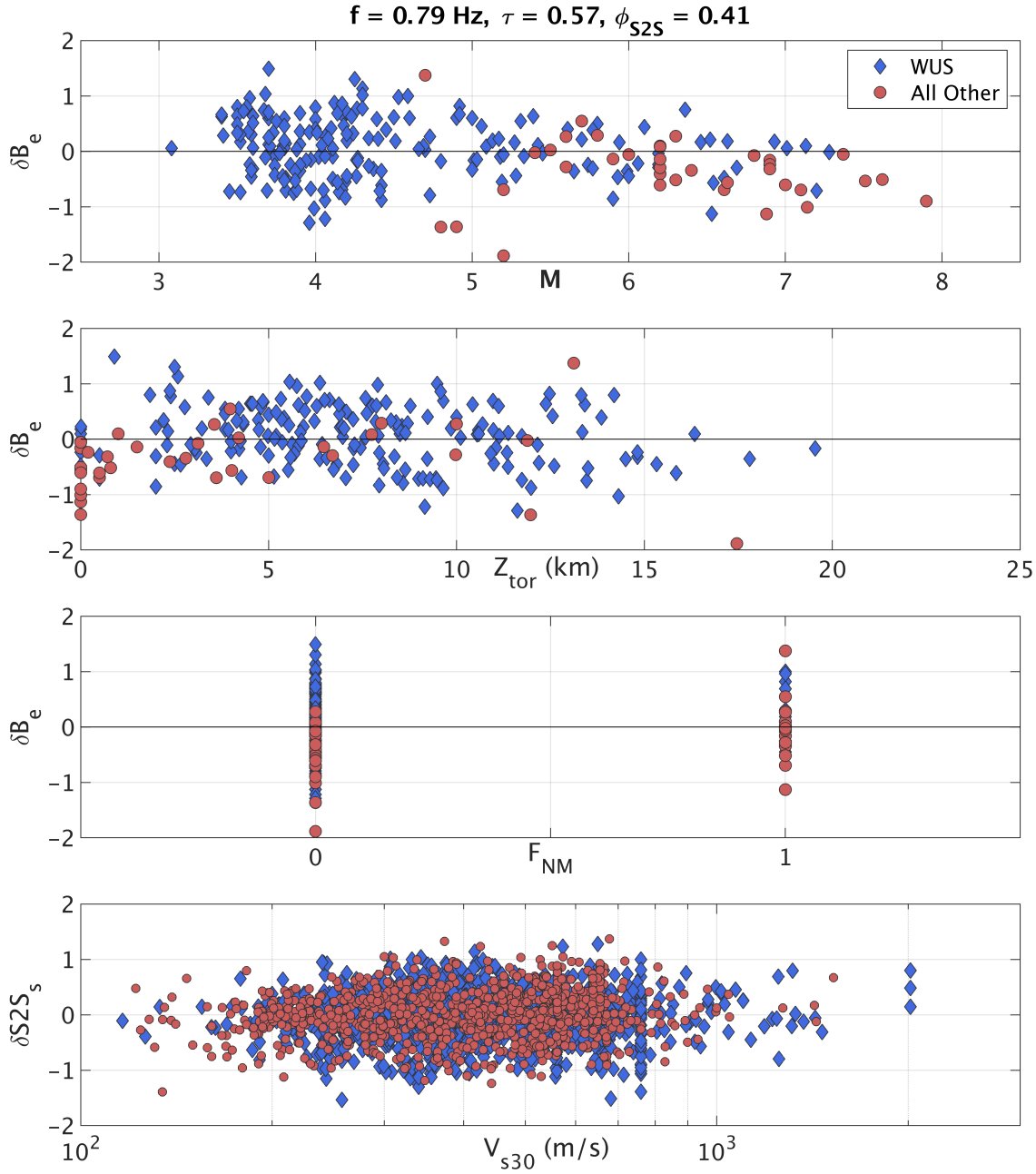

*Figure A-6. Between-event residuals (δB_e) versus **M**, Z_{tor}, and F_{NM} and between-site residuals ($\delta S2S_s$) versus V_{s30}, for $f = 0.8$ Hz.*

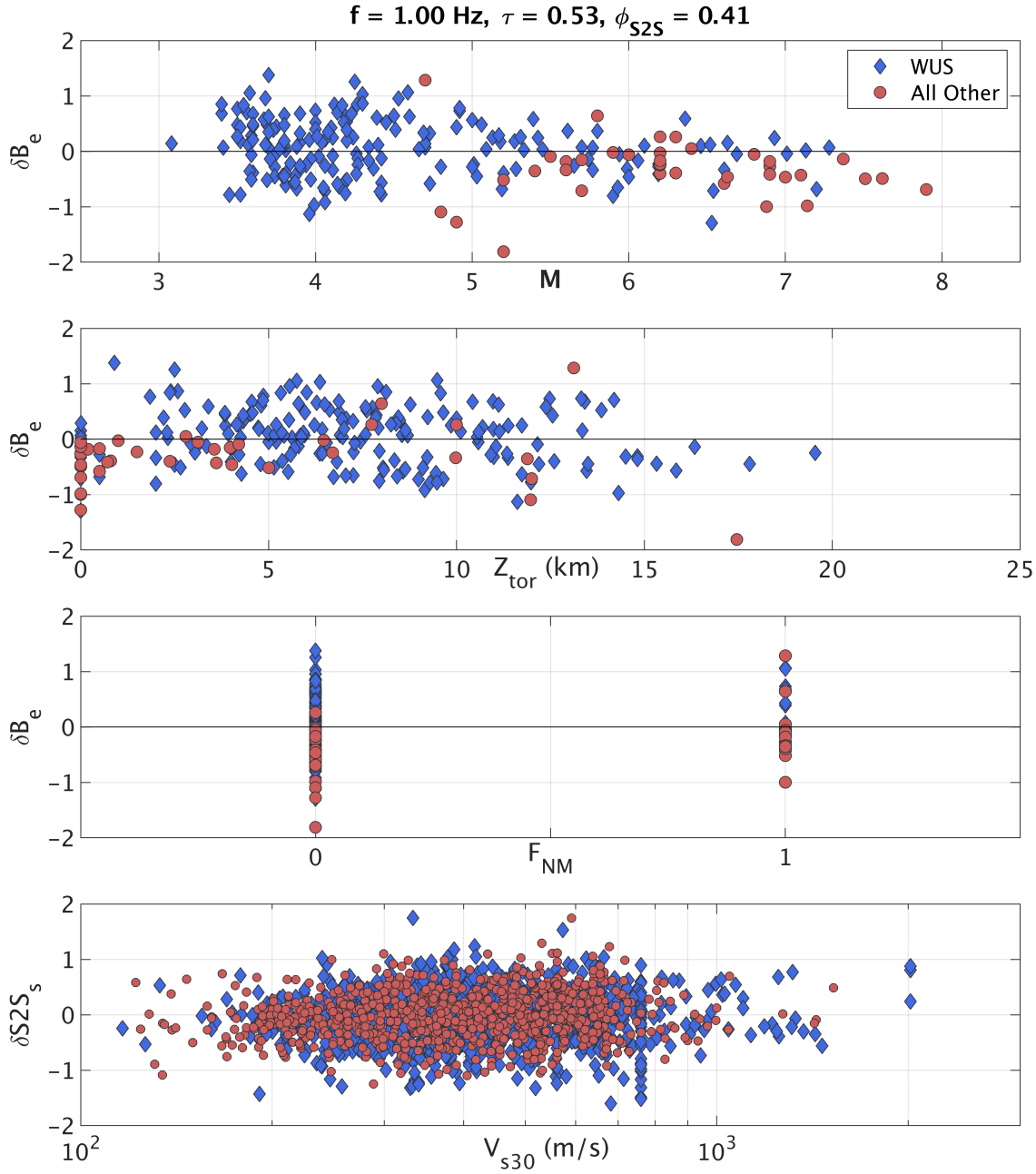

*Figure A-7. Between-event residuals (δB_e) versus **M**, Z_{tor}, and F_{NM} and between-site residuals ($\delta S2S_s$) versus V_{s30}, for $f = 1$ Hz.*

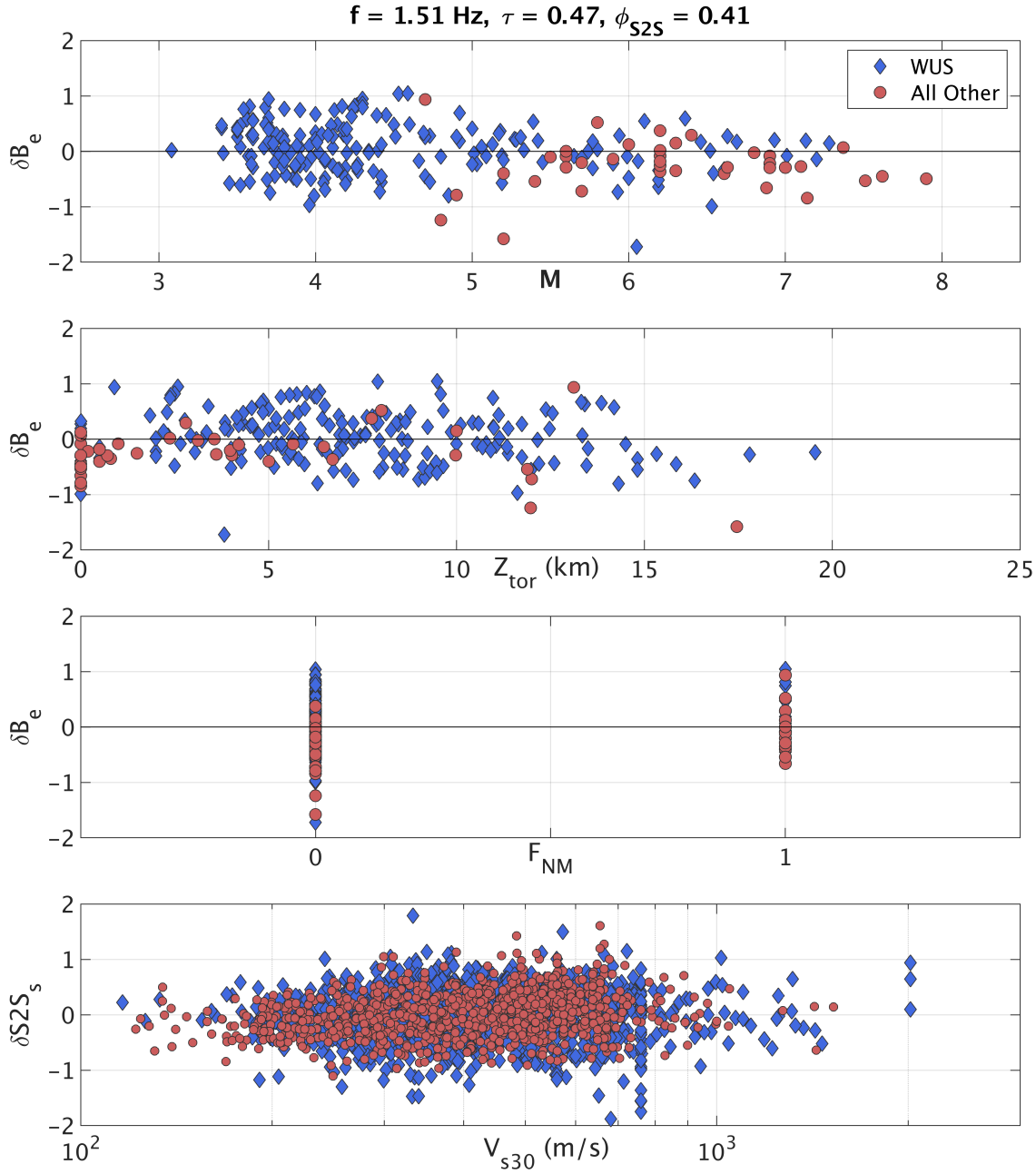

*Figure A-8. Between-event residuals (δB_e) versus **M**, Z_{tor}, and F_{NM} and between-site residuals ($\delta S2S_s$) versus V_{s30}, for $f = 1.5$ Hz.*

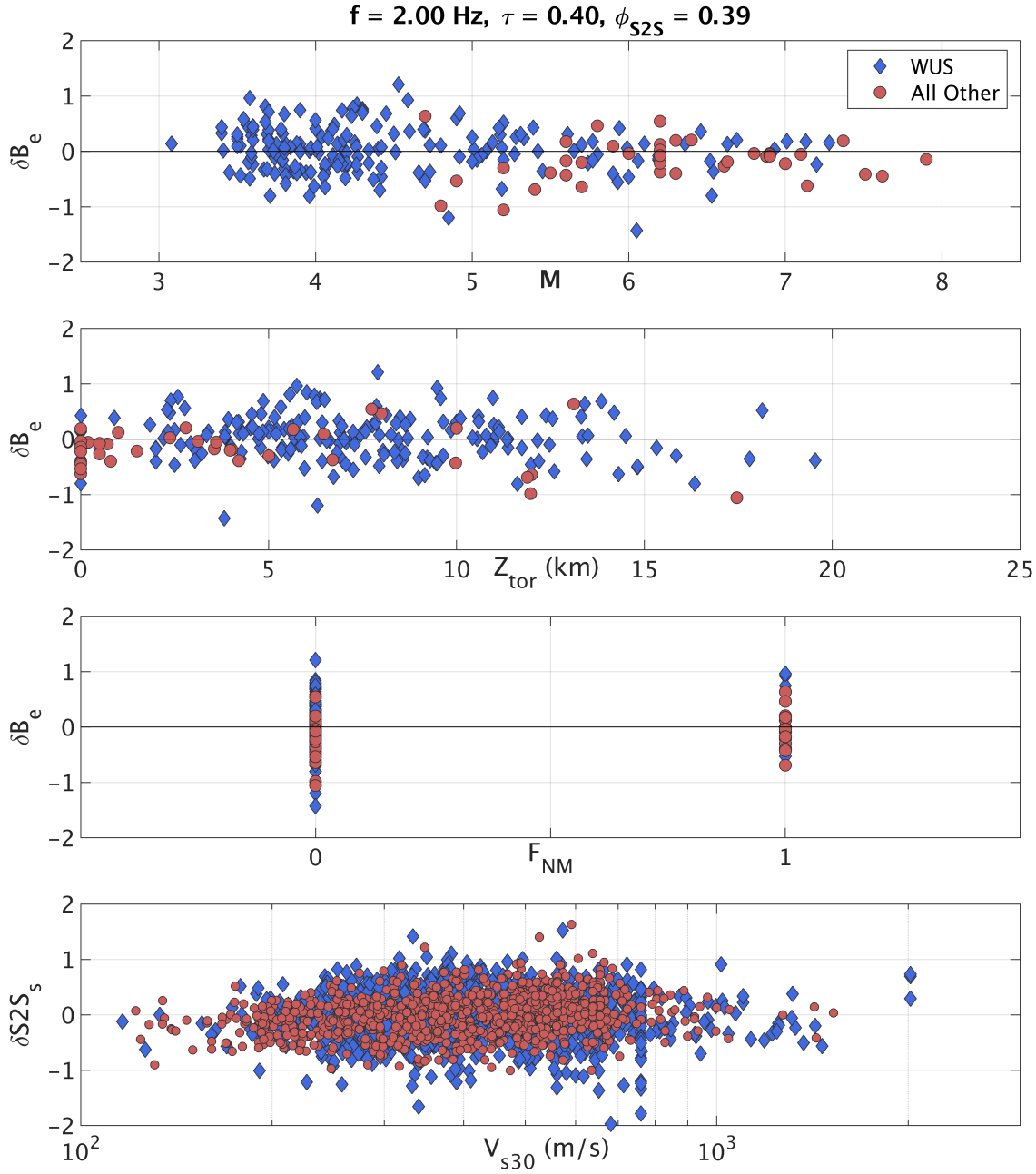

*Figure A-9. Between-event residuals (δB_e) versus **M**, Z_{tor}, and F_{NM} and between-site residuals ($\delta S2S_s$) versus V_{s30}, for $f = 2$ Hz.*

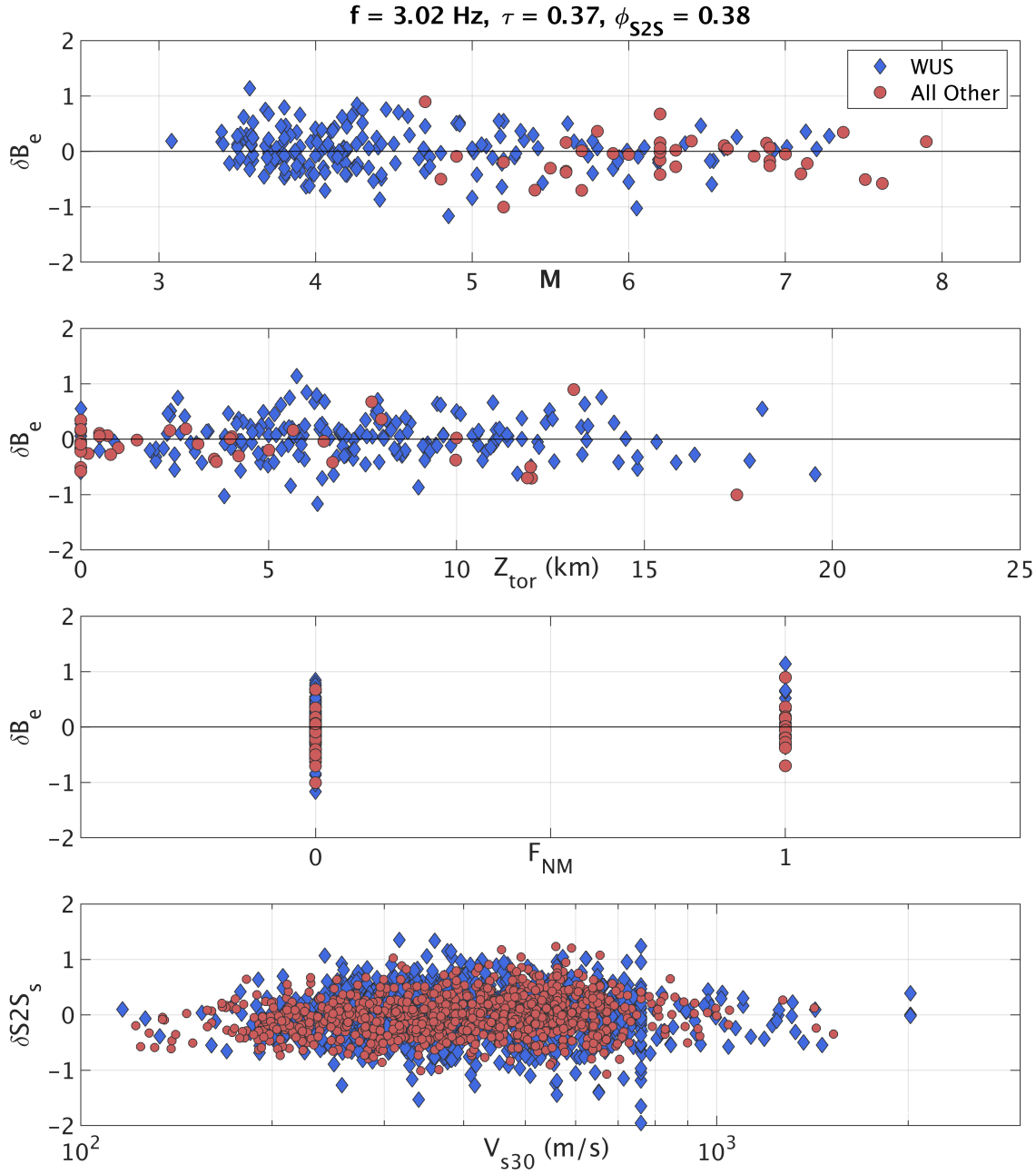

Figure A-10. Between-event residuals (δB_e) versus $\mathbf{M}$, Z_{tor}, and F_{NM} and between-site residuals ($\delta S2S_s$) versus V_{s30}, for $f = 3$ Hz.

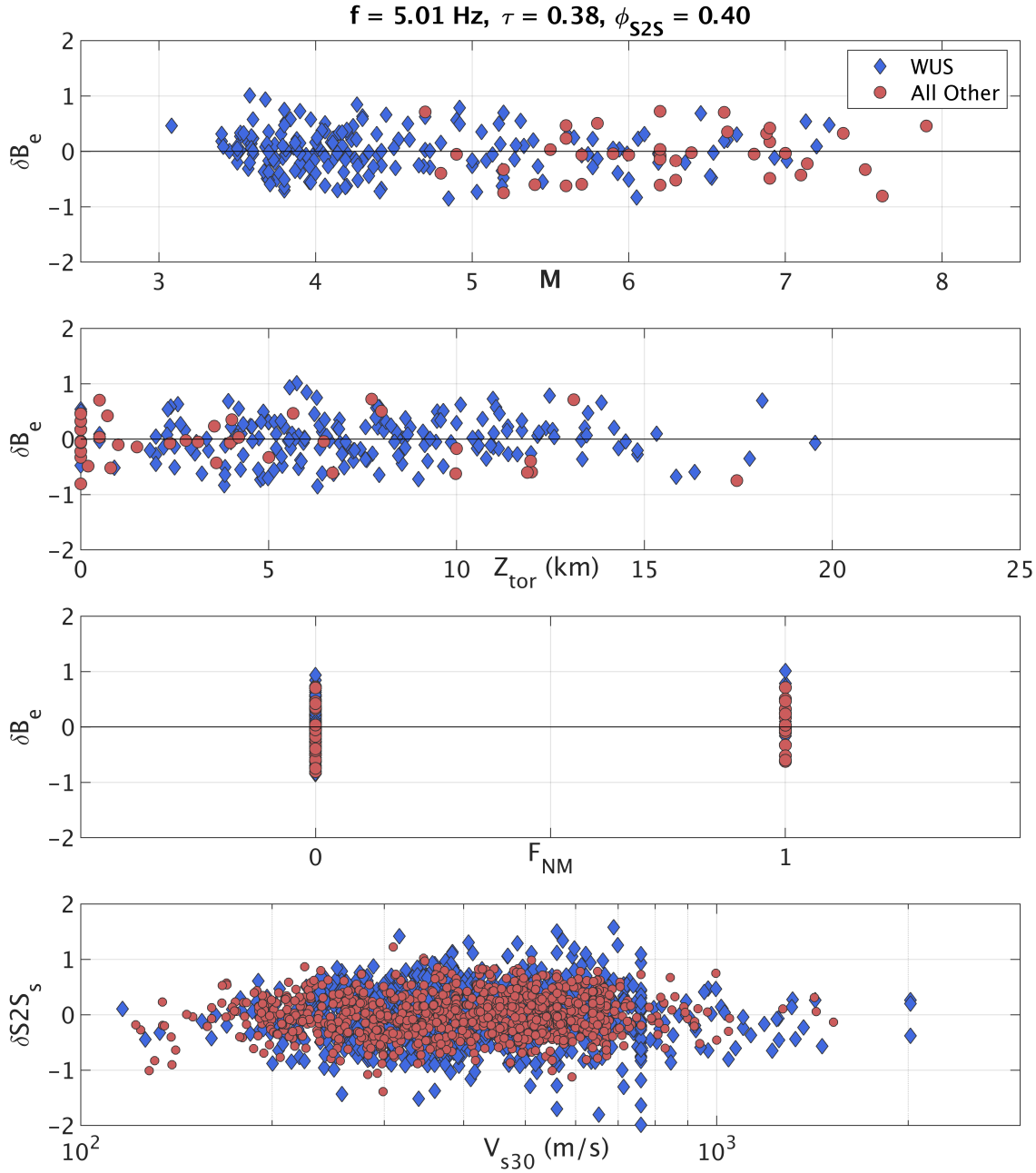

Figure A-11. Between-event residuals (δB_e) versus $\mathbf{M}$, Z_{tor}, and F_{NM} and between-site residuals ($\delta S2S_s$) versus V_{s30}, for $f = 5$ Hz.

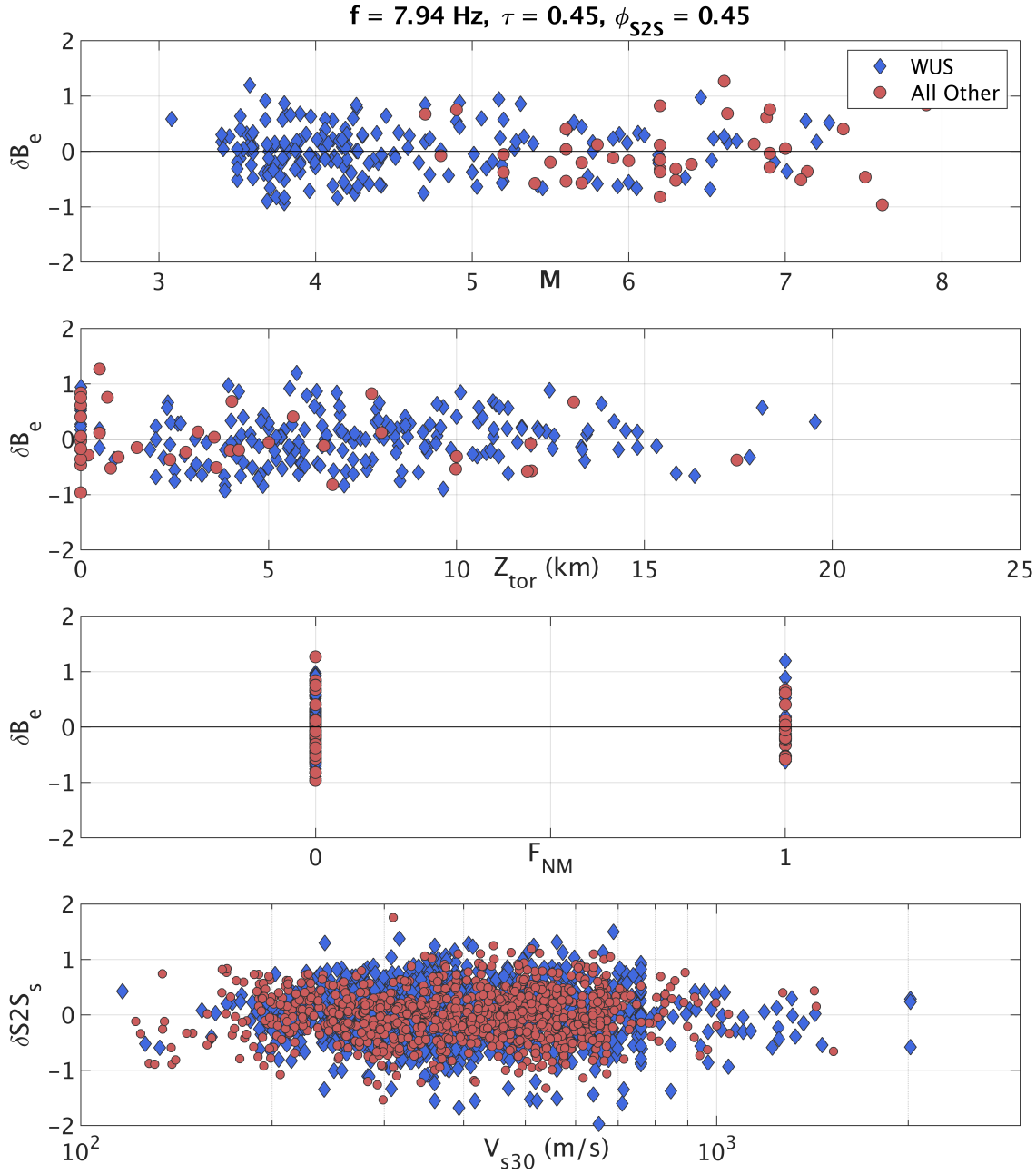

Figure A-12. Between-event residuals (δB_e) versus $\mathbf{M}$, Z_{tor}, and F_{NM} and between-site residuals ($\delta S2S_s$) versus V_{s30}, for $f = 8$ Hz.

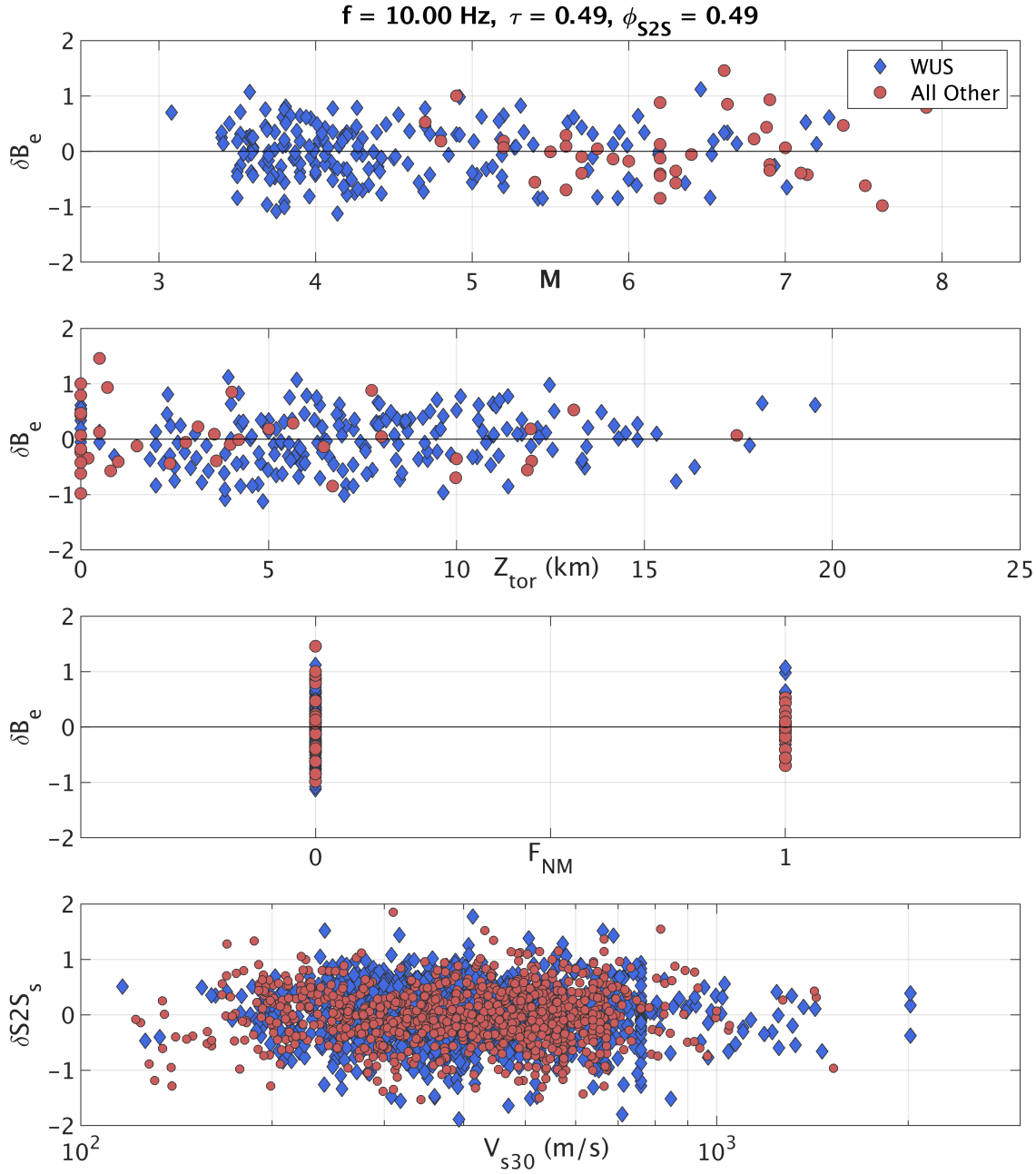

*Figure A-13. Between-event residuals (δB_e) versus **M**, Z_{tor}, and F_{NM} and between-site residuals ($\delta S2S_s$) versus V_{s30}, for $f = 10$ Hz.*

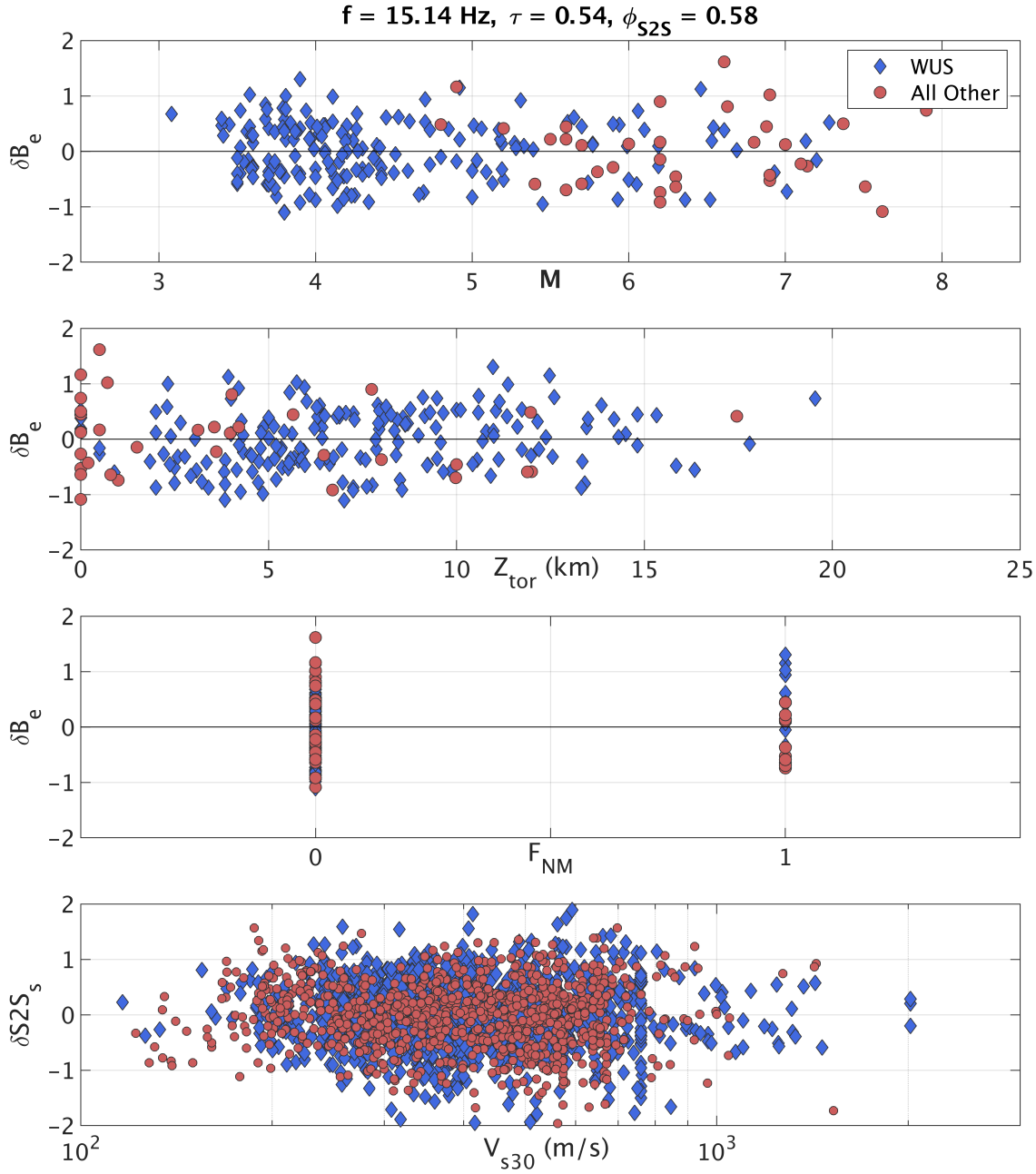

*Figure A-14. Between-event residuals (δB_e) versus **M**, Z_{tor}, and F_{NM} and between-site residuals ($\delta S2S_s$) versus V_{s30}, for $f = 15$ Hz.*

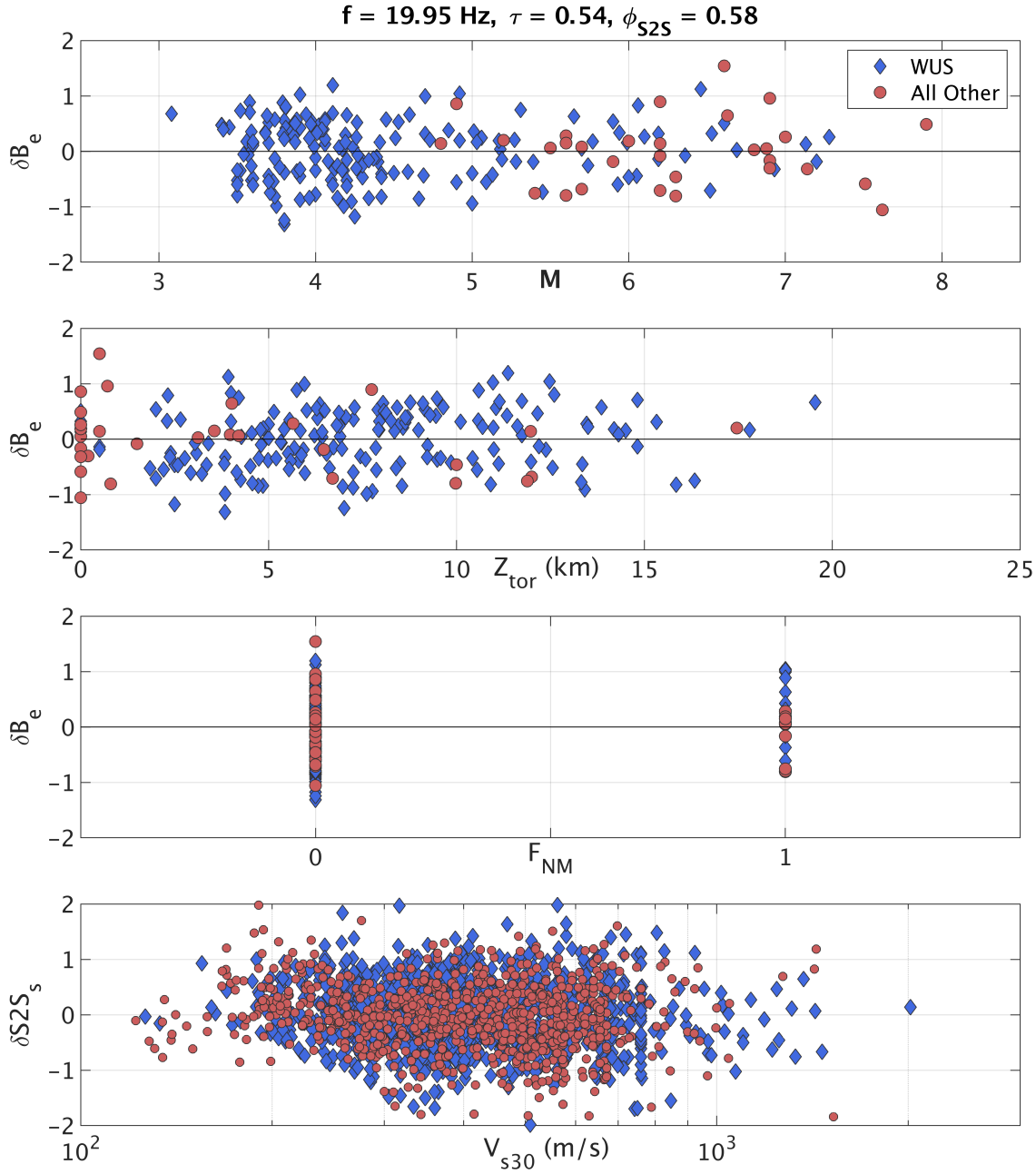

*Figure A-15. Between-event residuals (δB_e) versus **M**, Z_{tor}, and F_{NM} and between-site residuals ($\delta S2S_s$) versus V_{s30}, for $f = 20$ Hz.*

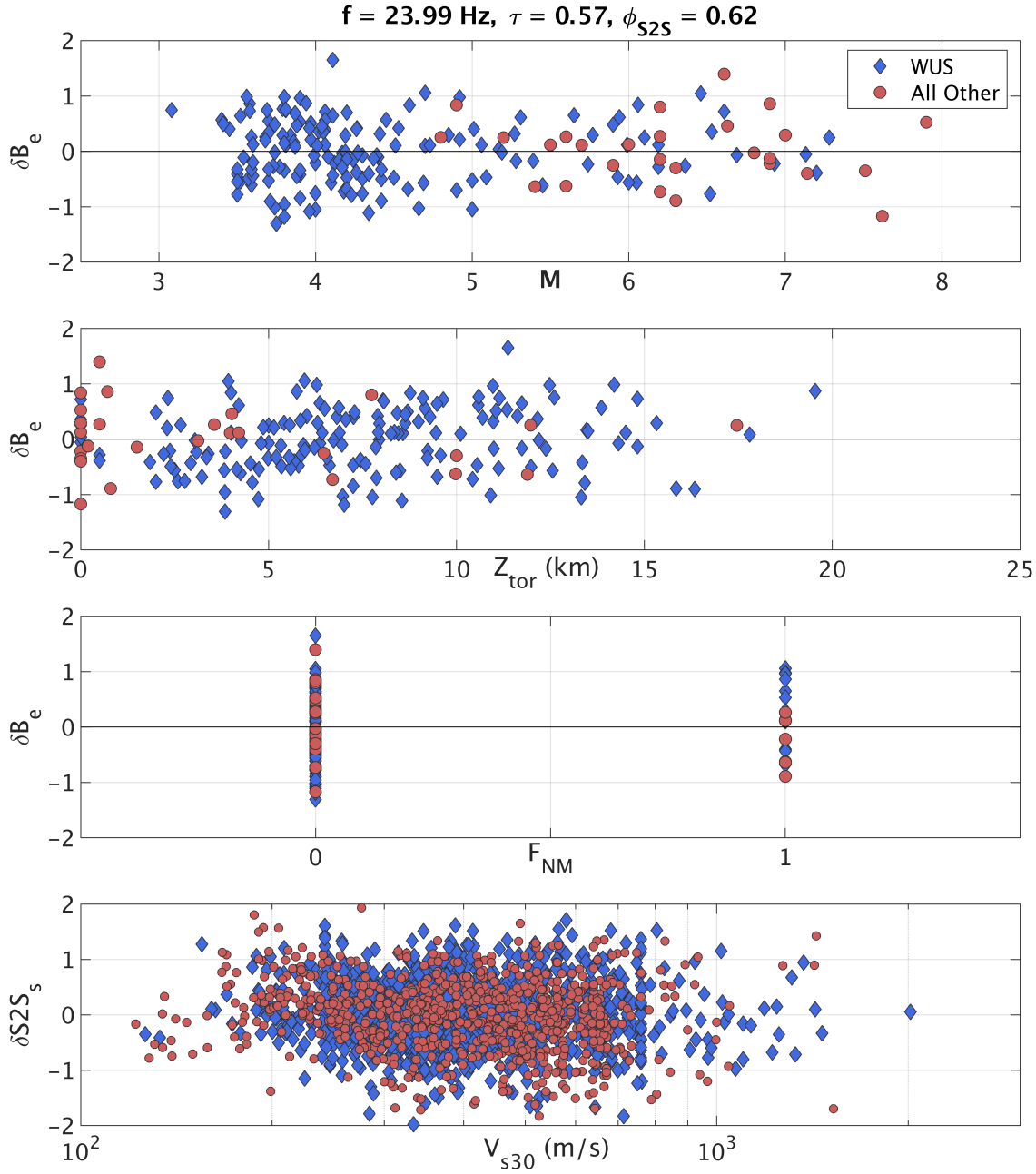

*Figure A-16. Between-event residuals (δB_e) versus **M**, Z_{tor}, and F_{NM} and between-site residuals ($\delta S2S_s$) versus V_{s30}, for $f = 24$ Hz.*

Within-site Residuals

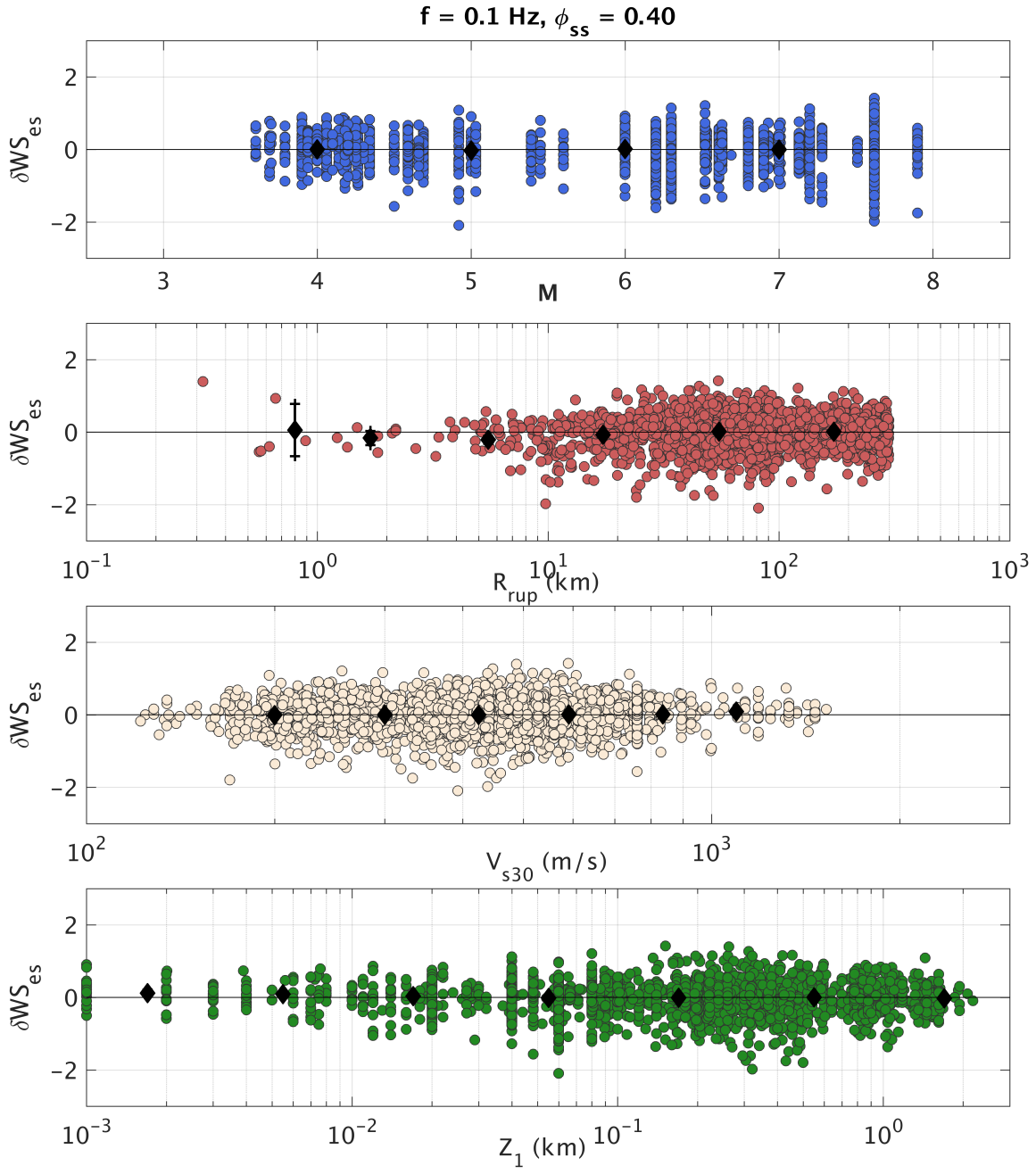

*Figure A-17. Within-site residuals (δWS_{es}) versus **M**, R_{rup}, V_{s30}, and Z_1 for $f = 0.1$ Hz.*

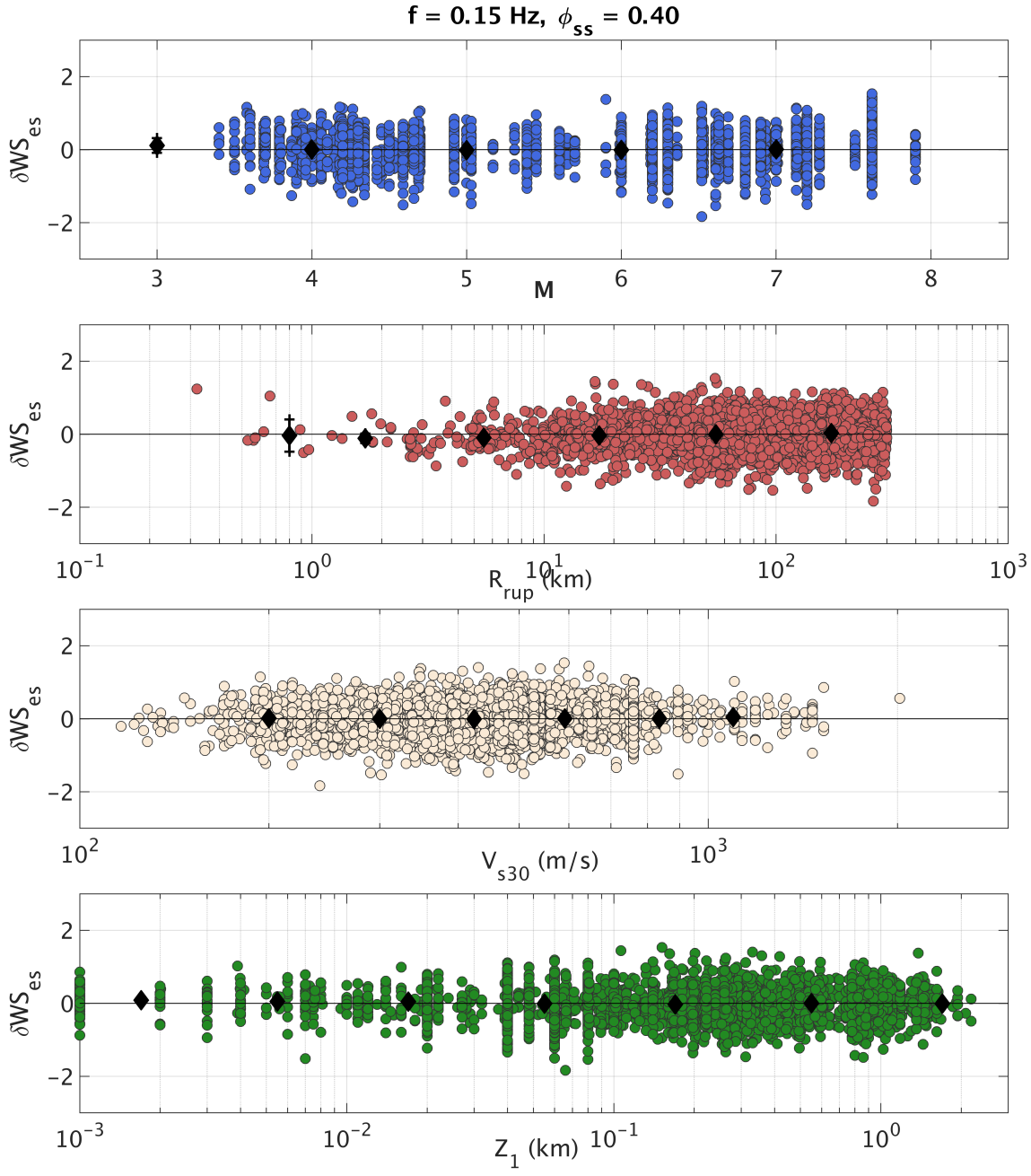

*Figure A-18. Within-site residuals (δWS_{es}) versus **M**, R_{rup}, V_{s30}, and Z_1 for $f = 0.15$ Hz.*

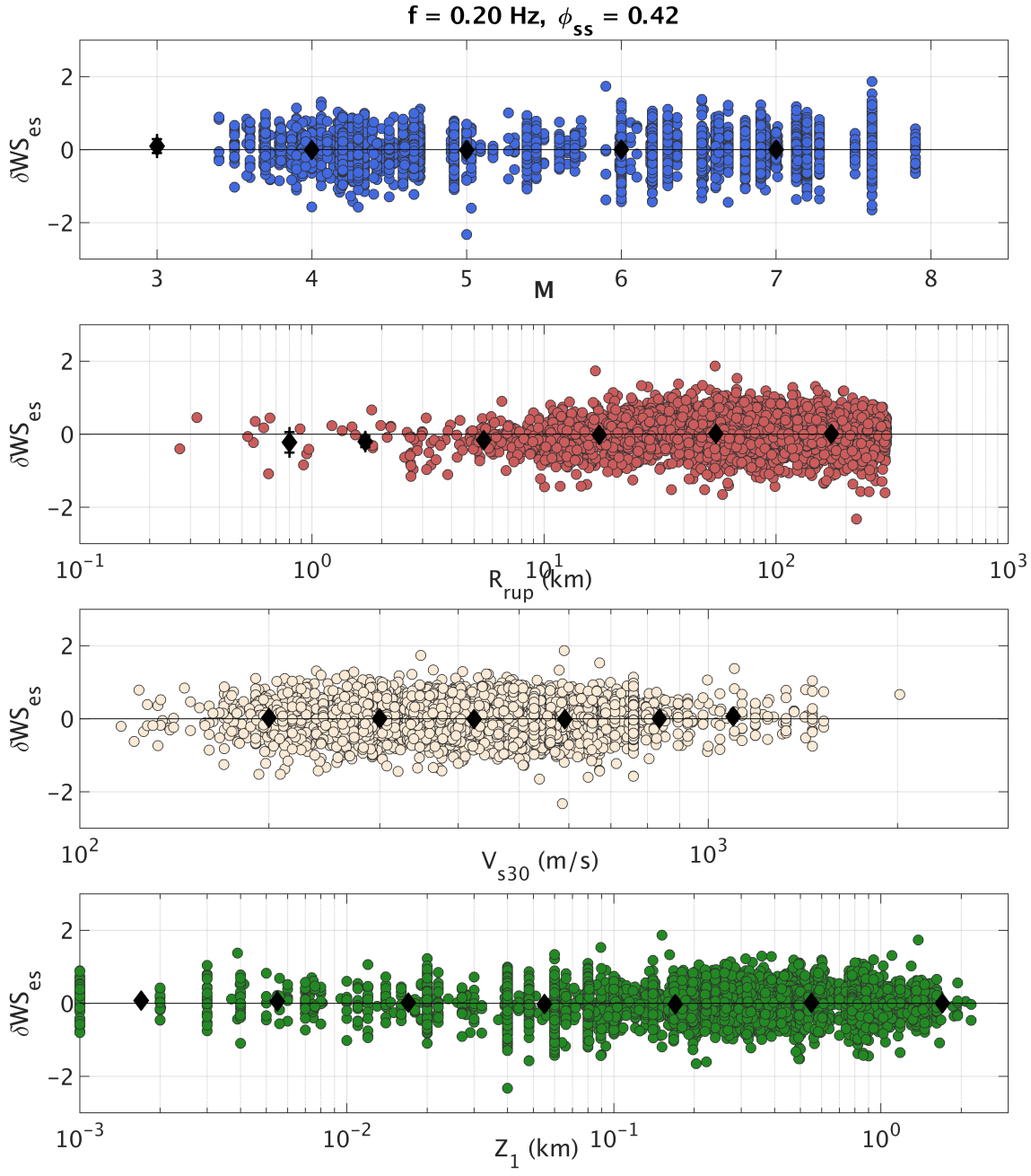

*Figure A-19. Within-site residuals (δWS_{es}) versus **M**, R_{rup}, V_{s30}, and Z_1 for $f = 0.2$ Hz.*

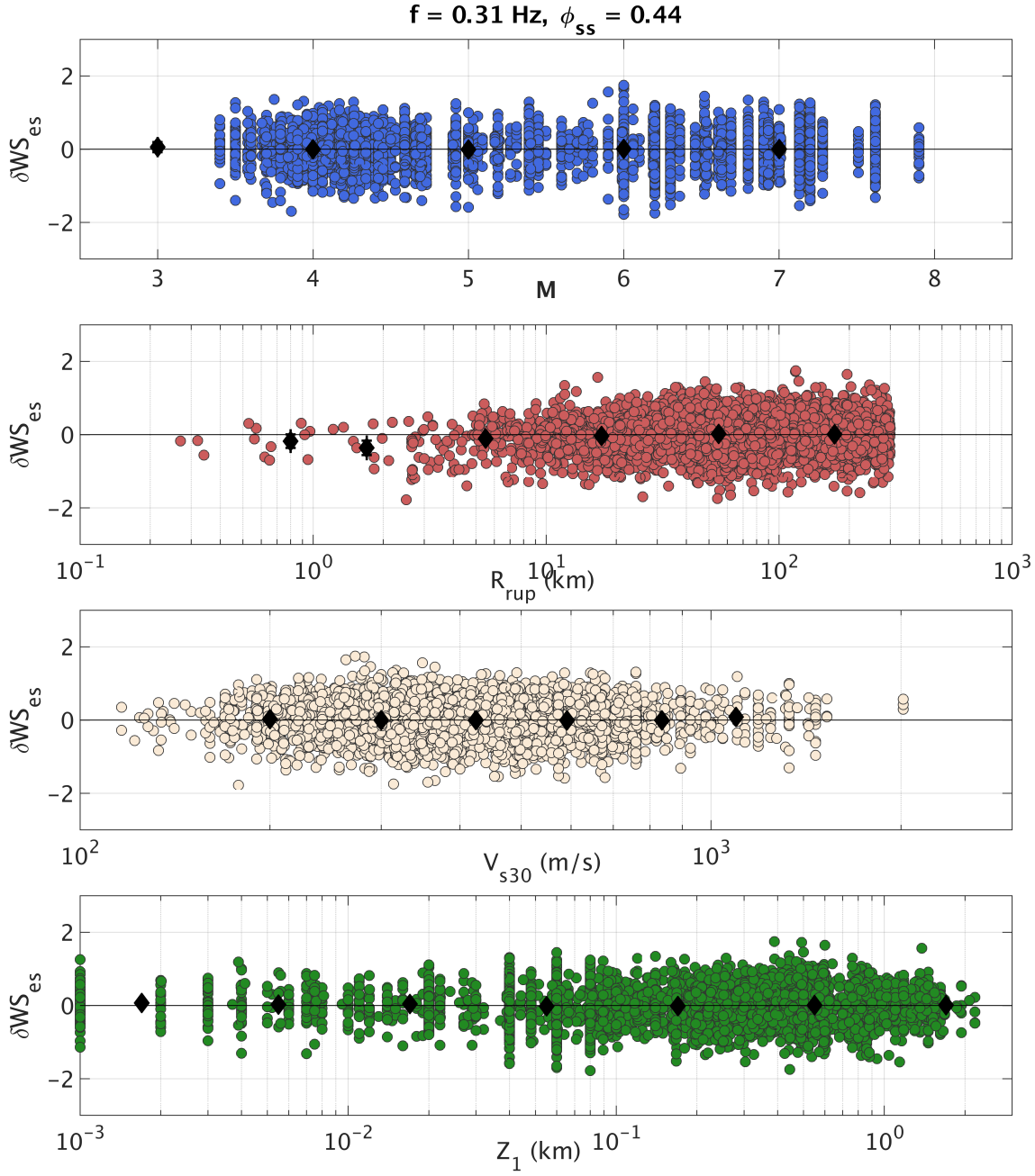

*Figure A-20. Within-site residuals (δWS_{es}) versus **M**, R_{rup}, V_{s30}, and Z_1 for $f = 0.3$ Hz.*

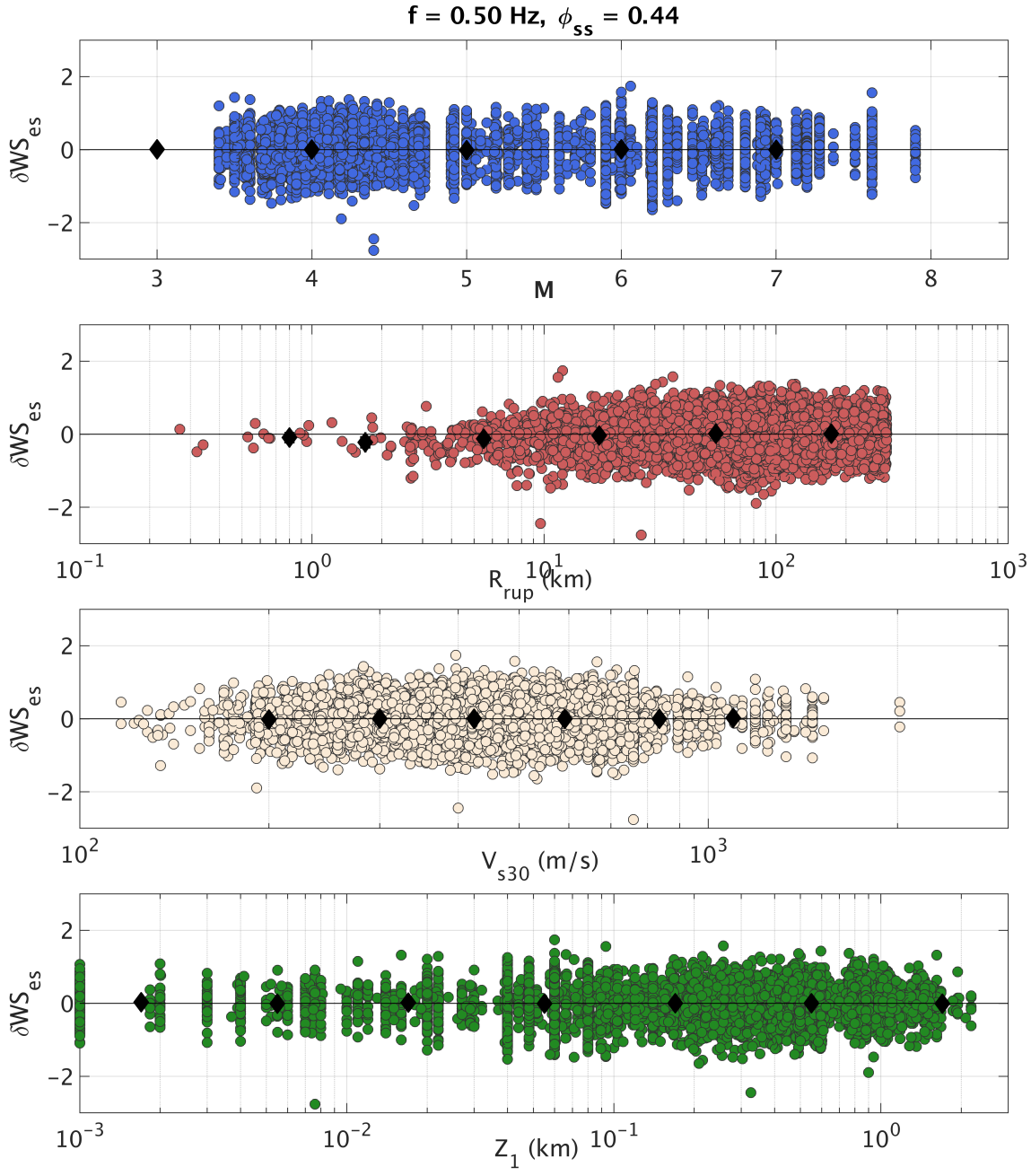

*Figure A-21. Within-site residuals (δWS_{es}) versus **M**, R_{rup}, V_{s30}, and Z_1 for $f = 0.5$ Hz.*

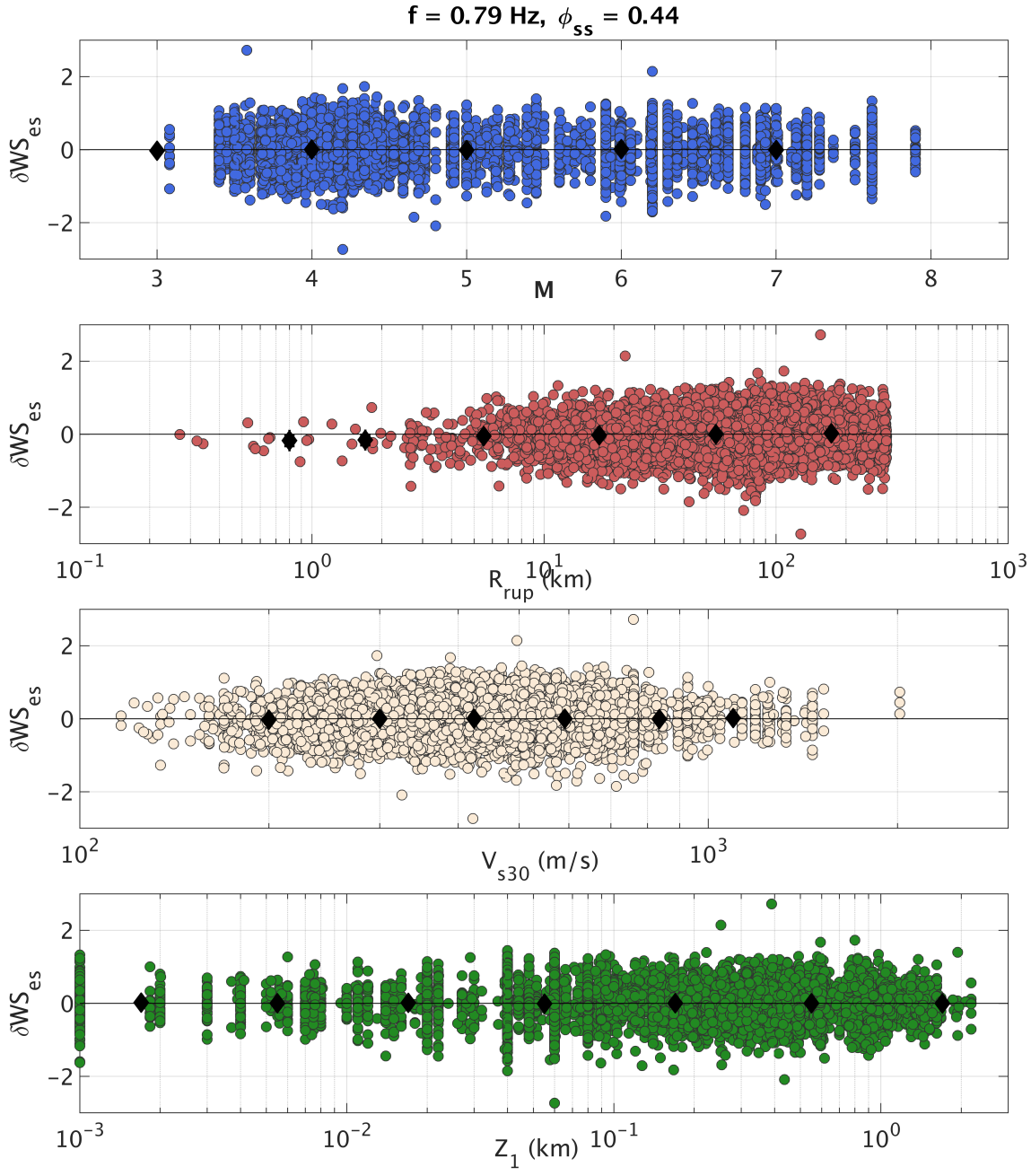

*Figure A-22. Within-site residuals (δWS_{es}) versus **M**, R_{rup}, V_{s30}, and Z_1 for $f = 0.8$ Hz.*

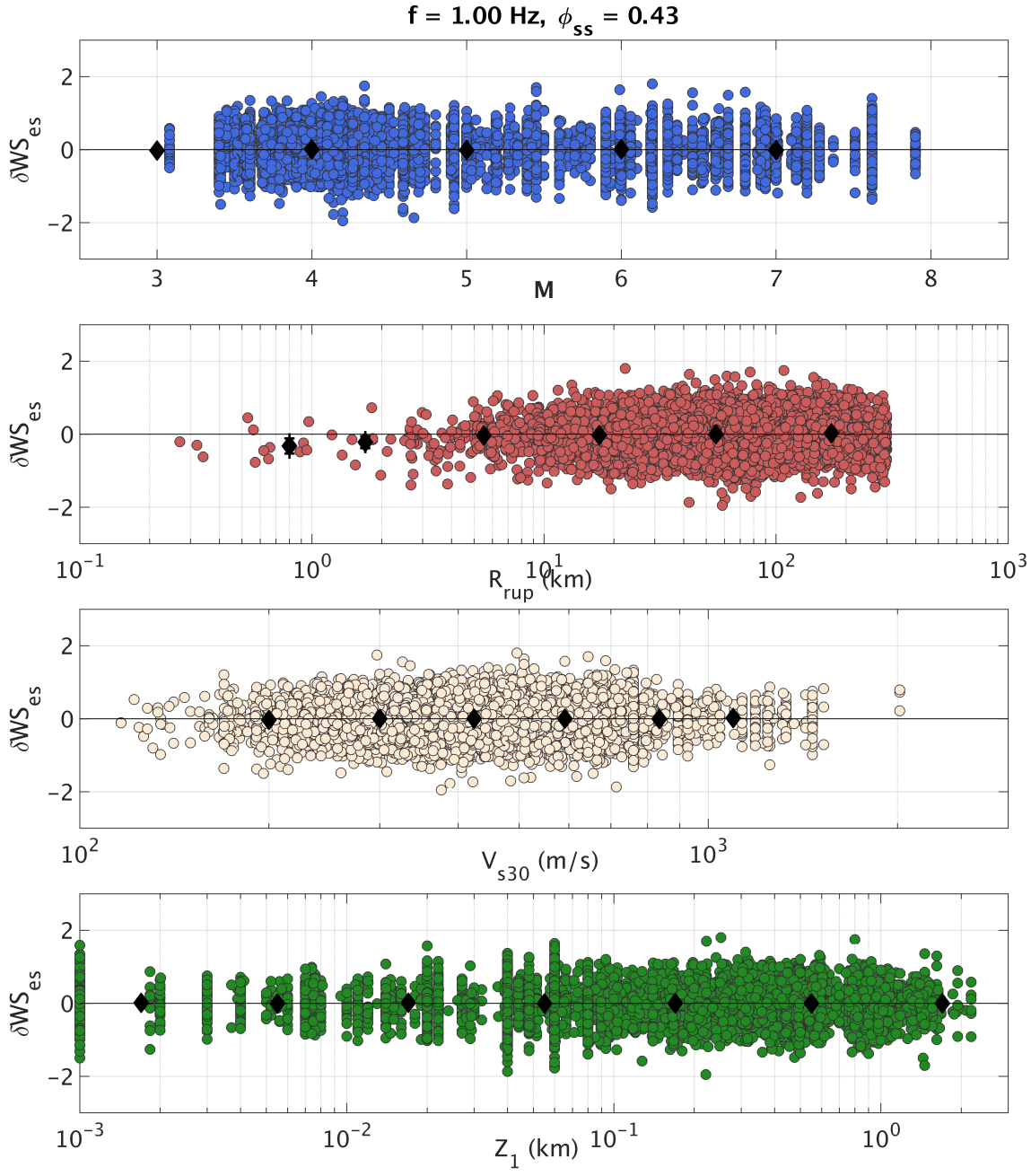

Figure A-23. Within-site residuals (δWS_{es}) versus $\boldsymbol{M}$, R_{rup}, V_{s30}, and Z_1 for $f = 1$ Hz.

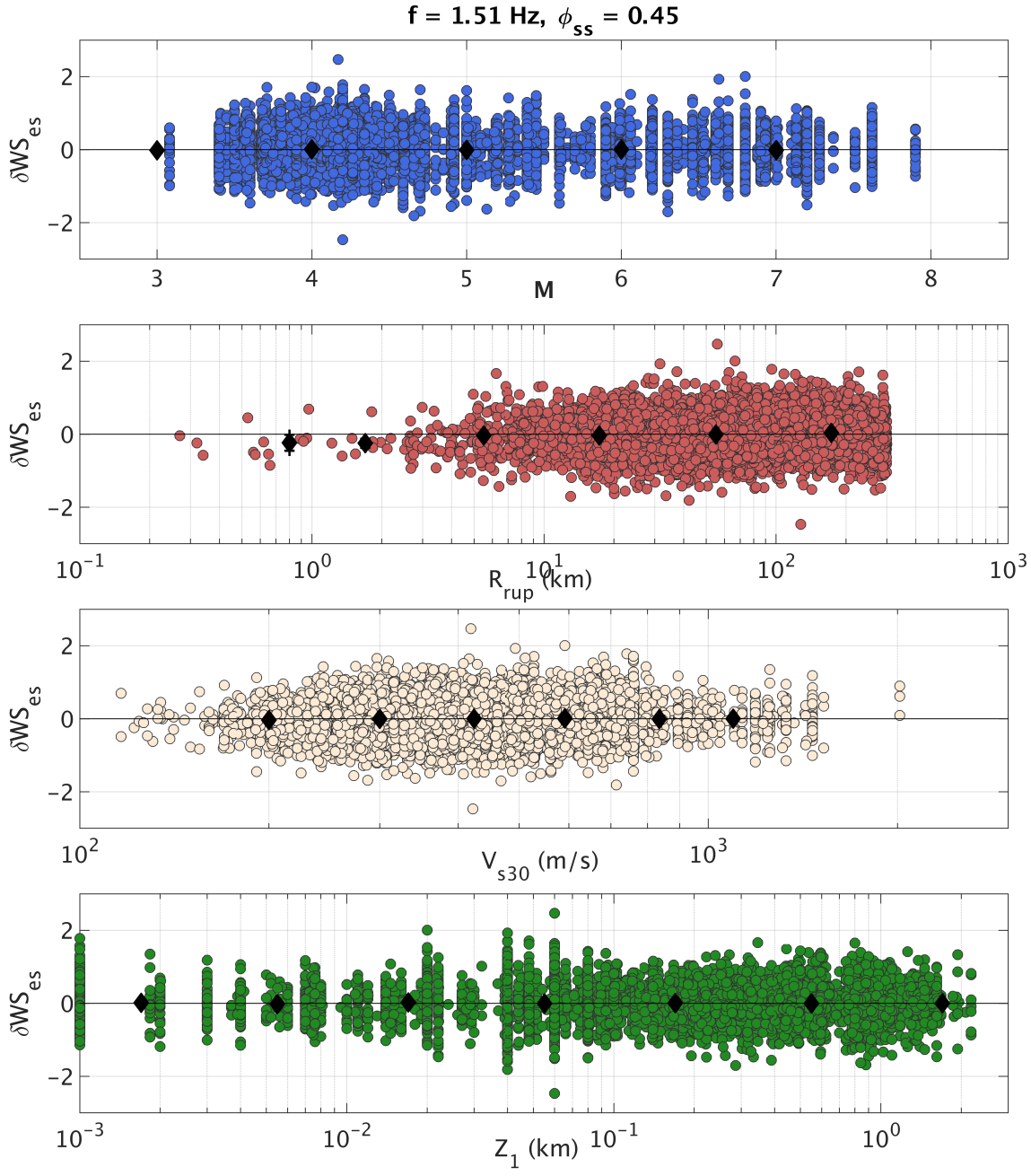

*Figure A-24. Within-site residuals (δWS_{es}) versus **M**, R_{rup}, V_{s30}, and Z_1 for $f = 1.5$ Hz.*

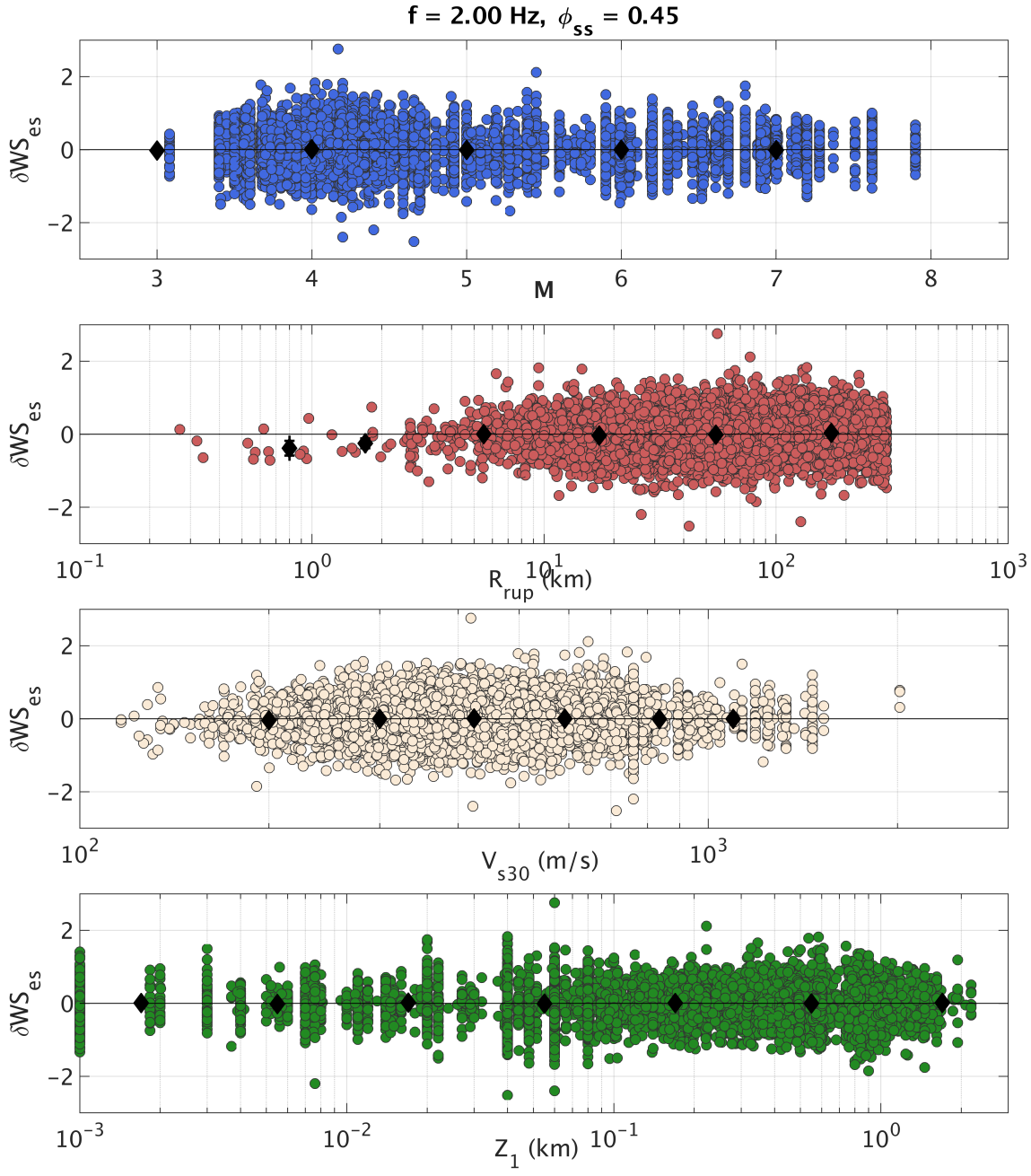

*Figure A-25. Within-site residuals (δWS_{es}) versus **M**, R_{rup}, V_{s30}, and Z_1 for $f = 2$ Hz.*

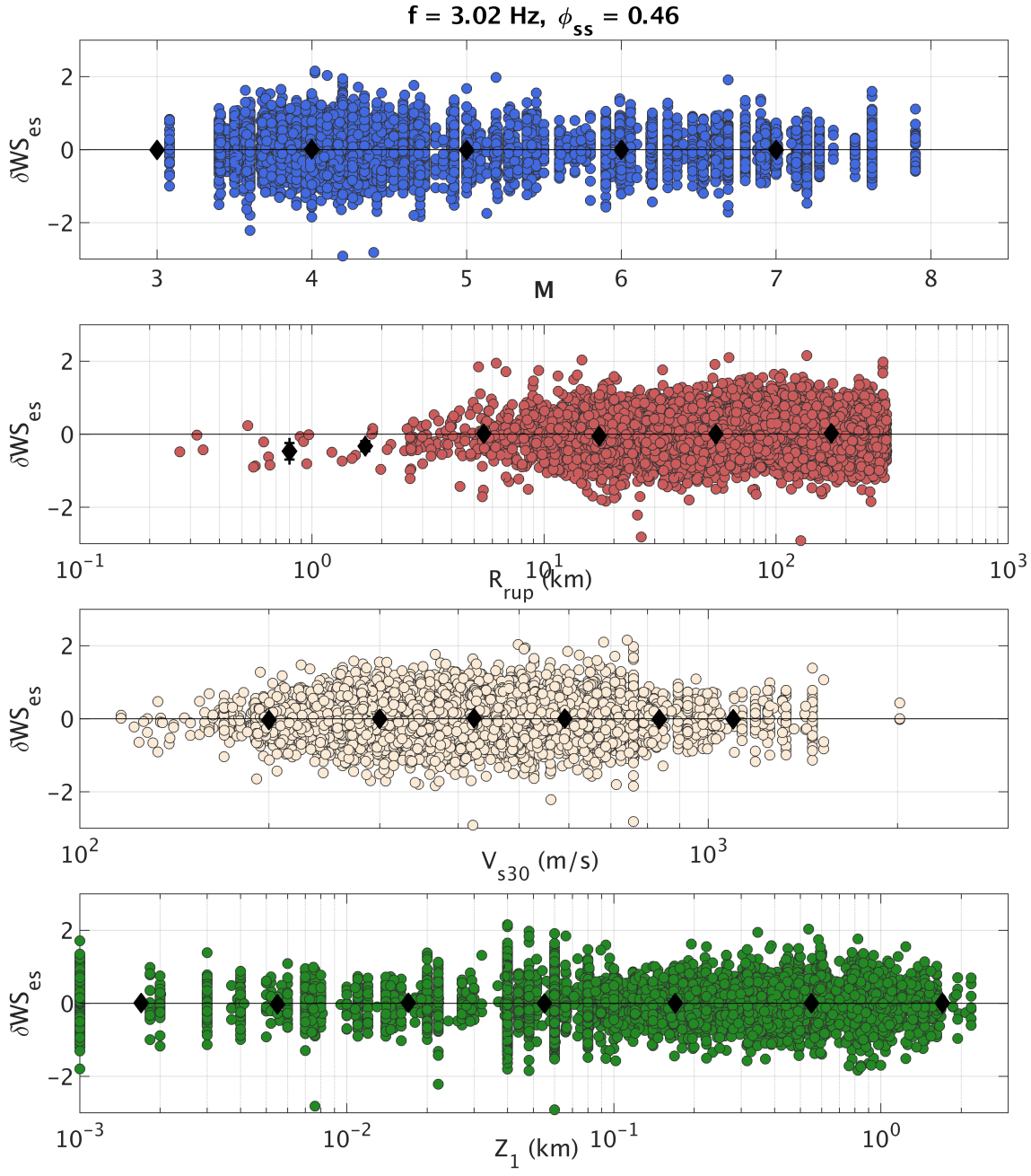

*Figure A-26. Within-site residuals (δWS_{es}) versus **M**, R_{rup}, V_{s30}, and Z_1 for $f = 3$ Hz.*

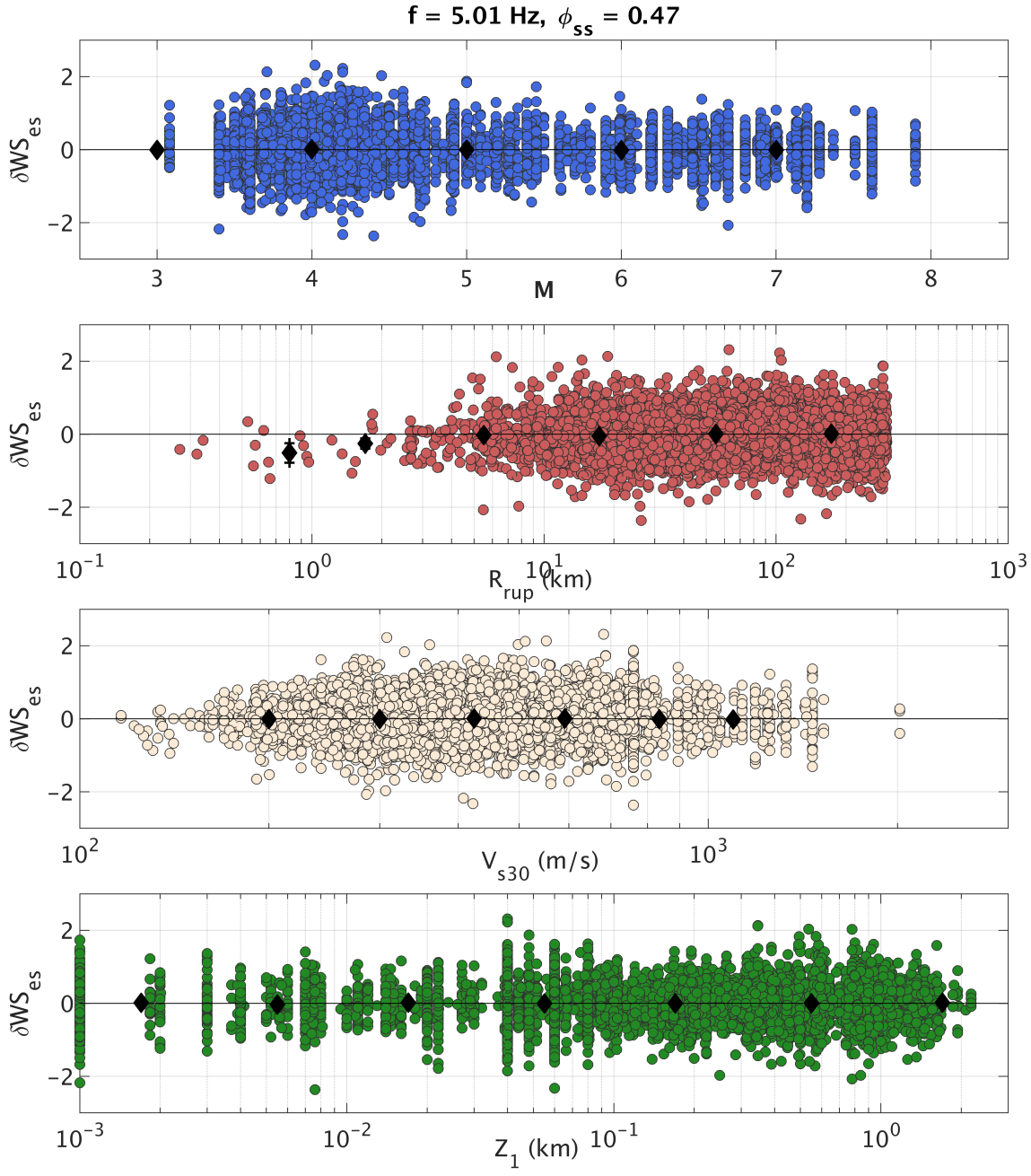

*Figure A-27. Within-site residuals (δWS_{es}) versus **M**, R_{rup}, V_{s30}, and Z_1 for $f = 5$ Hz.*

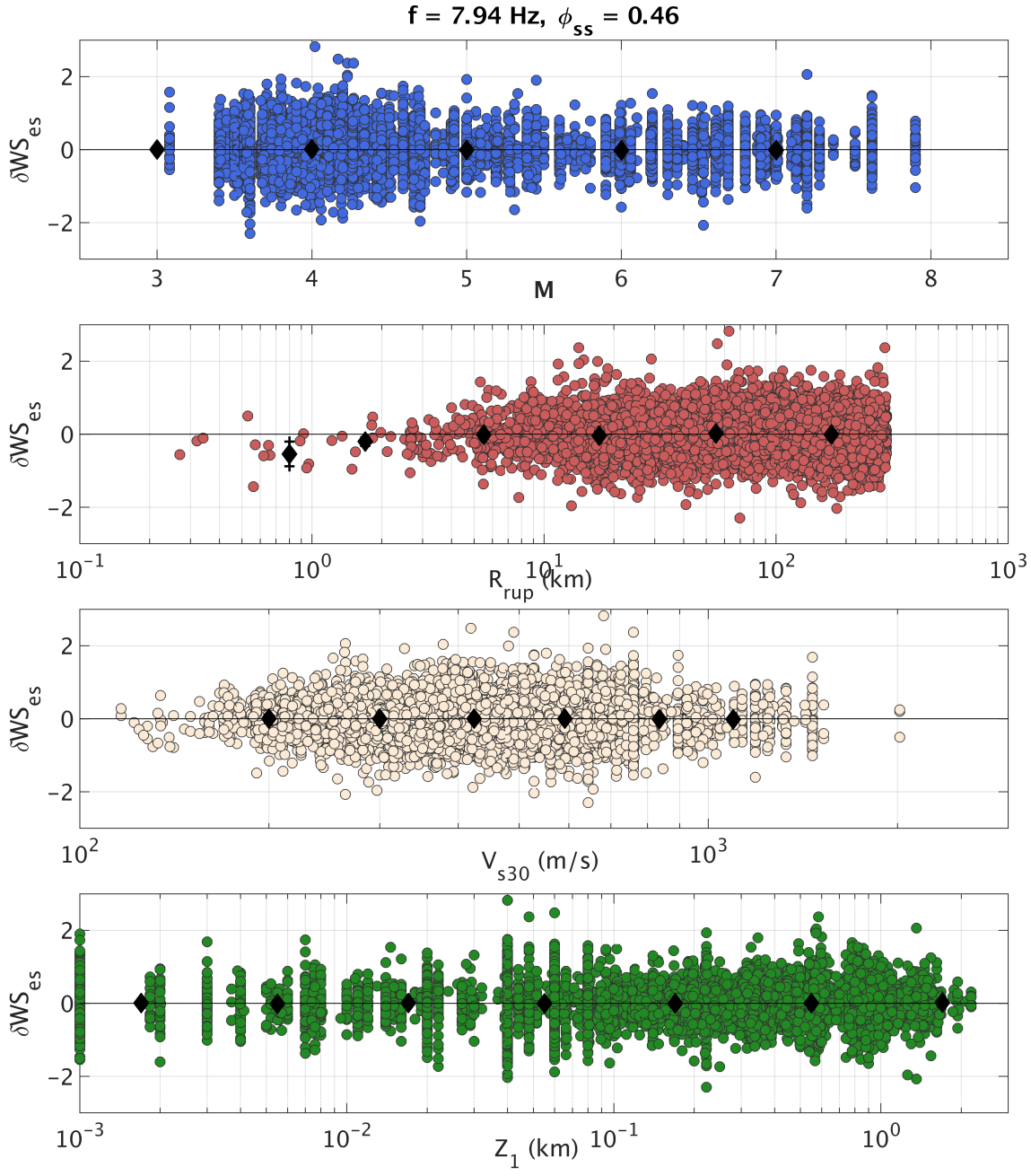

Figure A-28. Within-site residuals (δWS_{es}) versus $\boldsymbol{M}$, R_{rup}, V_{s30}, and Z_1 for $f = 8$ Hz.

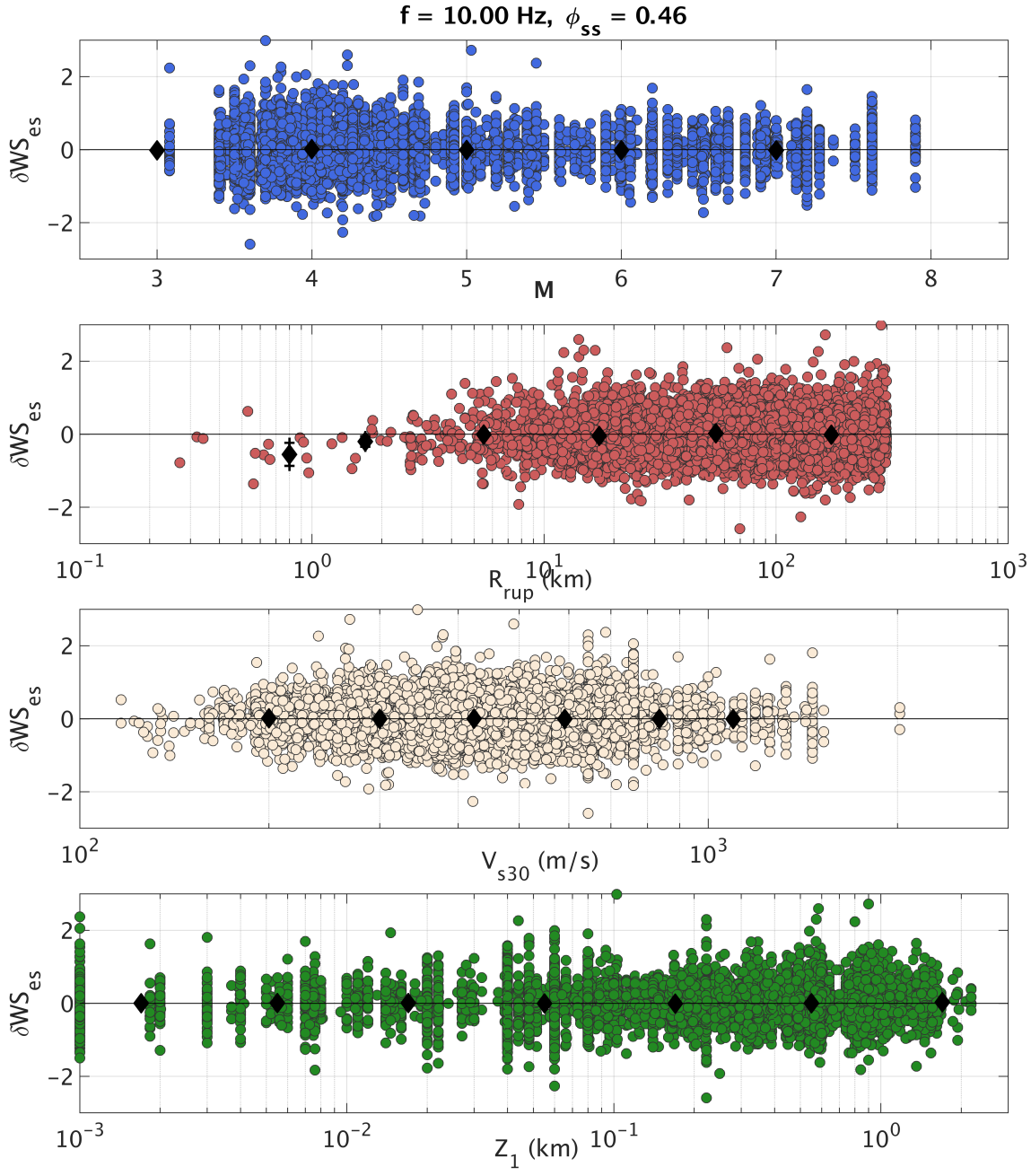

*Figure A-29. Within-site residuals (δWS_{es}) versus **M**, R_{rup}, V_{s30}, and Z_1 for $f = 10$ Hz.*

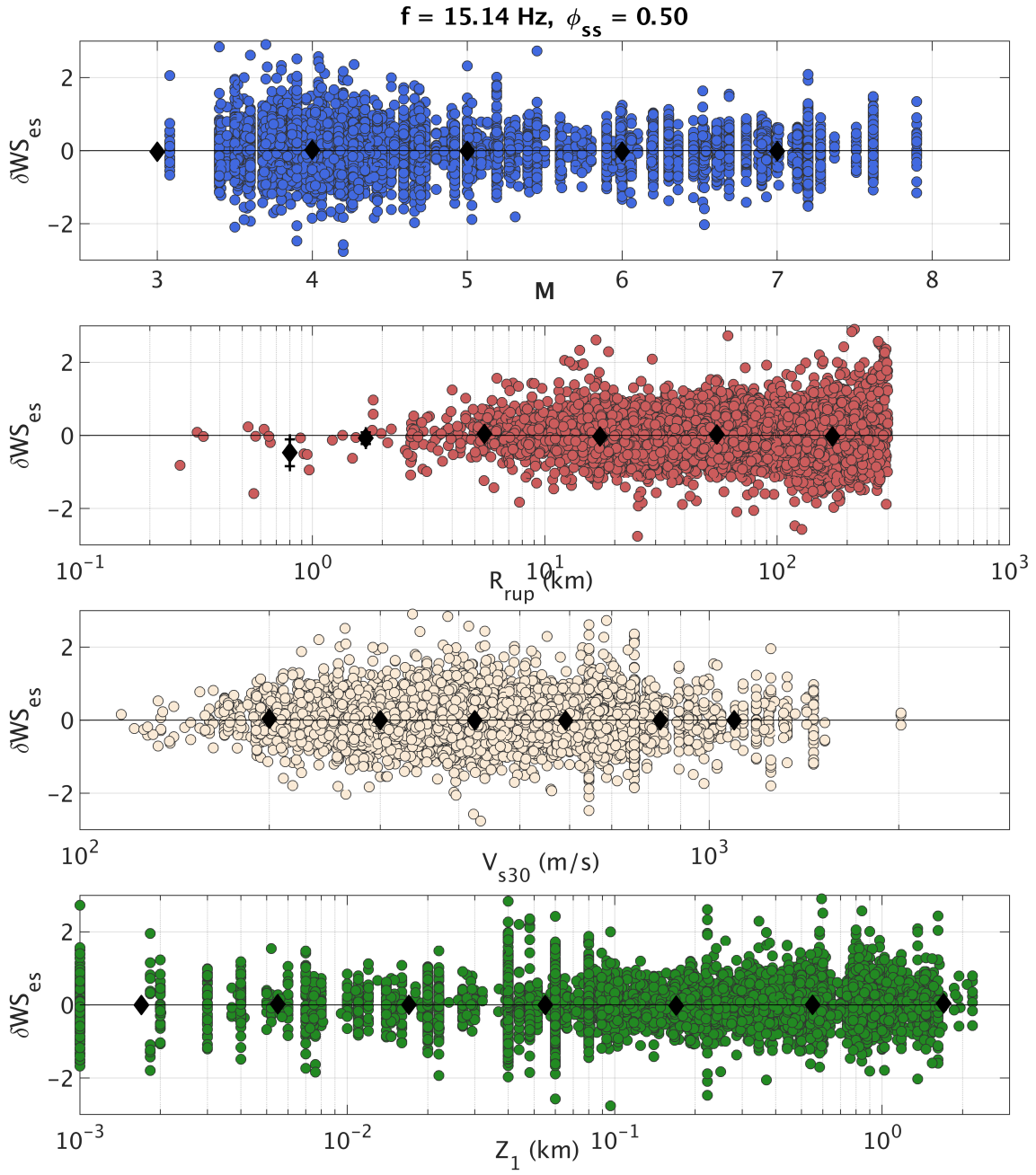

*Figure A-30. Within-site residuals (δWS_{es}) versus **M**, R_{rup}, V_{s30}, and Z_1 for $f = 15$ Hz.*

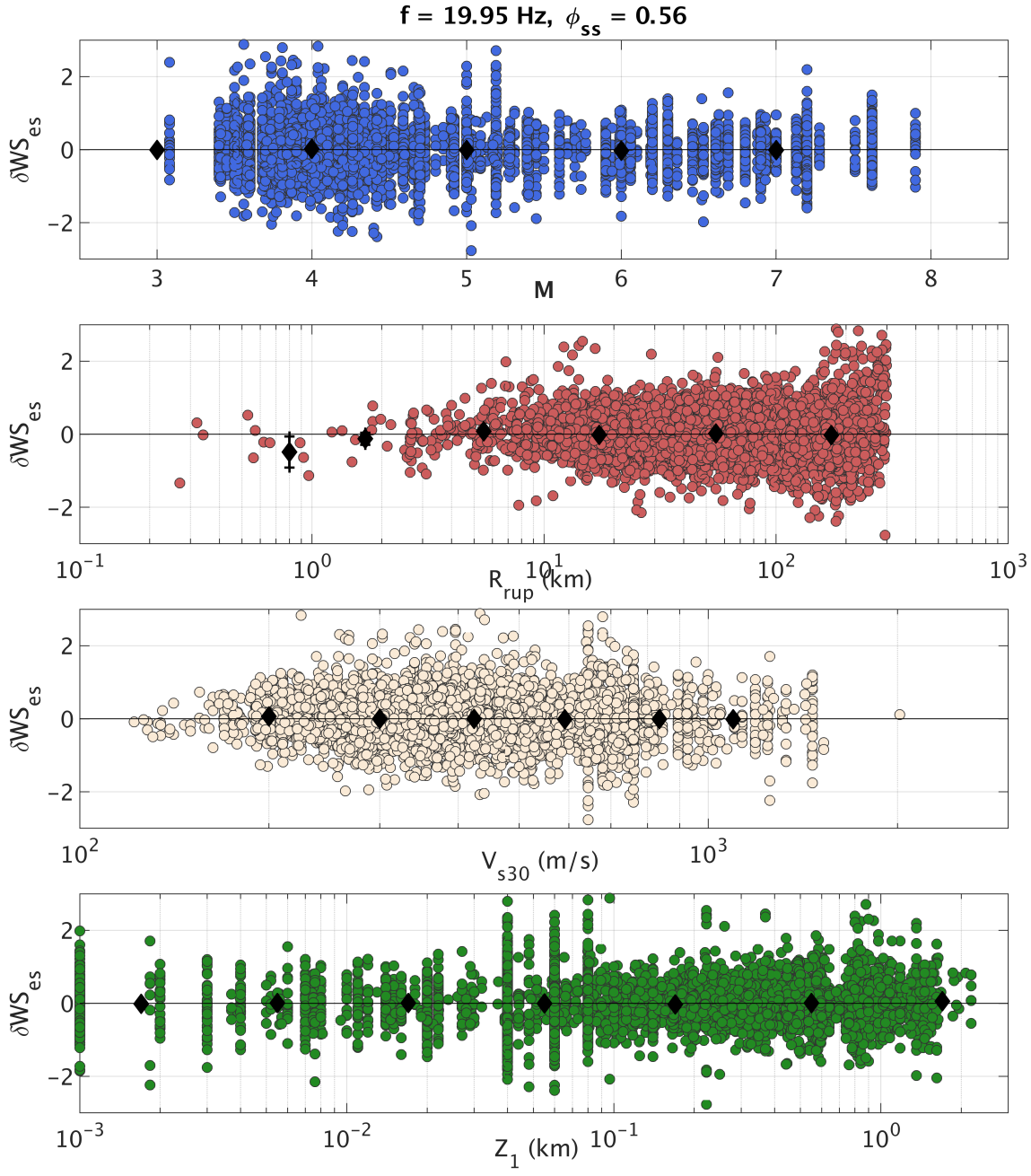

*Figure A-31. Within-site residuals (δWS_{es}) versus **M**, R_{rup}, V_{s30}, and Z_1 for $f = 20$ Hz.*

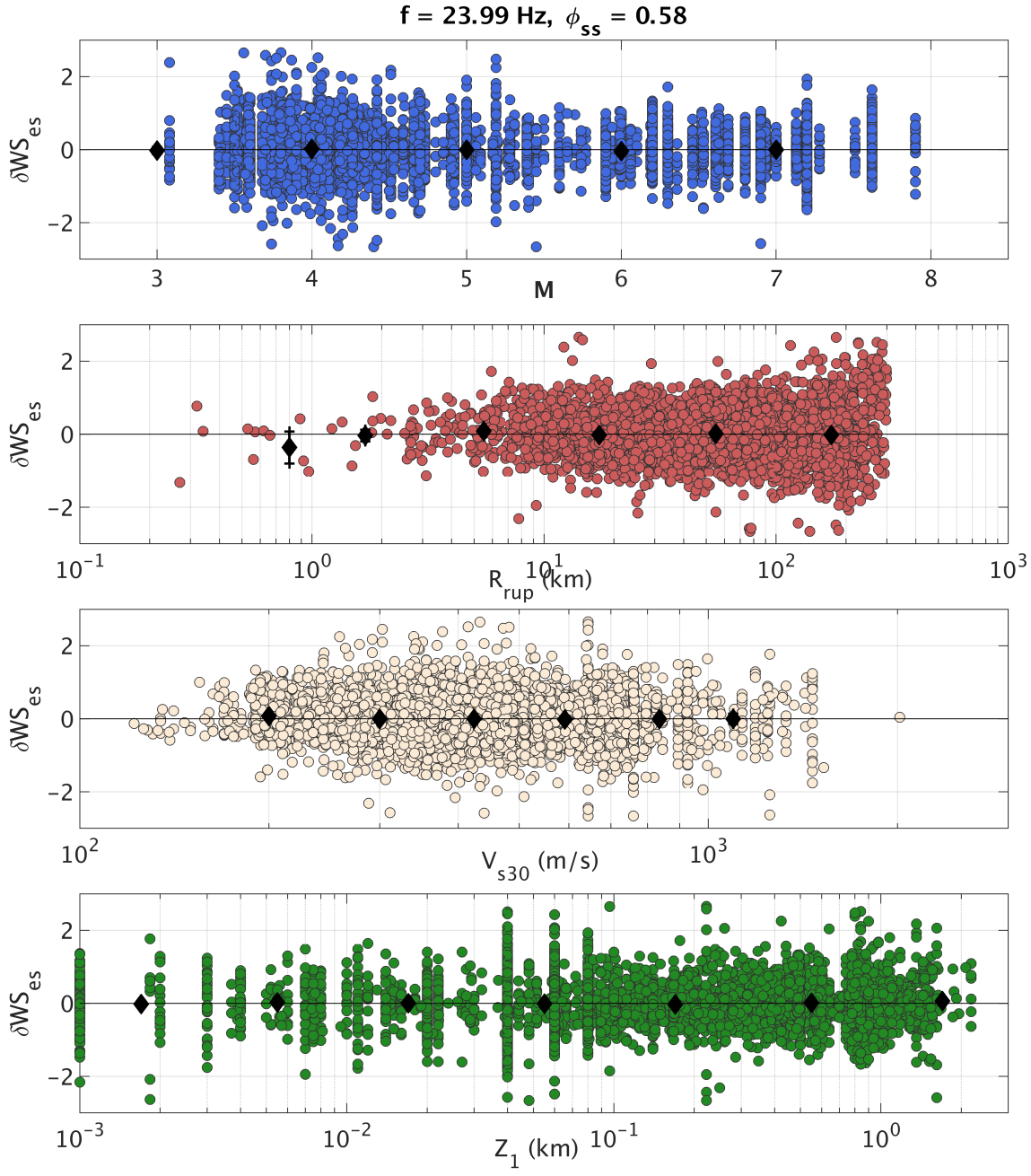

*Figure A-32. Within-site residuals (δWS_{es}) versus **M**, R_{rup}, V_{s30}, and Z_1 for $f = 24$ Hz.*

Within-site Residuals Binned by M

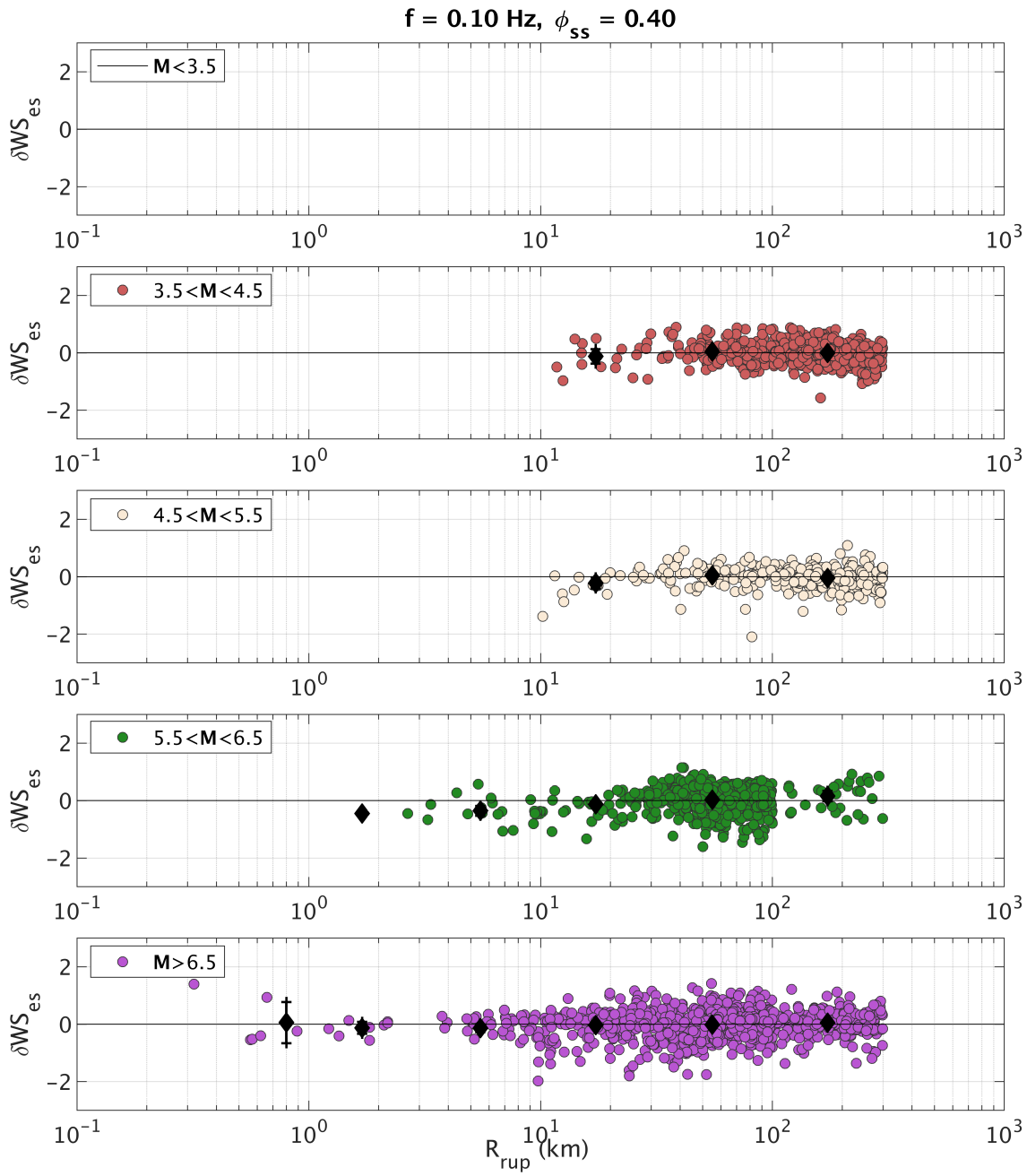

Figure A-33. Within-site residuals (δWS_{es}) versus R_{rup}, binned by ***M****, for $f = 0.1$ Hz.*

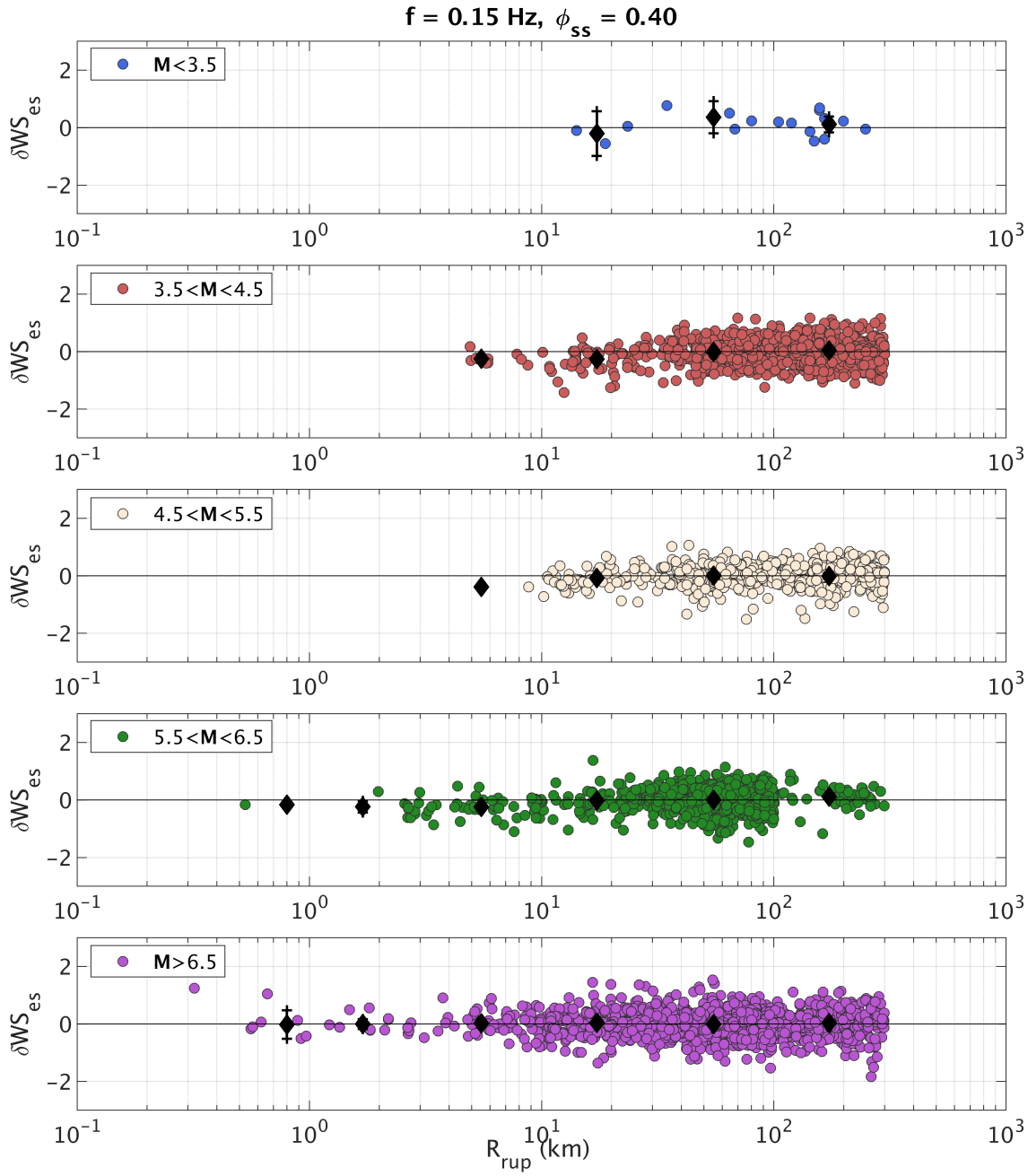

*Figure A-34. Within-site residuals (δWS_{es}) versus R_{rup}, binned by **M**, for $f = 0.15$ Hz.*

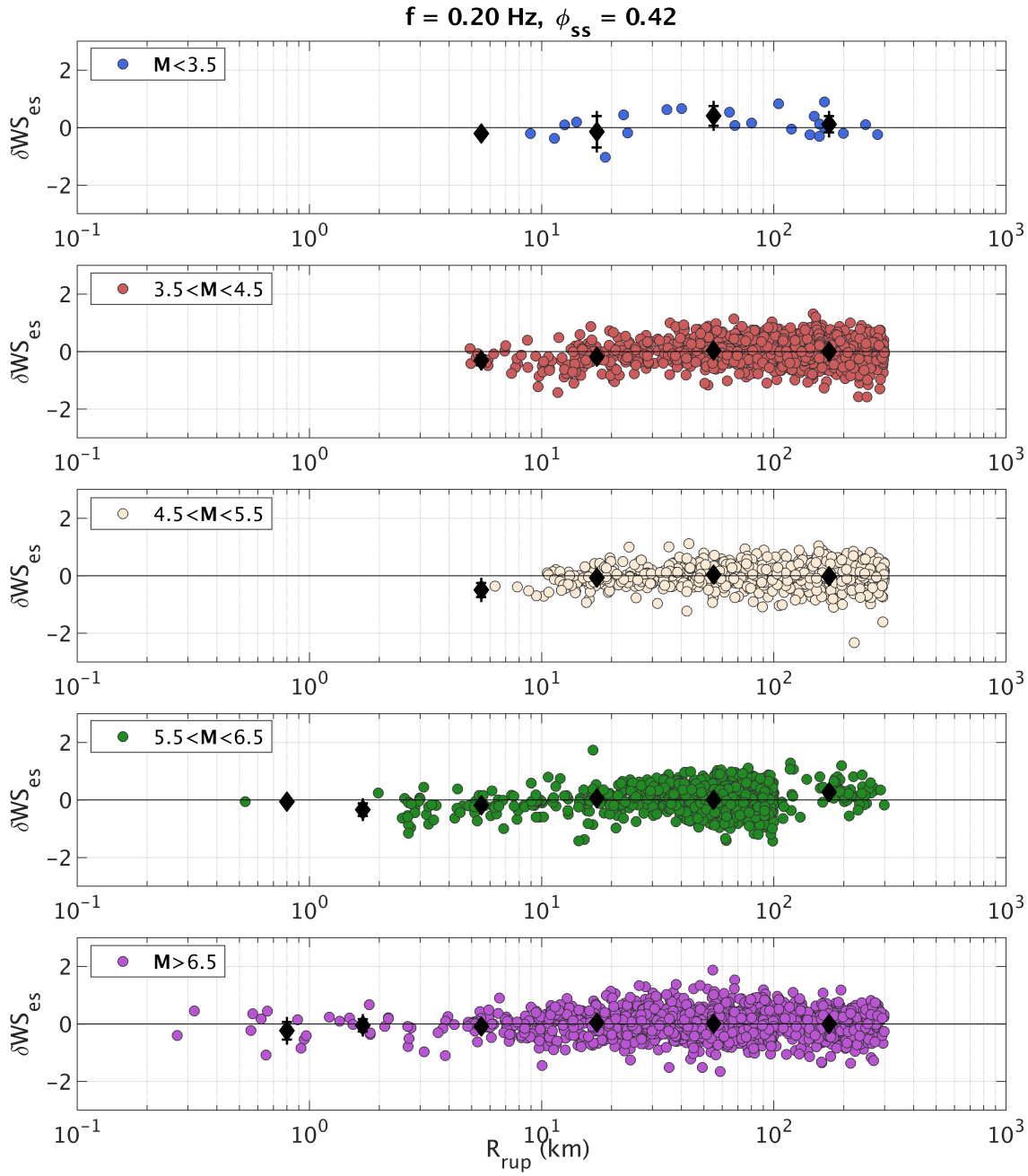

*Figure A-35. Within-site residuals (δWS_{es}) versus R_{rup}, binned by **M**, for $f = 0.2$ Hz.*

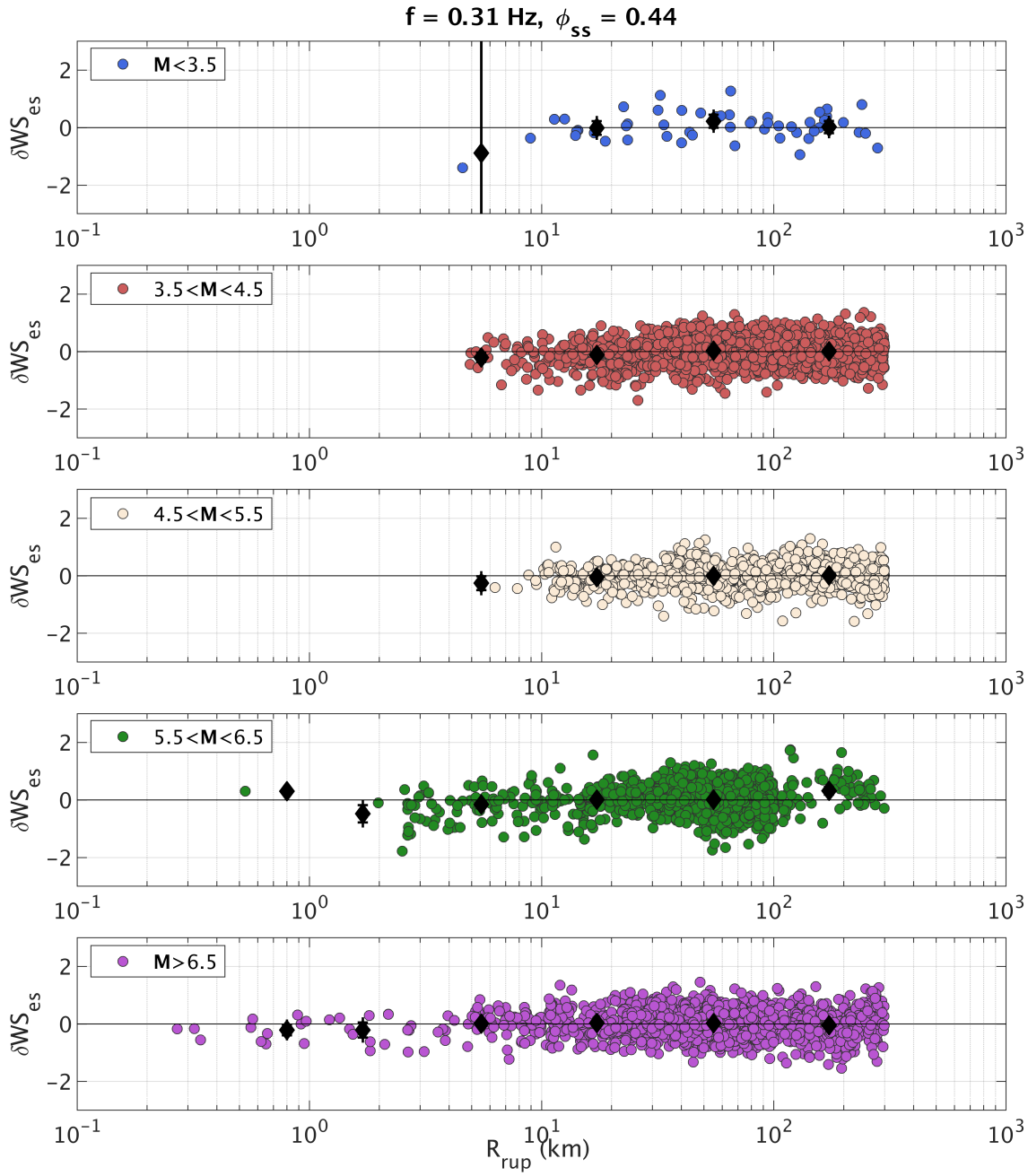

Figure A-36. Within-site residuals (δWS_{es}) versus R_{rup}, binned by $\boldsymbol{M}$, for $f = 0.3$ Hz.

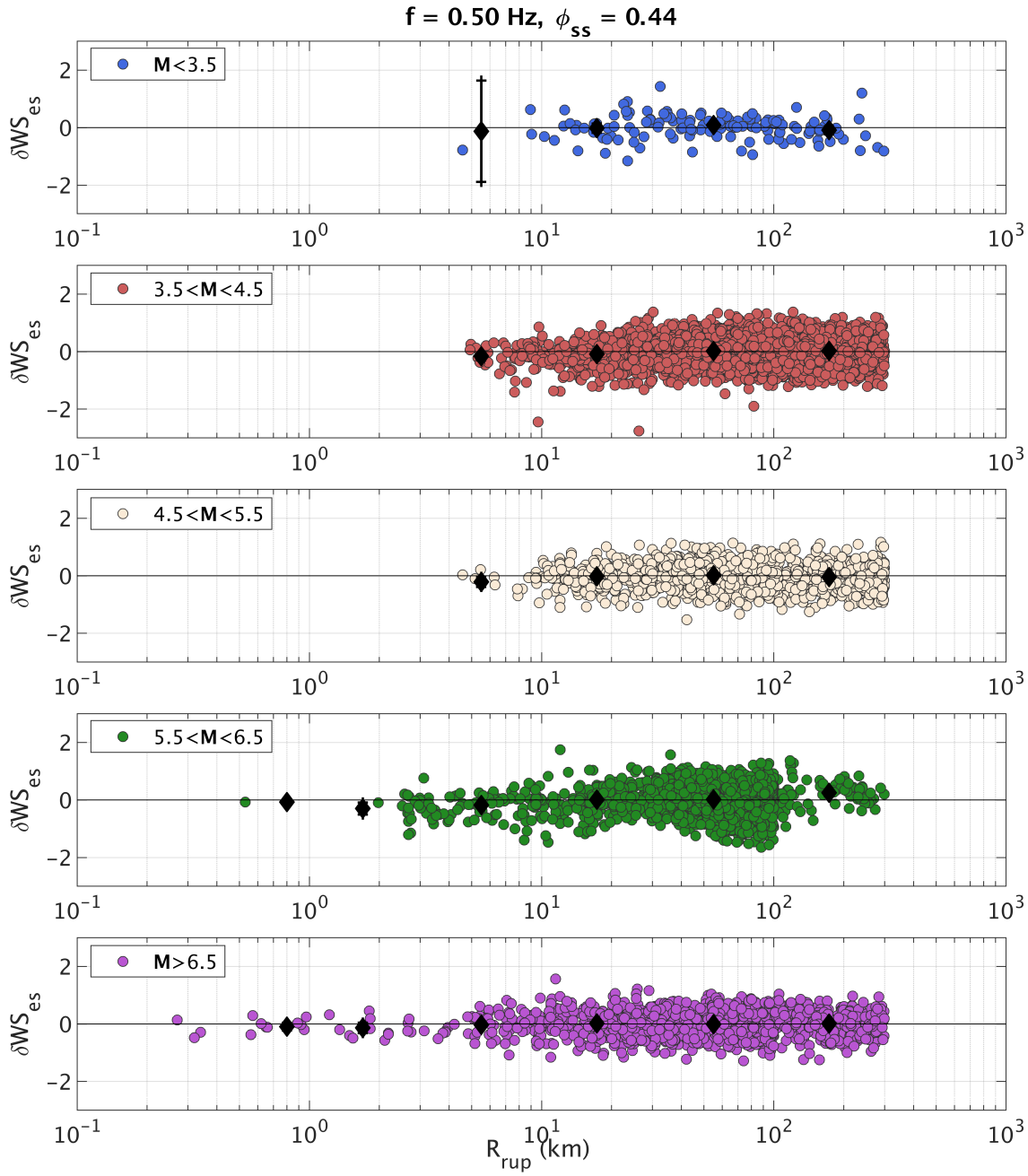

*Figure A-37. Within-site residuals (δWS_{es}) versus R_{rup}, binned by **M**, for $f = 0.5$ Hz.*

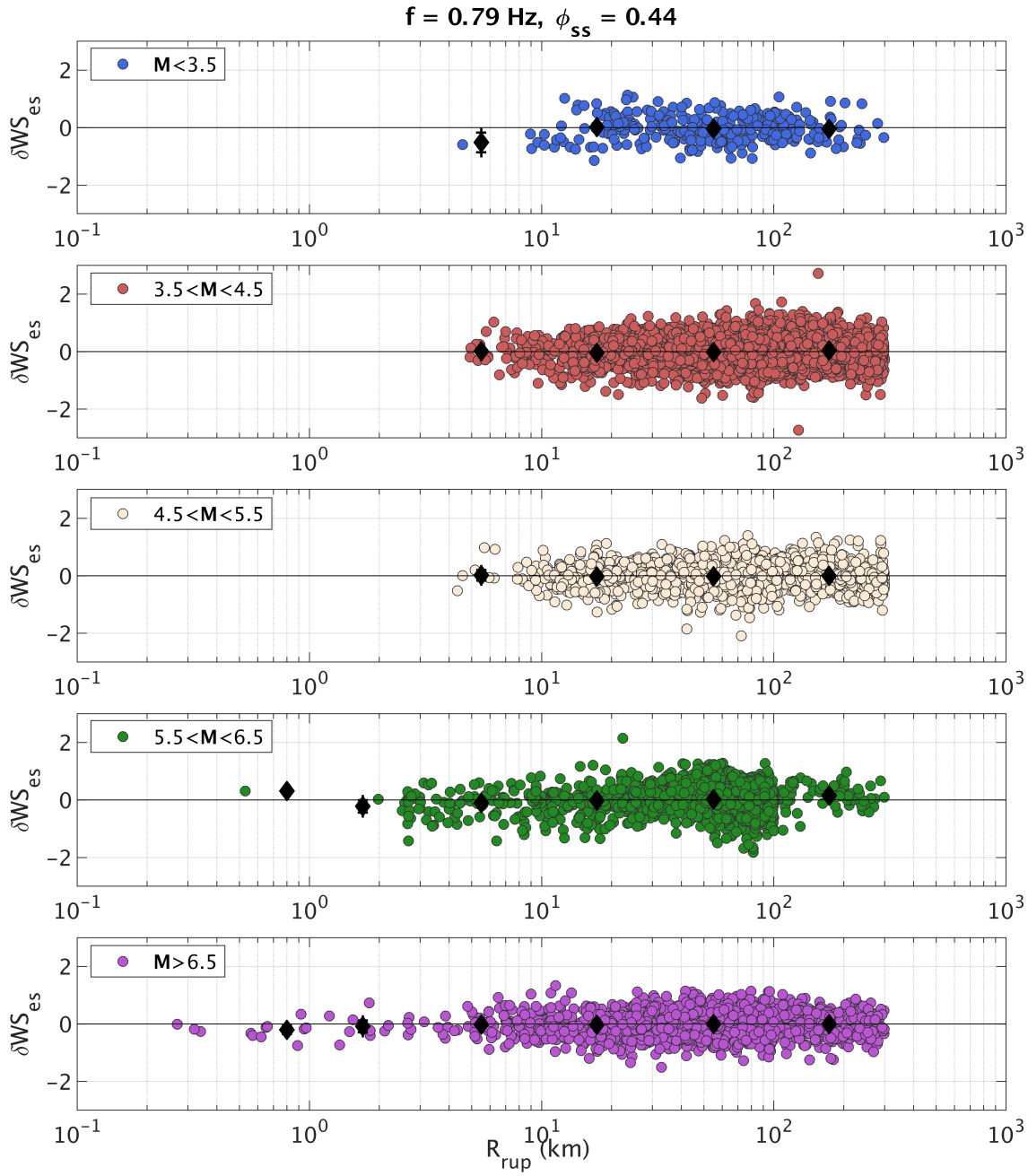

*Figure A-38. Within-site residuals (δWS_{es}) versus R_{rup}, binned by **M**, for $f = 0.8$ Hz.*

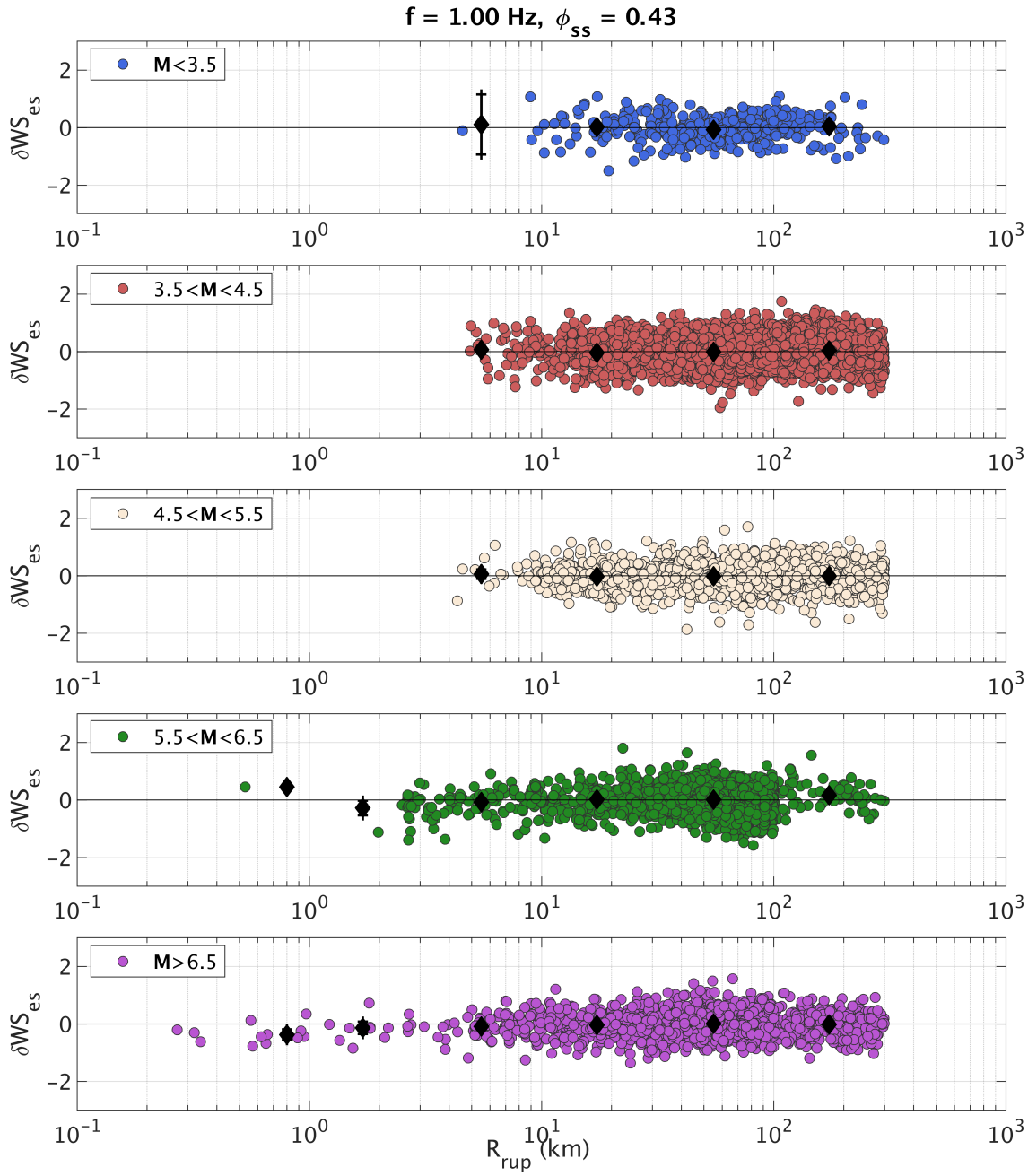

*Figure A-39. Within-site residuals (δWS_{es}) versus R_{rup}, binned by **M**, for $f = 1$ Hz.*

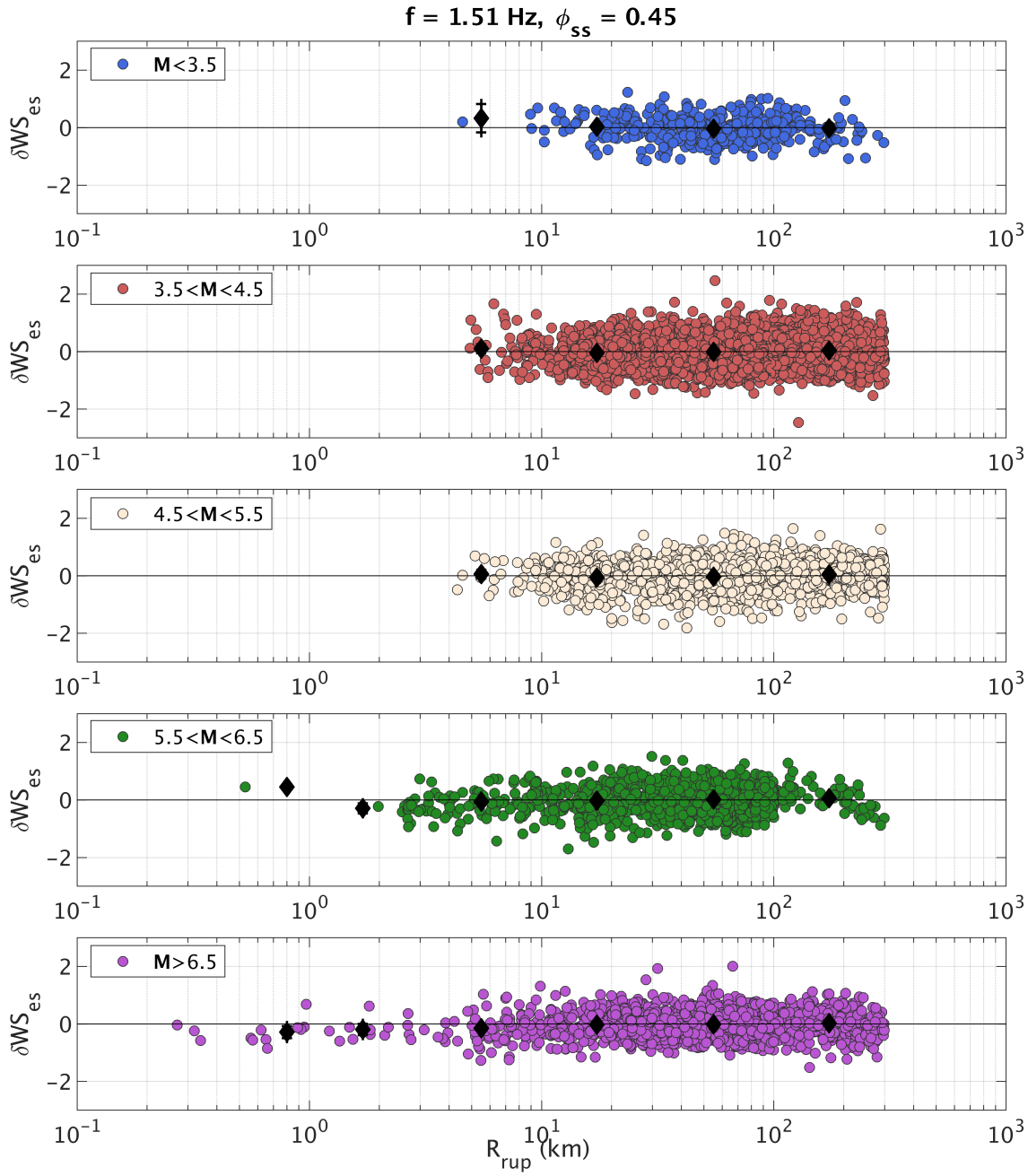

*Figure A-40. Within-site residuals (δWS_{es}) versus R_{rup}, binned by **M**, for $f = 1.5$ Hz.*

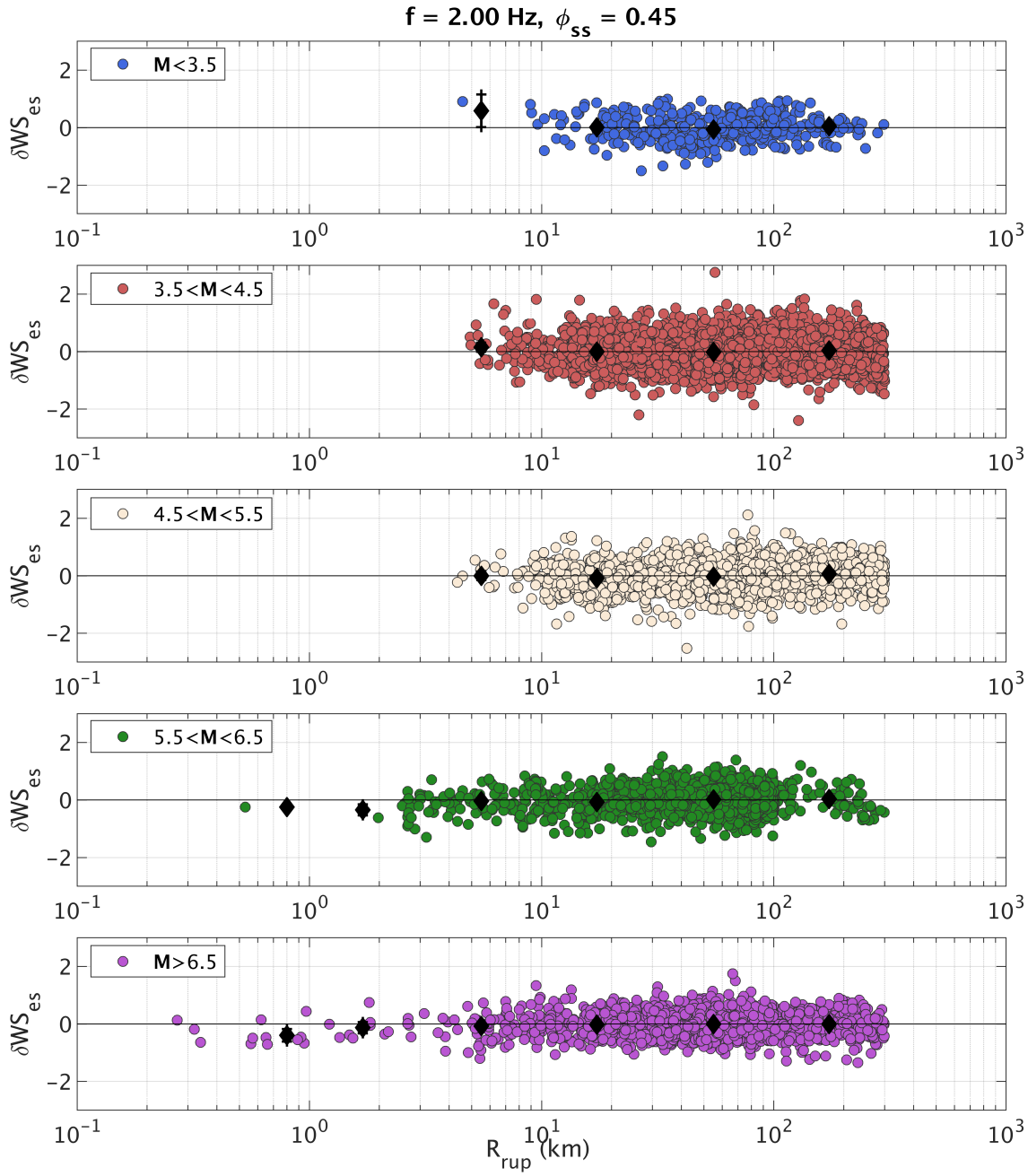

*Figure A-41. Within-site residuals (δWS_{es}) versus R_{rup}, binned by **M**, for $f = 2$ Hz.*

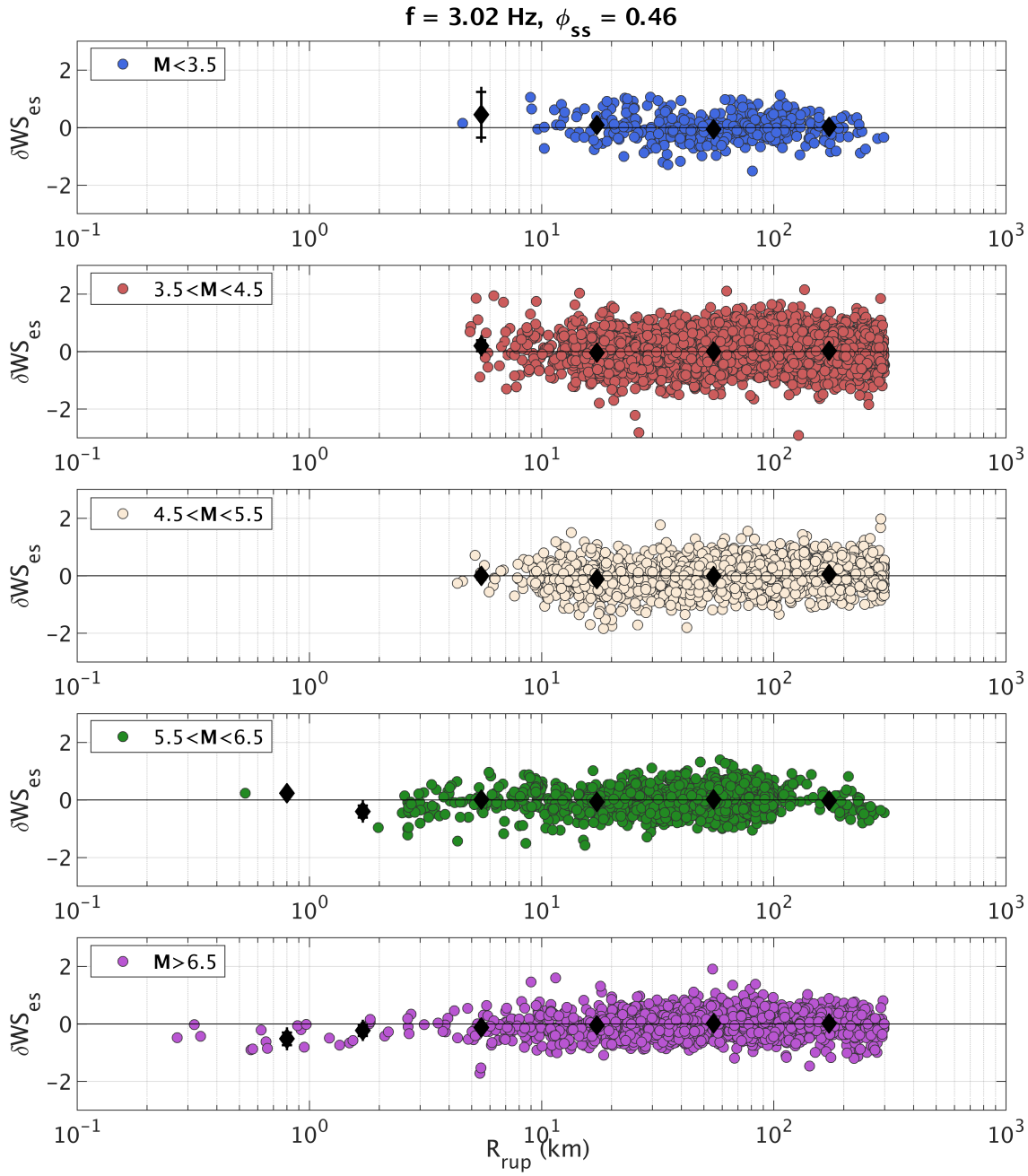

*Figure A-42. Within-site residuals (δWS_{es}) versus R_{rup}, binned by **M**, for $f = 3$ Hz.*

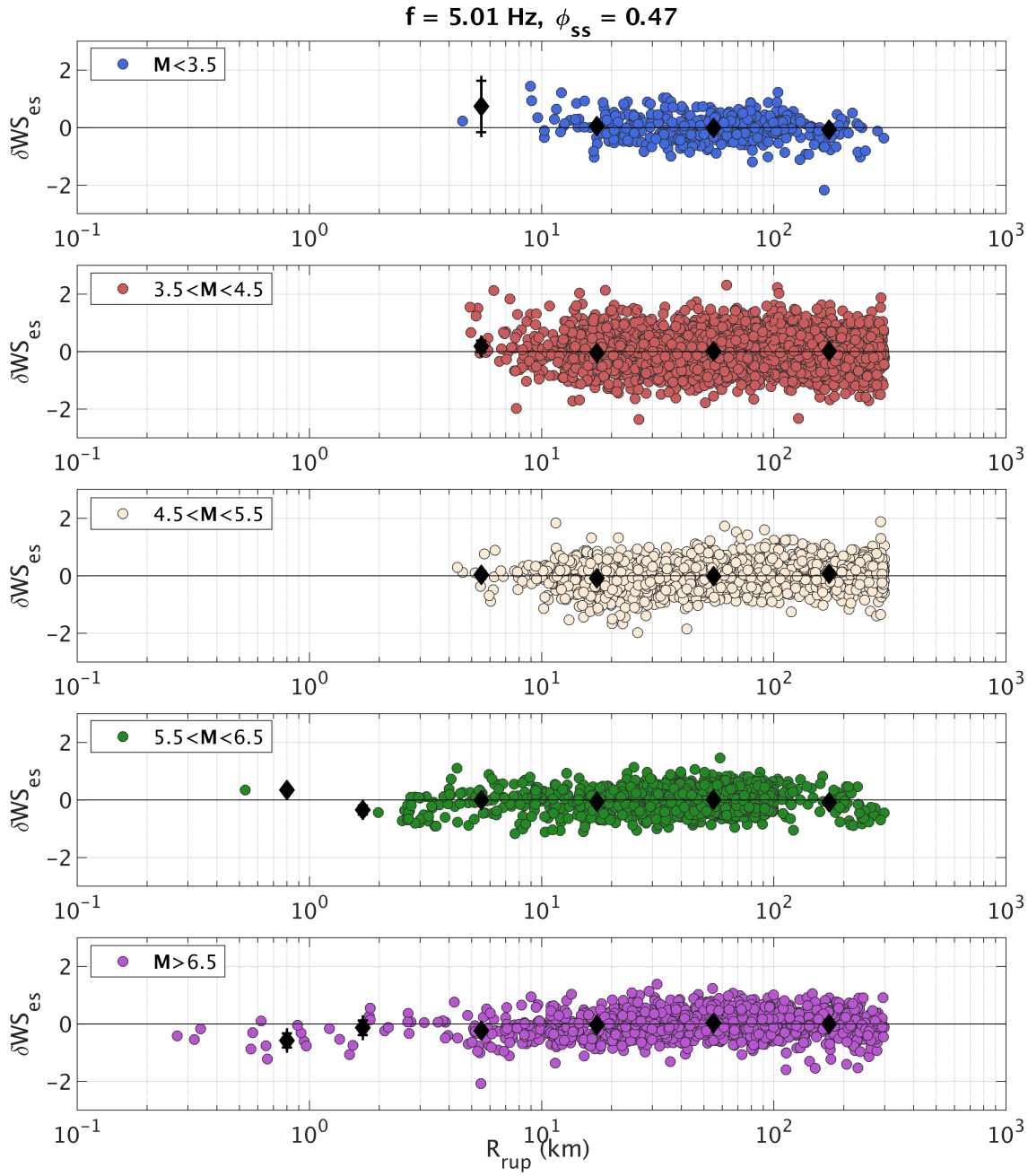

*Figure A-43. Within-site residuals (δWS_{es}) versus R_{rup}, binned by **M**, for $f = 5$ Hz.*

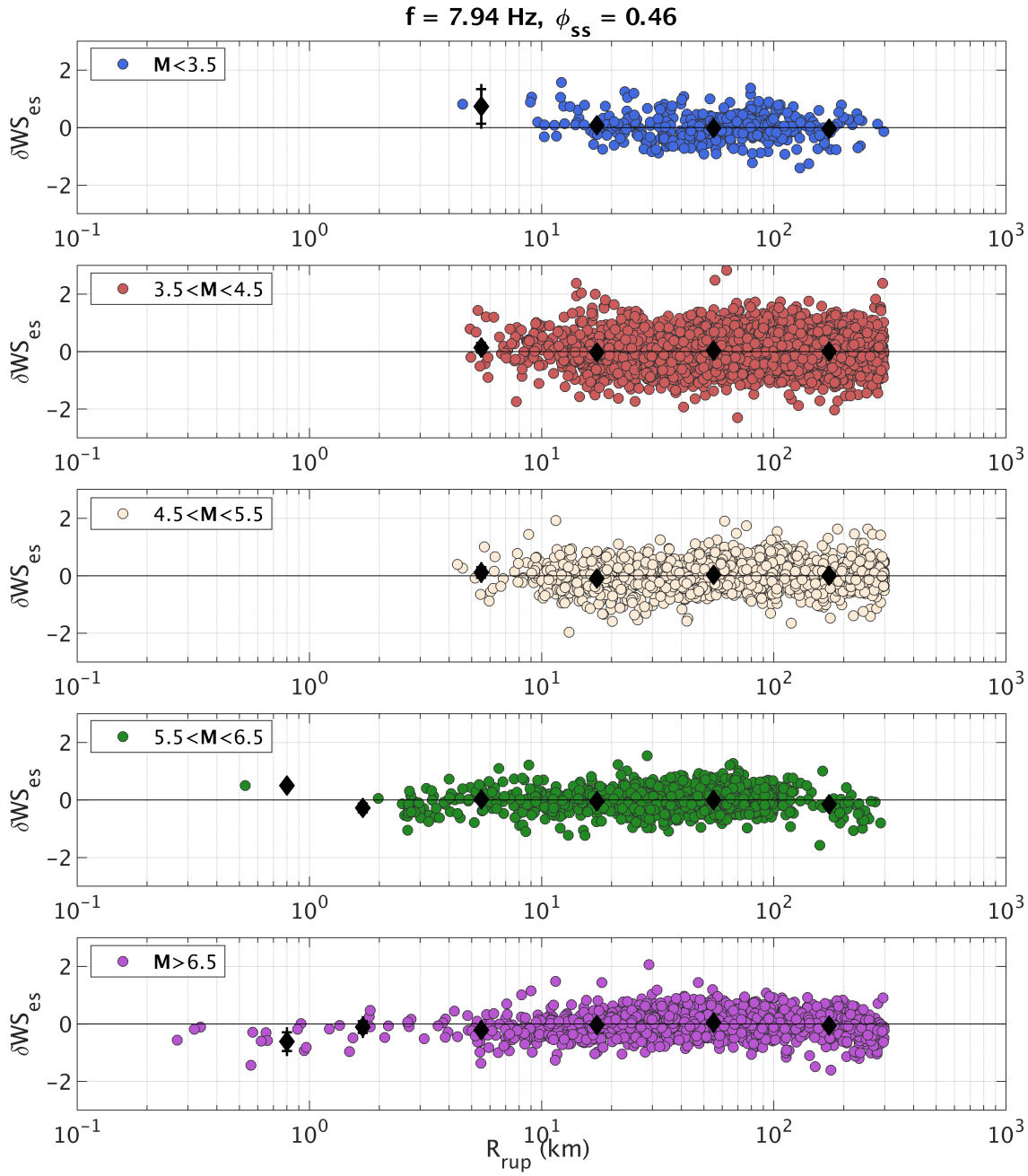

*Figure A-44. Within-site residuals (δWS_{es}) versus R_{rup}, binned by **M**, for $f = 8$ Hz.*

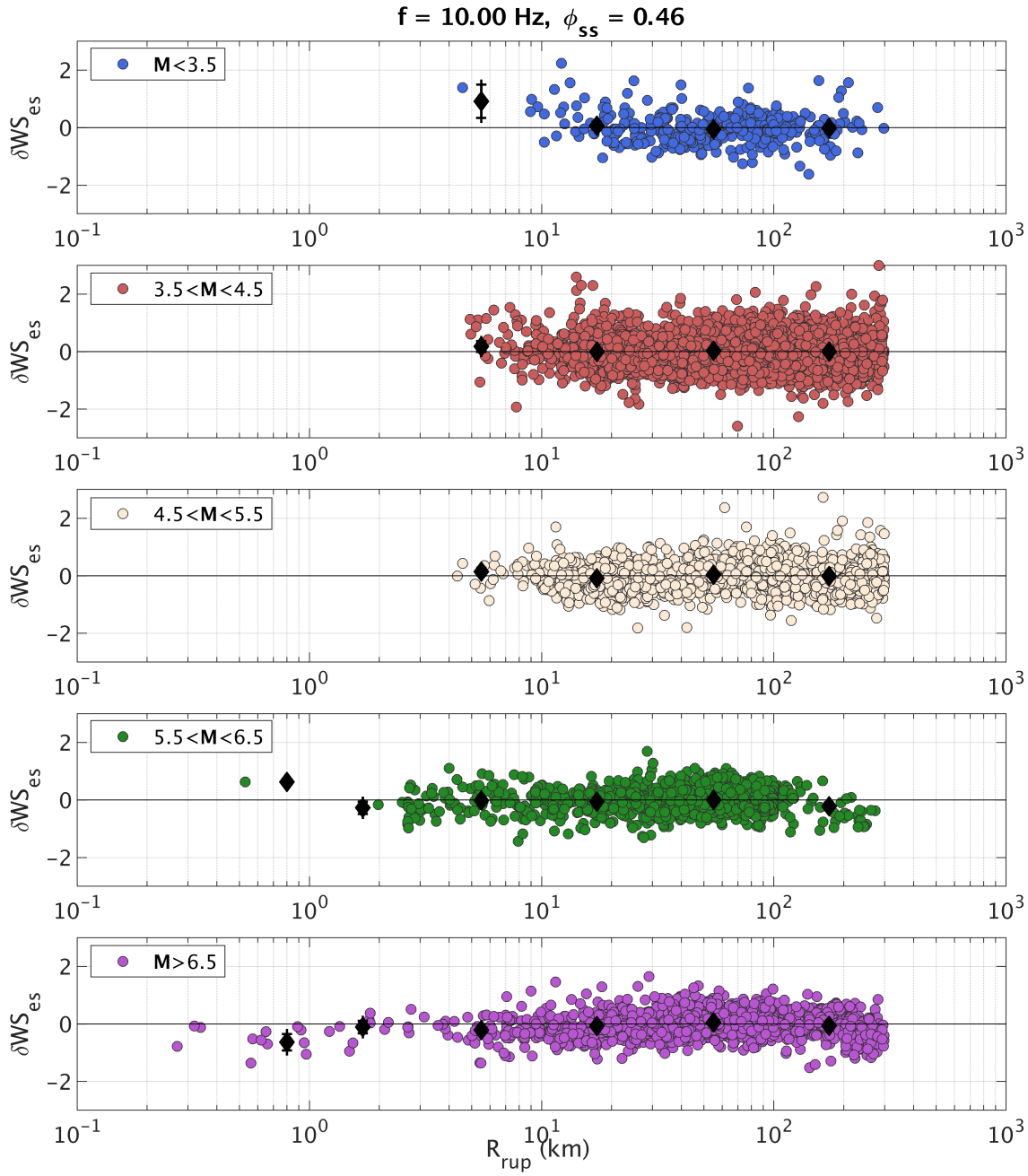

*Figure A-45. Within-site residuals (δWS_{es}) versus R_{rup}, binned by **M**, for $f = 10$ Hz.*

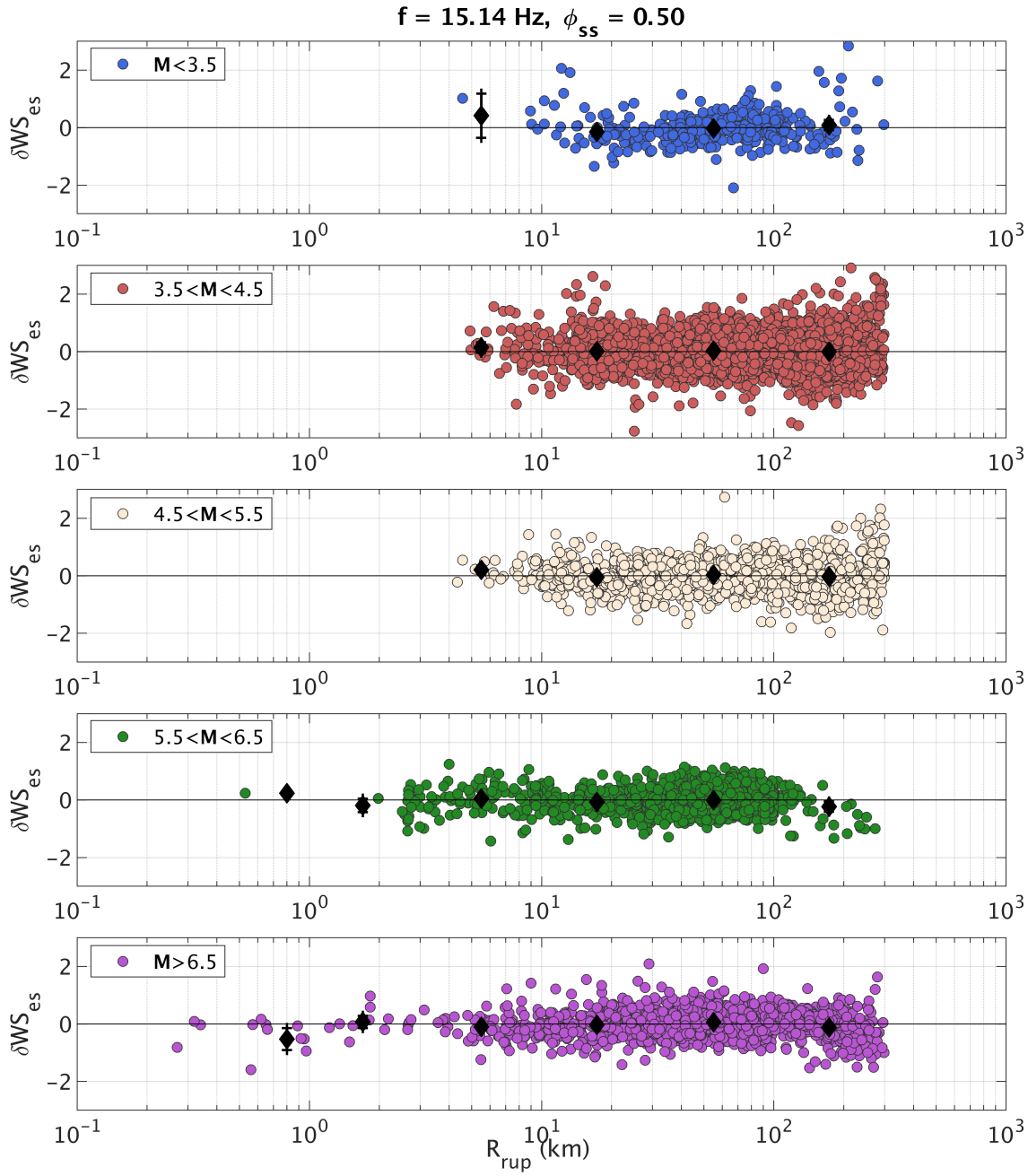

*Figure A-46. Within-site residuals (δWS_{es}) versus R_{rup}, binned by **M**, for $f = 15$ Hz.*

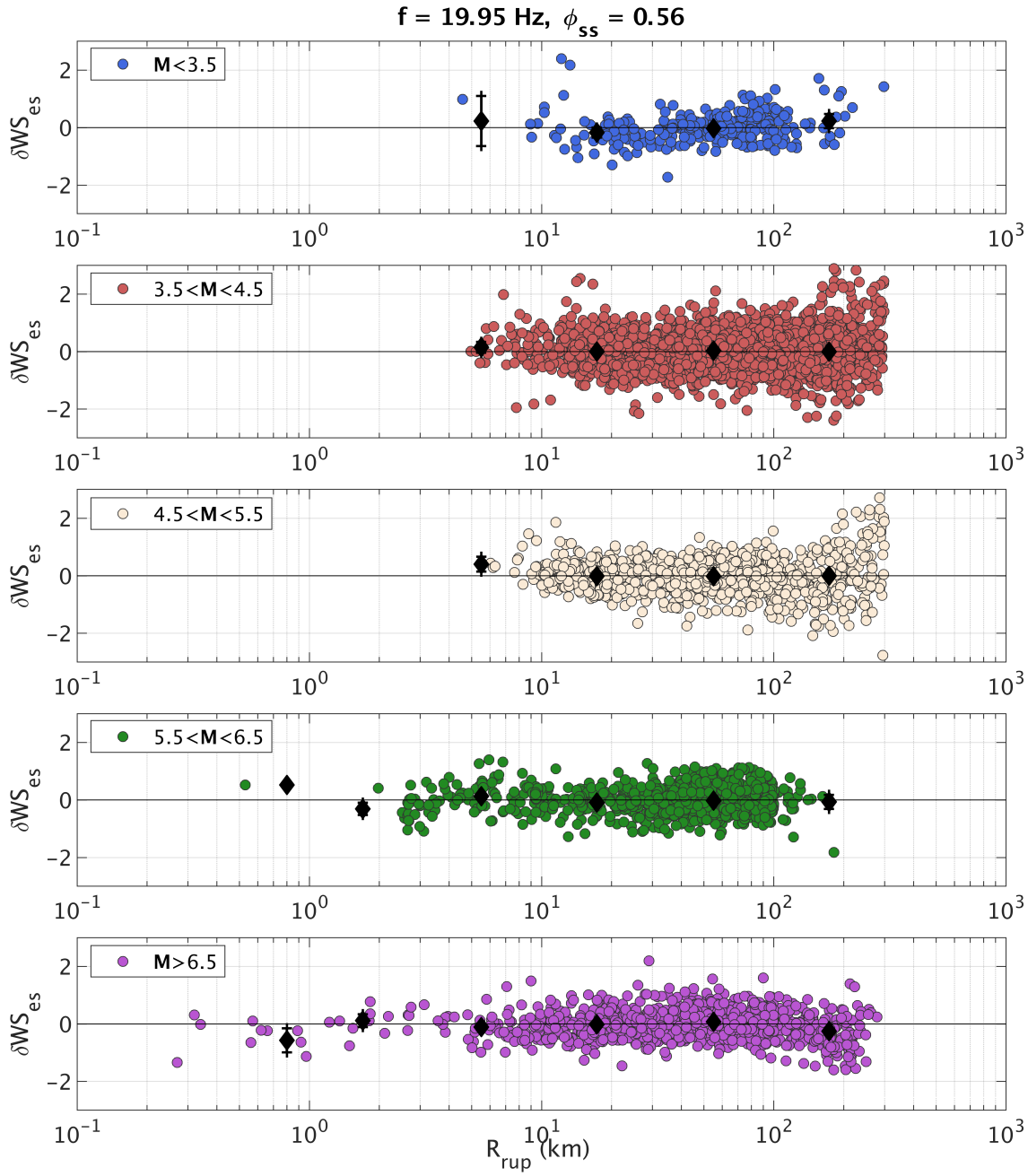

*Figure A-47. Within-site residuals (δWS_{es}) versus R_{rup}, binned by **M**, for $f = 20$ Hz.*

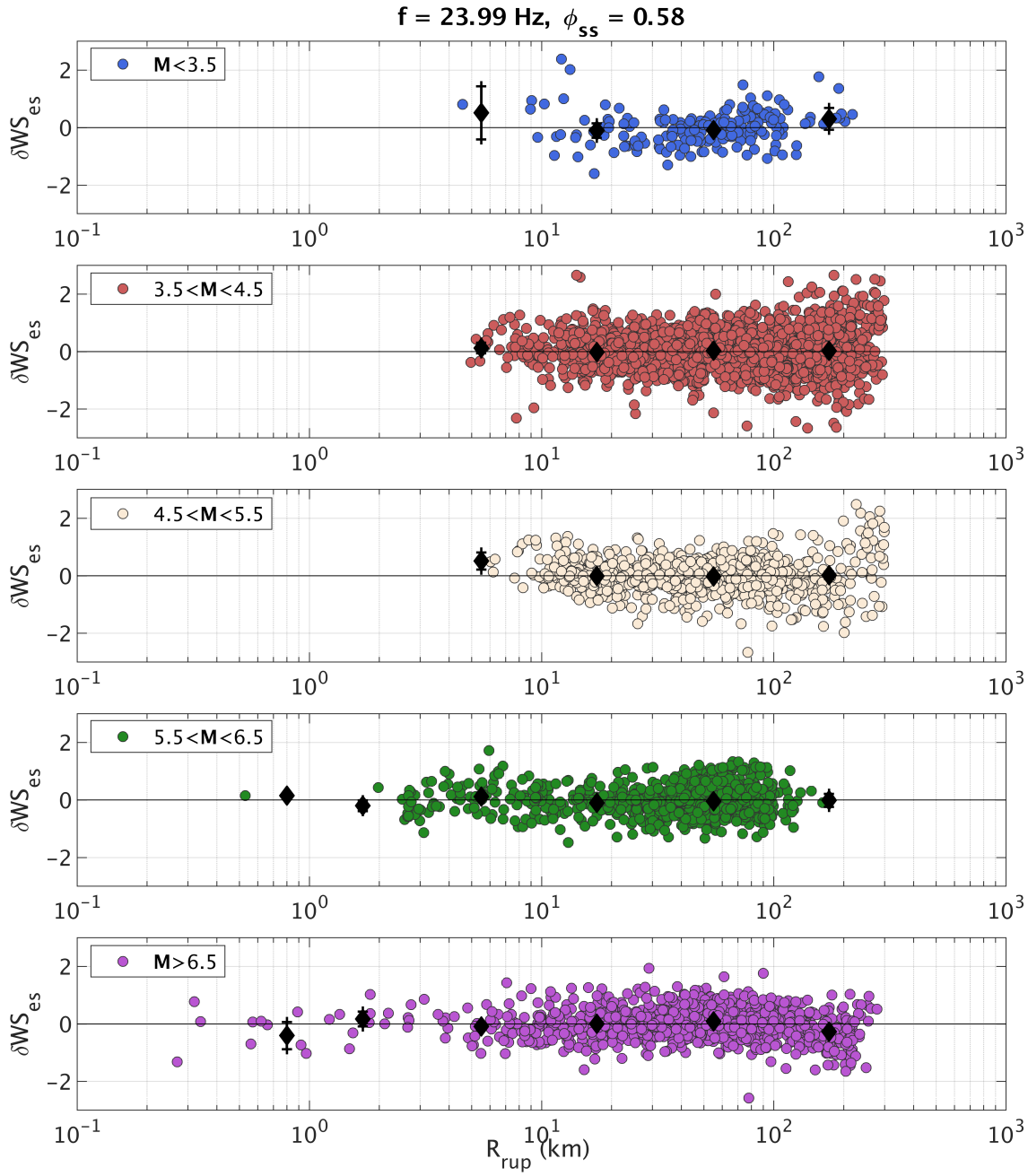

*Figure A-48. Within-site residuals (δWS_{es}) versus R_{rup}, binned by **M**, for $f = 24$ Hz.*

Appendix B:

MATLAB program for the EAS GMM

This appendix contains a MATLAB program to implement the EAS GMM developed in Chapter 2. The program includes tables of model coefficients. The program is included as an electronic attachment to this dissertation.

Appendix C:

Tables for the model for the inter-frequency correlation of epsilon for Fourier Amplitude Spectra

This electronic appendix contains tables related to the correlation model developed in Chapter 3. There are six tables. Table C1 lists the 239 frequencies spanning 0.1-24 Hz, and each 239x239 correlation matrix in Tables C2 through C6 aligns with these frequencies.

List of Tables:

- Table C1: The full range of frequencies, model coefficients, and EAS standard deviations for calculating the total correlation.
- Table C2: The empirical correlation matrix for Between-event residuals.
- Table C3: The empirical correlation matrix for Between-site residuals.
- Table C4: The empirical correlation matrix for Within-site residuals.
- Table C5: The total empirical correlation matrix.
- Table C6: The model total correlation matrix.